POLITECNICO
MILANO 1863

SCHOOL OF INDUSTRIAL AND INFORMATION ENGINEERING

Development and Characterization of Protective Coatings Resistant to Irradiation

PhD Thesis in
Energy and Nuclear Science and Technology

Author: **Davide Loiacono**

Advisor: Prof. Marco G. Beghi
Co-advisor: Dr. Fabio di Fonzo
Tutor: Prof. Lelio Luzzi

Abstract

This thesis leverages the Pulsed Laser Deposition (PLD) processes, recognized for producing robust and efficient coatings, and introduces novel applications in the nuclear sector and space exploration, particularly as resistant materials to ionizing radiation. On the nuclear side, the focus is on the Lead-cooled Fast Reactors (LFRs), a Generation-IV nuclear system offering promising safety features and efficiency advancements. The thesis meticulously investigates the use of corrosion-resistant bulk alloys, surface-alloying treatments, or coatings in the nuclear sector, attempting to address the existing gaps in the area of materials suitable for high-temperature, corrosive, and radiation-heavy environments found in LFRs. Specific focus is placed on applying Al_2O_3 PLD coatings to enhance existing materials' corrosion resistance, radiation tolerance, and mechanical stability.

On the other side, the research offers an innovative approach to enhance the effectiveness of solar cells used in space exploration, addressing the issues associated with the conventional solar cell stack. Applying a protective layer directly onto the solar cell aims at establishing an optical transparent radiation shield, combating the detrimental effects of low-energy particle. This endeavor is part of the SpaceSolarShield project and has significant implications for the solar cell manufacturing industry, promising improvements in performance efficiency, power density, and production control.

This work conducted various characterizations and experiments designed to mimic real operational conditions. It explored the unique properties of the materials and their behaviors under different scenarios, including irradiation exposure, mechanical stresses, and temperature fluctuations. A critical examination of the amorphous alumina , its radiation tolerance, plasticity, and the effects of radiation exposure on its structure is meticulously performed, contributing valuable data for potential practical engineering applications. In conclusion, the thesis innovatively expands the boundaries of the traditional coatings' performance and operational range by providing novel solutions and strategies. This comprehensive study stands to advance the fields of nuclear and space applications research and may potentially provide solutions applicable to other systems.

Keywords: Radiation Resistant Protective Coatings, Amorphous Alumina Coatings, Lead-cooled Fast Reactors (LFR), Space Solar Cells

Contents

Introduction

0.1. Advancing the Technology: Materials Science and Nanotechnology for a Greener Future

In the present century, our world stands on the threshold of an extraordinary era of innovation, predominantly propelled by advancements in materials science and engineering. The importance of materials is indisputable, as they constitute the very bedrock of technology and the systems upon which we depend daily [1]. As our civilization advances steadily, the need for unique materials with tailored characteristics grows more vigorous. At the same time, simultaneously, the urgency to address the environmental consequences of our consumption becomes increasingly important [2]. The global quest for a sustainable future requires pursuing innovative solutions encompassing material and technology development to address the many growing demands of our society [3].

Indeed, one of the paramount challenges confronting contemporary society is the finite capacity of Earth's resources and the constraints on waste disposal that our environment can withstand. This delicate equilibrium between resource consumption and environmental conservation has impelled researchers to explore inventive methodologies for minimizing the environmental burden and fostering sustainable development [4]. The European Environment Agency (EEA) has underscored the significance of material selection in diminishing the environmental impact of products and technologies since it accounts for a a substantial portion of greenhouse gas emissions and water usage [4]. Consequently, the demand for materials with enhanced properties and attenuated environmental impact is at an all-time high.

To meet this idea, one possibility is to support the development and utilization of sustainable materials characterized by their low environmental impact, high performance, and reduced dependency on finite resources [5]. Despite their potential for creating a more sustainable future, several challenges hinder the widespread adoption of these materials. These challenges include economic factors, technical barriers, and the need for a robust regulatory framework [6]. Economic challenges include the high production costs and relatively low economies of scale for sustainable materials compared to conventional alternatives [7]. Conversely, another solution is to use materials and existing technology more efficiently. This can be achieved by optimizing manufacturing processes to minimize waste, improving material recycling methods, and adopting innovative technologies that enable better utilization of the already existing materials. Another

possible route is through the exploitation of coatings and thin films, which have shown great potential in improving various materials' performance, durability, and sustainability [8]. Indeed, the emergence of nanotechnology has profoundly transformed the realm of materials, equipping researchers with the ability to design and construct materials at the nanometer scale. Nanotechnology offers unparalleled control over a material's characteristics, unlocking the potential for novel applications across diverse fields, from energy storage to drug delivery; paving the way for developing advanced materials that exhibit enhanced performance, diminished environmental impact, and heightened recyclability [9].

As we embark on a new era of innovation, the significance of materials science and engineering in shaping our world grows more apparent. The creation of groundbreaking materials and processes can substantially enhance our quality of life while addressing pressing issues of our time, such as climate change and resource scarcity [10]. The future of materials science is bright, yet it requires constant vigilance and a collective effort to balance the drive for innovation with the pursuit of sustainability. By focusing on the responsible development and use of materials, we can establish a foundation for a sustainable future that benefits all of humanity.

In the upcoming section, the critical role of material and coatings in sustainable material and technology advancement will be deepen, delving into their applications and examining two of the most compelling use cases: nuclear reactors and space applications and the challenges these two fields present in material science. Combining these two seemingly disparate fields of application might initially appear to be an audacious attempt, as their respective applications seem to be worlds apart. However, this unconventional fusion is firmly grounded in the ambitious objective of this thesis, which seeks to advance the development of innovative coatings that can withstand the onslaught of ionizing radiation. Indeed, both the nuclear and space domains are not only defined by the extreme and unforgiving conditions in which their corresponding materials are expected to perform, but also by the pervasive and ever-present threat of radiation in both environments. As will be explored in greater detail further on, radiation exposure poses significant challenges, necessitating the development of diverse and effective strategies to address these issues in the context of each unique field.

0.2. Green Nuclear Energy: Tackling Concerns with GIV Fast Fission Reactors

0.2.1. Nuclear and Renewable Synergy for Net-Zero Emissions by 2050

As we approach a critical juncture in international efforts to combat the climate crisis—a formidable challenge of our times—we witness many countries pledging to achieve net-zero emissions by mid-century or shortly thereafter. Yet, this commendable progress is shadowed by the simultaneous increase in global greenhouse gas emissions. Aligning global carbon dioxide (CO_2), emissions reduction efforts to achieve net zero by 2050 is essential to limiting the long-term average global temperature increase to 1.5°C [11]. Hence, climate change presents us with a stark challenge: to reduce greenhouse gas emissions to net zero much faster than we have done so far or to face the increasingly catastrophic consequences of an inexorably warming planet.

The net-zero emissions pathway detailed in the report "Net Zero by 2050" [12] produced by the International Energy Agency (IEA), envisions a world in 2030 where the global economy is 40% larger than it is today while consuming 7% less energy. This ambitious vision is a testament to the transformative change required to pursue a sustainable future. Furthermore, the ambitious target of reaching net zero by 2050 calls for not only the swift deployment of currently available technologies but also the widespread adoption of yet-to-be-commercialized innovations. Critical domains such as electrification, hydrogen, bioenergy, and carbon capture, utilization, and storage (CCUS) presently receive only approximately one-third of the public R&D funding allocated to more established low-carbon electricity generation and energy efficiency technologies [11, 12].

Moreover, the report [12] presents various scenarios for the development of the energy sector. These scenarios provide valuable insights and benchmarks for evaluating climate action and shaping sustainable energy policies. The Stated Policies Scenario (STEPS) projects the future of global energy consumption and greenhouse gas emissions based on current government policies and commitments. This baseline scenario assumes that countries will adhere to their plans and pledges for emissions reduction without accounting for any additional measures or actions necessary to achieve net-zero emissions by 2050. Instead, the Announced Pledges Case (APC) assumes that all declared national net-zero emissions pledges are fulfilled completely and on schedule, even if specific policies do not support them. This scenario aims at limiting global temperature rise to 1.5°C above pre-industrial levels by attaining global net-zero CO_2 emissions by 2050. Under the APC scenario, global electricity generation is projected to nearly double, exceeding 50000 TWh in 2050. Coal usage must decrease by 50%, while natural gas usage will expand by 10% in 2025, maintaining that level until 2050. Efficiency, electrification, and the substitution of coal with low-emission sources in electricity generation are pivotal in realizing net-zero goals in the APC, particularly leading up to 2030. The implications of the APC on total energy supply in comparison with the STEPS, implies the global total energy supply will experience a 15% increase between 2020 and 2050 in the APC while it expands by one-third in the STEPS. The remarkable escalation in energy consumption can be ascribed to the swift

expansion of economies and burgeoning populations in emergent territories, where commitments to achieving net-zero emissions are comparatively sparse nowadays. Addressing this challenge necessitates a multifaceted approach to the generation of energy. What discussed is encapsulated in Figure 1, which delineates the aggregate energy provision originating from diverse sources within the two distinct frameworks.

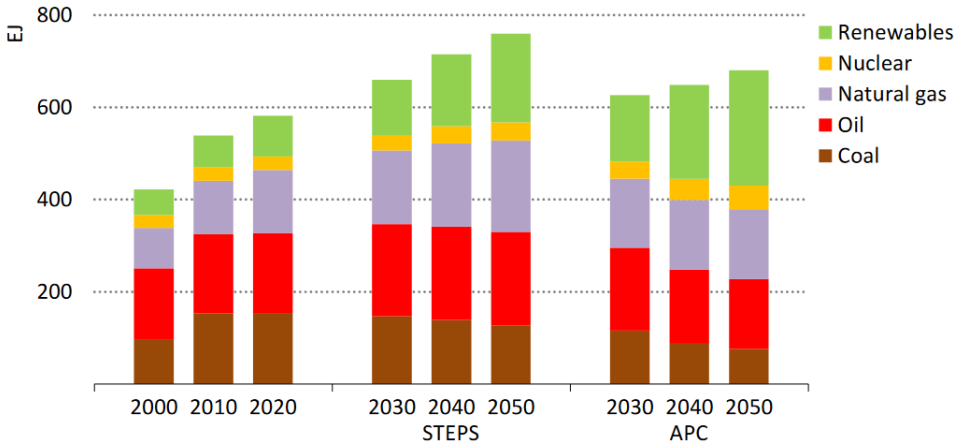

Figure 1: Global electricity consumption visualized in Exajoules (EJ): Unveiling the energy mosaic of diverse sources within interconnected frameworks (STEPS, APC) [12]

Among the scenarios outlined in the International Energy Agency's roadmap for the global energy sector, there is also the Net-Zero Emissions by 2050 Scenario (NZE)[12], which strives to align energy-related and industrial process CO_2 emissions with the reductions outlined in the IPCC's Special Report on Global Warming of 1.5°C [11]. In the NZE, the electricity sector is the initial primary target for rapid and significant emissions reductions. As the largest source of emissions in 2020, electricity generation emissions plummet by nearly 60% up to 2030, predominantly due to significant cutbacks from coal-fired power plants. This ambitious emissions reduction is achieved through electrification, pursuing all energy and materials efficiency opportunities, behavioral changes to decrease energy service demands, and a significant transition from traditional bioenergy use. By 2050, the energy mix in the NZE will be markedly more diverse than it is today. While, in 2020, oil accounted for 30% of the total energy supply, followed by coal at 26% and natural gas at 23%, in stark contrast, renewables constitute two-thirds of energy use in 2050, divided among bioenergy, wind, solar, hydroelectricity, and geothermal sources. Additionally, nuclear power will experience a significant surge, with the energy supply nearly doubling between 2020 and 2050 [12]. The Figure 2 summarizes the Global Electricity Consumption in Exajoules (EJ) from various sources within the context of the Net Zero Emission Framework.

As mentioned above, as the world grapples with the catastrophic impacts of climate change, it becomes increasingly vital to transition from fossil fuels to clean, sustainable energy sources [11]. To reach the objectives outlined in the IPCC's Special Report on Global Warming of 1.5°C,

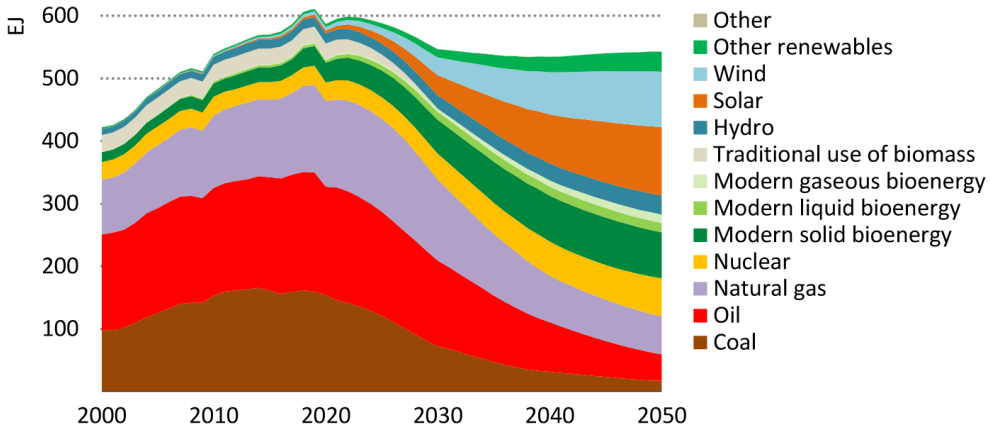

Figure 2: Visualization of the global electricity consumption in Exajoules (EJ) across diverse sources within the Net Zero Emission framework. [12]

a two-pronged approach is required: extensive electrification of the economy with low-carbon electricity from renewables and nuclear power and the deployment of other low-carbon energy carriers in applications less suited to electrification, such as hard-to-abate sectors in industry and transportation [12, 13]. A diverse mix of renewable energy sources, including solar, wind, and hydropower, has been deployed to combat three-quarters of greenhouse gas emissions attributed to the energy sector [14]. However, given the intermittent nature of these sources, it is imperative to develop complementary, reliable, and scalable technologies such as nuclear power, particularly Gen IV reactors [13, 15]. Nuclear energy, which has avoided roughly 70 gigatonnes of CO_2 emissions over the past five decades and continues to prevent more than 1 Gt CO_2 annually, is critical to achieving global net-zero objectives [13]. In partnership with renewable energy sources and other low-carbon options, nuclear energy forms part of a sustainable energy system that decarbonizes electric and non-electric energy production. Although variable renewable energy technologies like solar and wind, energy storage technologies, and low carbon fuels such as hydrogen will deliver the bulk of decarbonization, nuclear power plays a vital complementary role by ensuring 24/7 energy supply reliability and dispatchability [12, 13, 14]. Integrating nuclear energy with renewable energy expedites the objectives discussed above, as nuclear power's low material intensity makes it less susceptible to bottlenecks in critical mineral supply chains. Furthermore, advanced nuclear reactor designs, such as the six distinct Gen IV reactors [16], offer significant improvements over earlier generations in terms of safety, efficiency, sustainability, and waste management, solidifying nuclear power's pivotal role in the global energy landscape [13, 16]. These GEN IV cutting-edge designs include the Gas-cooled Fast Reactor (GFR), Lead-cooled Fast Reactor (LFR), Molten Salt Reactor (MSR), Sodium-cooled Fast Reactor (SFR), Supercritical Water-cooled Reactor (SCWR), and Very High Temperature Reactor (VHTR), offer unique characteristics and capabilities, thus enhancing the potential for a swift and effective transition to a more sustainable and decarbonized energy landscape [16].

0.2.2. Key Challenges Facing Nuclear Energy Production

Nuclear energy plays a significant role in global energy production despite the challenges it faces. Many older nuclear reactors are applying for license extensions, while newer and safer Generation III and III+ reactors are being developed [17]. Currently, there are 442 operational nuclear reactors worldwide, but this number can change due to aging infrastructure, decommissioning, and construction [17]. Investment in nuclear energy is ongoing, with 52 reactors under construction globally. However, the utilization of nuclear energy presents various challenges that need to be addressed for safe and sustainable production. It is important to tackle these challenges to ensure that nuclear energy can continue to contribute to global electricity generation. Below, major challenges confronting nuclear energy production are exposed.

Safety and Security:

The safety and security of nuclear power plants are crucial, with challenges including accident prevention, impact mitigation, and protection against unauthorized use of nuclear materials. The importance of robust reactor designs, comprehensive emergency response plans, and strict regulatory frameworks cannot be overstated.

The nuclear accidents at Chernobyl in 1986 and Fukushima Daiichi in 2011 underscore the necessity of these safety measures highlighting the critical importance of safety and security in nuclear power plants. They serve as reminders of the need for continuous improvement in reactor design, emergency preparedness, and regulatory oversight.

Nuclear Waste Management:

The current nuclear energy production method, known as the "once-through" cycle, has significant drawbacks in uranium resource utilization and produces a large volume of nuclear waste [18]. The long-term storage of this waste poses environmental and health risks, leading to ongoing research for better waste treatment technologies [19]. One promising solution is the transmutation process, which uses neutron-induced reactions to convert long-lived radioactive isotopes into short-lived or stable ones [18].

The efficient incineration of high-radiotoxicity waste components depends on the availability of a fast neutron spectrum, and options under consideration include Accelerator Driven Systems [18]. Generation IV reactors, particularly the Lead-cooled Fast Reactor (LFR), Gas-cooled Fast Reactor (GFR), and Sodium-cooled Fast Reactor (SFR), present further opportunities for efficient waste transmutation. These advancements could help reduce the environmental impact of nuclear energy production.

Non-Proliferation:

Nuclear energy production raises concerns about potential nuclear weapons proliferation due to the dual-use nature of nuclear technologies. International treaties like the NPT address this by

promoting disarmament and non-proliferation [20]. While the expansion of nuclear power and Gen IV systems in response to climate change could exacerbate these concerns due to the required reprocessing and recycling capabilities, Gen IV systems also offer a tool for disarmament. They can efficiently reduce weapon material stockpiles by converting high-enriched uranium and plutonium into less sensitive materials, potentially aiding in managing spent nuclear fuel's plutonium inventory [21].

High Capital Costs:

The high capital investment required for nuclear power plants' construction and operation presents a significant financial challenge. To address this, advancements are being made in reactor design and construction techniques [17]. However, recent studies suggest that small and medium-sized reactors might offer a more viable solution in certain scenarios, such as in countries with small electric grids or limited investment capabilities, and in remote locations [18, 22] . Moreover, these reactors could potentially reduce the financial risks associated with large capital investments required for larger nuclear power plants [18, 22].

Public Perception and Acceptance:

Public perception and acceptance of nuclear energy play a crucial role in its widespread adoption. Concerns regarding nuclear accidents, radioactive waste, and nuclear proliferation can influence public opinion and policy decisions. Promoting transparency, education, and public engagement are essential to address the challenges related to public perception and acceptance of nuclear energy [23].

0.2.3. Revolutionizing Nuclear Energy: Europe's Pursuit of Lead-cooled Fast Reactor Technology

The international pursuit of LFR technology promises to revolutionize the future of nuclear energy. Notably, LFRs stand to address many of the challenges previously discussed, such as waste management and safety concerns. By improving the safety profile and efficiency of nuclear reactors, this emerging technology could potentially overcome the public apprehension and economic barriers currently hindering the broader adoption of nuclear energy [16].

The LFRs' advantages are connected to the utilization of lead or lead-alloys as coolant. The key benefits include high thermal efficiency, passive safety features, and the ability to transmute long-lived radioactive waste into shorter-lived isotopes [24, 25]. The high thermal efficiency of LFRs allows for more effective energy conversion, while the passive safety features enhance their reliability and reduce the likelihood of severe accidents [24]. Furthermore, the transmutation capabilities of LFRs contribute to sustainable waste management solutions, thus addressing significant environmental concerns [25]. Overall, these advantages position LFRs as a promising option for the future of nuclear power generation.

LFRs have garnered considerable attention due to their numerous advantages. As a result, various European initiatives, supported by funding from the European Commission and Euratom, have emerged. Several projects related to LFRs have been undertaken in Europe, though there may be updates or newer projects since then. Notable projects include the European Lead Fast Reactor (ELFR) [26], Advanced Lead Fast Reactor European Demonstrator (ALFRED) [24], Multi-purpose hYbrid Research Reactor for High-tech Applications (MYRRHA) [27], Lead-cooled European Advanced Demonstration Reactor (LEADER) [28]. The development of nuclear materials for LFRs has also been pursued, evidenced by projects such asthe GEneration iv Materials MAturity (GEMMA) [29] in 2016 and the INNovative StrUctural MATerials for Fission and Fusion (INNUMAT) [30] in 2022. At present, the 600 MWe ELFR is under evaluation, and the 100 MWe ALFRED is under construction. European researchers are also making headway with MYRRHA, a state-of-the-art accelerator-driven system demonstrator featuring a Pb-Bi alloy coolant and neutron spallation source [31].

NEWCLEO [32], a prominent company contributing to LFR technology advancements in Italy and Europe, exemplifies the growing interest in this promising reactor concept. The company's innovative fuel designs and thermal-hydraulic models are specifically tailored for LFRs, playing a crucial role in enhancing the efficiency and safety of these reactors.

Russia, building upon its nuclear-fueled submarines, has pursued LFR technology [33, 34]. China has made significant strides through considerable investment over the past decade [35, 36], while in the United States, Westinghouse and Hydromine have identified the LFR concept as an economically attractive option for Generation IV power systems, partnering with ENEA and Ansaldo Nucleare [37, 38, 39]. The Figure 3 provides an overview of the advancements in nuclear reactor designs.

Figure 3: (a) Initial representation of a LFR reported in the Gen IV report concerning a lead-cooled fast reactor. [16] (b) The prototype depiction presently being developed by Newcleo [40]. The design representation showcasing Rosatom's BREST-OD-300 reactor [41].

LFR prototypes and demonstrators share similar characteristics such as electric power capacity (100-200 MWe), operating conditions, and efficiencies of approximately 40% at core outlet temperatures ranging from 480°C to 550°C [36, 42]. The key difference lies in coolant choice, with two options considered: pure Lead and Lead Bismuth Eutectic (LBE), a 45% Pb and 55% Bi mixture. Despite its drawbacks, LBE remains a strong contender due to its lower melting point (124°C) compared to pure Pb (327°C), allowing for operation at lower temperatures without solidification risks [43]. The long-term commercial objective involves increasing the core outlet temperature to 800°C, significantly enhancing power generation efficiency [36, 37, 38, 39, 42, 43].

0.2.4. Material challenges in future generation Lead-cooled Fast Reactor systems

As the quest for efficient, sustainable, and safe energy continues, nuclear power technology keeps evolving, with fast reactors at the forefront. Precisely, LFRs promise advantages such as higher energy efficiency, waste minimization, and enhanced safety characteristics [44]. However, realizing these advantages is not without its material-related challenges.

The reactor core's high-temperature, high-irradiation, and corrosive environment necessitate materials with exceptional resilience. This chapter delves into the material challenges of future generation LFR systems, focusing on corrosion resistance, radiation damage, mechanical integrity, and fuel cladding concerns.

Presently, high-temperature steels occupy the leading position as the preferred structural materials for LFRs [45, 46, 47], thanks to their resilience under strenuous operational conditions and the comprehensive knowledge accumulated over decades of rigorous testing.

We can categorize steel alloys into two primary groups based on their crystalline structures: austenitic alloys (AuS) and ferritic/martensitic (F/M) alloys. AuS, characterized by a Face-Centred Cubic (FCC) structure, offer commendable toughness, reduced susceptibility to fatigue-induced failure, superior creep resistance, and increased ductility due to a typically higher strain-to-rupture level compared to their counterparts [46]. Contrarily, F/M steels, which exhibit a Body-Centred Cubic (BCC) structure, possess greater mechanical strength, improved thermal conductivity, superior resistance to thermal cycling, and a more robust response to swelling, either from voids or gases [46]. In the context of LFR systems, F/M alloys, such as T91 steel (9% Cr and 1% Mo, by weight), were initially proposed given the unsuitable compatibility of austenitic steels with lead alloys. However, a shift in preference has occurred towards austenitic steels, primarily due to their superior mechanical performance under irradiation. Notably, 316L and Ti-stabilized 1515-Ti have emerged as the most plausible options [45, 47].

While materials like Oxide Dispersion Strengthened (ODS) steels, MAX (Mn+1AXn) phases, SiCf/SiC (Silicon Carbide fiber-reinforced Silicon Carbide) composites, and refractory metals exhibit enticing properties, their potential extends to providing a more long-term perspective on materials [45]. Yet, for the foreseeable future, F/M steels and AuS retain their standing as the most promising candidates. These two types of structural materials stand on the precipice of delivering commercially viable, near-term solutions for the structural material requirements of LFRs [45, 48, 49].

Having understood the distinct properties and preferences of AuS and F/M steel alloys in the context of LFR systems, it is crucial now to delve into the specific influence of lead and radiation on these materials, thereby gaining a more comprehensive perspective on their performance and applicability in high-stress environments.

High-temperature corrosion by heavy liquid metals and corrosion-related effects

Lead, as a coolant, as mentioned above, showcases remarkable chemical stability, extraordinary heat transfer capabilities, and efficient neutron economy. However, when this element is utilized as the primary coolant, either in its pure form or as LBE, its inherent corrosive characteristics pose notable challenges to the traditional materials used in the construction of reactor systems, as highlighted by [50].

The onset of corrosion is a complex process stemming from direct chemical interactions, potentially leading to oxidation and intergranular corrosion, and from dissolution, which could result in liquid metal embrittlement of the structural elements [51]. The pillars that hold the key to understanding the behavior of heavy liquid metal systems are the oxygen concentration contained within and the ambient temperatures [51].

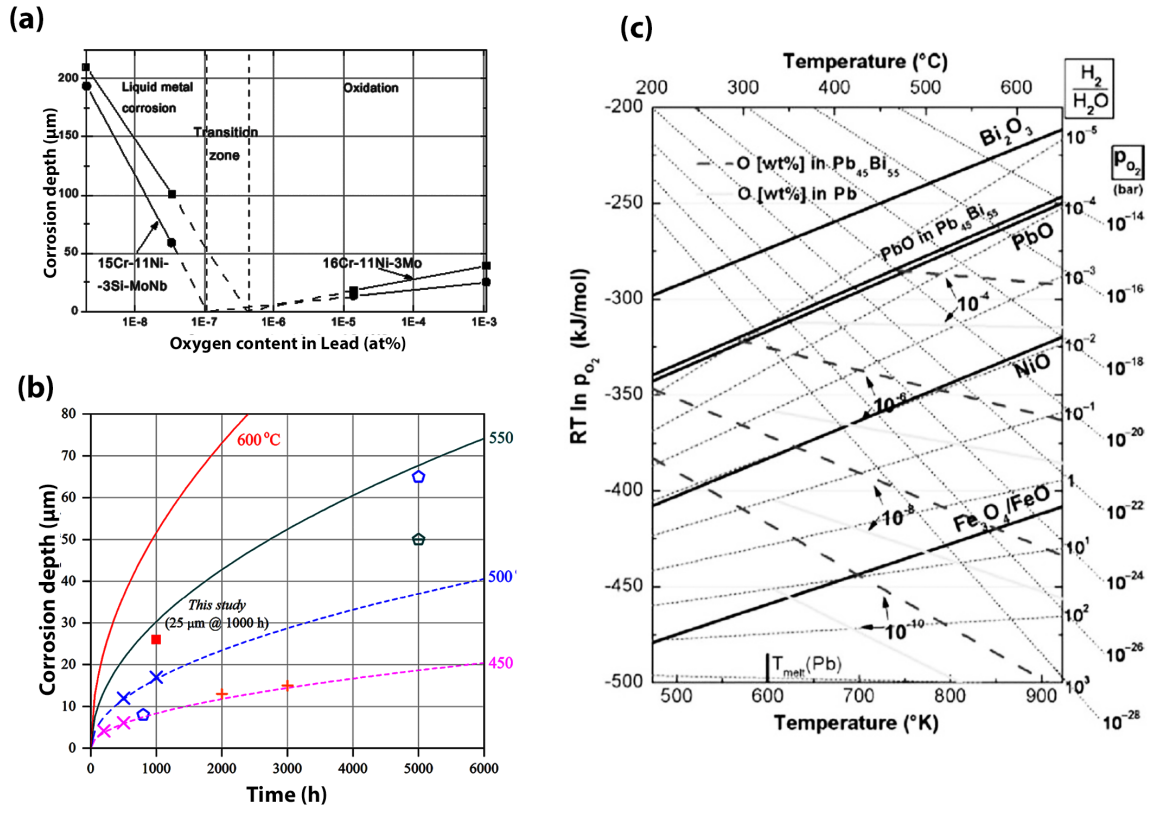

Figure 4: (a) Corrosion and oxidation dynamics of austenitic stainless steels in the presence of molten lead at 550°C, with varying oxygen contents [52]. A similar behaviour has been found for several other steels in similar conditions [53]. (b) Predictions of Corrosion Depths of HT9 Steel using the Parabolic Law [54] at Different Temperatures [55]. (c) Ellingham-Richardson diagram containing oxides of steel components and of Bi and Pb [53]. It shows the molar free energy of formation for oxides of nickel, iron, and chromium in comparison to lead and bismuth oxides

Regarding the oxygen content effect, in their research, Gorynin et.al [52] investigated the impact of varying oxygen concentrations on the corrosion and oxidation processes of two types of austenitic stainless steels. These experiments were conducted in a lead environment at a temperature of 550°C, over an extended period of 3000 hours. It was observed that for oxygen concentrations ranging between 10^{-8} and 10^{-10} wt.%, the steels experienced corrosion through dissolution (Figure 4 (a)). During the dissolution process, two phases can be distinguished. Initially, there is the *cleavage* of atomic bonds within the solid metal, leading to the formation of novel bonds with the atoms of the liquid metal or its contaminants in the boundary layer. Upon this occurrence, the dissolved atoms permeate through the boundary layer and into the liquid metal. The primary catalyst for this corrosion phenomenon is the solute metals' chemical activity disparity between the surface and the liquid metal. This chemical activity is contingent on the solubility and the respective chemical activity of the element in solid phases. Instead, in the case reported in [53], when the oxygen concentrations exceeded 10^{-7}-10^{-6} wt.%, the steels underwent oxidation (Figure 4 (a)). Corrosion at lower oxygen concentrations (10^{-8}–10^{-10} wt.%) began with pit formation on the material's surface. Over time, these pits expanded and coalesced to form a porous layer of corrosion, with its thickness growing linearly over time. This type of behavior was also observed across a wide variety of iron alloys [52, 53].

Extensive research has also investigated the crucial relationship between temperature and corrosion, especially in the lead or Lead-Bismuth Eutectic (LBE) systems [51, 56]. Numerous sources consistently indicate that corrosion rates in these systems also increase as the temperature rises [55, 57, 58, 59, 60, 61]. The effect of temperature on the corrosion rate can be explained by the thermal activation of species diffusion: as the temperature increases, the diffusion coefficients and the corrosion rate both exhibit an upward trend [62], as evidenced by the data presented in Figure 4 (b).

As mentioned above, increasing the dissolved oxygen levels in molten lead or LBE has been identified as a means to induce oxidation, resulting in the development of an oxide layer on the surface of structural materials upon direct contact with lead or LBE. An active oxygen control technique could be employed to safeguard underlying steel or alloys, wherein the formation of this oxide layer serves as a protective barrier against further corrosion. This technique is based on lead and bismuth chemical inactivity compared to the primary alloying elements found in structural steels [51, 53]. The Ellingham diagram in Figure 4 (c) demonstrates the lower molar free energy of formation for oxides of nickel and iron in comparison to lead and bismuth oxides. In the case of alloys containing iron, such as structural steels, the minimum concentration of oxygen is determined by the decomposition potential of magnetite (Fe_3O_4), which is considered the least stable oxide that can form on structural steels. Conversely, the maximum value is dictated by the precipitation of lead oxide. Once oxide films are established, the dissolution of structural materials becomes negligible due to the sluggish diffusion rate of steel's alloying elements within the oxide [53].

The ideal protective oxide layer, as described in [53], should possess certain characteristics: it

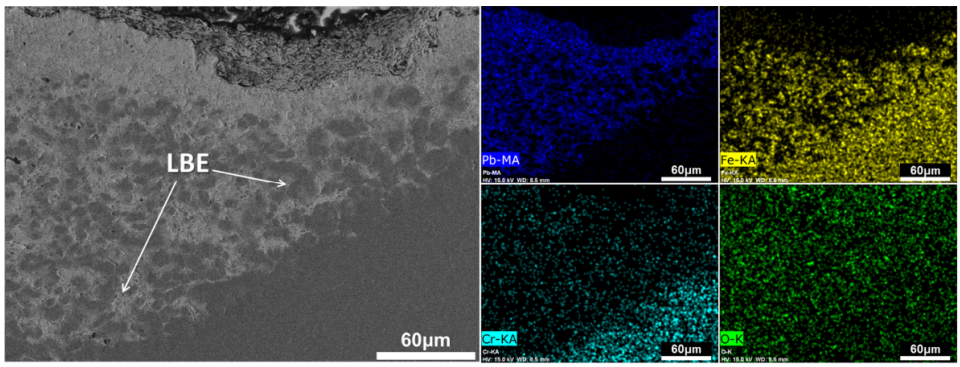

Figure 5: The image shows severe penetration of LBE (lead-bismuth eutectic) into HT9 material after 2000 hours at 600 °C. This penetration occurred following the delamination of the oxide layer formation observed at 1000 hours [55].

must be pore-free, crack-free, stress-free at operating temperatures, and resistant to spalling or damage during cooling or heating. However, achieving such a perfect layer is extremely challenging, especially in practical lead-alloy coolant systems. While an oxide layer can initially act as a protective barrier against corrosion, problems can arise if it becomes excessively thick or flakes off. Research has shown that prolonged corrosion processes can progressively destroy the oxide layer [53, 55]. Several factors can explain this destruction. As the oxide layer thickens, excessive lateral compressive stress can lead to out-of-plane strain on the layer. Indeed, when compressive in-plane stress is applied to a material, it induces internal forces trying to balance the applied stress. If the layer of the material has any asymmetry or imperfections, the force equilibrium may not be uniform across the depth. This non-uniform force distribution can lead to a moment or torque, causing the external layer to deform out-of-plane to achieve a new equilibrium state. Moreover, the stress within the oxide can increase due to compositional changes, as the transition from the metal lattice to the cation lattice of the oxide involves a volumetric change. Compressive stress in the transverse direction can induce upward normal stress, and the mismatch in thermal expansion coefficients of the components can also contribute to the cracking of the oxide layer. [53, 55].

The Figure 5 captures the extent of LBE penetration into HT9 material after a prolonged exposure of 2000 hours at 600 °C. Notably, this severe penetration occurred subsequent to the delamination of the previously formed oxide layer, which was initially observed after 1000 hours of testing [55]. The visible evidence underscores the significant challenges posed by LBE corrosion. The Figure 5 is the representation of the impossibility to induce the development of a flawless protective oxide layer in practical applications.

The interaction between heavy liquid metals and various materials, regardless of their chemical composition, is a subject of considerable interest due to the significant impact these metals can have on the mechanical properties of those materials. Among the well-documented phenomena resulting from this interaction is Liquid Metal Embrittlement (LME), liquid-metal-assisted creep,

and liquid-metal-assisted low fatigue cycle failure [63]. LME, in particular, is a phenomenon that has been thoroughly observed and investigated. This process occurs when a liquid metal comes into contact with a solid metal, decreasing the solid metal's ductility and toughness. This effect can occur even at temperatures where the liquid metal should not be corrosive or reactive. The mechanism of LME is often attributed to the penetration of the liquid metal along the grain boundaries of the solid metal, which weakens the bonds between the grains and results in the embrittlement of the material [64]. While the exact atomic-scale mechanisms are still a topic of research, it is generally agreed that LME is a surface phenomenon requiring tensile stress [64, 65]. This intergranular attack occurs because the atoms at the grain boundary have higher potential energy than those inside the grains. Therefore, the activation energy of the grain boundary atoms for dissolution is lower, and the probability of their transition to the melt and, hence, the dissolution rate is higher. If the concentration of higher solubility elements increases in the grain boundaries, the dissolution rate may increase due to the preferential dissolution of these elements [66].

On the other hand, liquid-metal-assisted creep [67, 68] and liquid-metal-assisted low fatigue cycle failure [69, 70] are two other effects that have been reported, albeit with inconsistent experimental evidence. The former refers to the accelerated deformation of a solid metal under mechanical stress in the presence of a liquid metal, which is typically more pronounced at high temperatures. The liquid metal can enhance diffusion, leading to faster creep rates [68]. The latter refers to reducing a material's resistance to fatigue failure, especially when in contact with liquid metal in low cycle conditions. This can lead to premature failure of the material under cyclic loading conditions [69, 70]. Nevertheless, the literature lacks complete understanding and data regarding these two phenomena. Their occurrence seems sensitive to many factors, including the specific material pairings, the applied mechanical stress, temperature, and certain impurities.

Mechanical Integrity

The preservation of structural robustness in reactor components is indispensable, particularly in light of the presented extreme stress situations to which these elements are exposed. The manifestation of embrittlement, fatigue, and creep, as previously elucidated, can be notably exacerbated in the presence of lead or LBE.

To ensure a thorough discussion, it is imperative to systematically examine the aforementioned phenomena. Their significant relevance to *the nuclear topic* regardless the presence of lead or LBE, necessitates a succinct yet comprehensive discourse, which is reported below.

- **Embrittlement** is a complex process that drastically reduces the ductility and fracture toughness of materials, transforming them into a brittle state, and consequently heightening the risk of material failure [71]. This process, precipitated by atomic-scale changes, is particularly critical in environments such as nuclear reactors where the utmost importance is placed on safety. Embrittlement can occur via multiple mechanisms, each dependent on

the material in question and the conditions it is exposed to. For instance, in metals, embrittlement can occur through grain boundary segregation, where certain impurity atoms migrate to the grain boundaries and weaken the overall structure [71, 72, 73]. This is a particular concern in Ni-Cr steel, where elements such as phosphorus can segregate to the grain boundaries and cause embrittlement [74]. Additionally, in the particular context of a nuclear reactor, phenomena such as irradiation [75] and hydrogen [73, 76] embrittlement may occur. These processes lead to displacement damage and considerable material hardening.

- **Fatigue.** Due to the extreme conditions within the reactor, including high temperatures, corrosive environments, and intense neutron flux, the materials used in LFRs are subjected to significant stresses over time. This prolonged exposure to cyclic loading and thermal fluctuations can lead to fatigue, where the material's structural integrity and performance gradually deteriorate [77].
- **Creep** behavior, referring to the tendency of a material to slowly deform permanently under mechanical stresses, is another significant challenge. Creep occurs especially at high temperatures, and results from several processes. These include dislocation creep, driven by dislocation movements [78]; diffusion creep, resulting from atomic diffusion under stress [79]; and grain boundary sliding, where grains slide past each other [80]. The high operational temperatures in LFRs can accelerate the creep rates, thereby reducing the longevity of these materials [49].

Fuel Cladding Concerns

In LFRs, the fuel cladding material faces direct exposure to the lead coolant and intense radiation from the fuel. The selection of fuel cladding materials is thus crucial to prevent fuel-cladding chemical interactions (FCCI) and to sustain the harsh conditions within the reactor [81]. The development of advanced cladding materials, such as those with high-density composite layers or ceramic coatings, is one of the promising strategies to address this challenge [82], as it is discussed later in this manuscript.

The Intricacies of Radiation effects in Nuclear Materials

The operating temperature of next-generation reactors surpasses that of their predecessors significantly, promising greater thermal efficiency, and thereby boosting electrical output and overall performance [83]. Despite the benefits, this increment in operational temperature places a substantial demand on the materials involved, requiring exceptional thermal resistance. The materials must maintain their mechanical strength and structural integrity under these heightened temperature conditions to guarantee the reactor's safety and durability [84]. In addition, the materials employed within these reactors must exhibit high radiation tolerance.The issue of radiation damage is of great significance during the operation of nuclear reactors. It arises

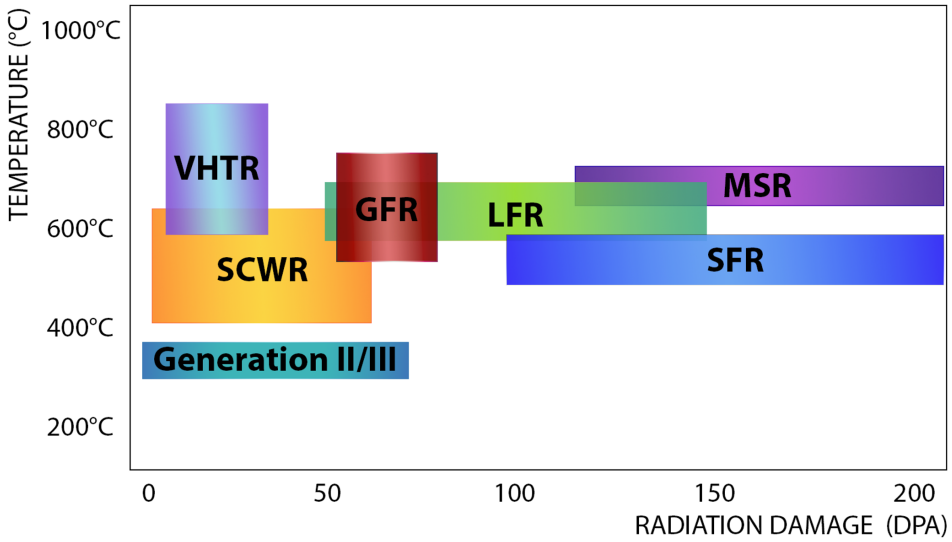

Figure 6: Temperature and radiation dose demands for in-core structural materials for the operation of the six proposed GIV advanced reactor concepts, contrasted with existing gen ii/iii systems. (Adapted from [85])

from the interaction of high-energy neutrons with the atoms present in the reactor's materials, resulting in their displacement from their typical locations within the crystal lattice. This displacement has the potential to generate point defects, such as vacancies (where atoms are absent) and interstitials (where atoms are inserted between others), as well as the formation of defect clusters. [47]. Over time, these effects can deteriorate the material's mechanical properties, compromising the reactor's operation.The intricate relationship between the formation of these point defects and the subsequent alteration of the materials' overall properties will be addressed at a later stage, following the discussion on the impact of radiation in space power production technologies.

The aforementioned operational conditions are summarized in Figure 6. It illustrates how these conditions epitomize the potential severity of radiation damage and temperature fluctuations in Gen IV reactor concepts. Referring to Figure 6, "dpa" (displacements per atom) is a metric used to assess the number of atomic displacements in a material due to irradiation. This metric is closely tied to the collisional cascade, a phenomenon associated with irradiation damage, detailed in Section 0.5. When the dpa value exceeds 1, it indicates significant atomic displacement, but while these damage events occur, simultaneous recovery processes work to offset the effects of the damage. A comprehensive understanding of dpa and its impact is detailed in Section 0.5.

The following provides a succinct yet comprehensive exploration of the impacts that radiation can induce in materials. This includes intriguing insights into the concurrent effects of radiation and corrosion in LFR. Such combination of factors can potentially induce more severe outcomes compared to those produced in other technological systems, such as Light Water Reactors (LWR)

[85].

In the following a bullet list presents the major radiation induced effects in materials.

- **SWELLING:** Certain materials experience a process of isotropic expansion, commonly called swelling. This intricate transformation is propelled by the build-up of radiation-induced defects, seamlessly interwoven with nuclear reactions and the atomic composition of the material. Central to this process are the atomic displacements prompted by high-energy particles. Such displacements result in vacancies or interstitials within the crystal framework. Notably, while individual vacancies may not have a direct impact on swelling, even in substantial numbers, their cumulative effect gives rise to voids. Upon interaction with gaseous fission byproducts, especially helium, these voids transform into structures termed as bubbles. Further complicating the scenario, radiation-induced dislocation loops augment the swelling phenomenon. These loops primarily capture interstitials, resulting in a predominant presence of vacancies. Instead of diminishing, these vacancies converge, further enhancing the swelling. [86, 87, 88, 89].

- **TRANSMUTATION:** Neutrons have the remarkable ability to induce nuclear reactions within materials, forming new elements or isotopes when captured. Neutron absorptions may give rise to the production of unstable isotopes, which subsequently undergo decay, emitting additional radiation. Consequently, the overall radioactivity of the material is intensified through this transmutation process This process significantly impacts the performance and properties of these materials. It affects crucial aspects such as structural integrity, thermal conductivity, and corrosion resistance. [90, 91].

- **IRRADIATION CREEP & STRESS RELAXATION:** Irradiation creep and stress relaxation are two distinct manifestations of the same underlying phenomenon: viscous flow. This flow arises due to defects, whether induced by temperature or irradiation. In the context of irradiation creep, it represents the time-dependent deformation observed when a material is subjected to a constant irradiation flux, compounded by the inherent thermal creep present in materials. This deformation is primarily attributed to the migration of vacancies and interstitials, propelled by the thermal gradients and stress fields induced by irradiation. As these imperfections migrate and interact with dislocations, they lead to a continuous deformation of the material [92, 93]. Conversely, under constant strain conditions, the viscous flow results in stress relaxation. This process entails gradually reducing internal stresses within a material over time. Such relaxation occurs as defects, like dislocations and vacancies brought about by irradiation, undergo annihilation and recombination. As these defects are annihilated, the internal stresses within the material progressively dissipate, leading to an overall reduction in stress levels. [94, 95].

- **EMBRITTLEMENT:** The embrittlement induced by radiation presents substantial difficulties in maintaining the structural stability of materials employed in nuclear reactors. The exposure of materials to radiation may cause a decline in their mechanical proper-

ties, notably their capacity for deformation (ductility) and resistance to fracture (fracture toughness). After high-energy neutrons interact with the atomic structure of the material, a variety of defects, such as vacancies and interstitials, alongside dislocation loops and clusters, can be generated. These point defects may obstruct dislocation movements, which are line defects in the crystal structure that facilitate plastic deformation. Consequently, the material's capacity to sustain plastic deformation and absorb energy diminishes, thereby causing an increase in brittleness. The stress-strain curves of materials under tension or the utilization of Ductile to Brittle Transition Temperature (DBTT) curves can well illustrate this phenomenon [96, 97, 98, 99]. DBTT curves delineate a unique temperature specific to certain materials, particularly metals, and alloys, signifying the shift from ductile (capable of plastic deformation) to brittle (prone to fracture without significant deformation) behavior. The influence of radiation on DBTT is a critical factor to consider for materials subjected to radiation environments, especially in nuclear applications. Radiation can notably modify a material's DBTT, pushing it towards higher temperatures and thereby escalating the potential for brittle fractures [100, 101].

- **HARDENING:** This refers to the enhancement in material hardness and resistance to deformation, which results from the accumulation of radiation-induced defects and their interplay with the material's microstructure. Various processes are involved in the hardening induced by radiation. One such process involves the build-up of point defects that obstruct the movement of dislocations, which are instrumental in the plastic deformation of materials. This hindrance to dislocation movement leads to an increase in material hardness. Another process is associated with the creation of radiation-induced dislocation loops. These loops hinder dislocation movement and contribute to the material's hardening. Moreover, dislocation loops can interact with point defects, such as vacancies and interstitials, ensnaring and restricting their mobility, further boosting the hardening effect [102, 103]. It is imperative to underscore that hardening and embrittlement are intrinsically linked, representing two facets of the same fundamental phenomenon: the accumulation of defects impeding the motion of dislocations.

Radiation resistance is a critical property for materials used in LFRs due to the high radiation levels within these reactors. Ferritic/martensitic steels, such as Grade 91 or T91, demonstrate impressive resistance to radiation. According to some authors, this can be attributed to their body-centered cubic (bcc) lattice structure, which effectively accommodates and recovers from radiation-induced defects, minimizing material degradation during irradiation. In contrast, austenitic steels with their face-centered cubic (fcc) lattice structure do not offer the same level of radiation resistance [104, 105]. Some authors criticize this idea of higher susceptibility of FCC structures to radiation-induced swelling and phase instability under high neutron doses due only to the crystalline structure. Iwase et al. [106] suggest that the differences in crystal structure does not significantly affect the primary damage production and observed radiation-induced annealing. Instead, they propose that electron-phonon coupling, which refers to how the

energy deposited in the electronic system relaxes, may play an important role even in low-energy ion irradiations. Additionally, Ward's findings [107]indicate that ferritic swelling resistance is not solely attributed to the lattice structure but is influenced by various factors, including impurity content, damage depth, and pre-irradiation microstructure. However, it is essential to stress that while ferritic/martensitic steels seem to outperform austenitic steels regarding radiation resistance, they generally exhibit inferior corrosion resistance, especially in liquid metal environments commonly encountered in LFRs. Therefore, the choice between these steel types will often depend on the specific conditions and requirements of the reactor environment [67]. This differences in materials behaviour seems to disappear when temperature increases above a certain threshold [56].

The combined effects of corrosion and irradiation in Liquid Metal Fast Reactors pose unique challenges in maintaining materials' structural integrity and long-term performance. While radiation alone can cause material damage, the corrosive environments exacerbate degradation mechanisms, resulting in complex interactions between radiation and corrosion. It is essential to comprehend and address the combined effects of corrosion and irradiation to ensure the safe and efficient design and operation of LFRs.

Several studies [45, 108, 109, 110] have reported that the Liquid Metal Embrittlement (LME) of standard F/M steels can be significantly intensified by irradiation, leading to a more severe reduction in tensile elongation and fracture toughness compared to non-irradiated conditions. A comparison of stress-strain curves between irradiated and non-irradiated steels tested in liquid lead-bismuth eutectic (LBE) reveals notable differences, as reported in Figure 7 (d).

The mechanical behavior of steels is affected by irradiation and the unique LBE environment, contributing to these distinctions [45, 108, 109, 110]:

1. Yield Strength: Irradiated steels exhibit a higher yield strength in LBE than non-irradiated steels. It is worth mentioning that this phenomenon generally occurs on irradiated steels independently of the Lead exposure.

2. Strain Hardening: Strain hardening behavior shows discrepancies between irradiated and non-irradiated steels in LBE. Irradiated steels demonstrate a reduced strain hardening rate, resulting in a more gradual increase in stress with increasing strain compared to non-irradiated steels.

3. Ductility: Irradiation affects ductility, further influenced by the LBE environment. Non-irradiated steels generally exhibit higher and better uniform elongation in LBE than irradiated steels. The presence of LBE exacerbates embrittlement by promoting corrosion and accelerating crack propagation.

4. Ultimate Tensile Strength: Irradiated steels tested in LBE may show a reduction in ultimate tensile strength (UTS) compared to non-irradiated steels

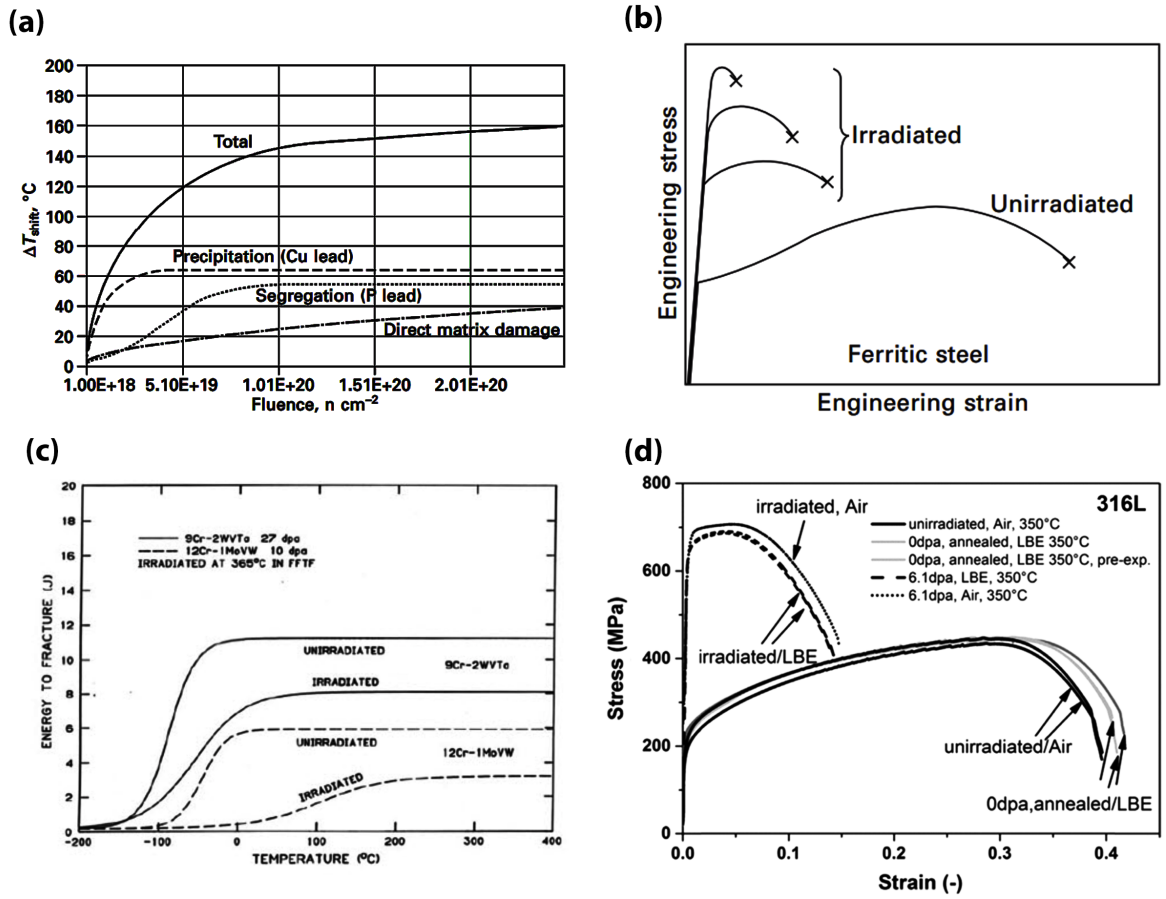

Figure 7: (a) Schematic diagram showing the effect of three damage mechanisms on the shift to higher temperatures of the ductile-to-brittle transition temperature (DBTT) due to the irradiation embrittlement of RPV steel [111]. (b) Schematic diagram showing the effect of increasing neutron fluence on the tensile stress–strain diagram for typical ferritic steel [111]. (c) Comparison of the unirradiated and irradiated DBTT Charpy curves for specimens of HT9 and ORNL 9Cr-2WVTa steels irradiated at 365ºC [112]. (d) Comparison of stress–strain curves of irradiated and non-irradiated T91 F/M steels tested in tension in both air and liquid LBE. [108]

Figure 7 reveals the intricate relationships between irradiation and the behavior of steel materials. Figure 7 (a) illustrates how damage mechanisms influence the ductile-to-brittle transition temperature (DBTT) shift to higher temperatures in RPV steel. Figure 7 (b) demonstrates the correlation between increasing neutron fluence and the tensile stress-strain diagram in ferritic steel. Figure 7 (c) compares DBTT Charpy curves for different steels, highlighting the contrast between unirradiated and irradiated specimens. Lastly,Figure 7 (d) presents a comparative analysis of stress-strain curves for irradiated and non-irradiated T91 F/M steels, emphasizing the combined effects of radiation and exposure to liquid LBE.

So far, the multidimensional challenges posed by corrosion in LFRs and the radiation effects on materials have been explored, delving also into the nuances of how radiation could accelerate corrosion issues. These challenges are valuable opportunities to redefine conventional materials. This brings the discussion to the next phase: the potential solutions to these pressing issues by revisiting materials. The upcoming examination will focus on innovative materials' potential, considering both their inherent properties and possible modifications as prospective solutions. Their ability to endure the severe conditions within LFRs and to effectively alleviate corrosion and radiation hazards will be meticulously assessed.

0.2.5. Advancements in Corrosion and Radiation Resistant Materials for Liquid Metal Fast Reactor: Exploring Beyond Traditional Steel Alloys

The preceding part has revealed the primary categories of steels, namely F/M and Aus, which extensive research has focused on regarding the corrosion resistance of LFR structural materials. However, in pursuing progress in this field, numerous alternative materials have emerged as potential game-changers in the last two decades. Motivated by this ambition, the scientific community has aimed at deploying innovative bulk materials with corrosion-resistant properties and radiation tolerance. Achieving this ambitious objective requires replacing materials like 316L, 1515-Ti, or low-activation EUROFER-97 steels and establishing a thorough qualification and testing process for the new alloys. Identifying suitable candidates for licensing involves surmounting challenges related to meeting structural requirements and demonstrating satisfactory mechanical performance, particularly in the presence of irradiation. Moreover, these materials must be not only desirable but also cost-effective, offering significant enhancements in terms of chemical compatibility, gas retention, and an expanded operational range when compared to the current state-of-the-art technologies [16, 85].

For the reasons mentioned, it is necessary to expand upon the present discussion by providing an overview of several alternative materials that have emerged as potential enhancements in the field over the past two decades. The following section highlights the main alternatives.

Oxide Dispersion Strengthened Steels

Oxide dispersion-strengthened (ODS) steels, specifically ODS-FeCr steels, are renowned for a distinctive microstructure characterized by the uniform dispersion of nanoscale Y-Ti-O clusters within a fine-grained, ferritic (bcc) matrix [113]. This characteristic microstructure is reported in Figure 8 (a). These tiny oxide clusters act as barriers, impeding the movement of dislocations and endowing the steel with unparalleled resistance to creep at high temperatures, surpassing dispersoid-free F/M steels like T91. Moreover, the several interfaces between the nanoclusters and the matrix serve as effective traps for radiation-induced defects [114], fortifying the steel against embrittlement and swelling caused by irradiation. With its fine-grained composition, this unique microstructure not only bestows higher strength but also preserves a desirable pinning effect on grain boundaries [115].

The ODS-FeCr Al-enriched steels [116], in particular, combine the advantages of ODS-FeCr steels with the ability to form passivating alumina (Al_2O_3) scales due to the inclusion of aluminum (Al) [117]. Alumina, as it will be discussed deeply later, is known for its unwavering stability under extremely low oxygen conditions, and shields the bulk steel from corrosive dissolution, making these steels one of the appealing choice for fuel cladding materials in cutting-edge LFRs.

However, the wide-scale adoption of ODS-FeCrAl steels faces two significant hurdles. Firstly, the lack of mature, large-scale manufacturing methods and joining technologies remains a pressing challenge. The intricacies of joining processes, capable of disrupting the crucial dispersion of

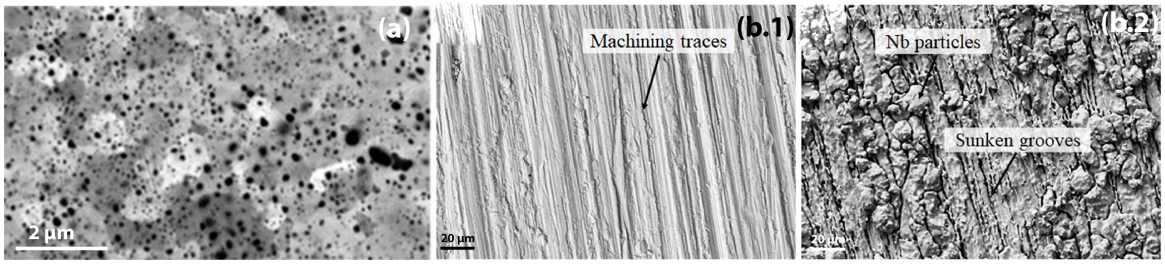

Figure 8: (a) Typical microstructure of the Fe–Al–O ODS alloy, SEM. [117]. (b) SEM surface morphology of Nb before and after exposure: (b.1) before exposure; (b.2) after exposure in LBE for 1000 h [119].

fine oxide particles within the steel, require further development. Furthermore, the occurrence of LME poses a significant concern for bcc-structured steels of this kind when subjected to low temperatures [45].

Refractory Metals

Refractory metals, namely tungsten (W), molybdenum (Mo), niobium (Nb), and tantalum (Ta), exhibit favorable characteristics for high-temperature engineering applications due to their high melting points and excellent strength. These metals demonstrate notable resistance to creep, void swelling, and low solubility in oxygen-poor liquid lead-bismuth (Pb) and lead-bismuth eutectic (LBE), making them potential candidates for future use in Liquid Fluoride Reactors [118].

However, employing these metals in nuclear systems presents challenges, including their susceptibility to low-temperature irradiation embrittlement, limited oxidation resistance (a concern for high-oxygen-content High-Level Molten systems), poor weldability, and manufacturing difficulties [118].

To illustrate the impact of corrosion on this metal class, a specific case involves exposing Nb to LBE containing $5*10^{-6}$ wt% oxygen at 700 °C. As depicted in the Figure 8 (b), after 1000 hours of exposure, severe and uneven corrosion occurs, resulting in deep grooves aligned with the machining traces. Additionally, observable Nb particles with sizes ranging from approximately 5 to 20 μm further exemplify the deleterious effects of corrosion [119].

MAX Phases

The class of materials known as MAX phases represent a group of ternary carbides and nitrides. These unique compounds are described by the general formula Mn+1AXn, where the subscript 'n' can take values of 1, 2, or 3. In this formula, 'M' represents an early transition metal, 'A' denotes an element from groups 13–16 in the periodic table, and 'X' can be either carbon (C) or nitrogen (N) [120, 121, 122]. What makes the MAX phases truly captivating is their hcp

crystal structure (P63/mmc space group), which imparts their various properties, combining characteristics of both ceramics and metals. Depending on their precise composition, the MAX phases can exhibit significant thermal stability, high strength, excellent thermal and electrical conductivity, appealing damage tolerance, low hardness, and machinability comparable to graphite. The choice of elements M, A, and X and the value of 'n' in the Mn+1AXn formula determine the specific properties of the MAX phases.) [123]. Notably, the MAX phases offer the intriguing possibility of creating solid solutions by partially substituting the M, A, and/or X elements with other elements, denoted as M', A', and/or X'. This capability allows for precise tailoring of the MAX phases' properties, such as phase purity, coefficient of thermal expansion, oxidation/corrosion resistance, and radiation response, to meet the specific requirements of the desired application [124, 125, 126, 127]. When considering potential applications in nuclear environments close to the reactor core, such as fuel cladding tube coatings, a careful preselection of elements used in MAX phases has to be assessed. For example, elements with high neutron cross-sections, like Hf, Ta, and Mo, must be excluded due to the significant high neutronic absorption cross-sections associated with MAX phases containing substantial fractions of such elements, rendering their use impractical .

The resistance of MAX phase compounds to liquid metals and corrosive environments has been the subject of extensive research. Utili et al. explored the possibility of using Ti_3SiC_2 as a material for Gen-IV LFR pump impellers by exposing it to flowing liquid Pb (approximately 1 m/s) [128]. Later investigations by Lapauw et al. exposed various MAX phase ceramics to oxygen-poor static (with O concentrations below $2.2*10^{10}$ wt%) and fast-flowing (with O concentrations around $5*10^9$ wt%) liquid LBE at 500°C for durations ranging from 1000 to 3500 hours. These studies revealed that the quasi phase-pure $(Nb,Zr)_4AlC_3$ MAX phase ceramic displayed excellent resistance to dissolution and erosion/corrosion [125].

Despite their outstanding properties, MAX phase-based ceramics have relatively low fracture toughness, albeit considerable for ceramic materials. This characteristic limits their suitability for structural applications requiring monolithic forms. For example, the highest fracture toughness reported for MAX phase ceramics was approximately $K_{IC} = 17.9$ MPa$*$m$^{1/2}$ for highly textured Nb_4AlC_3 [129]. The SEM micrographs exhibit distinct damages on the fracture surfaces, portrayed in Figure 9 (a,b). These intricate patterns of fractures and fissures provide insights into the critical material's response to external forces.

However, MAX phases possess another remarkable feature that makes them appealing for Gen-IV LFRs operating at temperatures above 600°C: their exceptional neutron radiation tolerance [132, 133, 134]. Figure 10 (a) illustrates that in neutron-irradiated Ti_3SiC_2 at 735°C, grain boundaries (GBs) act as sinks for radiation-induced defects, resulting in large defect-denuded zones adjacent to the GBs, that is a region where the presence of radiation-induced defects is notably reduced or absent. This phenomenon signifies that the defects generated by radiation tend to accumulate and concentrate at the grain boundaries, leaving the adjacent region relatively defect-free. At higher irradiation temperatures (1085°C), Ti_3SiC_2 grains appeared to be

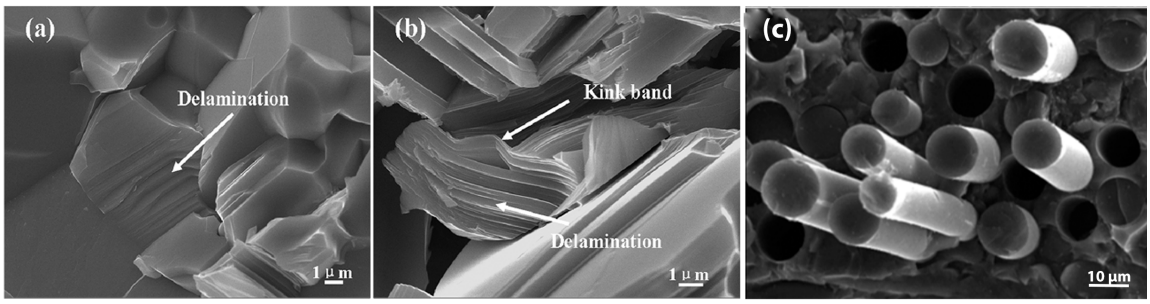

Figure 9: SEM micrographs of the damaged modes observed in fracture surfaces of (a, b) Ti_2AlC MAX phase [130]. A fracture morphology of SiCf/SiC composite [131]

essentially defect-free, indicating effective self-healing of radiation-induced defects (Figure 10 (c)). These findings further support the promising use of MAX phase ceramics in Gen-IV LFRs [133].

MAX phase ceramics are expected to be used in Gen-IV LFRs in the future due to their pros and cons. They are particularly suitable for certain purposes like protecting fuel cladding tubes, pump impeller blades, bearings, and bushings. It's important to recognize that the drawbacks of these structural materials can be reduced through smart engineering design. By utilizing the material's strengths and avoiding harsh operating conditions, we can overcome its inherent limitations to a certain degree. [135].

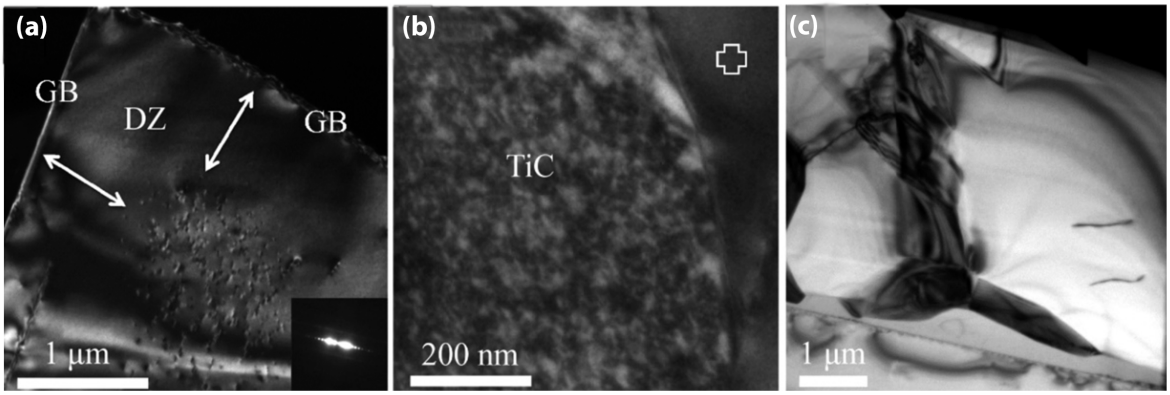

Figure 10: TEM Bright Field images of Ti_3SiC_2, neutron irradiated to 3.4 dpa at 735 °C (a, b) and 1085 °C (c). (a) Large defect-denuded zones (DZ, arrows) next to GBs suggest that the latter act as sinks for radiation-induced defects, showing the self-healing potential of the MAX phases. (b) The strong mottled contrast indicating radiation damage in the parasitic TiC grain makes a sharp contrast to the defect-free neighbouring Ti_3SiC_2 grain (cross). (c)Defect-free Ti_3SiC_2 grains irradiated at 1085 °C suggest the effective self-healing of radiation-induced defects at elevated temperatures [45]

SiC fiber-reinforced SiC matrix composites

SiC fiber-reinforced SiC matrix composites (SiCf/SiC) have a range of desirable properties that make them highly suitable for LFRs applications. These composites exhibit excellent radiation tolerance, with minimal (≈1%) radiation swelling up to temperatures around 1200°C [65]. SiCf/SiC also possesses high mechanical strength, resistance to creep at high temperatures, good oxidation resistance, neutron transparency, and chemical compatibility with liquid lead-bismuth (Pb and LBE) [136, 137].

Despite their advantageous properties, SiCf/SiC composites still encounter technical challenges restricting their widespread usage as a long-term material solution. One significant challenge is the hermeticity of fuel cladding tubes, which has not been fully guaranteed thus far. Progress has been made with concepts like the CEA sandwich design, which incorporates a ductile metal liner between two SiCf/SiC composite layers, and the production of highly dense SiCf/SiC composites through liquid phase sintering (LPS), such as the nano-infiltration and transient eutectic phase (NITE) process [138]. However, ensuring reliable hermeticity remains a concern, especially for fuel cladding tube applications.

The brittleness of monolithic SiC (with a fracture toughness of approximately 2.5-3 MPa $m^{1/2}$ [139]) presents another challenge for SiCf/SiC composites. The brittle nature of the SiC matrix leads to microcracking at low-stress levels, which compromises the hermeticity of SiCf/SiC composites during service. Overcoming this issue is crucial for successful implementation. A fracture morphology of SiCf/SiC composite is reported in Figure 9.

Furthermore, the absence of mature joining techniques and cost-effective manufacturing technologies capable of producing SiCf/SiC composites on an industrial scale is a significant obstacle that needs to be addressed. Additionally, cost-effective manufacturing processes are required to enable large-scale production and make SiCf/SiC composites economically viable for widespread use [45].

Moreover, advancements in manufacturing technologies, such as additive manufacturing (3D printing) and advanced sintering techniques, offer the potential for the cost-effective production of SiCf/SiC composites on an industrial scale. These manufacturing methods allow the creation of complex geometries and have the potential to reduce production costs through improved material utilization and process efficiency [140], although challenges related to licensing this approach need to be addressed.

Surface Alloying: Potentials and Challenges in Steel Enhancement

Surface alloying treatments constitute a significant segment within surface modification methods. Such processes typically involve modifications to the external layers of substances, predominantly steel alloys, leaving the internal composition unaltered [141, 142, 143, 144, 145] . A subset of such alloys, the Alumina-Forming Austenitic (AFA) steels, are a class of high-temperature stainless steels devised to offer superior resistance against oxidation and creep compared to conventional

steels [146]. The term 'AFA' stems from their unique capability of developing a defensive alumina (Al_2O_3) layer under high-temperature oxidizing conditions [147]. This alumina layer is fundamentally stable and forms a formidable barrier against further oxidation, which imparts significant anti-corrosion qualities [148]. Unlike traditional austenitic steels such as type 304 and 316, where chromium forms a protective layer, the alumina layer in AFA steels provides enhanced stability and protection, thus making them suitable for high-temperature applications [148]. Surface alloying methods present several advantages, especially for nuclear-grade steels. They provide improved corrosion resistance in harsh environments [142, 143, 149], and the adherent-formed ceramic scale enhances surface hardness, which improves the material's resistance against erosion, fretting, and wear [150]. The layer can be up to 100 μm thick and possess self-healing properties [141], [144]. Nonetheless, such methods have inherent limitations. They demand a specific oxygen level, which can complicate oxygen control in a power plant context. Moreover, high temperatures are often required for establishing a stable and homogenous interlayer, which might not always be compatible with the steel substrate following thermal treatments and cold-working procedures [141, 144].

The Gepulste Elektronen-Strahl Anlage (GESA) is another prominent example of a surface alloying technique. In this technique, an aluminum foil of about 20 μm is applied on the substrate and is exposed to an electron beam. This high-energy radiation melts the Al foil and the top micrometers of the substrate, forming a new alloy surface [144, 149]. The alloy layer provides improved corrosion resistance, thus minimizing the dissolution of steel components [144, 149]. However, the GESA alloying technique faces obstacles under radiation due to radiation-induced embrittlement. Radiation appears to reduce the threshold for the onset of cracks and alters the density and width of these cracks [151]. This suggests that under radiation, the protective benefits of the GESA-alloyed layers could be jeopardized due to localized cracking and embrittlement.

Coatings

The discussed methods for safeguarding steels from dissolution attack in heavy liquid metal (HLM) environments include controlling oxygen concentration to form an oxide layer and modifying the steel matrix with reactive elements like Al, Cr, and Si. However, both methods face challenges including temperature sensitivity, uncertain longevity, and complex interplays with oxygen and temperature [152, 153, 154, 155]. Potential solutions such as metallic glasses and high entropy alloys show promise for nuclear reactor applications due to their strong mechanical properties and corrosion resistance. However, they require further investigation, especially their corrosion resistance in HLM, and more feasible production methods [155, 156].

Coating technologies, specifically metallic and ceramic ones, offer advantages including cost and time efficiency, and the ability to engineer surface properties without affecting structural integrity. However, issues including lack of self-healing properties, compatibility with substrates, and risk of delamination limit their acceptance. The effectiveness of coatings depends greatly on

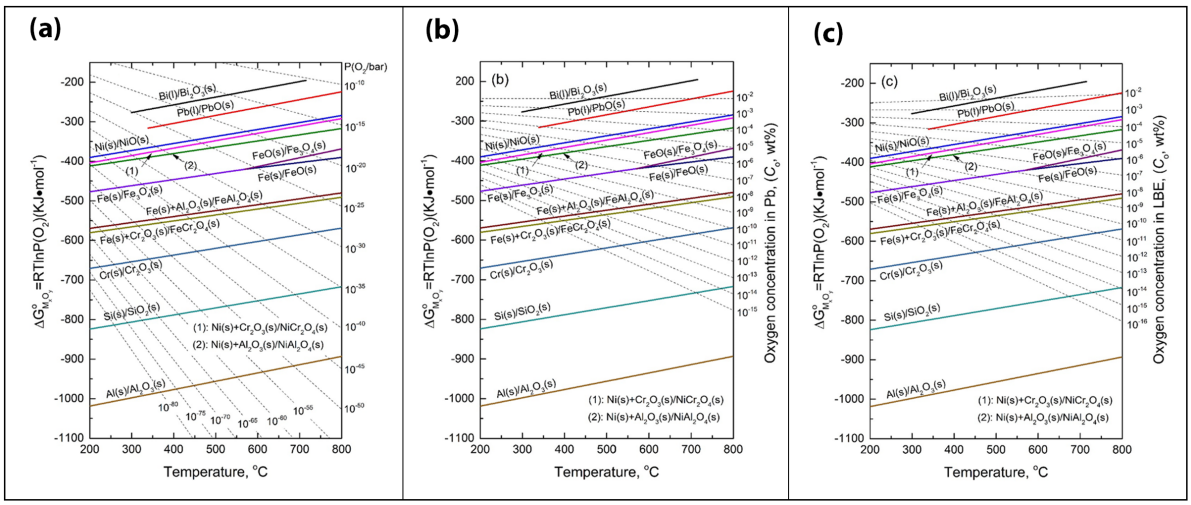

Figure 11: Ellingham diagrams of the standard Gibbs free energy of oxide formation per mol O2 (left y-axis) as a function of: (a) the oxygen partial pressure in the gas plenum above the HLM melt, (b,c) the concentration of dissolved oxygen in liquid Pb and liquid LBE, respectively, (right y-axis), and temperature (x-axis) for the formation of oxides due to the oxidation of the main steel alloying elements in liquid Pb and LBE [45].

the application technique, with Physical Vapour Deposition (PVD) showing particular promise [155]. For example, the corrosion and irradiation behavior of Fe-based amorphous metallic glass coatings have been studied, revealing superior corrosion resistance and irradiation tolerance compared to uncoated steels [156]. High Entropy Alloys (HEA) coatings have also shown promising characteristics such as phase stability and oxidation resistance [155, 157, 158]. However, their response to temperature changes and irradiation needs further investigation [159]. Ceramic coatings, especially Al_2O_3 and Cr_2AlC, offer corrosion protection due to their mechanical, chemical, and thermal properties [155]. However, issues remain in terms of their toughness and adhesion on substrates. Nitride and carbon-based coatings present improved toughness and compatibility [160], with the latter demonstrating superior corrosion resistance, smoothness, and self-lubricating qualities, making them suitable for dry friction environments.

Despite the challenges, protective coatings are considered crucial for future-generation nuclear systems and are already in the licensing process for enhancing the performance of current LWRs according to Westinghouse and Framatome research programs [161, 162].

Finally, the amorphous alumina coating, a product of research at CNST @PoliMi [163] of IIT and x-nano [164], is promising. This material is a focal point of this thesis, thus, a comprehensive examination of its properties will be initiated in the subsequent section.

One of the reasons behind the choice of studying this material comes initially from a thermodynamic perspective, because Al_2O_3 is considered an excellent choice for protecting steel in liquid lead environments for several reasons. Firstly, the favorable properties of alumina include its

high thermal stability and exceptional resistance to corrosion in various environments, including in contact with molten metals such as lead [45]. From the standpoint of thermodynamics, the Ellingham diagram is a key tool for understanding reactivity and stability. Ellingham diagrams plot the Gibbs free energy change (ΔG) for oxidation reactions against temperature. A substance with a more negative ΔG of formation will be more stable than one with a less negative value. Alumina is lower in the Ellingham diagram, indicating a more negative free energy of formation than many other oxides, including iron ones. This means alumina is thermodynamically more stable than iron oxides at a given temperature, making it less likely to react. Ellingham diagrams of the standard Gibbs free energy of oxide formation considering the oxygen partial pressure in the gas plenum above the HLM melt, and the concentration of dissolved oxygen in liquid Pb and liquid LBE are reported in Figure 11 showing what just discussed.

Therefore, when alumina is used as a protective layer, it acts as a barrier that prevents the steel from reacting with liquid lead.

0.2.6. The Cutting-Edge Advances in PLD-Grown Alumina Coatings

A previous discussion examined the benefits and drawbacks associated with coatings. The disadvantages of coatings, such as the lack of self-healing properties and coverage issues, argue against their utilization. Furthermore, ceramic materials, specifically alumina films developed by IIT, have been discouraged due to their inherent brittleness. Expanding upon these initial considerations, this section focuses on the properties of alumina and alumina-based films created through the Pulsed Laser Deposition (PLD) technique. The subsequent pages provide a detailed account of the characterization tests conducted on the candidate material and highlight the noteworthy accomplishments. Additionally, the section provides an overview of the upcoming chapters by introducing the main objectives of the Ph.D. thesis.

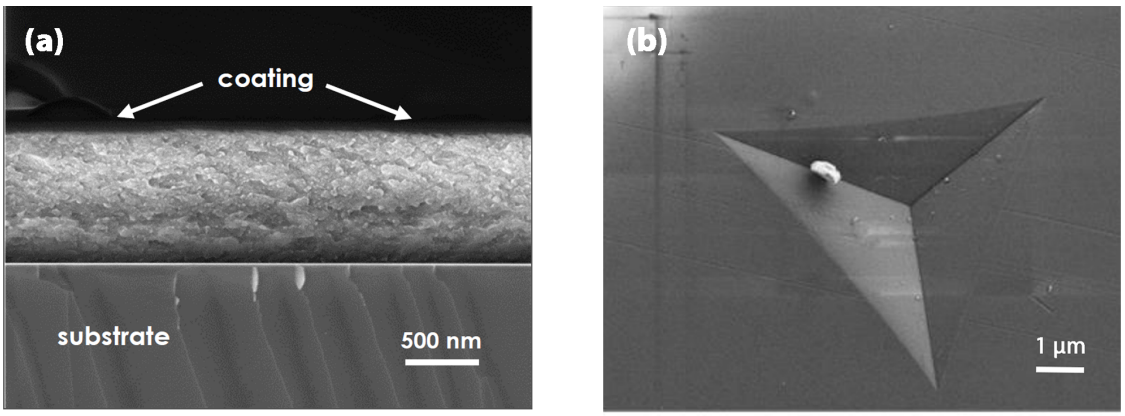

Figure 12: (a) SEM and cross-sectional image of as-deposited PLD-grown Al_2O_3 films. The material appears fully dense (i.e. no porosities) and well attached to the surface. The film quality is very high, with minimal defects.No evidence of grain boundaries is found by SEM, suggesting the amorphous nature of the material [165]. (b) Top view SEM images of nano-indented alumina film. The coatings can undergo severe plastic deformation without cracking or delaminating: no cracks are found at the edges of the indentations or departing from imprint corners [166]

The investigation into PLD-grown alumina coatings for nuclear reactor applications commenced in 2010 within the NanoLab research group at Politecnico di Milano. However, significant advancements were later made, particularly at the CNST@PoliMi - IIT laboratories, with the contributions of F.G. Ferré and F. Di Fonzo [166, 167, 168]. The authors employed PLD, a specific Physical Vapor Deposition technique [169, 170, 171], to develop a nano-ceramic alumina coating. The fabrication process is not described here, but further information can be found elsewhere [172]. Nevertheless, Pulsed Laser Deposition enabled researchers to achieve the deposition of a fully dense amorphous film at room temperature. The as-deposited films exhibited a smooth and uniform surface, characterized by high compactness without any porosities (Figure 12 (a)), and showcased minimal defects and sharp interfaces. Atomic Force Microscopy (AFM) was employed to measure the roughness, which closely resembled the substrate's one. The den-

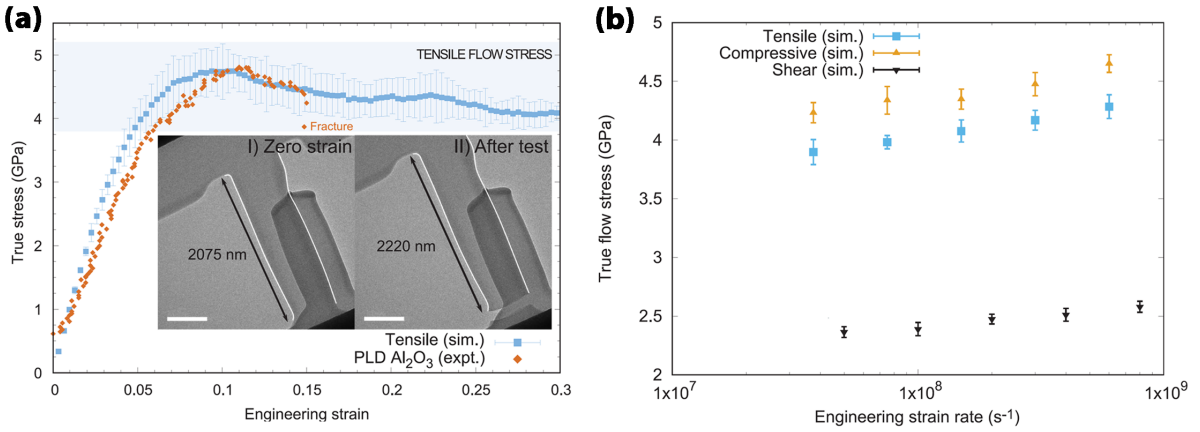

Figure 13: Mechanical response of amorphous Al_2O_3 at room temperature: simulations and experimental data. (a) Experimental tensile stress as a function of strain. Inset I shows the length of the free-standing tensile sample at the onset of elastic contact (strain 0.0), and inset II shows the length of the tensile sample after its fracture from the bottom part (scale bars, 500 nm). In the insets, the sample is highlighted with white borders, while another piece of the PLD film partially overlaps the sample in the image but does not interact with the sample during the test [176]. (b) Simulation of time-dependent flow behavior of amorphous Al_2O_3 at room temperature:Averaged simulated (N = 6 for each data point) flow stress as a function of the strain rate measured and averaged between total strain of 25 and 50%. Error bars show standard deviation [176].

sity and compactness were evaluated using Ellipsometry. Ferré et al. [166] reported a density value of 3.47 ± 0.02 g/cm^3 for the pristine film deposited at room temperature. These values indicate a more compact material than usual, as the density of amorphous alumina generally falls within the range of 2.8 to 3.2 g/cm^3 according to existing literature [173, 174]. The amorphous nature of the room temperature films was confirmed through X-Ray Diffraction (XRD), Raman Spectroscopy, Infra-Red (IR) Spectroscopy, and other techniques [165, 168, 175]. In terms of mechanics, the mechanical properties of alumina coatings grown through PLD were initially assessed using the Ellipsometry - Brillouin - Nano-indentation (EBN) technique [166]. The results indicated a combination of mechanical properties resembling metals and exhibiting higher hardness. While the hardness remained above 10 GPa, which is typical for ceramics, the measured mechanical moduli and Poisson's Ratio were similar to those found in traditional structural steels like austenitic 316L [166]. These properties contribute to the coatings' high resistance against erosion, scratching, and fretting. Unlike bulk ceramics, the Al_2O_3 films do not display typical brittleness but rather can undergo plastic deformation under mechanical loads due to shear band mechanisms inherent in ductile materials as visible in Figure 12 (b).

Recent studies have provided further evidence of the plastic behavior exhibited by PLD-grown alumina films. E.J. Frankberg conducted in situ nano-mechanical testing on independent Al_2O_3 layers as part of his Ph.D. research [175, 176]. The experiments revealed a deformation to

rupture of approximately 15% under compressive and tensile loading, while traditional aluminas fracture at much lower levels [175, 176]. Molecular Dynamics (MD) simulations were employed to support these experimental findings, suggesting that this remarkable plasticity results from the material's viscous creep, which can be activated under mechanical load even at room temperature [175, 176]. Hence, this plastic behavior is expected to persist as long as the material maintains its original amorphous structure. This study was recently published on Science [176].The Figure 13 provides a comprehensive view of amorphous Al_2O_3's room-temperature behavior, blending empirical (Figure 13 (a)) data with theoretical simulations (Figure 13 (b)).

In the context of nuclear reactor research, alumina coatings were characterized in relevant environments. The chosen environments were pure lead for application in Lead-cooled Fast Reactors (LFRs) and Lead-Lithium Eutectic (LLE) for fusion blanket systems. Ferré et al. conducted chemical compatibility analyses in a static lead environment [167]. Short-term corrosion tests were performed on T-91 steel plates, with and without Al_2O_3 coatings, under oxidizing conditions for 500 hours at 550 °C. The results demonstrated the protective nature of alumina coatings in oxidizing conditions within the specified timeframe. Similarly, D. Iadicicco conducted similar tests as part of his Ph.D. research [177]. EUROFER-97 steel substrates, both coated and uncoated with Al_2O_3, were exposed to Pb-16Li in a static dissolutive regime for 1,000 hours at 550 °C. Although the complete effectiveness of the alumina layer in LLE environments could not be fully determined due to chemical interactions with the liquid medium, the underlying substrate remained unaffected by the Pb-16Li, indicating positive outcomes from the conducted tests.

Moreover, the response of the films to irradiation was investigated (Figure 14). Heavy ions were utilized to study the radiation-induced damage in the material to gather efficient and timely data. Irradiation experiments were designed based on sample geometry, and PLD-grown films were subjected to 12 MeV Au^{5+} and 18 MeV^{8+} W ions at 600 °C, resulting in a total displacement per atom (dpa) of 150 [168, 178]. dpa is a unit used in radiation damage science to quantify the extent of damage experienced by a material exposed to irradiation. It signifies the average number of times each atom in a material has been displaced from its original position due to interaction with high-energy particles such as neutrons or ions. Following irradiation, the samples were collected and subjected to various characterization techniques such as Scanning Electron Microscopy (SEM), Transmission Electron Microscopy (TEM), Scanning Transmission Electron Microscopy (STEM), X-ray Diffraction (XRD), and Nano-indentation. The evolution of the material under irradiation is illustrated in Figure 14 [168, 178].

Under irradiation, the material transformed its original amorphous matrix to a micro-crystalline state. The specific crystalline phases that formed depended on the irradiation conditions. Importantly, no failures, delamination, or cracking were detected during the investigations [168, 178, 179]. The energy delivered by the ions was effectively absorbed and dissipated through local rearrangement, resulting in a final configuration with increased stability in the form of a crystalline structure. The initial amorphous alumina film provided a significant advantage in this regard due to its nanostructured configuration [175]. From a mechanical perspective, radiation-

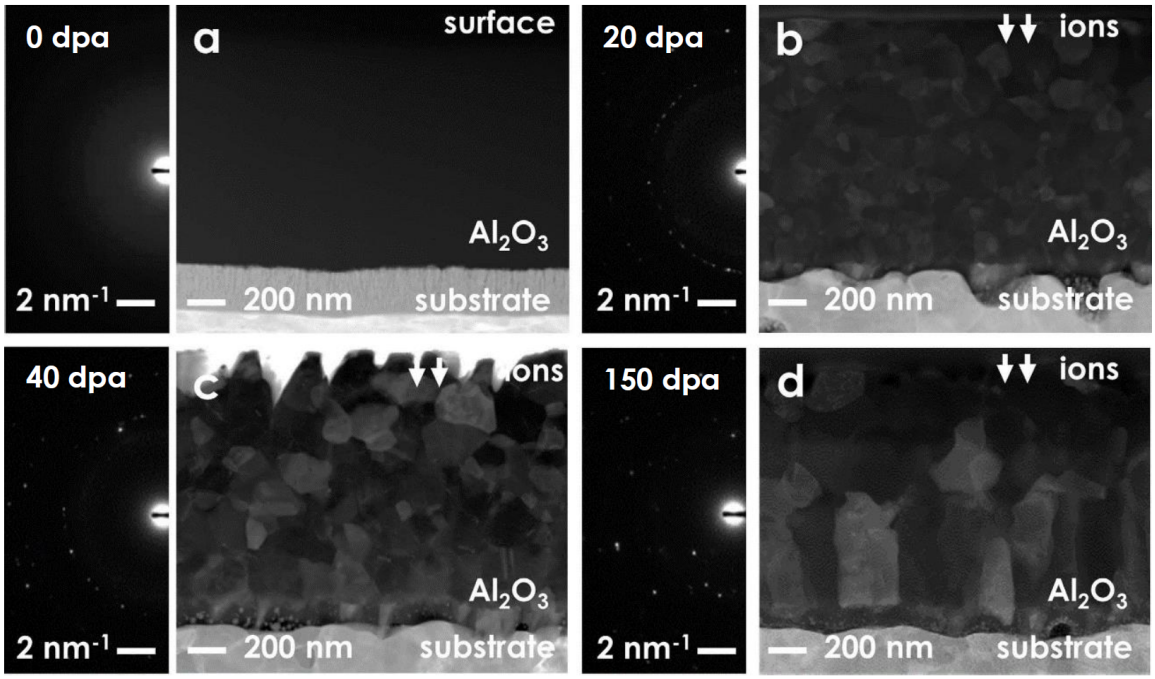

Figure 14: The bright field transmission electron microscopy (TEM BF) and electron diffraction patterns provide insights into the transformation of pulsed laser deposition (PLD) grown Al_2O_3 under the influence of heavy ion irradiation. Initially, in its pristine state (a), the material presents an almost entirely amorphous structure. However, the exposure to irradiation triggers crystallization, as depicted in figures (b, c, and d). This phenomenon prompts a continued process of grain growth and phase transition, which progressively intensifies as the displacement per atom (dpa) increases [178].

induced crystallization (RIC) led to an enhancement in hardness and stiffness compared to the pristine material. However, the irradiated films did not exhibit brittleness. Nano-indentation and nano-scratch tests performed after ion irradiation demonstrated a certain level of remaining plasticity in the system [168, 178].

At room temperature, recent findings indicate that even at 25 dpa, there is no evidence of crystallization [180]. This significant observation buttresses the assertion that amorphous Alumina has inherent radiation tolerance properties. As such, it is being touted as a promising candidate for radiation-resistant coating applications.

Lastly, the formation of voids was observed as the primary radiation damage product in the coating near the 150 dpa threshold [178]. This observation suggests that specific factors may influence the material's radiation tolerance. Further studies are necessary to gain a deeper understanding of this dependence.

0.3. Bridging Terrestrial and Cosmic Challenges: Material Solutions from Lead-cooled Fast Reactors to Space Solar Power Systems

The preceding sections conducted a comprehensive analysis of the material challenges encountered in the environment of Lead-cooled Fast Reactors (LFRs). Special attention was dedicated to the dual constraints of radiation and corrosion, both of which are prominent factors in this high-stress context. The exploration focused on advanced material solutions to address these challenges, highlighting the paramount importance of material engineering in extreme environments. Coatings, particularly PLD Al_2O_3, were given specific attention as they pertain to the subject matter of this work.

Transitioning to the subsequent chapter, the focus will shift from the nuclear reactor environment to the expansive and demanding realm of space. The parameters and challenges in this context vary, yet the underlying principle remains consistent: materials must be meticulously engineered to withstand the rigors of extreme conditions. Moreover, nuclear and space environments are united by ionizing radiation, which can induce detrimental effects on materials.

Furthermore, power generation through solar panels presents distinct material challenges in space applications. The inhospitable conditions of space, encompassing radiation, significant temperature fluctuations, and impacts from micrometeoroids, necessitate the implementation of advanced material solutions. Additionally, due to the inherent restrictions of weight and size in space missions, these materials must exhibit characteristics such as lightweightness, compactness, high efficiency, and reliability.

The upcoming chapter will provide an in-depth analysis of these challenges and potential solutions. As observed in the case of the LFR environment, it will be evident that innovative material technologies are pivotal in surmounting these obstacles. The ongoing research and development endeavors aimed at producing materials capable of enduring the harsh space environment while optimizing the harvesting of solar energy will be thoroughly investigated.

This transition signifies the commencement of an exploration into material challenges and solutions within the domain of space-based power generation. Although, as previously mentioned, the shared presence of radiation serves as a common factor between these environments, the utilization of coatings for developing radiation resistant solutions acts as a unifying element in this work. This aspect has already been discussed in the nuclear scenario and will be further expounded upon in the subsequent section relating to the space domain.

0.4. Conquering the Technological Challenges of Space Exploration: The Critical Role of Materials Science

Space exploration has captivated the human imagination for centuries, catalyzing advancements in knowledge and technology that enrich people's lives worldwide. Delving into the cosmos enhances our understanding of the universe and our place within it and stimulates innovation, fosters international cooperation, and promotes economic growth. As we embark on daring space missions, we unveil new celestial bodies, deepen our comprehension of Earth's natural systems, and expand scientific knowledge through groundbreaking discoveries, such as exoplanets and the universe's age. Examples like the Hubble Space Telescope [181] and the Kepler Mission [182] underscore the far-reaching benefits of space exploration, as they have allowed scientists to study celestial bodies in unprecedented detail and conduct experiments that cannot be performed on Earth. In doing so, space missions have spurred the development of cutting-edge technologies with extensive applications on Earth, strengthened peaceful relations between nations, and created opportunities for global partnerships. This multifaceted value of space science and exploration transcends borders, uniting humanity through the shared benefits of discovery, innovation, and collaboration.

0.4.1. Materials Challenges and Innovative Solutions for Spacecraft Operations in Harsh Environments

The extreme environment of space poses significant challenges for spacecraft operations, necessitating the development of advanced materials and technologies to meet demanding operational requirements and ensure reliability, functionality, and safety. The different regions of the universe pose unique and diversified challenges , including temperature extremes, radiation events, thermal cycling, varying plasma densities, intense ultraviolet radiation, ionizing radiation, micrometeoroids and debris impacts [183, 184, 185, 186].

The orbits in space for earth proximity application, are classified as geostationary Earth orbit (GEO), which is a geosynchronous orbit 36,000 km directly above the equator, and medium Earth orbit (MEO), which is between GEO and the low Earth orbit (LEO), where LEO is defined as 200–1000 km above the Earth's surface. Each orbit is used for different applications. The GEO is primarily for communication satellites; MEO is used for navigation satellites such as the Global Positioning System; and LEO is for Earth monitoring [186].

Factors such as the harsh vacuum environment, solar radiation, and the rapid temperature cycling experienced by materials during orbital transitions strongly depend on the distance from the earth and contribute to accelerate fatigue processes. For example, temperature extremes in Earth orbit range from +200°C when fully exposed to the Sun, to -180°C when in eclipse, leading to thermal expansion/ contraction and consequently thermal fatigue [185, 187]. Engineers must account for thermal fatigue when designing spacecraft and satellite components to ensure their durability and longevity in these demanding conditions [186]. Additionally, on-orbit charging

(electrostatic discharge), atomic oxygen (AO), and micrometeoroids and orbital debris (MMOD) are primary concerns for space missions due to their potential to cause significant damage [183, 186, 188]. AO is of particularly concern. It is generated by the photo-dissociation of molecular oxygen by intense UV sunlight, and the vacuum conditions in LEO, resulting in a high concentration of reactive atomic oxygen, which can cause erosion and damage to the surfaces of spacecraft materials, as shown in Figure 15 (a), impacting their longevity and functionality [186]. Moreover, as it will be discussed below, radiation poses one of the most significant challenge for materials used in space, as exposure to ionizing radiation can result in degradation of structural integrity, mechanical performance, and material properties [184, 185]. Indeed energetic particles such as electrons, protons, and heavy ions in the space environment can ultimately reduce the lifetime and functionality of spacecraft components.

Additionally, when materials traverse the vast void of outer space, they experience an outgassing phenomenon in which volatile components embedded within their constitution are liberated as gases [189, 190]. This occurrence, while seemingly negligible, poses a substantial hurdle, especially for materials with a porous nature. These porous materials, identified by their interlinked network of tiny voids or channels, demonstrate heightened susceptibility to outgassing, an attribute attributable to their expansive surface area. The gas emissions resulting from this process can instigate numerous adverse consequences, encompassing contamination of delicate instruments and devices, modification of thermal attributes, and diminishing mission efficacy. Moreover, the accumulation of outgassed substances on optical equipment, like cameras or sensors, can reduce their effectiveness, and in some instances, outgassing can lead to the degradation of the material's structural integrity over time, potentially leading to failures in structural components [189, 190]. The preceding discussion highlights several effects, the magnitude of which is captured in Figure 15. This visual representation vividly portrays the profound and calamitous repercussions that the space environment imposes on exposed materials.

These environmental factors necessitate the development of advanced materials that can withstand these harsh conditions, ensuring the survivability and functionality of spacecraft and their components [184]. Traditional solutions may not adequately address all the requirements to address all the mentioned issues and various conditions. Thus, new materials, such as self-healing structures, are being considered to ensure long-term survival of space structures in outer space [183]. However, self-healing materials may not always be the ideal solution for space applications due to the unique challenges posed by the space environment, such as the harsh vacuum, extreme temperature fluctuations, low-gravity conditions, and exposure to ionizing radiation [191, 192]. To address these concerns, the use of advanced coatings can play a vital role in enhancing the durability and resilience of materials used in space. By engineering multifunctional coatings with tailored properties, it is possible to mitigate the environmental effects while simultaneously providing passive protection against radiation, oxidation, and thermal fatigue [193, 194].

In conclusion, addressing the diverse challenges posed by the space environment requires the development of advanced materials that offer improved performance, reliability, and affordability.

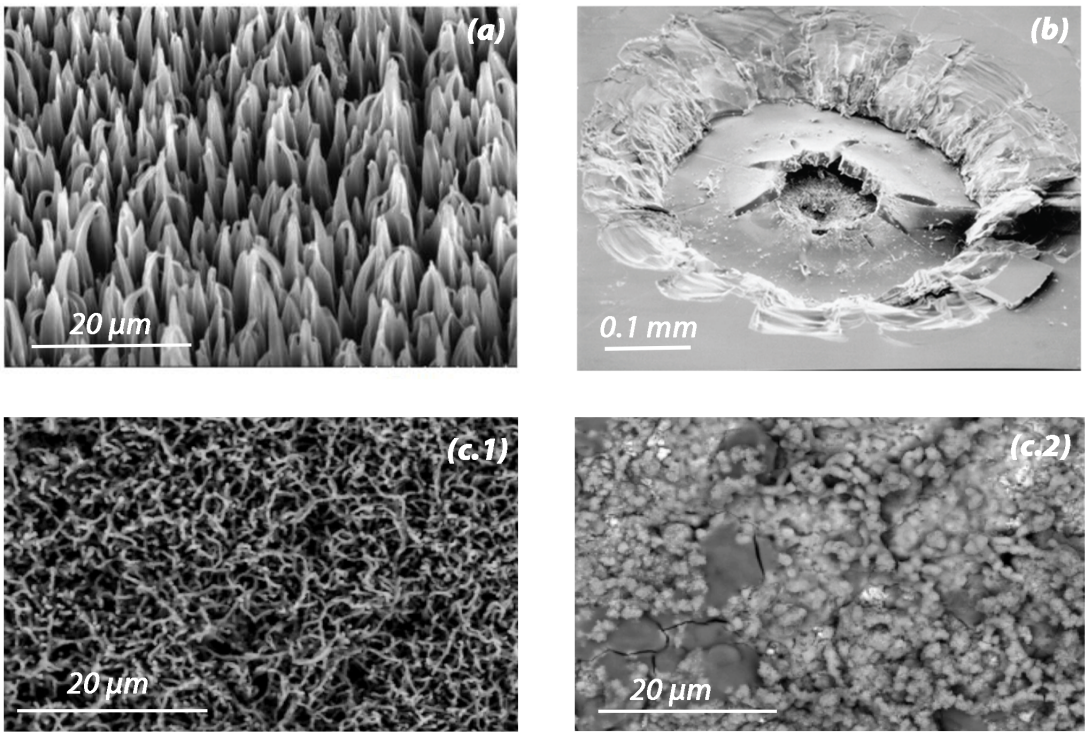

Figure 15: SEM images of the profound and devastating consequences of the space environment on exposed materials. (a) Kapton surface erosion after exposure to Atomic Oxygen (AO) [195], (b) Impact of debris on a solar cell [196], (c.1, c.2) Corrosion products on Cu foil with and without UV light irradiation [197].

These materials should provide enhanced functionality and safety and contribute to environmental sustainability. Emphasizing materials efficiency, implementing self-healing mechanisms or the use of coatings and fostering a culture of responsible resource management within the space industry are essential steps toward achieving these goals and ensuring the long-term success of our space exploration endeavors.

0.4.2. Space Power Generation for Diverse Mission Environments

Efficient power production has always been a significant challenge in space exploration, especially considering the vast distances and diverse environmental conditions encountered in the solar system [198]. The power generation system (PGS) is a critical component of spacecraft, whether in Earth orbit or on missions to far-reaching destinations. The choice of power generation technology depends on mission duration, distance from the Sun (expressed in astronomical units, AU), and the required electrical power [199]. Electrochemical power sources like non-rechargeable batteries and fuel cells can be employed for short-duration missions. However, for longer missions lasting several years, options such as photovoltaic (PV) devices or nuclear power systems (NPSs) in combination with rechargeable batteries become necessary to ensure uninterrupted and stable electrical power [198, 199].

In situations where the distance from the Sun or planetary surfaces poses challenges, such as low solar light intensity levels and extreme temperatures, alternative power generation systems are required. These systems may impose additional power burdens on mission budgets due to specific operating temperature requirements [199]. For outer planet missions, where working conditions are characterized by low light intensity and low temperatures, NPSs emerge as the optimal solution to meet mission requirements [199]. Radioisotope power sources, such as Radioisotope Thermoelectric Generators (RTGs) and Radioisotope Heater Units (RHUs), can provide thermal control and electrical power, making them suitable for such missions. The efficiency and mass of radioisotope power sources directly impact the overall mass budgets of science payloads and the range of mission scenarios. Plutonium-238 (^{238}Pu) has been the most commonly used isotope in space applications, primarily decaying by alpha emission and generating heat that can be converted into electricity [200]. However, concerns over the limited supply and cost of producing 238Pu have prompted the exploration of alternative isotopes, including ^{241}Am, ^{208}Po, ^{210}Po, and ^{90}Sr [198].

Conversely, satellites for inner planet missions, which are closer to the Sun, rely on solar cells (SCs) as their primary power generation technology [199]. This choice is driven by the fact that the power density of sunlight at these distances is sufficient to meet the electricity production requirements. By leveraging solar energy through SCs, these missions can efficiently generate the power needed to sustain their operations in the proximity of the inner planets, including Mercury, Venus, Earth, and Mars [199].

0.4.3. Advancements in Photovoltaic Technologies

Crystalline silicon-based solar cells (SCs) currently dominate the commercial market. However, a limitation of silicon is its indirect-bandgap nature. A misalignment between the conduction band's minimum energy and the valence band's maximum energy in the reciprocal lattice characterizes indirect-bandgap materials. As a result, the required momentum for an electron in the valence band to transition to the conduction band cannot be achieved through the only

absorption or emission of a photon with specific energy and momentum. To address this, silicon solar cells (SCs) require greater thicknesses (>100 μm) to optimize light absorption [201].

Other SCs typically comprise multiple materials stacked on a substrate. Various semiconductors, including germanium (Ge) and III-V semiconductors like gallium arsenide (GaAs), indium phosphide (InP), and their alloys (InGaP, InGaAs, InGaNAs, AlInGaP, and AlInGaAs), are commonly used as light harvesters in photovoltaic (PV) technologies for space applications [202, 203, 204, 205]. Notably, InGaP/InGaAs/Ge 3JSCs and AlInGaP/AlInGaAs/InGaAs/Ge 4JSCs, manufactured by companies such as Azur Space, Spectrolab, SolAero, and CESI, have become the standard in the aerospace sector due to their adherence to European and American Space Standards and superior performance compared to other PV technologies [202, 203, 204, 205].

Semiconductors play a crucial role in SCs by absorbing sunlight and generating electron-hole pairs, which are then transported and collected at the electrodes. The working principle of SCs can be divided into three main steps: i) absorption of light and generation of charge carriers, ii) separation and transport of charge carriers, and iii) collection of charge carriers. Optimizing these three aspects is essential for enhancing the performance of SCs. Efficient sunlight absorption specifically requires the use of semiconductors with an energy bandgap (Eg) within the visible to infrared (visIR) range, as the sun's emission spectrum is concentrated in this region [199].

The absorption of light is quantitatively described by the absorption coefficient (α), which should possess two crucial characteristics: panchromaticity (to absorb the majority of sunlight) and high value (enabling the use of thin samples to capture the entire solar spectrum and reduce the cost of solar cells) [206, 207, 208]. Subsequently, efficient separation and transportation of the generated free electrons and holes toward the electrode interfaces are essential. This is achieved through strategies that utilize both drifts (resulting from an electric field at junctions between the light harvester and charge transporting layers) and diffusion (caused by carrier concentration gradients) processes [206, 207]. Efficient electron and hole transport throughout the various layers of the solar cell contributes to low recombination rates and enables fast movement [206, 208]. When electron-hole pairs are generated through photogeneration, they can form excitons, neutral bound states that reduce the number of available free carriers and increase the probability of recombination events [209]. All of these factors significantly influence the solar cell's power conversion efficiency (PCE), which is defined as the ratio of the electrical power produced by the solar cell to the incident power. It is important to highlight that the maximum theoretical PCE is limited by the processes involved in solar energy conversion. The detailed balance limit is also known as the Shockley-Queisser limit [210]. The Shockley-Queisser limit, named after William Shockley and Hans-Joachim Queisser, represents a fundamental theoretical constraint based on thermodynamics and semiconductor physics. It takes into account various factors such as photon absorption, electron-hole pair recombination, and losses due to thermalization and radiative recombination. For an ideal infinite sequence of light harvesters, the maximum limit of PCE increases to 66% [199].

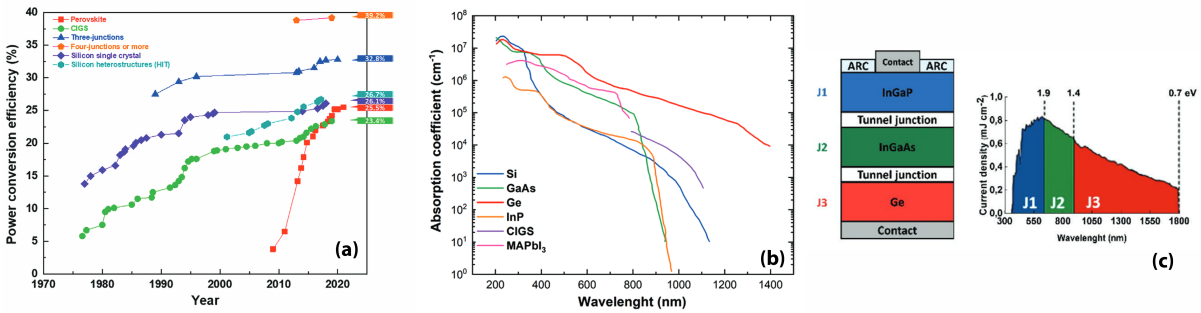

Figure 16: (a) Evolution of the PCE of some PV technologies.(b) Dependence of the absorption coefficients to excitation wavelenght for several semiconductors used in the PV industry. (c) Schematic representation of the fabrication processes of a MJSC and its absorption spectrum. [199]

The Shockley-Queisser limit is critical for photovoltaic technology, particularly for solar cells constructed with crystalline silicon (c-Si), a predominant material in the field. For these c-Si solar cells, the Shockley-Queisser limit stipulates the highest conceivable efficiency, a cap largely influenced by silicon's bandgap energy of roughly 1.1 electron volts (eV). This corresponds to a hypothetical maximum efficiency of about 33.7% at room temperature. Nonetheless, actual efficiencies of commercial c-Si solar cells fall short due to a variety of factors and constraints [199, 211].

Several strategies have been put forth in an effort to surpass the Shockley-Queisser limit, including the employment of lenses and mirrors to amplify the intensity of incoming solar radiation (concentrated PV systems)[212] and the development of Multi-Junction Solar Cells (MJSCs). The latter employs multiple light-absorbing subcells, often composed of III-V alloy semiconductors with increasing bandgaps, stacked sequentially and wired in series[213]. This layered structure facilitates more efficient absorption of the solar spectrum. Indeed, the highest recorded PCEs both in laboratory and module instances (47.1% and 40.6% respectively) were achieved by 4-junction MJSCs operating under concentrated conditions [199]. Yet, despite their potential, emerging photovoltaic technologies often present complex manufacturing processes and higher costs, which means crystalline Si-based technology remains the benchmark. Figure 16 (a) offers an illustrative depiction of the advances in PCE that have been achieved in diverse PV technologies, as previously described. Conversely, the subsequent Figure 16 (b) outlines the correlation between absorption and the excitation wavelength across a range of semiconductors commonly employed within the photovoltaic industry. This graphical analysis helps to illustrate the dynamic relationship between these variables and their implications for PV technology performance.

MJSCs, although bulky and rigid,[18,19] have garnered attention in the realm of photovoltaic technologies intended for space applications due to their superior performance (PCE = ≈32% on industrial scale)[14–16] and impressive radiation resilience (retaining between ≈90% and ≈87%

PCE upon electron or proton irradiation) [202, 203, 204, 205]. As mentioned above, MJSCs consist of a series of subcells (each with progressively increasing bandgaps) grown epitaxially on a single substrate and stacked, forming a standard structure with two terminal contacts. To prevent the formation of inverse p-n junctions, which could obstruct current flow, tunnel junctions are introduced to connect the subcells in series[214]. However, the fabrication of these devices can pose challenges due to the requirement for high-quality crystalline materials[50] and the complexities associated with the monolithic deposition of several light-harvesting layers on top of each other [215].

Currently, the pinnacle of space-intended devices is the 3JSC Ga0.50In0.50P/Ga0.99In0.01As/Ge model grown on a Ge substrate (Figure 16 (c)). Despite the nearly perfect lattice-matching (LM) of all the materials, the bandgap combination is suboptimal. The Ge bottom cell produces approximately 50% more current than the other two layers. Since the current of an MJSC is restricted by the layer generating the minimum photocurrent (as per Kirchhoff's current law), the surplus current is wasted as thermal energy [216]. The 4JSC overcomes this issue by incorporating an additional absorbing layer between the InGaAs and Ge, which successfully reduces the light incident on Ge and thus its photocurrent [199].

In addition to advances in metal-organic junction solar cells , another area of interest is the exploration of innovative strategies to improve their performance and stability. In recent decades, hybrid organic-inorganic perovskites, specifically methylammonium lead triiodide ($CH_3NH_3PbI_3$, commonly known as $MAPbI_3$), have also emerged as significant materials in the field of perovskite solar cells (PSCs). These materials have enabled the development of PSCs with remarkable Power Conversion Efficiency (PCE) values of up to 25.5% under standard conditions (lab-scale devices, under 1 sun AM 1.5G conditions) [199]. This breakthrough has yielded promising results, particularly for space applications [217, 218]. Several key factors contribute to the advantageous features of these devices. Firstly, they are manufactured using cost-effective solution-processed techniques [219], making them economically viable. Secondly, their flexibility and low weight, with a thickness of less than 5 μm and the highest specific among all photovoltaic technologies, make them highly desirable [220]. Lastly, these materials exhibit notable radiation hardness, further enhancing their suitability for space applications [221, 222].

Recent researches have focused on employing 2D materials like graphene and MXenes as Transparent Conductive Electrodes (TCEs), aiming at finding viable alternatives to indium, a critical raw material traditionally used in indium tin oxide (ITO) TCE fabrication. Successful development of TCEs based on 2D materials could have significant implications for photovoltaics and other fields, such as light-emitting diodes (LEDs), where substantial advancements have been made utilizing these materials [223].

0.4.4. Radiation Effects and Damages on Solar cells and their Components

As aforementioned, when the solar wind approaches Earth, it interacts with the geomagnetic field, trapping the incoming charged particles in two regions known as the Van Allen radiation

belts. These belts consist of an inner zone, extending from an altitude of 3200 to 16,000 km, and an outer zone, ranging from 13,000 to 60,000 km, that capture high-energy protons and electrons. Specifically, the inner Van Allen belt, situated between 1000 km and 6000 km altitude, encompasses substantial concentrations of electrons in the 100 keV range and energetic protons exceeding the 100 MeV threshold. Meanwhile, the outer Van Allen belt primarily contains high-energy electrons in the 0.1-10 MeV range and a modest concentration of protons in the 0.1-10 MeV energy range. The irradiation profile, including the energetic distribution and integral flux of the incoming particles affecting a satellite's solar panels, can significantly vary, and it relies entirely on mission-specific factors such as the final orbit altitude and the trajectory of the transfer vector relative to the Van Allen radiation belts [224, 225, 226].

Both directly and indirectly, ionizing radiations pose significant threats to the stability of spacecraft components. Directly ionizing radiations, such as protons and electrons, lead to ionization and the formation of defects. Indirectly ionizing radiations, including neutrons and γ-rays, have the potential to release charged particles within materials or instigate atomic displacement due to nuclear scattering or recoiling [227, 228]. Therefore, gaining insights into these radiation sources' average energies and fluxes is of utmost importance. Damaging radiation fields can be categorized into three main components: high energy photons (gamma and X rays), neutrons, and charged particles (electrons, protons, and ions). Despite having relatively small interaction cross sections, high energy photons and neutrons present a substantial interaction rate if the incoming flux is severe, owing to their macroscopic mean free paths (ranging from millimeters upward). This makes shielding against these types of irradiation a challenging task. Conversely, low energy charged particles, whose penetration depths range from sub-millimetric to micrometric, depending on the particle type and energy, are highly likely to interact with unprotected cells, leading to significant damage concentration. Nevertheless, it is practical to create effective shielding against these particles, a practice that is currently in use [199].

Key performance indicators for valuating the radiation response of SCs are the open-circuit voltage (Voc), short-circuit current (Isc), and the maximum power (Pmax) produced by the SCs. Various studies [229, 230] have demonstrated that SC structures suffer losses in Voc and Isc (and consequently Pmax) as electron and proton fluences increase. SC performance has declines with rising fluences at fixed energy values for both ionizing radiations, with performance degradation being more significant with increased electron energy. These effects are summarized in Figure 17.

When contending specifically with proton irradiation, an effective strategy involves a protective layer capable of stopping low energy protons (from 0.1 MeV to 10 MeV) but not the more energetic ones (above 10 MeV), which would demand impractically thick protective layers on the order of millimeters. These high-energy protons induce few atomic displacements and thus barely contribute to solar cell degradation. Protons of low energy possess larger interaction cross-sections and, hence, can cause significant displacement damage. This inverse correlation between damage and proton energy is demonstrated in Figure 17, where lower proton energies

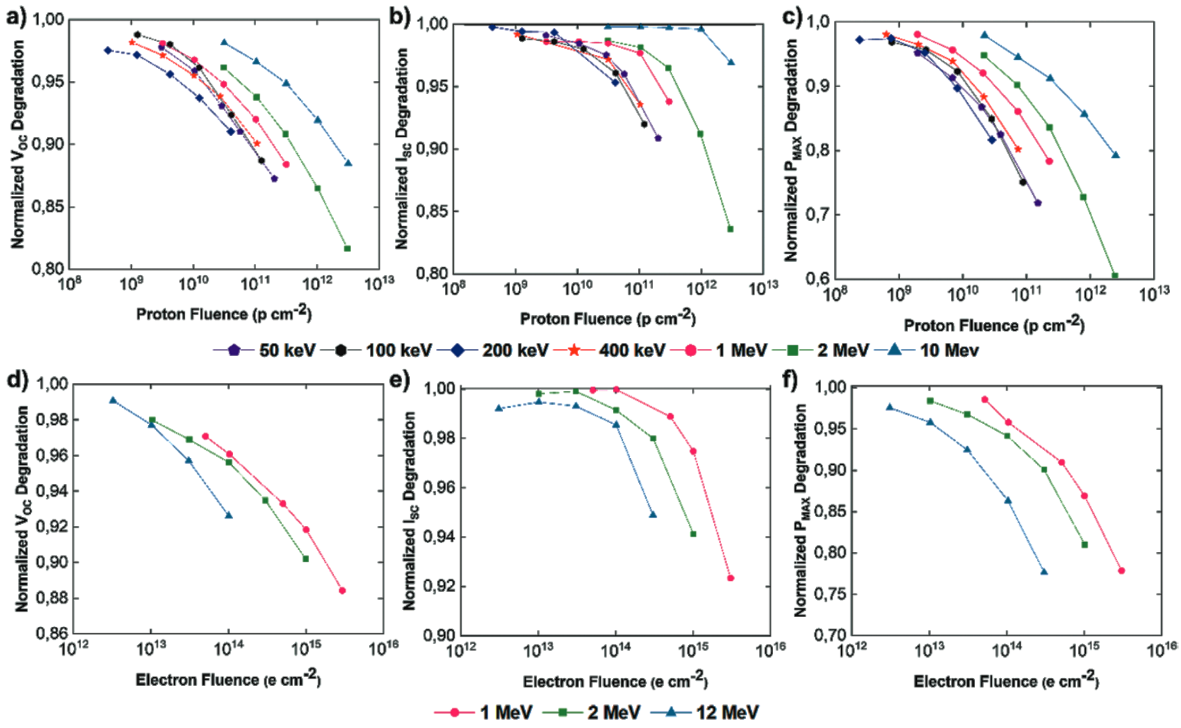

Figure 17: Degradation of VOC, ISC, and Pmax of an a GaInP/GaAs/Ge cell as a function of proton and electron fluence for various particles energies [229] .

correspond to higher damage rates. Understanding this inverse relationship is crucial for devising appropriate safeguards. Thus, based on the material's properties, the shield is designed with a thickness such that most protons of a pre-determined energy are stopped within the shield, while higher energy protons, with their smaller cross section that makes them less harmful, cross the shield itself.

The overall performance reduction in triple-junction (3J) solar cells is predominantly due to the sub-junction most susceptible to radiation, typically the middle InGaAs sub-cell. This particular sub-cell tends to degrade faster when exposed to proton and electron irradiation, thereby determining the overall radiation response of the entire cell [231]. Consequently, developing a robust shield capable of effectively stopping these charged particles becomes necessary to ensure the protection of the solar cell. Nonetheless, the protective elements are not impervious to damage and experience degradation over time, potentially affecting their functional properties.

Moreover, it is of utmost importance to maintain optimal transparency in the wavelength range of 350–1250 nm throughout the entire lifespan of the solar cell to ensure efficient transmission of sunlight. Any reduction in transparency would inevitably lead to decreased solar cell efficiency [232]. Currently, in LEO and GEO operations, 3J solar cells are safeguarded by space-ready glass sheets, which offer limited configurations. The prevailing solution involves utilizing borosilicate glass enriched with Cerium, with a thickness typically ranging from 100 to 150 μm. Cerium enhances the glass's radiation resistance, preventing it from darkening progressively, protecting

it against ultraviolet (UV) degradation. Moreover, these cover glasses commonly incorporate an anti-reflective coating, such as MgF_2, on their front side to minimize sunlight reflection [232]. For missions in MEO and GEO that encounter higher irradiation doses, protective glasses are chosen based on their thickness, as thicker glasses can obstruct a broader spectrum of energetic particles. Multiple studies have reported significant degradation of these cover glasses over their lifetime due to the harsh space environment [233, 234, 235]. For example fused silica and Corning 0214 cover glasses have been observed to darken when exposed to high-energy electrons, which is compounded by the accumulation of contaminant films [236]. Given the factors above, there is a growing interest in developing flexible cover glass for solar cells in space. These cover glasses aim at being lightweight, expandable, and cost-effective for space solar panels [237]. However, the spacecraft industry still heavily relies on traditional rigid cover glasses from the borosilicate family [238, 239]. For more detailed discussions on innovations and materials related to cover glasses, refer to the work by Plis et al. in [232].

The traditional method for attaching an anti-irradiation cover glass to a silicon solar cell uses silicone adhesive or Teflon, as documented in studies [240, 241]. More modern techniques have also been proposed such as electrostatic bonding, which can be used to bind the cover glass directly to silicon (Si) or gallium arsenide (GaAs) solar cells, provided that they share a matching thermal expansion coefficient [241].

However, the gluing process is fraught with potential issues, the most crucial being the distribution of the adhesive layer. The glue must be spread evenly across the solar cell surface to ensure complete adhesion of the glass sheet, and it must be devoid of any air bubbles. The reason is that any air bubble trapped during the gluing process can eventually rupture in space, leading to the failure of the adjacent solar cell. Furthermore, the adhesives could be degraded by UV light exposure, resulting in a significant decrease in transparency. This, in turn, inhibits the solar cells underneath, thereby reducing the device's overall efficiency. To prevent this degradation, a spectral filter could be used to eliminate the UV component of the incident solar light. However, this also reduces the photogeneration yield of the top Indium gallium phosphide (InGaP) cell, adversely affecting overall cell performance [204, 241].

Thermal factors also pose challenges in bonding. When silicone is used as an adhesive to bond different elements, and the coefficients of thermal expansion (CTEs) of those elements do not match, cracking can weaken the bond strength. From a chemical standpoint, high temperatures or extreme thermal variations can trigger new chemical reactions in organic molecules, resulting in undesirable post-curing or aging, bond breakage, and material discoloration [242]. As a result, the silicone adhesive can further lose the optical properties that make it particularly problematic in space solar cells or similar applications. This can occur due to the combined effects of high-vacuum and thermal cycles, which, along with other space environmental factors, can create harsh operational conditions [242, 243].

Various adhesive coating and bonding technologies have been developed for industrial applications considering these challenges. The Silk Screen Printing technique is currently the most

commonly used method for coating with adhesives, but it struggles to maintain uniformity in the adhesive layer's thickness during practical operation [244]. Spray-coating technology, which offers benefits such as uniform coating and good stability, is also extensively used for adhesive deposition on substrates [241]. The spin-coating technique relies on the centripetal force by rotating the substrate platform to deposit the adhesive on the substrate film [245]. However, each technique brings its own challenges, and research is ongoing to refine and develop new approaches[241].

0.5. Quantifying Radiation-Induced Structural Changes and Material Degradation

In the brief span of just over half a century, humanity has made remarkable strides in the two frontier domains deepen in this work: space and nuclear technology. Not so long ago, in 1957, the launch of Sputnik marked the beginning of mankind's endeavors in the celestial expanses [246]. The ensuing leaps in space exploration and related technology have been astonishing. Paralleling this story of progress and exploration, the nuclear field has followed a similar timeline. The genesis of nuclear materials dates back to the mid-1950s, gaining global recognition as a significant scientific pursuit towards the end of the decade. The inaugural foundations of this discipline were laid in the First and Second International Conferences on the Peaceful Uses of Atomic Energy, convened in Geneva in 1955 and 1958 [247].

Delving into the study of materials exposed to ionizing radiation reveals the relative infancy of this field. A span of merely fifty years has witnessed remarkable strides, yet the complexity of the subject indicates that our understanding is still in a state of evolution. Navigating through this discourse, it becomes unmistakable that numerous knowledge gaps persist, inviting deeper exploration and rigorous investigation.

For more than this half century, extensive knowledge has been gathered on the effects of radiation damage in metals, specifically in alloys with face-centered cubic (FCC) and body-centered cubic (BCC) structures, due to their relevance to the industry [248, 249, 250]. The current understanding and comprehensive data on radiation damage indicate that there is still much to explore regarding the time-dependent evolution of microstructures under the influence of irradiation effects [248, 250, 251, 252].

When radiation interacts with matter, it generates a primary knock-on atom (PKA), displacing multiple atoms from their lattice positions [248, 250, 252]. This PKA, resulting from the collision with a neutron or particle, undergoes both elastic and inelastic interactions. The inelastic interactions transfer some of the initial energy to an excited state of the impacted atom, thereby reducing the kinetic energy of both the neutron/particle and the PKA (Figure 18) [252]. After the primary collision, the PKA dissipates its kinetic energy through electron excitation and elastic collisions with other atoms in the irradiated material, nearly conserving the total kinetic energy of the involved atoms [253, 254]. This energy dispersion leads to the displacement of numerous secondary atoms, initiating a series of cascading collisions often represented as a tree-like structure. However, most displaced atoms quickly reposition themselves into vacant lattice sites or merge with other defects and sinks within nanoseconds, resulting in significantly fewer vacancies and interstitials than the original displacement count. As briefly introduced before the final assessment of this effect is measured by dpa which is further discussed later also in Section 0.5.2.

The clustering and interaction of the vacancies and one or two-dimensional interstitials lead to

several effects, the same described in the section related to radiation damage in nuclear materials above [248, 252]. The whole process of point defects, vacancies, and interstitials production, ultimately resulting in macroscopic phenomena like volumetric swelling, is illustrated in the Figure 19 (a), where the spatial-temporal scales of void swelling processes are depicted.

At the same time, neutron-induced transmutations play a crucial role in determining the suitability of a material for nuclear applications [255]. These transmutations cause stoichiometric changes as nuclei undergo nuclear reactions with incident neutrons, transitioning into stable or radioactive states.

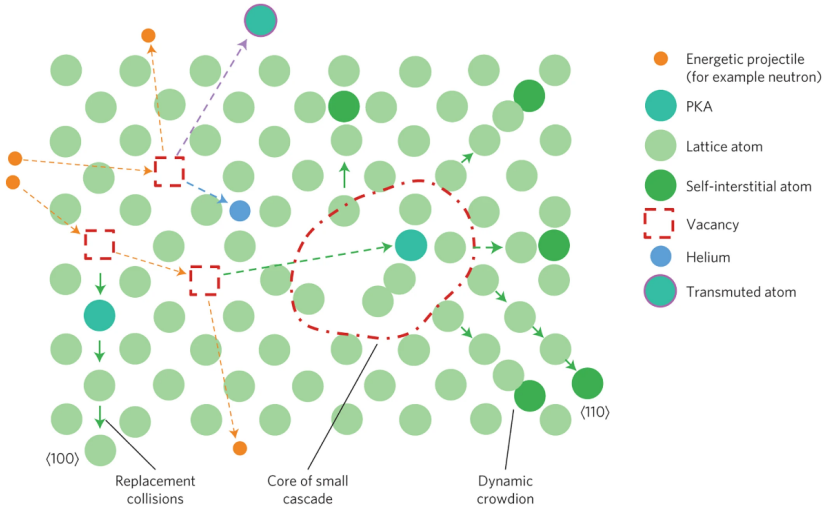

Figure 18: Schematic illustration of irradiation damage cascade [252].

Deciphering the various interactions involved proves challenging due to the complex dynamics. The damaged lattice rapidly evolves towards more stable states through intricate many-body processes [256, 257]. These unstable microstructures often lead to the clustering of remaining defects, resulting in significant degradation of material properties. While understanding individual processes and their interconnections is already a daunting task, comprehending the processes leading to macroscopic effects over the lifetime of a nuclear reactor (30-80 years) or solar panel in space (10-20 years) poses an even more significant challenge [248]. For example, despite the presence of microscale descriptions [248, 258] and macroscale descriptions [259] of void swelling, the sudden onset of this phenomenon as a function of imposed state variables remains unpredictable [248].

Radiation damage in materials involves intricate dynamic processes operating across multiple scales. It is rooted in rate-equation formulations and transition-state theory, considering specific details like point defect concentrations [249, 260]. A significant part of the damage produced, as mentioned above, is attributed to the formation and migration of interstitial-vacancy couple (Frenkel pair) defects produced, atomic disturbances that do not return to their initial position, leading to an increase in atom replacements over the actual defects produced. These defects often migrate to interfaces, triggering alloy dissolution, segregation, and grain-boundary embrit-

tlement, thereby hastening the aging of materials [248].

Recent developments have highlighted the role of self-interstitial atom clusters, their one-dimensional mobility, and the bias in producing isolated vacancies versus interstitials and their clusters in the context of irradiation defect growth [249, 260]. This emphasis on the evolution of point-defect clusters in varying local environments exemplifies the role of self-organized defects in Materials Science and Simulation (MSS). It emphasizes the multiscale and multifaceted nature of material aging, underlining the importance of different disciplines in understanding this complex phenomenon [248].

The exploration of the governing mechanisms and processes of irradiated structural materials is facilitated through the utilization of a multiscale strategy. This strategy involves both computational materials science and high-resolution experimental validation. The hierarchical multiscale modeling methodology, depicted in Figure 19 (b), generally combines various computational approaches. These include ab initio structure calculations at the atomic scale, molecular dynamics simulations, kinetic Monte Carlo simulations, discrete dislocation dynamics, and rate theory. This methodology also integrates continuum calculations, which cover thermodynamics and kinetics, as well as phase field calculations [252].

The requirement for ab initio methods arises to calculate parameters such as the most stable defect–cluster configurations, their dissociation energies, and the most likely paths of lattice diffusion. The findings from ab initio studies can then provide input data for molecular dynamics, kinetic Monte Carlo, rate field theory, and thermodynamics computations. Figure 19 (b) shows additional connections between the varying simulation methods through the depicted arrows [252].

Experimental validation technologies, such as in situ micromechanics, high-resolution electron microscopy techniques, atom-probe tomography, neutron, and X-ray scattering sources, play a significant role in verifying computational modeling results. The fusion of these computational and experimental modeling approaches represents a considerable challenge. This is primarily due to the requirement of incorporating more traditional structure-property correlations and irradiation-induced defect characteristics into a single integrated framework [248, 252].

The simulation of the effects of light particles, such as protons and electrons, on materials destined for space applications can be readily conducted in a laboratory setting. While replicating the influence of neutrons proves significantly more challenging. This challenge stems from the necessity of a nuclear reactor that can emulate the precise neutron spectrum conditions required for these crucial experiments, a resource that isn't always within reach.

With this research thesis delving into the comprehensive investigation of the irradiation effects on amorphous oxide ceramic materials, the forthcoming discussion will be primarily centered on comprehending the impact of irradiation on these types of materials. Particular emphasis will be placed on understanding the influence exerted on Al_2O_3 materials. This material was specifically chosen due to its pertinent role in the nuclear application component of this research.

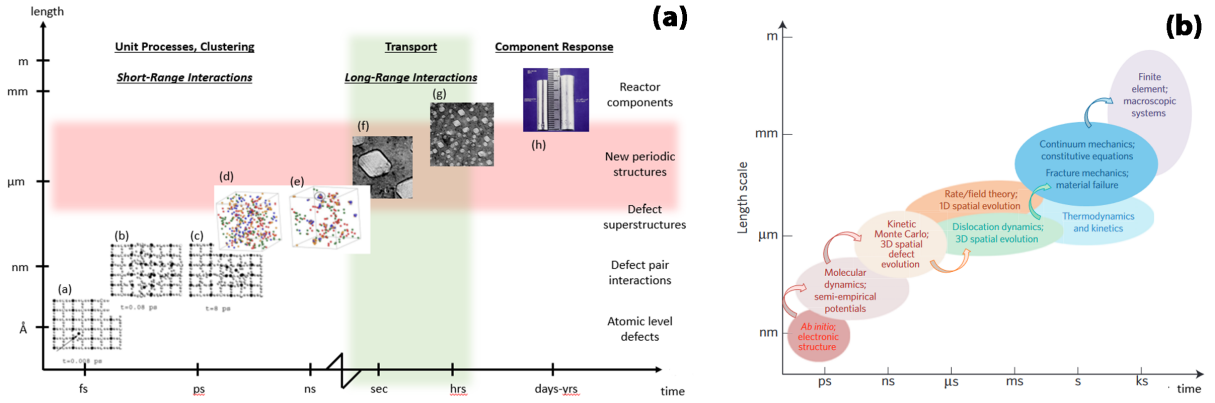

Figure 19: (a) The spatial-temporal scales of void swelling processes are depicted. The interaction of radiation leads to the generation of primary knock-on atoms (a_a), initiating a thermal spike (a_b) and subsequent annealing (a_c). Lattice point defects (a_d) quickly form and relax into local defect structures a_e through short-range interactions. These structures act as nucleation sites for voids (a_f), which organize into a semi-regular lattice (a_g) through long-range interactions. The growth of voids and evolution of lattice spacing result in macroscopic swelling in the material component (a_h)[248]. (b) Commonly employed integrated computational materials science (CMS) methods utilized to comprehend the correlations between structure and properties influenced by irradiation, aiding in material research and development [252].

Thus, its in-depth analysis is not only essential but also intriguing within the broader scope of this work. Then a small section will be dedicated to the different strategies used for evaluating the radiation damage induced by light particles for the specific case of space applications.

0.5.1. Ion Irradiation as an Emulation Tool: Understanding Material Behavior, Damage Accumulation, and Crystallization in Amorphous Al_2O_3 under Neutron Irradiation

The primary still unsolved uncertainty surrounding PLD Al_2O_3 pertains to its response under neutron irradiation. Current efforts are underway to collect data on neutron irradiation of this amorphous material. However, this work may take some time due to its high cost and complexity. In the meantime, ion irradiation is a valuable instrument for initial investigations. Over the years, heavy ion irradiation has become a powerful emulation tool for studying material behavior under neutron irradiation. It bypasses the intricacies of in-reactor testing and enables achieving high damage rates without residual radioactivity [248, 252]. Consequently, ion irradiation allows considerably shorter and more affordable irradiation campaigns, including irradiation and post-irradiation analyses, making it a vital tool in predicting and understanding neutron damage in materials [261]. Furthermore, it is acknowledged as an unparalleled tool for producing controlled defects, structural disorders, stress, phase transformations, and altering the physical properties of materials in general [262].

However, designing an experiment with heavy ions that accurately represents neutron behavior requires careful consideration of the differences between neutrons and heavy ions. Unlike neutrons that only lose energy through specific collisions with the material's nuclei, energetic ions suffer depth-dependent energy losses due to collisions with both target nuclei and target electrons during their passage through matter. The energy losses due to these interactions, defined as nuclear (S_n) and electronic (S_e) energy losses, delineate the interaction modes between the incident ions and the exposed material. The Electronic to Nuclear Stopping Power (ENSP) ratio (S_e/S_n) becomes a critical parameter [263]. Notably, even under neutron irradiation, the S_e term and, thus, the ENSP ratio are not null. Although there is no direct energy transfer from neutrons to electrons, atoms displaced by neutron collisions do interact with electrons, thereby transferring some energy. Nuclear and electronic energy losses primarily depend on the energy and mass of the accelerated ions. Generally, the ENSP ratio increases with rising energy, while increasing the ion mass reduces it [264]. In metallic materials and alloys, the energy deposited to target electrons dissipates quickly, leading to localized heating of the material without structural transformations. Conversely, ionization effects are expected to be more significant in covalent/ionic bonding materials, possibly causing artefacts due to electrostatic interactions [265, 266, 267]. It is widely accepted that higher S_e/S_n ratios tend to slow damage accumulation as more energy released to electrons equates to more energy available for local heating, promoting annealing and recovery processes along the ion path [266, 267]. However, a comprehensive understanding of the influence of electronic and nuclear energy losses on glassy amorphous ceramics, particularly the material class studied in this work, is lacking. Thus, all the work following presented, related to irradiation, have been designed using data related to crystalline ceramics and crystalline alumina as a preliminary reference. This approach may not fit amorphous materials like a-Al_2O_3 and may require further refinement as the understanding

in this field is increased.

Past research into the material-dependent impacts of electronic energy losses on ceramic crystalline materials [263, 268, 269] has shown that combining nuclear and electronic energy losses can drastically reduce accumulated damage. Thomè et al. highlighted that this "healing effect" may occur in certain ceramic crystalline materials when the S_e exceeds the S_n, depending on a balance between defect creation and annihilation. This balance depends on the physicochemical properties of the irradiated material and irradiation conditions like temperature, low/high energy ion fluences, and dose rates [263, 268, 269].

Zinkle et al. [264] suggested the theoretically appropriate ENSPs for systems characterized by a fast neutronic spectrum, (such as LFRs and fusion reactors), pointing to values below 13 as the correct range. Their suggested ENSP value [264] was based on the effect of ionization-enhanced migration of oxygen vacancies on the development of dislocation loops in Al_2O_3 crystals. The impact of the irradiation spectrum observed was found to have significant implications [270]. Specifically, light ions irradiation (like protons and electrons), having ENSP ratios exceeding 1000, is inappropriate for simulating ceramics' behavior under typical fission or fusion neutron irradiation conditions. An ENSP ratio of around 10 may be more appropriate [270]. However, considering the interplay between these mentioned effects on a-Al_2O_3 has not been fully clarified yet, based on the current knowledge, minimizing the ENSP ratio in the experimental design of ion irradiation experiments is deemed a good practice.

As shown previously in Section 0.2.6., PLD amorphous material crystallizes under irradiation. At this point, the governing mechanisms of crystallite nucleation and subsequent particle growth observed can be speculated upon.

The transition phenomenon between amorphous and crystalline states triggered by electron or ion irradiation has been a long standing, complex issue [271]. The "thermal spike" model is one of the simplest models to explain observed nucleation processes in an amorphous system [271]. This model suggests that a localized energy deposition region, the thermal spike, is created when an ion traverses the amorphous material. Structural changes, chemical reactions, and nanoscale feature formation could occur within this region [271]. Recent molecular dynamics simulations propose that thermal spikes could be effectively explained through the collision cascades caused by ion passage. Numerous target atoms are dislodged from their lattice sites during each ion passage, followed by a subsequent thermal spike phase where the cascade region attains thermal equilibrium with its surroundings [272]. Moreover, energy deposition to the electrons by slowing down incident ions could play a crucial role in thermal spike creation [273]. The deposited energy may eventually induce atomic movement and the creation of cylindrical damage along the ion path [271]. During the thermal spike, atoms inside the displacement cascade may reach a partially melted state (cascade melting)[272]. The combined electronic and ballistic thermal spikes associated with each ion trajectory are often used to explain and model observed ion irradiation grain growth in ceramic polycrystalline oxides [273] and carbides and may even be used for describing the nanocrystal nucleation in amorphous materials.

Koroni et al. described the radiation-induced nucleation in amorphous material in their paper [271], characterizing it as a disordered state transitioning from ordered configurations towards crystalline states by irradiation-assisted atomic rearrangement. The underlying assumption is that atomic ordering may occur as the free energy reduction of the irradiated amorphous region declines. The evolution of ordered atomic configurations into crystal nuclei depends on whether the crystal nuclei are more stable than the disordered situation.

0.5.2. Evaluation of Displacements Per Atom (dpa) in Heavy Ion Irradiation

In the sphere of irradiation, as previously outlined in preceding sections, the term "dpa" signifies "displacements per atom." This essential parameter is utilized to ascertain the damage inflicted on materials subjected to irradiation [104].

The dpa depicts the mean number of atomic displacements in a material for each impinging particle. This is ascertained by dividing the cumulative atomic displacements by the total number of atoms in the material [104]. For the designing and evaluation of materials to be used in severe conditions, such as in nuclear reactors, particle accelerators, and space exploration, understanding the dpa values is vital.

Dpa computation can be carried out utilizing the SRIM-2013 [274] code using the equation [275]:

$$DPA\left[\frac{Displacements}{Atoms}\right] = \frac{SRIM_{output}\left[\frac{Vacancies}{\text{Å}\cdot ions}\right] \cdot IonFluence\left[\frac{ions}{cm^2}\right] \cdot 10^8\left[\frac{\text{Å}}{cm}\right]}{AtomicDensity\left[\frac{atoms}{cm^3}\right]} \quad (1)$$

While there is no significant difference in ion implantation depth calculated by the two different modes present in SRIM ("Ion Distribution and Quick Calculation of Damage - cascades" mode or the "Full Cascade Damage" mode) the damage production is not the same. This inconsistency has been examined quantitatively in numerous papers. Furthermore, the results of these simulations heavily rely on the selected values for the threshold energies for displacements. The scientific community continues to discuss the best method for evaluating dpa based on SRIM simulation [276, 277, 278], as different papers propose slightly varied procedures. Despite certain limitations, the Norgett, Robison, Torrents (NRT) standard [279] is the standard procedure for computing dpa in all reactor Monte Carlo codes. Initially formulated for mono-elemental materials, it is a straightforward and comprehensive form ideal for analytical computations and computer code applications [279]. The "quick damage" SRIM simulation alternative is usually chosen for comparison with reactor radiation dpa data because its outcomes align best with the "NRT standard dpa" as recommended by simulation studies [279]. Utilizing other alternatives could lead to deviation from the established standard. Utilizing the SRIM "Quick calculation" option as a fallback choice has also been proposed when calculating the effective damage energies for compounds is impossible or when one wants to avoid manually handling SRIM data files [279]. The "quick calculation" mode employing the Kinchin and Pease model is also crucial to avoid anomalies recently found in its full-cascade model [275]. However, the authors in [279] admit that moderate quantitative inaccuracies may occur, with a maximum computed vacancy production error of around 30%. Notably, the dpa value in isolation is generally inadequate to portray ceramic ion irradiation effects. Most energy lost by heavy ions may be transferred to lattice electrons, causing ionization.

The effects of ionization are more prominent in ceramics than in metals, and these need to be considered when comparing results derived from different irradiation environments in ceramic experiments. The ENSP ratio discussed earlier seems to be a beneficial extra parameter for evaluating irradiation spectrum effects in ceramics, as discussed in [264].

0.5.3. Accelerated Irradiation Challenges and Implications for Microstructural Evolutions

Accelerated irradiation poses multiple difficulties, primarily the influence of an enhanced damage rate on the ensuing microstructure and the requirement to consider significant transmutation reactions happening in-reactor. To mimic the gas production caused by transmutation, pre-injection, or even better, simultaneous gas implantation and damage creation are proposed [280]. The more significant challenge is the damage rate, for which Mansur's invariance theory is a solution [281, 282]. The theory posits that alterations in an irradiation variable from reactor conditions are offset by shifts in other variables (like temperature), aiming at maintaining the collective behavior of defects during irradiation. Such adjustments were devised for specific microstructure processes like radiation-induced segregation or void growth. In both instances, the greater dose rate in an accelerator than in a reactor necessitates an equivalent temperature increase to achieve the same outcome [280].

As for using ion irradiation as a tool for radiation damage, it is crucial to determine the irradiation mode. Irradiations can be executed with a raster-scanned [283] or defocused [284] beam. Raster scanning assures a uniform dose distribution over expansive areas, but this mode has to be perceived as pulsed irradiation. In a study by Brimhall et al., pulsed irradiation was compared with continuous irradiation in pure nickel [284]. The study revealed a minimal difference in the resultant void microstructure across all temperatures, and any variation in void swelling fell within the error range. Another study [285] investigated the impact of beam scanning on self-ion irradiations of pure nickel, indicating that defocusing led to more pronounced void growth at all examined temperatures (350-800 °C).

Hishinuma et al. [286] applied pulsing to a Ti/Si-modified austenitic alloy using 4 MeV Ni2+ up to 50 dpa at 675 °C. The study found that pulsing had a minor impact on void nucleation and growth, and it did result in a size reduction of loops and a two-fold increase in the number density of loops attributed to the annealing of point defects. Regardless of the alloy with helium pre-implantation, defocusing consistently resulted in larger swelling and increased void diameter and number density compared to raster-scanning. This was consistent for alloy T91 as well. The swelling disparity between HT9 and T91 became insignificant with 100 appm He pre-implantation, suggesting a minimal difference in swelling resistance at these dosages[285]. For clarity, both HT9 and T91 are ferritic/martensitic steel alloys, with HT9 being primarily used in fast reactors due to its radiation resistance, while T91 is known for its enhanced creep strength and corrosion resistance in high-temperature environments.

A similar set of effects is shown in Figure 20 (a) which presents a comparative analysis of the T91 and HT9 alloys exposed to 5 MeV Fe^{2+} irradiation at 440 °C to a damage level of 140 dpa, with 100 appm He implanted using both raster-scanned and defocused beams. The figure 20 (b) further illustrates the increase in diameter, number density, and swelling in the HT9 alloy when the beam in irradiation is defocused.

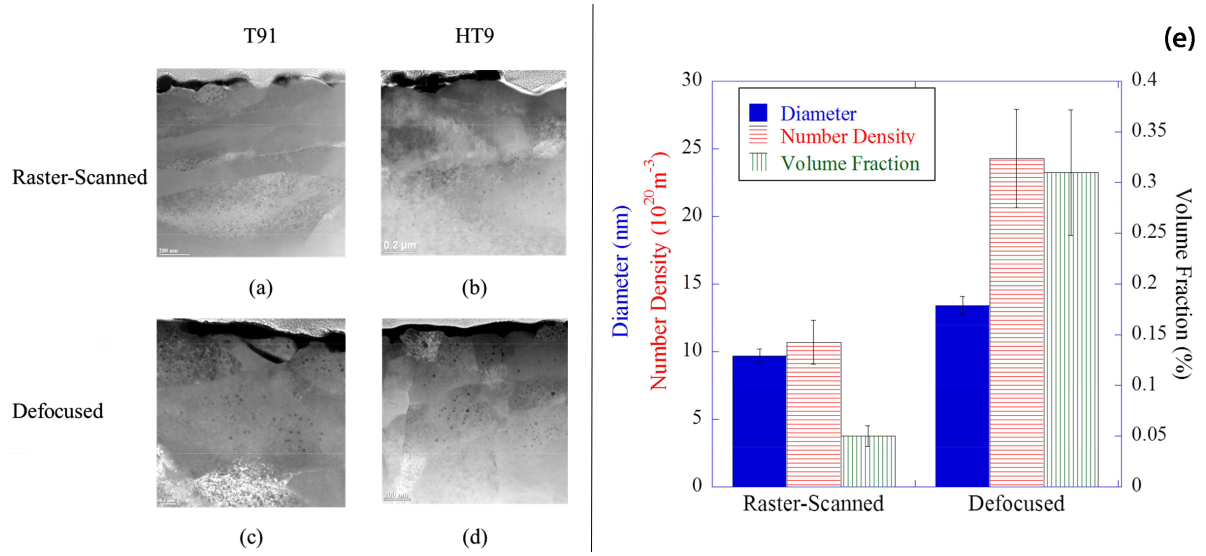

Figure 20: Assessment of T91 and HT9 Exposed to 5 MeV Fe^{2+}. Irradiation at 440 °C up to 140 dpa with 100 appm He, implemented via raster-scanned (a-b) and defocused (c-d) beam. Augmentation in diameter, number density, and swelling observed in HT9 following beam defocusing during irradiation at 440 °C, 140 dpa with 100 appm He using 5 MeV Fe^{2+} (e) [285].

The computational model described in [285] addresses a mechanism where in-cascade annealing of defects between pulses reduces the level of vacancy supersaturation [287]. As corroborated by Brailsford and Bullough [288] and Little [287], lower vacancy supersaturation will lead to decreased nucleation and growth. Key findings from these pieces of evidence suggest that pulsing or raster-scanning should be carried out at a sufficiently high frequency to avoid in-cascade annealing while the beam is off in a volume element. For example, for the specific case of stainless steel irradiated at 450 °C, it is estimated that there was no difference in void behavior in pulsed versus continuous irradiation above 500 Hz [285]. However, it is critical to exercise caution when comparing outcomes from ion irradiation studies executed with different beam modes. Ideally, only irradiations with nearly identical defocusing or raster-scanning conditions should be compared directly [280, 285].

0.5.4. Solar Cell Degradation in Space: Comparing JPL and NRL Methods for Radiation Damage Modeling

The degradation of solar cells in space is a critical challenge largely instigated by incident protons and electrons, either trapped within Earth's radiation belts - the Van Allen belts - or emitted during solar events. This degradation is a consequence of the interaction between the cells and particles with energies extending from nearly zero to hundreds of million electron volts. To project and manage this degradation, several steps has to be undertaken. Firstly, understanding how different energy particles affect solar cell degradation is vital, meaning the relationship between the energy of the particles and the resulting cell damage needs to be clarified. Secondly, the radiation environment, including any shielding materials, should be meticulously defined. The final step involves designing a method that marries the energy dependence of the damage coefficients with the radiation environment over the mission's duration, making it possible to compare with ground test results [289]. Two main methodologies currently hold sway in the modelling of solar cell degradation in space. One is the long-established approach from the US Jet Propulsion Laboratory (JPL) [289, 290] which uses the determination of 1 MeV electron fluence that induces equivalent cell damage to a defined space radiation environment. The other, a more recent approach from the US Naval Research Laboratory (NRL) [291], calculates the displacement damage dose using the energy dependence of damage coefficients, proton and electron spectra that a bare cell would experience. Calculating relative damage coefficients for omnidirectional particles on bare cells, based on normally incident particle data, is a crucial process in both methodologies. Generally, this results in halving the damage coefficients when considering only particles incident on the cell's top surface. Special attention is required for low-energy protons, though. Cover glass effects on the cell are accounted for via calculations based on 'continuous slowing down' approximation and range-energy tables for protons and electrons traversing different cover glass material thicknesses. This calculation is relatively straightforward for electrons and protons that traverse the cell without significant energy changes. For protons that stop in the cell, calculations need to account for a sharp increase in relative damage at the proton range's end [289].

The SRIM (Stopping and Range of Ions in Matter) computer code plays a crucial role in the NRL method, as it allows accurate calculations of displacement damage dose. SRIM can provide accurate values of Non-Ionizing Energy Loss (NIEL) for energies up to 10 MeV, an energy range crucial for most space applications, thus facilitating assessments of cell materials new to the market and bypassing lengthy analytical calculations. This underlines the increasing significance of dpa (displacements per atom) evaluations in understanding and predicting solar cell degradation [289].

While both JPL and NRL methods offer valuable insights into predicting solar cell degradation in space, they differ significantly in their implementation. The JPL model requires an extensive set of ground measurements to ascertain the energy dependence of the damage coefficients, whereas the NRL approach calculates these from the NIEL, typically only needed for proton energies

less than 10 MeV. Thus, the NRL method is simpler to implement in most cases, particularly with new and emerging cell technologies due to its fewer ground measurement requirements. However, for pre-established experimental databases, the JPL method, with its successful track record, remains the only direct method to address thick crystalline Si cell technologies [289].

As delineated in the preceding sections of this document, including the discourse related to nuclear interactions, SRIM (Stopping and Range of Ions in Matter) [274] software was selected in this work for as the reference Monte Carlo code for simulating radiation damage. This powerful simulation tool emerges as the preferred software for our preliminary evaluations of radiation-induced damage in materials. The decision is rooted in SRIM's proven efficiency and accuracy in modeling particle interactions and energy dissipation processes in a solid target, thereby providing critical insights into the radiation environment a material is subjected to.

The following stages of this manuscript will detail the crucial role played by the SRIM software. A detailed examination will illustrate how this advanced computational resource provides the means to investigate the complex interactions between radiation and materials. By leveraging the capabilities of SRIM, a more comprehensive insight into radiation damage and its impact on material longevity and reliability in radiation-rich environments is expected to be gained. Consequently, this understanding is predicted to assist in advancing more durable and radiation-resistant materials suitable for various applications, ranging from space technology to nuclear energy production.

Aim of the Work

Pioneering Pulsed Laser Deposition: Exploring Applications in Nuclear Industry and Space Exploration

Drawing from the above mentioned advancements, this thesis comprehensively explores materials science and technology. It began with a detailed study of the pulsed laser deposition processes, grounded in the substantial knowledge compiled by the Nano2Energy (N2E) group at the Italian Institute of Technology (IIT). This robust foundation paved the way for a daring venture: leveraging the state-of-the-art coating production process of pulsed laser deposition in two distinct areas - the nuclear sector and space exploration, which share a connection via ionizing radiation. The design of this doctoral research was meticulous, aiming at building upon previous work regarding amorphous thin films produced through Pulsed Laser Deposition (PLD). The promising initial findings outlined in earlier chapters provided a propitious base for this research, which embarked on a unique trajectory. The following chapters will illustrate the thesis as a wholly novel contribution within the pertinent area of next-generation Lead cooled fast nuclear reactors and antireflection coatings for space applications.

The work associated with the nuclear section relies on the robust groundwork laid in the past decade, as detailed in the previous sections. The goal was to push the boundaries further, attempting to address the existing gaps and advancing the possibility of implementing PLD Al_2O_3 coatings in LFRs. The specific segment of work executed within the advanced materials development framework for the issues described in the SCs space application pertains to the revolutionary SpaceSolarShield project [292] , supported by the Cariplo Foundation [293]. This initiative was meticulously structured with a clear objective: to transform the operational context of solar cells (SCs) by establishing a comprehensive optical radiation shield on the Multi Junction (MJ) SC, utilizing a PLD coating. This objective addresses current challenges and aims at enhancing the effectiveness of exposed solar cells. CESI [204], a collaborator in this initiative, focused on improving solar cells, while the Politecnico di Milano and IIT primarily handled the coating creation. The methods utilized for depositing the protective layer align with those used for the solar cell stack, leading to seamless integration of both production stages. This harmony promises significant advantages in materials logistics and process uniformity. The strategy to deposit a protective layer directly onto the solar cell aims at creating a shield against low-energy particles, primarily protons, as outlined in Section 0.4.4. A segment of this thesis work was dedicated to the initial selection of coating materials with a high optical band gap, ensuring optical transparency up to the UV spectral range, and their characterization. This

approach will enable the InGaP top cell in the MJSC to capture the entire UV spectral range, thus enhancing its operational point and the overall efficiency of the solar cell stack. This innovative approach can substantially improve solar cell performance efficiency and power density and facilitate meticulous production control. This method will enable the creation of custom protective coating setups for each unique mission, a groundbreaking achievement in this domain. Furthermore, the direct deposition of coatings is projected to tackle the issues related to cover glass and adhesive, directly removing the needs to use them.

After conducting an initial evaluation of various materials for antireflection coatings, then in order to focus the efforts, the research narrowed its focus exclusively to alumina coatings, considering them as potential candidates for both the applications mentioned.

This thesis began by employing an array of specific characterization techniques and methods to identify the missing material properties vital for the qualification process of the nuclear reactor anti-corrosion coatings and space solar panel antireflection coatings applications. The experiments were carefully designed to emulate real operational conditions closely. Significant efforts were dedicated to defining the concept of radiation damage relevant to both fields previously mentioned, which will prove beneficial in the subsequent chapters where radiation effects on the material are thoroughly discussed, presenting the results obtained through irradiation experiments and Monte Carlo simulations.

This work also addressed additional technological challenges, such as the mechanical behavior of the coating/substrate system, demonstrated by the deformation of coated dog-bone steel samples in tensile tests. While earlier findings have uncovered exceptional properties, this study aims at enhancing these traits further. As such, the relationship between the film's mechanical performance and its structural characteristics will be examined. The film's response was manipulated by modulating internal stresses within the coatings via the deposition process parameters.

After these experiments, focus shifted to examining the amorphous alumina structure and its evolution under radiation exposure. A significant effort was expended on controlling the level of *radiation resistance* in PLD-grown Al_2O_3, given the crucial role of the amorphous matrix in radiation tolerance and plasticity. The primary objective of this study was to accumulate valuable data for potential practical engineering applications. Ensuring the stability and effectiveness of alumina coatings under various testing conditions was of utmost importance. As such, numerous experiments were conducted by general standard conditions. The focus was placed on understanding the physical mechanisms responsible for the material's unique properties and understanding the underlying mechanisms comprehensively. In conclusion, innovative strategies were proposed to provide new tools and expand the operational range, thereby enhancing the performance of the material. As observed mechanisms may apply to other systems, this thesis offers novel solutions that advance the field of nuclear and space applications research.

1 | Pulsed Laser Deposition Ceramic Coatings - Properties Investigation

1.1. Multifunctional Radiation Shield Coatings: A Formal Exploration via Monte Carlo Simulation

As stated in the introductory chapter of this work, the primary solution for safeguarding SCs against damage from low particle radiation involves the utilization of a protective coverglass. The SpaceSolarShield project, funded by the Cariplo Foundation, aimed at investigating, among the several objectives, the possibility of using a multi-functional radiation shield coating explicitly tailored for space triple-junction solar cells. The aim was to overcome various issues associated with these cells, such as coverglass darkening and adhesive problems. At the core of this strategy lies a brilliantly simple yet powerful idea: applying a robust and densely packed coating, produced using the advanced technique of pulsed laser deposition (PLD), directly onto the top layer of the space solar cell. This innovative approach eliminates all the challenges associated with conventional coverglass solutions discussed in the Introduction. A meticulous selection process was undertaken to identify the most suitable coating materials to ensure optimal effectiveness. This comprehensive assessment considered various factors, including the materials' optical properties, mechanical strength, and chemical attributes. The initial part of this work provides detailed insights into this selection process. At the same time, the deposition of the chosen materials was expertly executed through a collaborative effort involving counterparts from both IIT and Polimi.

In light of the stringent and pressing specifications associated with the radiation shield function, it was considered crucial to start developing this part of the project first. Given this, the advancement of the anti-reflection feature was placed on hold since its successful realization was heavily contingent on the breakthrough achieved concerning the radiation shield. Pinpointing appropriate constituents for the radiation shield coating was navigated through an exhaustive evaluation of several material properties, corroborated by insights gathered from the scientific literature. The primary characteristics required for a comprehensive and effective coating are delineated below:

- **Optical Band Gap.**The optical band gap embodies the capability of a material to either absorb or allow the passage of light of different wavelengths. The objective is to leverage

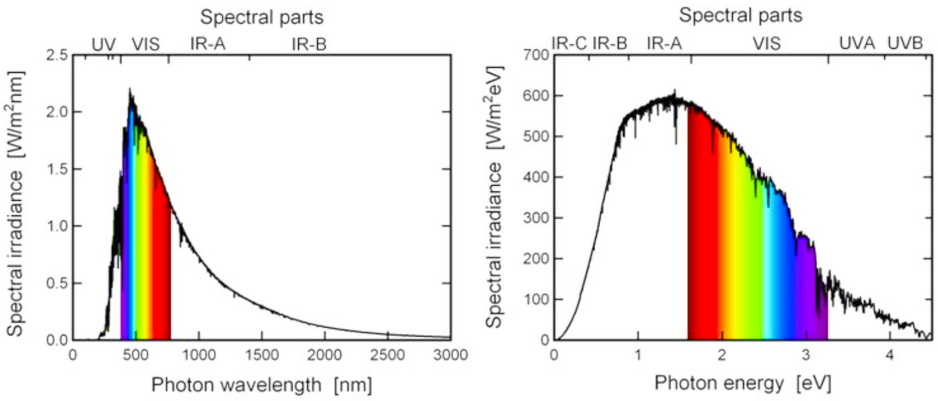

Figure 1.1: Spectral irradiance of the AM0 spectrum vs photon wavelength (left) and photon energy (right) [294].

the full spectrum of wavelengths embedded in the solar spectrum, typically harnessed by space triple-junction solar cells. Consequently, an exemplary coating should uphold maximum transparency within this spectral realm, forestalling any superfluous absorption that may undermine the total efficiency of the solar cell.

The illustration provided below Figure 1.1 illustrates the sunlight's intensity across wavelength (on the left) and photon energy (on the right), captured from the highest regions of Earth's atmosphere. Also shown are the various spectral colors.

The observed spectrum is the Air mass zero (AM0) spectrum. AM0 represents a scenario where the spectrum is measured without atmospheric interference between the sun and the recording device. As can be observed from the Figure 1.1, the required imposed was to find a material possessing a bandgap higher than 5 eV for the reasons mentioned.

- **Coefficient of Thermal Expansion.** The coefficient of thermal expansion (CTE) is pivotal in guaranteeing a functional coating. Considering the extreme thermal variations encountered by operational space solar cells, any significant difference between the thermal expansion of the coating and the solar cell could instigate considerable mechanical stress, potentially triggering fractures, delamination, and, eventually, the demise of the coating. Hence, the CTE of the shortlisted materials should, ideally, align with that of the solar cell.

- **Formation Gibbs Free Energy.** The Gibbs free energy of formation (ΔG) represents the variation in Gibbs free energy due to creating a specific substance from its elemental components. This parameter provides a window into a material's thermodynamic or chemical stability, underscoring its ability to maintain its composition and structure in the face of external disruptions. Materials with high ΔG values generally exhibit enhanced resilience against transformations triggered by electron, proton, and deep-UV irradiation.

After undertaking a scrupulous examination of extant literature and assessing them against the criteria stipulated above, an initial compilation of potential materials is reported below in Table 1.1, where the average values od the different parameters are reported:

MATERIAL	BAND GAP [eV]	CTE [10^{-6} °C^{-1}]	ΔG [Kj mol^{-1}]
Al_2O_3	7.2 [295, 296, 297]	8.2 [298, 299, 300]	-1050 [301, 302]
HfO_2	5.5 [303, 304]	7.3 [299, 305, 306]	-1050 [302, 307]
La_2O_3	5.2 [308]	8 [299, 309]	-1104 [302]
$MgAl_2O_4$	8 [310]	5.6 [299]	-1075 [302]
Y_2O_3	5.2 [311]	6.7 [299]	-1200 [302]
ZrO_2	5.8 [310]	10[299]	-1033 [302]
COVER GLASS	3.5	5.5 - 6.5	n.a.
Threshold value	>5.0	6 ± 15%	/

Table 1.1: Properties of candidate materials compared to reference coverglass.

To proceed with the coating fabrication, it is crucial to conduct theoretical groundwork to adequately address the upcoming experimental tasks. The first step involved determining the necessary thickness value to protect the underlying solar cell against proton irradiation at a specific energy level. This was achieved through simulations using the SRIM (Stopping and Range of Ions in Matter) [274] software. The simulations were conducted using a simplified configuration of the solar cell, consisting of a 5μm layer of GaAs on top of a thicker Ge substrate, surrounded by a uniform radiation shield.

Various simulations have been conducted to explore a wide range of possibilities, explicitly focusing on the primary contenders: HfO_2 (hafnium oxide), $MgAl_2O_4$ (magnesium aluminate), and Y_2O_3 (yttrium oxide), in conjunction with Al_2O_3 (aluminum oxide). However, the latter's properties are deemed inadequate when considering the CTE. It is worth mentioning that the values referenced here align with those found in the existing literature [298, 299, 300] and may deviate significantly from the final values for the PLD alumina variant. A detailed analysis of the extrapolation of CTE values will be conducted in a subsequent section of this research.

The simulations were performed with varying thicknesses, aiming at identifying the optimal thickness that would completely block 2 MeV protons while minimizing the thickness required for an efficient deposition process. The choice to focus on 2 MeV protons was based on the local maximum in the energy distribution of proton flux commonly observed during Medium Earth Orbit/Low Earth Orbit (MEO/LEO) missions [312]. By successfully shielding the solar cells from all protons below 2 MeV, the radiation-induced damage to the cells is projected to be significantly reduced.

The interaction cross section for charged particles decreases as their energy increases. As a result, high-energy ions pass through the outer layer of the material with minimal interactions

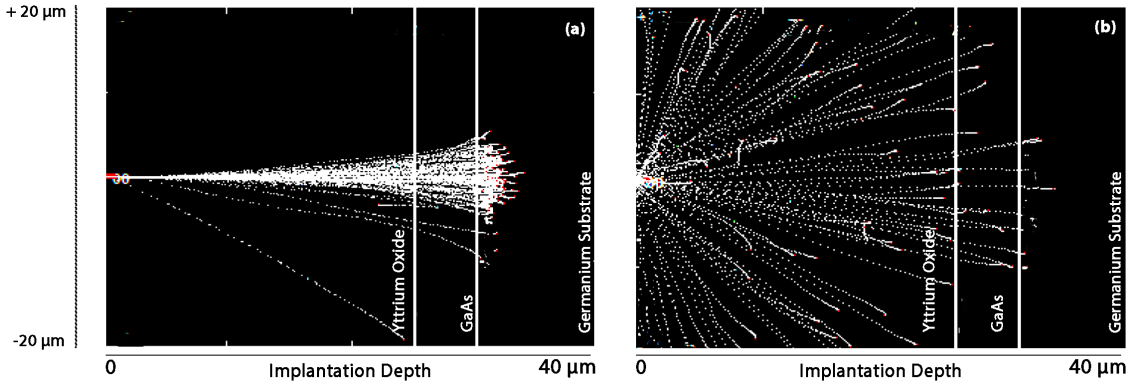

Figure 1.2: SRIM simulations showcasing proton beams interacting with the SC structure (Y_2O_3 cover coating). The conducted simulations include: (a) a focused 2 MeV proton beam, and (b) a 2 MeV proton beam with an isotropic distribution.

and cause minimal damage. However, as they lose energy, their cross section increases. This leads to a self-enhancing effect where the energy loss causes an increase in the cross section, which in turn promotes further energy loss. Consequently, the ions are stopped within a relatively small depth, as explained by the Bethe Bloch equation [313]. Within this depth, they deposit most of their energy and cause the maximum damage, resulting in a peak known as the Bragg peak [314]. The goal of a radiation shield is to ensure that the Bragg peak remains within the shield's thickness. Specifically, it aims at containing the Bragg peak for the aforementioned 2 MeV protons. Protons with significantly higher energy are relatively less harmful because, due to the limited thickness of the entire cell, they can pass through it with a small cross section and a low damage rate.

The results of SRIM simulations for the described cell structure (5μm GaAs / Ge substrate) with a 25 μm yttria shield are demonstrated in Figure 1.2. The simulations used a 2 MeV proton beam aimed in one direction and a 2 MeV proton beam with directions evenly spread out. A procedure developed by prof. M. G. Beghi, allowed to achieve this isotropic distribution, starting from the initial TRIM file, which SRIM then processed for the simulation.

It's evident that the beam with isotropically distributed directions shows less penetration depth compared to the beam directed in a single line. This suggests that a shield built to guard against a single direction beam would afford even more protection against a beam with multiple directions. However, it's important to note, as further simulations have shown, that ions with higher energy, which typically cause minor damage when striking directly due to limited interactions, become more destructive when they hit at a slanted angle. This is due to the longer path they travel which leads to a higher energy deposit and therefore causes more harm within a lesser depth.

The conducted simulations established that all the chosen materials, with a thickness of 35 μm,

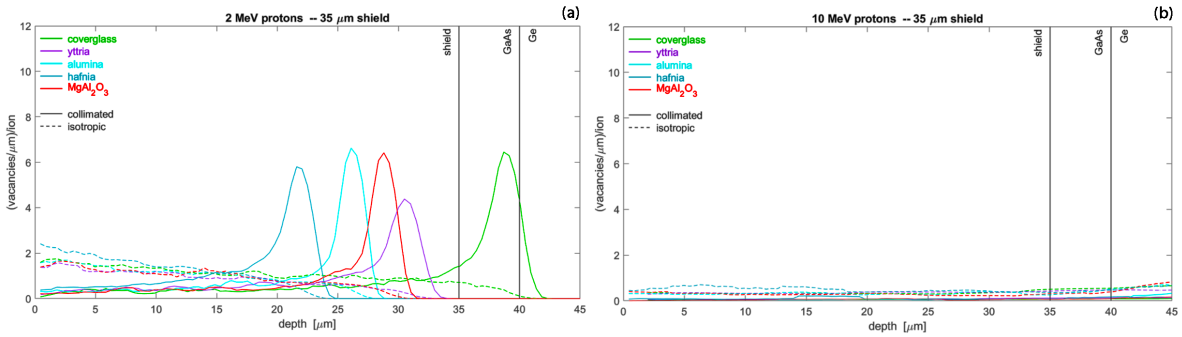

Figure 1.3: SRIM simulations of proton beams interacting with a SC layered structure. The figure compares shield materials, proton energies, and beam types (collimated and isotropic), all indicated in each part.

successfully can block the 2 MeV proton beam in both focused and isotropic incident scenarios. These results are depicted in Figure 1.3 (a). The disparity in protective characteristics among the materials is observable; but notably, all the investigated oxides provide more excellent protection than the common coverglass.

From the multiple SRIM results, the depth distribution of vacancies produced by the incident ions was identified as the most representative of the resulting damage. As discussed previously, it's evident that the 10 MeV beam is less harmful (Figure 1.3 (b)), as high energy ions have a smaller interaction cross-section. Nonetheless, it's also clear that the statistical data from the fewer vacancies left by this beam may not be entirely conclusive, suggesting a need for a more thorough simulation.

1.2. Advancing Thermomechanical Analysis for Thin Film: Coefficient of Thermal Expansion and Intrinsic Stresses Determination

Coatings experience residual stresses present after deposition, as reported in [315]. These stresses originate from two primary sources:

- Intrinsic stresses result from the deposition process and the properties mismatch between the coating and substrate materials.
- Thermal stresses occur due to a mismatch in thermal expansion between the coating and substrate, particularly when the sample is cooled to room temperature after deposition. Additional thermal stresses are generated when the coated components operate at variable temperatures.

These stresses, which intensify at the coating-substrate interface, can lead to coating failure, as observed in previous studies. Therefore, it is crucial to predict and monitor these stresses to assess the operational stability of coated devices [316].

To engineer the performance of coatings, intrinsic stresses play a significant role, as mentioned in [317, 318]. These stresses are primarily associated with the physics of the deposition process, such as the kinetic energy of deposited particles. In highly energetic physical vapor deposition techniques like PLD, the intense kinetic energy of the particles leads to compressive stresses within the growing film due to the *Atomic Shot Peening* process described in [317]: the incident particles with high kinetic energy cause local atomic displacement, densification, and an increased concentration of structural defects. The stresses in physical vapor deposition processes can be tuned by adjusting various fabrication parameters, as mentioned in [319, 320]. The background pressure during deposition and the kinetic energy of the emitted particles have the most significant impact on stress control. Lowering the background pressure or increasing the kinetic energy by adjusting laser fluence in PLD reduces the number of collisions between emitted particles and background species. This ensures the particles reach the substrate surface with sufficient energy to induce the atomic shot peening effect. However, it should be noted that residual stresses depend on other parameters, including coating thickness, as observed in [317, 318, 321]. The influence of coating thickness on residual stress, especially for amorphous coatings, requires further investigation. Since measuring residual stress in amorphous films is challenging with the employment of X-ray diffraction (XRD) or Raman spectroscopy [317, 318], in this thesis, the monitoring of intrinsic and thermal stresses are obtained by optimization of a setup based on the optical implementation of the substrate curvature method. The original development of the setup with all the technical information is reported in [316].

The Stress Curvature method [322, 323, 324], maintains its importance as a non-destructive technique with great versatility, applicable to both opaque and transparent coatings. It operates on the fundamental premise of adhesion between a coating and substrate, leading to system

bending due to differences in material attributes like elasticity,CTE, and lattice parameter. The method leverages laser technology to measure the curvature radius of the coating-substrate system at room temperature, which aids in ascertaining the coating's stress condition, especially residual stress [325]. The heating of the samples exposes varying thermal expansion properties of the coating and substrate, causing additional system bending. This observed bending assists in determining the CTE and tracking the thermal stress development in the coating. For a bilayer system where the film is significantly thinner than the substrate, resulting in near-uniform stress across the film, Stoney's equation [326] can express the coating's stress in relation to the bending curvature radius R:

$$\sigma_f(T) = \frac{E_s}{1-\nu_s}\frac{t_f}{t_s^2}\frac{1}{6}\left(\frac{1}{R(T)} - \frac{1}{R_0}\right) \tag{1.1}$$

In this context, the subscripts 'f' and 's' refer to 'film' and 'substrate', respectively, while 't' denotes the thickness of the coating or substrate. The residual stress can be determined exploiting equation 1.1 if the curvature radii after and before the deposition, namely R(T) and R0, are measured. When there's a discrepancy in the CTE between the coating and the substrate, causing thermal stresses during heating or cooling, the CTE of the coating can be inferred using the subsequent equation [316]:

$$CTE_f = CTE_s + \frac{\delta\sigma_f}{\delta T}\frac{1-\nu_f}{E_f} \tag{1.2}$$

The equations (1.1) (1.2) show that knowledge of the elastic properties of the films is necessary to determine the internal stresses and CTE. Moreover, the equations assume temperature-independent elastic moduli and allow finding a single value of CTE. However, both Elastic Moduli and CTE do exhibit some temperature dependence. A more comprehensive approach would consider the temperature dependence of the elastic moduli of both the substrate and the film. Nonetheless, measuring these dependencies is challenging. In this work, the thermal treatments used maintain temperatures well below the melting and recrystallization temperatures, where significant variations in elastic moduli could be expected. Therefore, neglecting the temperature dependence of the elastic moduli only introduces minor inaccuracies. Moreover, it is essential to note that the measured CTE refers to the in-plane component of the linear expansion thermal coefficient. For anisotropic samples, the in-plane CTE can differ significantly from the out-of-plane CTE, which must be determined using other techniques.

Operationally a 2x2 laser beam array with 1 cm spacing is used in this setup, generated by a laser diode and two etalons. The array hits a sample at a 60-degree angle, allowing investigation of both metallic-coated and uncoated polished substrate surfaces. However, only the substrate can be studied for transparent coatings due to laser scattering interferences. The array's position on the CMOS sensor is tracked by identifying the laser spot centroids with an intensity algorithm

implemented in MATLAB developed in [316]. Despite noise factors affecting accuracy, using multiple laser beams ensures precise measurements, as the relative beam spacing is less sensitive to vibrations than the beam's absolute position, providing insight into sample curvature changes [316].

1.2.1. Curvature Measurement Setup Optimization

Part of the work undertaken in this thesis centered on optimizing the experimental setup, which was developed as part of a doctoral thesis at NanoLab [316]. The primary aim was to improve the characterization of the CTE and monitor thermal stresses in films. At the outset, the existing setup encountered challenges related to the heating module, vacuum leaks, and measurement instability, impeding the accurate measurement of higher temperature curvatures. These issues required resolution in order to establish a fully functional system capable of effectively performing such measurements.

The substrate curvature equipment utilizes laser arrays to measure deflection in a bi-layer film-substrate structure. The setup was initially designed for experimental trials with a maximum temperature ramp of 1200°C. It included a programmable power supply, a heating module, a vacuum system, a gas inlet, and a primary viewport. The setup's components are summarized in Figure 1.4, and all the information about it is reported in [316]. The setup was enhanced from its original version by installing a ceramic heating plate, improving heating efficiency, stability, and control accuracy. The ceramic heating plate offers fast heating rates, uniform temperature distribution, and high surface power capability. Silicon nitride was chosen for its stress and wear resistance, making it suitable for this application. To ensure accurate measurements, a transparent sapphire view port was installed to replace the previous one, allowing for improved transmission of infrared radiation, and avoiding the radiative heating coming from the heater to heat up excessively the port during the thermal cycling for measuring CTE. The sapphire window is highly durable, with low thermal expansion and excellent optical properties.

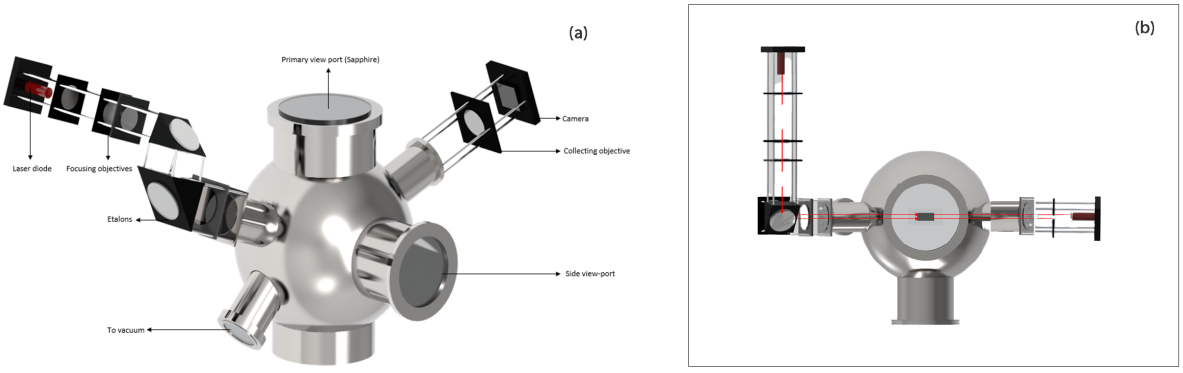

Figure 1.4: (a) Inventor®CAD representation of the ubstrate curvature setup. (b) Laser path tracing (top view).

Due to the existing setup's space containments, the new heating plate was placed in direct

contact with the existing sample holder. A thermocouple was located to record the temperature in the middle of the plate for accurate monitoring. Another thermocouple was set at the junction tip of the connectors, monitoring any temperature excursions that could surpass the maximum tolerable threshold of the connectors. This arrangement is illustrated in Figure 1.5 (a).

For precise calibration of the system, initial tests were executed, examining the peak temperature achievable to different input voltages; by adeptly charting the plateau values attained for each input, a valuable understanding of the system's rate of temperature rise and the corresponding maximum limit was attained. The results in Figure 1.5 (b) revealed a linear pattern, underscoring the system's performance. Notably, the system demonstrated an average temperature plateau with a voltage rate equal to 12.16 °C/V.

1.2.2. Heat Transfer Kinetic Finite Element Modeling

Delving into a comprehensive examination of the thermal module as a whole entity, the investigation encompassed a thorough analysis of the heat transfer kinetics and heat losses associated with the alumina mounting plate. Furthermore, the heating component, encompassing the plate and the sample positioned upon it, was modelized. To maintain simplicity within the model, a uniform temperature boundary condition along the lower side was implemented to emulate heat source.

The mounting plate was meticulously designed to accurately represent its actual dimensions. Subsequently, a comprehensive analysis was conducted to quantify the thickness's temperature gradient, thereby gaining insight into the temperature reduction within the section housing the mounting sample holder. Crafted from alumina, this plate features a strategically positioned hole to accommodate the thermocouple (Figure 1.5). Given that the temperature experienced by the sample during the CTE measurements holds immense importance in extrapolating the CTE value, this model was deliberately formulated to ascertain whether the temperature measured by the thermocouple, placed at the center of the alumina plate, could consistently provide reliable information regarding the temperature of the sample positioned atop the alumina plate.

The understanding of the heat transfer within the thermal module has been achieved through COMSOL Multiphysics [327] exploiting Finite Element Modelling (FEM). The FEM works representing any continuous domain using an assortment of elements and nodes, with behavior at any point being informed by the aggregated behaviors of the linked nodes within an element. Therefore, it's essential to precisely model the relationships among the variables, facilitating behavior deduction at unspecified locations within an element based on associated nodes' behaviors [328].

Element models generated from the governing equations of engineering problems establish the basis of the FEM model. The solution relies on examining differential equations subjected to specific boundary conditions. The governing equations, directly linked to the unique engineering problem, maintain adherence to the essential principles of conservation, encompassing mass, mo-

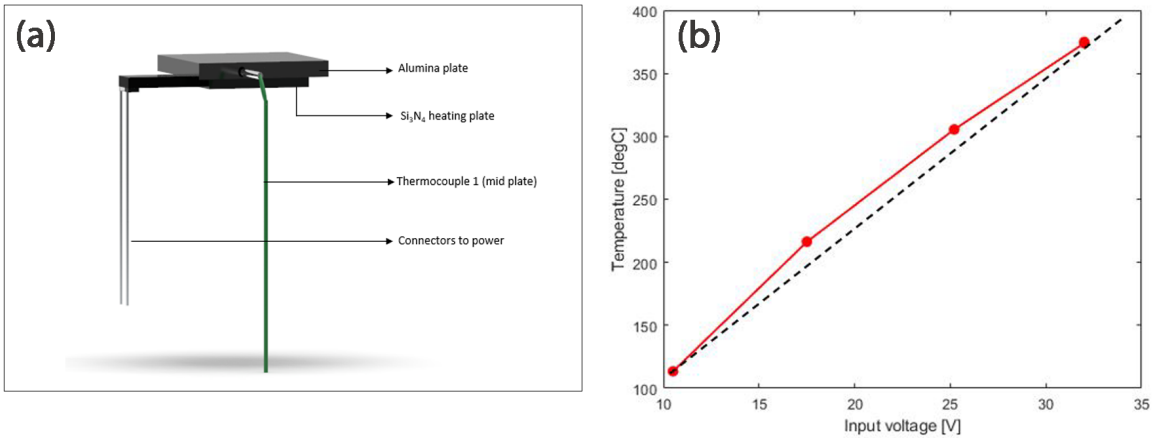

Figure 1.5: (a) Schematic representation of the heating module. (b) Temperature/Voltage calibration curve.

mentum, and energy conservation. These principles are depicted as partial differential equations (PDEs), serving as a means to interpret the conservation principles mentioned above [329].

As mentioned, the design and subsequent exploration were conducted as an initial attempt to understand heat losses within the system, assuming conditions the closest as possible to the real one to a vacuum. In this particular scenario, two different pathways for heat transfer were assumed:

- **Heat conduction through the alumina plate structure.** Heat conduction is the diffusive transfer of thermal energy, considering the physics of simple conduction. Fourier's law of heat conduction governs the phenomenon, asserting that the heat transfer rate across a material is proportional to the negative temperature gradient and the area perpendicular to the gradient through which the heat flows [330].
- **Additional heat losses are attributable to radiation from the system.** Radiation from the surface to the ambient environment is an influential component when assessing heat transfer within a system. This heat transfer is facilitated by the emission of electromagnetic waves, which subsequently carry energy away from the source [330].

  The physics governing this phenomenon is encapsulated in Stefan-Boltzmann's equation. For practical purposes, the emissivity value of bulk alumina - a measure of the material's ability to emit energy as thermal radiation - is approximated based on literature values [331], ranging between 0.7 to 0.75, facilitating the evaluation of radiative emission.

It is important to note that convective heat transfer is essentially absent due to the vacuum conditions under which the system is intended to function. Moreover, in light of the system's capacity to endure high temperatures of up to 1200°C, radiative heat transfer was identified as a crucial player in the overall thermal management process. This mode of heat transfer is aligned with the operational norms of systems designed to function at high temperatures and working

in vacuum, which aids in preventing oxidation.

To accurately represent the sample inside the model, it was deemed necessary to incorporate it being modeled onto the same plate. Then a time dependent analysis, based on the boundary condition of 1000°C at the base of the plate, was carried out to assess the temperature decrement across the plate, thereby facilitating a more profound comprehension of the thermal attributes of the system. Two distinct point probes were placed - one alongside the drill hole to simulate the thermocouple temperature readings and the second on the sample surface. This examined the total temperature disparity between the measurements the two probes took and the time each took to attain a steady state. The latter was analyzed through a dynamic study that yielded valuable insights. In the quest for a comprehensive representation of the actual system, the presence of coatings on the sample was also modeled, exploiting the thin layer approximation in Comsol. Thin structures often introduce high aspect ratios in the geometry, which can complicate or distort meshes and are computationally expensive to solve [332]. Hence, specific tools and assumptions are implemented for studying such structures. The 'thermally thin' approximation is used when the films can be considered as boundaries of thickness considerably smaller than the typical lengths of the overall model [333]. This supposition is generally valid for thin structures that are good thermal conductors compared to the surrounding domains and/or exhibit rapid convection along the tangential direction. This formulation applies predominantly to a thin structure where heat transfer follows the tangential direction, as further elucidated in [333]. The decision to utilize this node of *Layered shell material* instead of modeling the films as a 3D structure was made to circumvent the significantly high aspect ratios, which could potentially lead to complexities in meshing and be computationally burdensome to process [332]. This notion of thermally thin approximation infers that the temperature variation across the film thickness is minimal, rendering the distinction of the temperature difference across the opposite faces of the layer insignificant . This means that instead of the traditional 3D heat transfer equation, a 2D equation is solved only on the boundaries, with each term multiplied by the film thickness [333].

Given the lack of specific knowledge about the actual value of thermal contact resistance, between the coating and the substrate, this value was automatically computed based on the model of an equivalent thin resistive layer, wherein thermal conductivity and layer thickness serve as controlling parameters to calculate the equivalent contact resistance. This includes the contribution of the radiative conductance evaluated through the 'gray-diffuse parallel surfaces'. This thermal contact resistance approach comes into play when a junction is formed by two similar or dissimilar materials, for considering also roughness of the contacting surfaces [334].

Moreover, as the system encompasses a bi-layered structure free to expand under the imposed temperature load, a minimum constraint had to be added without imposing additional artificial stresses [335]. The 'Rigid Motion Suppression' boundary condition is a valuable method to automatically create a set of constraints sufficient to inhibit rigid body modes without introducing any reaction forces as long as the external loads are in equilibrium [336].

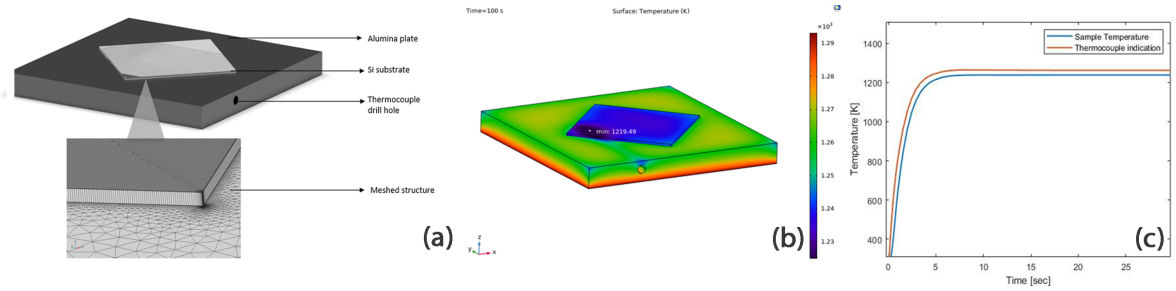

Figure 1.6: (a) Meshed geometry. (b) Visual representation of temperature drop across the Alumina mounting plate and (c) temperature time evolution

Lastly, since the system operates under vacuum conditions, the boundary condition of radiative heat loss to ambient condition was imposed onto the system [333]. This was accomplished while considering the corresponding properties of the system, as indicated in Table 1.2 :

Parameters	Values	Unit
Plate length	50	[mm]
Plate height	5	[mm]
Si wafer (sample substrate) thickness	0.525	[mm]
Drill hole Diameter	1	[mm]
Ambient temperature	293.15	[K]
Boundary temperature	1273.15	[K]
Emissivity bulk Al_2O_3	0.70	[-]
Emissivity Si Wafer (sample substrate)	0.60	[-]
Heat capacity (Mount plate) C_p	900	[J/kg K]
Density (Mount plate) ρ	3900	[Kg/m^3]
Heat capacity (Si wafer) C_p	678	[J/kg K]
Density (Si wafer) ρ	3900	[Kg/m^3]

Table 1.2: Mounting plate's and sample's characteristics and specifications used for assessing the impact of heat transfer throughout the system

The simulation results reported in Figure 1.6 (b) and (c) demonstrate a minimal difference between the temperature recorded by the thermocouple positioned at the mid-plate and the average temperature felt by the probe setup on the top of the sample. The impact of thermal contact resistance doesn't result in any substantial temperature decrease across the system. Moreover, the delay for the system to achieve a steady state is negligible since the system stabilizes within a 10-second timeframe.

The previously mentioned model showed a negligible discrepancy in the temperatures sensed by the thermocouple and the sample, and it has been substantiated via a series of experiments.

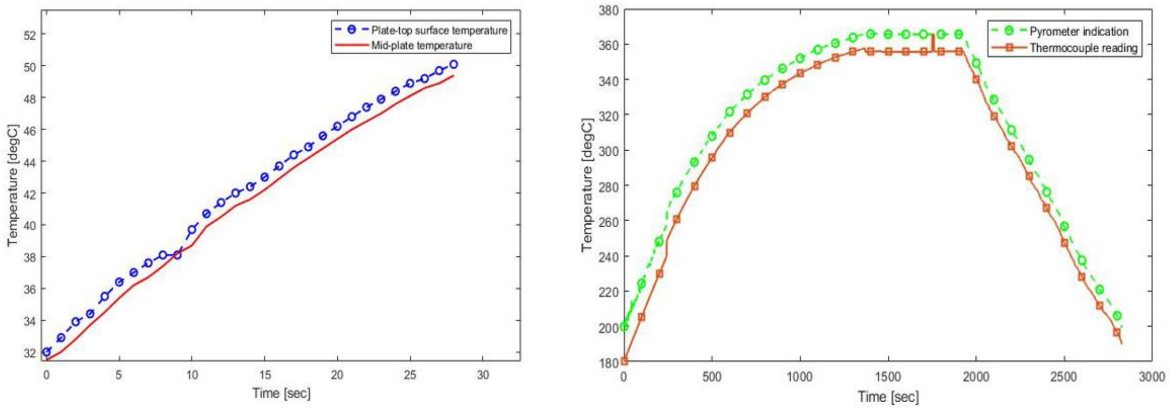

Figure 1.7: (a) Temperature comparison between the mid-plate location and top surface thermocouples. The graph illustrates a noteworthy consistency between these readings, validating the numerical model and demonstrating the negligible discrepancy in temperature sensed by the thermocouple and the sample. (b) Pyrometer and mid-plate thermocouple readings showcasing minimal temperature difference in the measurements

Firstly, two placed thermocouples were utilized. One thermocouple was embedded into the plate at the mid-plate drill hole, whereas the other was positioned in immediate contact with the plate's upper surface. This setup aimed at mimic the temperature probes used in the simulation. The temperatures registered by these thermocouples were tracked over time to evaluate their variability.

Figure 1.7 (a) demonstrates the alignment between the temperature recordings at the top surface and the corresponding mid-plate location. To further enhance our understanding, a pyrometer was used to corroborate the plate's temperature. The readings from the pyrometer also revealed a trifling variation in temperature (Figure 1.7 (b)). These results have crucial implications:

1. The computational model created has been verified through the results mentioned above, establishing that the temperature difference between the actual sample and the thermocouple readings is minimal. This temperature disparity is of the same scale as the value derived from the simulation.

2. An approximately 10°C temperature discrepancy was noticed between the pyrometer reading and the thermocouple temperature. This divergence may be due to intrinsic errors within the system, encompassing uncertainties related to both measurements.

The above-mentioned experiments effectively finalized the calibration studies of the equipment, validating the trustworthiness of the input temperature ramps and the system's overall stability. Consequently, the system has been considered appropriately equipped and prepared to engage in subsequent experimental inquiries, inclusive of tasks such as the evaluation of CTE.

1.2.3. Alumina Coatings Intrinsic Stress determination

Benefiting from the promising results yielded by the advanced configuration and driven by the results detailed in the preceding Section 1.1, the measurements of the intrinsic stress and CTE for Al_2O_3 coatings were carried out because this was the material with already established deposition procedure. Given its extensive refinement for nuclear applications, this process indeed emerged as the most prudent choice during the foundational stage of the setup.

Amorphous alumina coatings with varying thicknesses (250nm, 500nm, 1 μm, and 2 μm) were deposited on Silicon wafer substrates. The mechanical properties of the film were extrapolated from existing literature sources [166].

Assessments of residual stress were performed at room temperature on Alumina films of varied thickness utilizing the Equation 1.1. The parameters employed in the said equation are documented in the Table 1.3. The objective of each test was to yield numerous data points to aid the calculation of a precise average approximation. The MATLAB® software developed in [316] was employed to analyze stress values and curvature radius. The results of this study, depicted in Figure 1.8, illustrate that the Alumina films, which were deposited via PLD, manifest compressive stress. The results of this study are also consistent with extant literature concerning thin films of alumina by Physical Vapor Deposition (PVDs). For instance, Cibert et al. [337] documented a compressive residual stress of approximately 500 MPa for a 1 μm-thick PLD-grown Al2O3 film, which is similar to the observations made in this study. The figure shows a notable disparity in the standard deviation for each sample. The large error bar for the 250 nm sample is predominantly attributable to inaccuracies in curvature measurements resulting from extensive spot divergence when gauged along each axis. This disparity can be linked to a significant non-uniform distribution of residual stresses in the thinnest film [338]. However, this variation among samples diminished with increased film thickness. It can be observed that the error bar declined with an increase in film thickness, suggesting a trend towards greater uniformity in the distribution of residual stress as the film thickness increased. The disposition of particles significantly influences the distribution of residual stress; longer deposition duration results in denser and more uniform particle stacking, thereby enhancing the uniformity in the distribution of residual stress within the thin film. Consequently, as the thickness of the film increased, the distribution of residual stress became increasingly uniform [337].

Material	Young's Modulus [Pa]	Poisson Ratio	Reference CTE [1/K]
Al_2O_3	$1.95\ 10^{11}$	0.29	$7.5\ 10^{-6}$
Si wafer	$6.55\ 10^{10}$	0.22	$2.6\ 10^{-6}$

Table 1.3: Thermo-Mechanical properties of a Al_2O_3 film [166] and properties for the Si substrate.

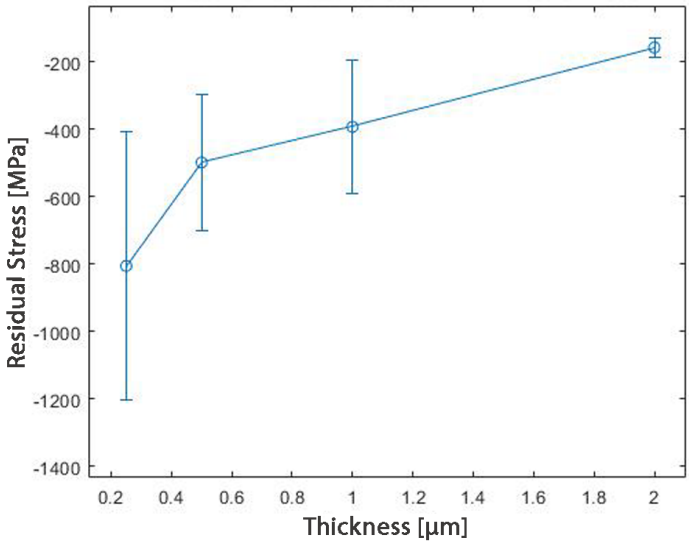

Figure 1.8: Evolution of residual stress with film thickness in Al_2O_3

Moreover, the paper [317] proposed "isothermal stress relaxation" as the primary factor for the observed stress decrease. The authors postulated that the creation of thicker films triggers a general reorganization within the layers. The accumulated heat over time initiates thermal phenomena such as dislocation climb, grain boundary, and volume diffusion. Drawing from a similar paradigm, the authors in [339] proposed a recovery process. The shot-peening effect produces intense compressive stresses in extremely thin films. As the growth of the film progresses to a certain stage, the predominant mechanism transitions to recovery. During this process, the arrangement of atoms and eradication of cavities and defects result in volume contraction and local densification. The model mentioned above aligns well with the observations made in this study. Thus, it appears to be the most suitable model for representing the present material. In conclusion, the experimental results have confirmed the dependency of residual stresses on the thickness of PLD-grown alumina. The effect of residual stress on the mechanical performance of the coating will be discussed in a later section once the results of the mechanical tests have been reported.

1.2.4. Alumina Coefficient of Thermal Expansion determination

Operating at peak input voltage, the system accomplished to reach 375°C. Implementing a heating ramp of 18.5°C/min and a cooling ramp of 13.6°C/min (natural temperature decay) permitted the determination of the CTE for Alumina samples. A pyrometer was employed to affirm the veracity of the temperature recordings derived from the thermocouple. This served the dual purpose of comparing surface temperature with the thermocouple's readings.

Figure 1.9 (a) illustrates the stress-temperature curve for an Al_2O_3-Si sample with a thickness

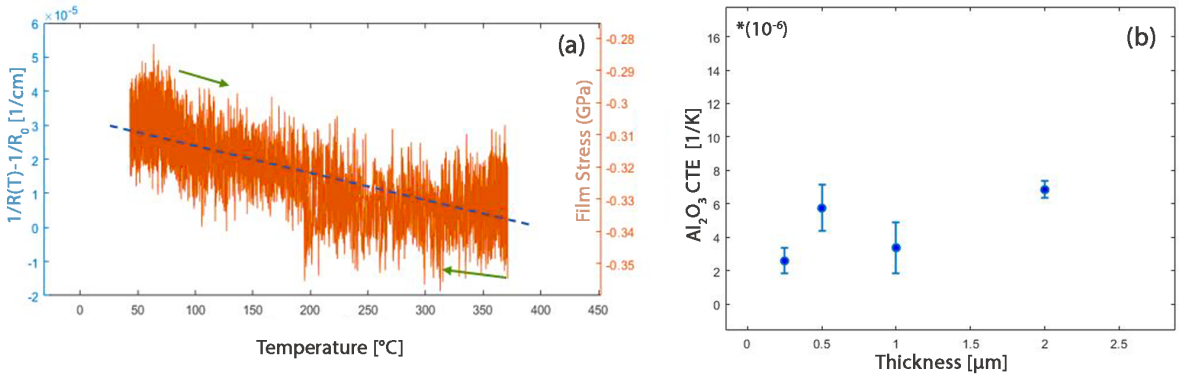

Figure 1.9: (a) Depiction of the thermal cycle conducted on alumina, illustrating the alterations in curvature and the corresponding stress-temperature evolution. (b) CTE of Alumina samples of varying thickness

of 1µm. The arrows, colored green, symbolize the direction of the thermal cycles for heating and cooling, while the dotted line demarcates the linear range where the CTE was computed. The uncovered CTE values have been depicted in Figure 1.9 (b). A remarkable linear and reversible pattern was discerned within the defined temperature range, implying that the Alumina-Si samples underwent elastic deformation[[316]. The films were subjected to compressive stress, which lessened with increased temperature, tapering off to roughly -0.35 GPa at 375°C. After the cooling phase, stress returned to its preliminary value, suggesting a lack of stress relaxation during the thermal cycle [340]. A similar trend was observed in other Alumina samples. The CTE values measured across all thicknesses presented a value that was notably lower than those observed for amorphous alumina, approximately 7.5 x 10^{-6}, within the same temperature range [341]. While all samples exhibited comparable variances, the CTE values for different thicknesses revealed system instabilities due to the absence of a distinct trend. Nevertheless, these findings suggest a probable range of CTE values for varying thicknesses, from 250nm to 1 μm. A noteworthy comparison emerges when juxtaposing CTE values of the Alumina coating and the bulk, crystalline alumina, which displays a CTE of around 8.5 to 9.1 x 10^{-6}. The values obtained for the film in this study are lower.

Despite the variability that presently precludes the determination of a definitive CTE value, it is encouraging to note the lower observed value, which may carry positive implications for applying alumina coatings in the aerospace sector as antireflecting coatings for solar panels. The CTE value documented in existing literature was previously identified as a potential obstacle, which could have resulted in the exclusion of alumina as a viable option for an anti-radiation protective coating. The lower observed value infuses optimism in reconsidering alumina for this crucial application.

In order to rectify the variability encountered during this study, further steps must be taken to fortify the reliability of measurements. For instance, the existing power supply unit allows

a maximum asymptotic temperature of 375°C. Although initial CTE evaluations could be conducted within this operating temperature, higher temperatures could unveil opportunities to explore phase transformation and crystallization studies in thin oxide films such as alumina. This stems from the ability of PLD alumina to undergo a phase transformation beyond 600°C. Additionally, augmenting the number of laser beams reaching the sample and forming an array of spots could enhance the evaluation process by enabling the extrapolation of measurements from multiple distances between the spots, thereby obtaining a less disturbed measurement.

1.3. Unveiling Alumina Thin Film's Optical Properties and Density: Ellipsometry measurements

Ellipsometry, a non-destructive optical methodology, uses a beam of polarized light to shine on the sample that is being analyzed. This technique quantifies the transformation in the beam's polarization state used for measurement, which is instigated by its reflection or transmission through the sample [342]. The resulting alteration in the polarization state is typically characterized by the ellipsometric parameters: Psi (Ψ) and Delta (Δ), as specified in the following Equation 1.3:

$$tan(\Psi) = e^{i\Delta} = \tilde{\rho} = \frac{\tilde{r_p}}{\tilde{r_s}} \tag{1.3}$$

Within this equation, rho (ρ) represents the ratio of reflectivity for p-polarized light (r_p) to that for s-polarized light (r_s). ρ is identified as a complex number, with the ellipsometric parameters expressing this value in a polar form: tan(Ψ) communicates the magnitude of the reflectivity ratio while Δ indicating the phase. Ellipsometry presents three key advantages over simple intensity-based reflection or transmission measurements [342, 343]:

- **Precision:** The modification in the polarization state, determined by a ratio, allows ellipsometry to remain indifferent to changes in the absolute intensity of the beam used for measurement. Therefore, the sample acts as the 'reference' for the measurement, ensuring that the technique maintains accuracy without the requirement of 'absolute' intensity values.
- **Sensitivity:** The phase details encompassed in the ellipsometric Δ parameter yield heightened sensitivity to exceedingly thin films, capable of detecting even sub-nanometer thickness levels.

These superior accuracy, precision, and sensitivity strengths make ellipsometric measurements remarkably suitable for rigorous thin film metrology applications. In Spectroscopic Ellipsometry (SE), the acquisition of Psi and Delta values varies with wavelength. This broadens the quantity of information in the dataset, allowing simultaneous determination of multiple properties of the sample [343]. However, deducing parameters like film thickness and optical constants from the measured SE data necessitates the creation of an optical model that aligns with the data. The CompleteEASE software provides a graphical user interface, simplifying the construction of these models and visualizing measured data and model fits. The necessity of data analysis within SE cannot be overstated. SE, devoid of data analysis, merely quantifies ellipsometric parameters, Psi and Delta, against wavelength, thereby offering a relatively superficial overview. To unearth intrinsic sample properties such as layer thicknesses and optical constants, the execution of a model-based analysis on SE data is imperative [342, 343].

Specificaly for this work, the sample thickness is predetermined, as all depositions are precisely

calibrated to achieve the necessary thickness. Consequently, thickness transitions from being an outcome of measurements to an input parameter in this analytical context. For this specific experiment, 1 μm Al_2O_3 samples were deposited on Si wafers. In an attempt to glean additional insights from past measurements outlined in [166], the process of alumina sample production was altered, with a specific focus on modifying the repetition rate of the laser during the deposition phase. Historically, literature dedicated to Pulsed Laser Deposition (PLD) produced alumina, as outlined in the aforementioned section 0.2.6, consistently utilized a repetition rate of 20 Hz. However, the experiment under consideration deviated from this norm, electing a repetition rate of 50 Hz instead. This decision expedited the deposition process, producing the same thickness in just under half the time. While this affords an undeniable advantage in terms of efficiency, it also provokes a poignant question regarding the material's properties. It becomes challenging to predict the material's properties as an outcome of the deposition process, as it results in a fully dense, amorphous, and compact material layer that mirrors the morphology of the sample fabricated at 20 Hz. Further investigation into the impact of deposition rates on various materials will be presented at a later stage, providing a comprehensive and engrossing analysis.

From a preliminary examination, it is evident that the coatings appear nearly transparent, at least within the visible spectrum. Consequently, an initial approach to modeling the refractive index involves utilizing frameworks designed for transparent materials. The refractive index of transparent films in the visible spectral range is typically defined using the Cauchy dispersion equation:

$$n(\lambda) = A + \frac{B}{\lambda^2} + \frac{C}{\lambda^4} \tag{1.4}$$

where the parameter A represents the approximate amplitude of the material's index. The parameters B and C outline the shape or curvature of the index versus wavelength.

Measuring the alignment between the data generated by the optical model and the empirical data forms a crucial element of the SE data analysis process. This is facilitated through an automated process that quantifies the "fit" or "concordance" of the data, denoted by the Mean Squared Error (MSE). Achieving the optimal fit, or the lowest MSE, necessitates adjustment of the optical model's parameters.

The Cauchy layer is frequently employed to ascertain the optical constants of a transparent or semi-transparent film, specifically for Dielectrics and Semiconductors that fall below the fundamental bandgap. For a portion of the spectral range, the optical constants of such materials can be depicted by a slowly varying index as a function of wavelength and an exponential absorption tail. This is usually called Urbach tail and represents an exponential segment in the energy spectrum of the absorption coefficient and typically materializes near the optical band edge in amorphous, disordered, and crystalline materials [342, 343].

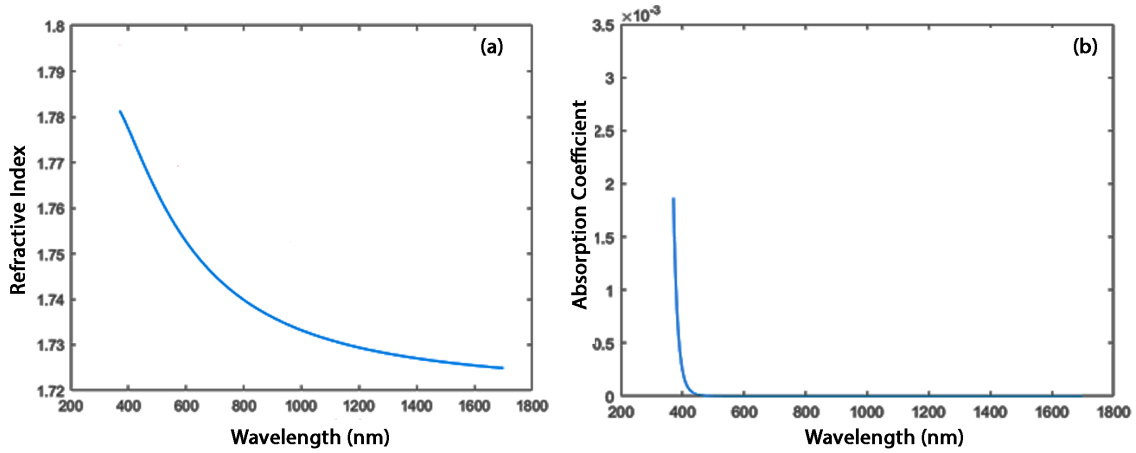

Figure 1.10: Dispersion curves for the refractive index and absorption amplitude of Al_2O_3 films

Figure 1.10 presents the dispersion curves of the index and the absorption amplitude for Al_2O_3, which was achieved by modeling the system starting from a model containing Silicon substrate. This substrate was modeled including a layer of silicon oxide from natural oxidation at room temperature and a subsequent layer of 1-micron-thick alumina. To enhance the measurement's reliability, three different reflective angles were evaluated: Ψ and Δ as a function of wavelength, and the fitted model was represented for three incidence angles 55°, 60°, and 65°.

Notably, most transparent materials within the visible spectral range show a slight upward curve in their index at shorter wavelengths, a characteristic aptly captured by the Cauchy dispersion equation also for Al_2O_3 case.

The MSE for the results in question yielded a value of 17, which strongly underscores the notable conformity between the selected computational model and the system's actual responses. As a result, it is plausible to interpret the representation of the data in the Figure 1.10 as a precise visual analogue of the material's behavior.

It's worth noting a specific observation concerning the absorption coefficient of the film in the Ultraviolet (UV) spectrum. Despite the instrument's limitations, which could not cover the entire UV wavelength range and halted at 400 nm, it is evident that even at the edge of the UV spectrum, the absorption coefficient remains remarkably small, falling within the range of 10^{-3}. Even though it might be projected that the increasing trend could persist as we move toward shorter wavelengths, the low value found at 400 nm instills optimism for using the alumina coating as a protective layer in space applications; since, in such contexts, the absorption in the UV range is a crucial factor affecting the performance of solar cells.

Interjecting with a few noteworthy observations at this juncture in the discourse is imperative. Firstly, a direct comparison must be conducted between the measurements performed on the same material as elucidated in [166], with the only discernible distinction being the deposition frequency employed—20 Hz as opposed to the current 50 Hz. In the aforementioned article

[166], the refractive index, assessed at a wavelength of 532 nm, was found to be 1.647, while this study yields a value of 1.758. Unfortunately, the absence of explicit details regarding the fitting model employed in the referenced article precludes a definitive determination as to whether this disparity can be attributed solely to the different deposition conditions or may be influenced by discrepancies in the fitting model.

Nonetheless, after further investigation, another study [344] was unearthed that deposits alumina via PLD utilizing conditions akin to those delineated in the aforementioned article [166]—namely, a deposition frequency of 20 Hz and comparable magnitude of deposition pressure. In this study, the refractive index was assessed at a wavelength of 1550 nm, yielding a value of 1.65, which is relatively closer to the value obtained in our research, measuring at 1.7289.

Now the discourse can be further deepened on a study by G. Reisse et al. [345] that investigates the refractive index of an array of variables, among all, the frequency of deposition. Their research targeted diverse amorphous oxide ceramic materials, such as Y_2O_3, under conditions that closely resemble the ones in our current study—using an ultra-high vacuum for deposition, an equivalent 248 nm UV laser pulse duration, and a comparable target movement. The findings of the Reisse et al. Reisse et al. [345] study bear relevance to this work as the observed effects also seem applicable to this context.

One interesting observation reported in the Figure 1.11, is that an increase in the laser repetition rate leads to an increased refractive index of the material. This could explain the behaviour observed in this case. This correlation between the refractive index and ion bombardment, as well as the growth rate, can be explained with the model proposed by Chrisey [346] regarding different growth modes in films deposited through pulsed laser deposition. According to this model [345, 346], the growth of the film primarily depends on the instantaneous growth rate and the temperature of the substrate.

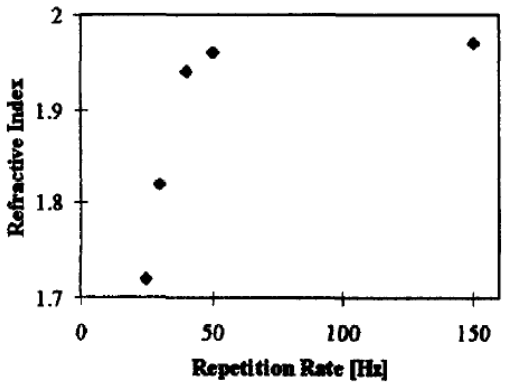

Figure 1.11: Refractive index of Y_2O_3 as a function of repetition rate (Reisse et al. [345]).

When the instantaneous growth rates increases, and the substrate temperatures are low, a continuous (liquid-like), layer-by-layer growth mode is facilitated, resulting in a predominantly amorphous increasingly dense microstructure. The forthcoming discussion will elucidate that this increased refractive index is directly related to a material endowed with higher density [346].

This result is particularly interesting for the discussed application of this PLD coating since the density of a material plays a significant role in shaping its mechanical and tribological properties. High-density materials typically exhibit increased mechanical strength, characterized by

improved hardness, rigidity, and resilience, all of which are paramount to the performance and longevity of material under various operational conditions. Furthermore, the density directly influences tribological properties, such as friction, wear, and lubrication. A denser material generally reduces wear rates and lower frictional coefficients, thereby providing enhanced resistance to sliding or rolling contact, which is particularly valuable in industrial applications. Consequently, understanding and manipulating the density of materials offers potential pathways to engineer materials with tailored mechanical and tribological characteristics [347, 348].

1.3.1. Determining the Density of Alumina Coatings

The justification for employing ellipsometry is twofold; not only does it afford the opportunity to derive crucial information about optical properties, but it also enables the construction of a link between the observable macroscopic properties and the inherent microscopic attributes of a specific medium. This link is made possible by exploiting the Lorentz-Lorenz equation [349]. This equation offers a profound connection between the medium's refractive index, which dictates how light navigates through the medium, and its physical density, a cardinal property intricately related to its molecular composition and organization.

This noteworthy correlation provides a comprehensive understanding of how a medium interacts with light. The refractive index measures the degree to which a medium influences the speed of light moving through it. On the other hand, density provides an instant view of the compactness of the molecules constituting that medium. The Lorentz-Lorenz equation shows the complex interaction between these two seemingly disparate elements . The true power of this correlation resides in the concept of polarizability. This critical parameter evaluates the extent to which an external electric field can alter the electron clouds surrounding the medium's molecules. When synchronized with molecular density, polarizability significantly contributes to defining the unique optical character of a medium [349, 350].

The equation employed in this study for the evaluation of the density of Al_2O_3 remains identical to the one utilized and reported in reference [166]:

$$\rho_a = \rho_s \left(\frac{n_a^2 - 1}{n_a^2 + 2} \right) \left(\frac{n_s^2 + 2}{n_s^2 - 1} \right) \tag{1.5}$$

It is worth noting that Equation (1.5) arises from the assumption that all the molecules have identical mass and molecular polarizability. The refractive index depends on the polarizability per unit volume, which in turn is influenced by the number of molecules per unit volume and the density. In a scientific context, it is crucial to ensure that when applying this Equation, the conditions above are met. Any deviation from these conditions may lead to inaccuracies in the results, and further investigations might be required to account for variations in molecular properties.

In order to derive the Al_2O_3 density ρ_a the Equation 1.5 is used. The mass density and refractive

index of sapphire are taken as reference parameters in this context. Sapphire's average refractive index, denoted as n_s, at a wavelength of 514.5 nm typically is around 1.770 [166]. Concurrently, the mass density, represented as ρ_s, can be averaged as 3975 kg/m^3 [166].

Leveraging the analytical model delineated in the preceding discussion and the parameters meticulously outlined in Table 1.4, a refractive index of 1.723 is yielded for Al_2O_3 at the identical wavelength of 514.5 nm. When integrated into Equation 1.5 along with the aforementioned parameters, this obtained index gives rise to a resultant value for Al_2O_3 density equal to 3779 kg/m^3.

Parameters	A	B	C
	1.720	9.407 10 ^{3}	0.4387

Table 1.4: Ellipsometry fitting parameters for the Cauchy model.

As anticipated, this ascertained density value manifests a higher figure to the one documented in reference [166], wherein the ρ_a was found to be 3471 kg/m^3. The comparison denotes the notable influence exerted by the choice of laser repetition rate, in this case, 50 Hz. This experimental setup catalyzes a perceptible increase in the material's density, showcasing the properties of the deposited material. These outcomes further affirm that the material deposition methodology can indeed wield a positive and consequential impact on the density of the Al_2O_3.

In the current body of academic literature, to the author's best understanding, there appears to be an absence of investigations that directly explore the implications of deposition rate on the density of deposited coatings. However, a wealth of studies have shed light on the transformative impact that repetition rate can have on both the morphology and the inherent properties of materials [351, 352, 353, 354]. A particularly interesting investigation [351] employed a pulsed kinetic Monte Carlo (PKMC) model to scrutinize the profound influence of laser repetition rate on island density and film morphology during PLD process.

The research [351] ventured to dissect the influence of laser pulse frequency on island aggregation during the first stages of material deposition onto a pristine substrate. The simulation demonstrated that increased pulse frequencies created more numerous, albeit smaller, islands. This reduced island size subsequently amplified the diffusion of adatoms, yielding a more refined and smoother film surface. Contrastingly, a reduction in pulse frequencies resulted in decreased island density and a decrease in surface smoothness. This comparatively rougher coalescence method of film growth could effectively instigate a lower coating density upon the culmination of the deposition process.

1.4. Revealing the Thermo-Elastic Attributes of Alumina Coatings: A Comprehensive Evaluation Using Ultrasonic Techniques

Elastic properties of materials, encapsulating their aptitude for reversible deformation, are essential in understanding how these materials respond to external forces. Examination of such traits typically requires a deformation process, focusing predominantly on reversible strains. Notably, the behavior of materials at the nanoscale tends to diverge, influenced significantly by the fabrication processes employed [355]. Even though these properties present considerable challenges in measurement, they can be studied effectively using vibrational excitation measurements[356].

Various experimental techniques utilize vibrational excitations to assess material properties, taking advantage of the small-amplitude displacements around equilibrium positions. Acoustic-type vibrational excitations, in particular, exhibit consistency across different scales, rendering them helpful in evaluating stiffness properties across objects of diverse dimensions [356, 357].

This suite of methodologies, known collectively as ultrasonic testing, exploits high-frequency sound waves to probe a material's elastic properties. The principle of extrapolation here rests upon the detailed description of propagating acoustic waves, or displacements and strains, within the elastic continuum model without body forces [357]. This principle is demonstrated through the elastodynamic equations for homogeneous media, which characterize displacement waves through dispersion relations. These relations factor in the medium's properties and vectors' relative orientations [356, 357]:

$$\rho \frac{\delta^2 u_i}{\delta t^2} = \sum_{j,m,n} C_{ijmn} \frac{\delta^2 u_m}{\delta x_j \delta x_n}, i = 1, 2, 3 \tag{1.6}$$

The properties of the medium (density ρ and tensor of elastic constants C_ijmn) dictate the determination of dispersion relations, symbolized as $\omega(k)$, where ω is the angular frequency, k the wavevevector. With the displacement vector u possessing three independent components, the dispersion relation branches into three, which can be categorized based on the relative orientations of the vectors u and k, i [356]. In isotropic mediums, one longitudinal and two transversal modes are observed. These modes' velocities can fluctuate in anisotropic mediums but remain consistent in isotropic ones, with thermodynamic stability mandating the transversal velocity to be less than the longitudinal one. Introducing boundary conditions that break the translational symmetry can lead to additional acoustic modes, such as standing or surface acoustic waves (SAWs), at the boundary [356, 357].

For a film supported by a substrate or stratified media, layer thickness emerges as a defining factor for the SAW mode. Waves with a wavelength equal to or larger than the thickness span across multiple layers, and their properties depend on the varied layers. Conversely, ultrasonic waves with a wavelength appreciably smaller than the thickness are unaffected by the finite size

of the medium or the shape of the supporting entity. Instead, their properties depend on the material characteristics, with the thickness influencing the existence of observable discrete modes. Hence, in supported films, the thickness plays a pivotal role in influencing wave properties. A detailed examination of ultrasonic techniques and the underlying physical mechanisms can be found in [356].

Two distinct ultrasonic techniques are explored in the context of this PhD thesis work. Initially, Brillouin spectroscopy is used, benefiting from accumulated experience at Nanoab in measuring the types of films studied in this work. This technique is used to examine the influence of thickness on the variability of the elastic mechanical properties of Al_2O_3. Subsequently, with the support of the Progetto Rocca fellowship, a significant research period was spent at the Mesoscale Nuclear Material Group at MIT. Here, Transient Grating Spectroscopy, another ultrasonic technique, is utilized for the first time to investigate the thermo-mechanical behavior of alumina thin film. Further discussion on these techniques is forthcoming.

1.4.1. Exploring Elastic Properties of Alumina Transparent coating Using Brillouin Spectroscopy

Brillouin spectroscopy (BS) serves as a robust and flexible approach for the non-destructive measurement of the elastic properties of films. It has recently been extensively used to evaluate opaque and transparent media [166, 358, 359]. The fundamental mechanism of BS is the inelastic scattering of photons, known as Brillouin scattering, caused by thermal acoustic phonons inherently present in any material at ambient temperature. This process involves the modulation of the optical constants of the medium, which, in the case of transparent media, is initiated through the elasto-optic effect [360, 361].

From a quantum mechanical perspective, this is seen as a collision between a photon and a phonon, where frequency and momentum are conserved through creating or annihilating a phonon, leading to either Stokes or anti-Stokes processes. Therefore, in a typical Brillouin light scattering experiment, the phonons under investigation have a wavelength close to the light, implying that their frequencies generally lie between 10 and 150 GHz. Given the relatively low cross-section of the scattering process, a high-resolution spectrometer is necessary to distinguish the small inelastic light component from the elastically scattered fraction. The ideal combination of high resolution and efficient throughput is achieved by using a multipass Fabry-Perot interferometer [361].

When examining opaque films, all detected modes correspond to surface acoustic waves. Specifically, the branch with the lowest velocity is the Rayleigh wave (R), which is altered by the film itself, while the remaining branches can be attributed to Sezawa waves (S) [316, 356]. Concerning transparent systems, like Al_2O_3 coatings, it's also feasible to measure bulk acoustic waves [361]. As this will be relevant in future discussions, it's important to note that the Rayleigh wave does not possess a particular polarization. Instead, it has its unique velocity, which is

slower than any bulk wave velocity [356, 362].It is essential to emphasize that examining different angles of incidence is advantageous for surface waves, as it facilitates the study of diverse wave vectors. Waves that exhibit behavior contingent on the wave vector are termed dispersive, a characteristic typical for surface waves but not seen in bulk waves. When investigating supported films, the displacement field associated with acoustic waves can potentially interact with the substrate. This effect is especially apparent for coatings whose thickness corresponds to the waves' wavelength. As a result of this interaction, supplementary surface modes may arise. These guided modes typically exceed Rayleigh and shear waves in velocity [361]. Both Rayleigh and other surface waves may be differently affected by the choice of the substrate material, which consequently establishes a specific acoustic impedance [361].

The conservation of the momentum component parallel to the surface makes it possible to directly establish the correlation between the frequency shift of Brillouin peaks and the phase velocity of the respective acoustic mode:

$$v_{Surface} = \frac{2\pi f}{Q_S} = \frac{\lambda f}{2sin(\theta)} \tag{1.7}$$

$$v_{Bulk} = \frac{2\pi f}{Q_B} = \frac{\lambda f}{2n} \tag{1.8}$$

Here, $Q_S = 2k_i \sin(\theta)$ stands for the acoustic surface wavenumber, with k_i representing $2\pi/\lambda$, and λ denoting the optical wavelength (532 nm) while θ is the angle of light incidence. Furthermore, as already mentioned, when the thickness of the film significantly surpasses the wavelength of light, "bulk-like" acoustic waves possessing the wavevector $Q_B = 2nk_i$ become involved in the scattering process, where n is the refractive index of the film. The specific case of surface acoustic modes garners considerable interest due to the dispersion relation between the angle of light incidence and the velocities of these modes (Equation 1.7) .

Brillouin scattering facilitates the measurement of the dispersion relations of the acoustic waves in a film-substrate system. When substrate properties are known, the elastic constants of the film can be derived from these dispersion relations. In situations where bulk waves are not discernible, a fitting methodology needs to be adopted to extract data on the elastic properties of the coating from the detected SAWs [361]. This strategy relies significantly on numerical computations underpinned by statistical assessments. Collecting Brillouin spectra at various laser incidence angles enables the acquisition of experimental dispersion relations for different SAWs [316, 361].

Concurrently, numerical dispersion relations for the coating-substrate system can be generated by solving Christoffel's secular equations [356]. These equations, governing mode propagation, are solved as a function of various material parameters such as mass densities and elastic constants of the film and substrate, the film thickness, and the exchanged wavevector. The

properties of the coating can be identified by minimizing the least square estimator between the experimental and numerically computed dispersion relations. The computation part of this process is semi-automated, facilitated by the Brillo Software developed in Matlab at Nanolab. Additional details can be sourced from other references [316].

Before concluding this part, specific Brillouin Light Scattering limitations must be noted. The first is the limited accuracy in determining phase velocities and the phonon lifetime, which in optimal conditions is constrained to be above approximately 0.5% due to inherent frequency and wavevector resolution limitations. Consequently, the calculated elastic constants have an uncertainty of around 1% [361]. Another limitation is the relatively long acquisition times for each spectrum, which can last multiple hours, as observed in the case of Al_2O_3 coatings.

Pursuing the investigative methodology previously established in [166], a suite of experiments was undertaken, fabricating alumina coatings utilizing the protocols reported in the previous sections. A deliberate selection of thicknesses was explored, namely 250 nm, 1 μm, 2 μm, and 45 μm, which were carefully deposited onto silicon wafer substrates.

The choice of 250 nm was explicitly designed to probe the influence of sub-micron thicknesses on the ultimate mechanical elastic response of the material. The intermediate thicknesses of 1 μm and 2 μm were selected as points of reference, offering a comparative standard against previously recorded measurements. The most thick layer, at 45 μm, was chosen to replicate a scenario resembling the end-use application of space solar panels. This broad spectrum of thicknesses enabled an exploration into whether escalating film thickness and correspondingly decreasing residual stress exerted any noticeable effect on the final mechanical elasticity of the material.

Figure 1.12 (a) presents the Brillouin spectra garnered for the 45 μm sample. The pale blue areas illustrate the central elastic peak, which does not contribute any information regarding the inelastic phonon scattering processes. Additionally, the diagram shows the "ghost" peaks which are instrumentally generated reproductions of the elastic peak at each end of the spectrum branch.

Given the symmetric processes involved in creating and annihilating photons, the expectation is to observe identical peaks in the Stokes and anti-Stokes regions of the spectrum, as the figure corroborates. Notably, the 45 μm sample displays a triptych of unique peaks. The highest peak can be linked to the bulk mode made possible by the substantial thickness of this sample, while the two smaller peaks, closer to the elastic peak region, represent two distinct surface modes.

Figure 1.12 (b) demonstrates the spectrum for the 250 nm sample adjusted in aa smaller frequency and intensity ranges. This was done to accentuate the presence of the surface acoustic peak near the elastic peak, which would not have been detectable in a full-size spectrum. Nevertheless, a sophisticated smoothing procedure employed in Brillo enabled the identification of a minor bulk peak in the frequency vicinity of 50 GHz. The 1 μm and 2 μm scenarios resemble the depiction for the 250 nm sample, yet they display a slightly higher peak intensity and more

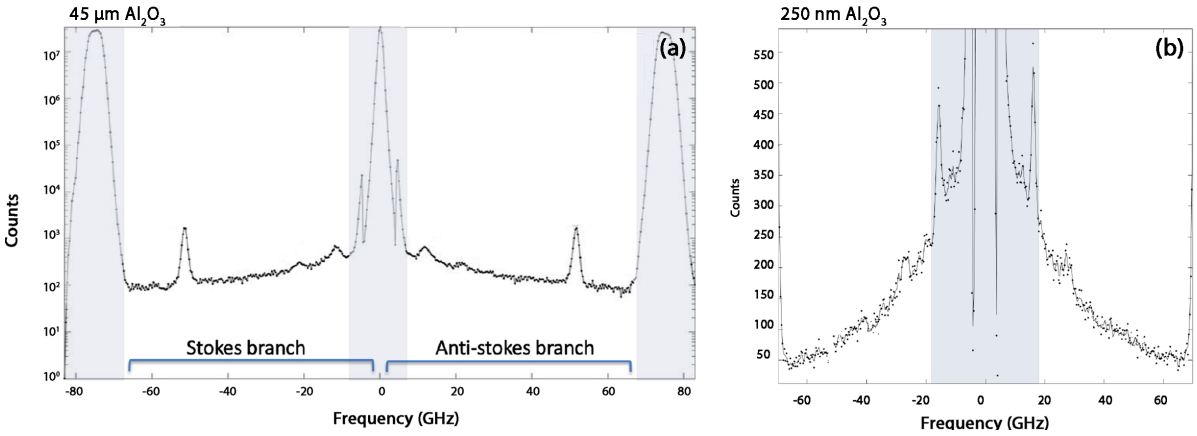

Figure 1.12: Collected Brillouin spectra for Al_2O_3 films, with a thickness of 45 µm (a) and 250 nm (b) thicknesses. The areas delineated in light blue portray the principal elastic peak, the so-called "ghost" peaks, situated at each extremity of the spectral branch.

defined peaks. Despite these low peak intensities, the approach developed in Brillo allowed the detection of many peak frequencies. These peak detections supply a broad swath of information, permitting the comprehensive estimation of independent elastic constants by frequency measurement. As alluded to earlier, some of the peaks, aligned with the Rayleigh wave and other surface modes, adjust their frequency position in accordance with Equation 1.7. Conversely, the bulk wave peak maintains near-constancy, regardless of angle changes, reflecting its interaction with bulk phonons per Equation 1.8.

It is pertinent to highlight further the scenario arising when dealing with submicrometric film thicknesses, where the film's thickness is equivalent to, or lesser than, the acoustic wavelength. Under such conditions, additional modes can surface. A thorough theoretical treatise of these modes' cross-section was presented in [363], illustrating that significant interference effects could emerge, taking into account all potential scattering mechanisms (ripple scattering from both the free surface and the interface, elasto optic scattering from the interior of the film) [364]. Another pivotal aspect discussed in [361] concerns the fitting procedure for submicrometric films. In the mentioned paper, it was shown the theoretical dispersion curves align well for film thicknesses only surpassing a specific threshold value. When the opposite occurs a notable error can be introduced.

The error reduction process highlighted above prompts the establishment of a confidence region within the space of the elastic constants, specifically pertaining to the elastic stiffness tensor constatnts C11 and C44. Using well-known correlations, these regions enable the extraction of the elastic moduli. This confidence region is then circumscribed by four physical constraints, defined as follows:

- The elastic coefficient C11 is determined from bulk longitudinal modes.

- The bulk modulus B of an amorphous structure cannot exceed that of its crystalline counterpart .
- The ratio G/B, representing the shear modulus to the bulk modulus, or in other words, the ratio of shape stiffness to volume stiffness, cannot surpass that of the crystalline structure. This ratio G/B is intrinsically tied to Poisson's ratio (ν), and serves as an indicator of ductility.
- Poisson's ratio (ν) must fall within the range of $0.0 < \nu < 0.5$.

All the specifics regarding this process are thoroughly documented in [166]. The key findings garnered from the procedures described above are concisely encapsulated in the following 1.5.

PARAMETERS	**250 nm**	**1 μm**	**2 μm**	**45 μm**
C_{11} [GPa]	176 ± 5.3	255 ± 2.2	291 ± 6.3	283 ± 0.9
C_{44} = G [GPa]	75 ± 2.1	73 ± 3	73 ± 3	72 ± 6.3
Poisson Ratio (ν)	**0.13± 0.01**	**0.3± 0.02**	**0.33± 0.02**	**0.32± 0.02**
E [GPa]	**169.7 ± 7.1**	**189.8± 9.1**	**194.5 ± 9.1**	**187 ± 10.9**
B [GPa]	76.7 ± 10.7	158.2 ± 12.4	193.6 ± 12.4	187± 10.9

Table 1.5: Brillouin extrapolated results form the least square error minimization process.

Observations for film thickness greater than 1 µm closely correlate with previous findings outlined in [166], thus signifying the material's elastic properties that remain static across a broad thickness spectrum. Regrettably, the aforementioned factors' complexity makes it infeasible to reach a conclusive result for the 250 nm case. Despite the substantial uncertainties presented within this initial analysis, there are indications that films of sub-micrometric dimensions could exhibit characteristics of lower elastic constants. But, on the contrary, several studies investigate the effect of thickness on elastic properties in micrometric approaching films, showing an opposite trend. A case in point is the study depicted in [365], which has demonstrated an amplification of atomic bonding at the surfaces as compared to the interior sections of a material, thereby leading to the assumption that the nominal Young's modulus of extraordinarily thin films at the nanoscale is ordinarily larger when the film thickness is reduced. This scaling phenomenon is identified, underpinned by the theoretical examination of the free energy of the surface-to-volume ratio of the film and outcomes from the elastic modulus measurement.

It has been disclosed [366] that there is a specific film thickness, denoted by where the film's surface energy becomes influential. The thickness exhibits an inverse proportionality to the bulk Young's modulus and is substantially contingent upon the in-plane strain. The uncertainty related to the 250 nm case, requires Further exploration of this latter point is necessary, as intriguing findings could appear.

The ambiguity inherent in the scenario involving the 250 nm case necessitates a more profound investigation of this subject matter. This latter aspect holds a substantial degree of importance as it could potentially unravel a series of compelling revelations.

1.4.2. Evaluating Elastic and Thermal Diffusivity Parameters in Alumina Thin Films via Advanced Transient Grating Spectroscopy

During a research visitation period at the Massachusetts Institute of Technology, transient grating spectroscopy (TGS) was selected as an efficient and non-invasive approach to gain a more profound understanding of the thermoelastic properties of alumina coatings.

The rationale behind utilizing another ultrasonic optic technique lies in the complexities of micromechanical testing, as they demand stringent sample design and preparation, making it particularly difficult to evaluate the properties of nanoscale materials. TGS emerged as a more rapid method and a means to enhance the findings obtained through Brillouin spectroscopy, given its capacity to examine various depth scales within the materials. A more detailed explanation of this aspect will be provided later.

TGS falls under the umbrella of pump-probe methods, it applies the interference of two intersecting laser pulses on the chosen sample, resulting in a spatially periodic excitation. The dynamics of this excitation are monitored through the diffraction of a probe beam [367, 368]. More specifically, a laser interference pattern (grating) acts as a pump source to create a standing wave on the sample's surface with an equivalent wavelength to the grating. A separate laser (probe), is employed for data acquisition. This optical technique relies on the monitored decay of the stimulated surface acoustic waves (SAWs) to ascertain sound wave velocity, acoustic damping properties, and thermal diffusivity [369].

Figure 1.13 provides the representation of TGS measurement signal, obtained from a calibration process using a reference sample. This signal is presented as a continuous black line, wherein distinctive segments have been color-coded for better visualization and understanding of the information they embody. The initially induced pumped surface thermal impulse offers invaluable insights into the thermal diffusivity of the uppermost layer of the material. Concurrently, the detection of the propagation of the acoustic wave imparts significant information regarding the material's elastic properties. This is predicated on the understanding that any acoustic wave's behavior can be comprehensively explained by the specific Equation 1.6. Lastly, the observed damping of the acoustic wave could potentially reveal the presence of defects within the examined portion of the material, further enhancing the analytical power of this technique.

Presently, TGS is being utilized to explore a variety of phenomena, including acoustic wave propagation [370], phonon-polaritons [371], thermal transport [372], molecular diffusion[373], carrier and spin dynamics in semiconductors [374], charge-density waves [375], and heavy ion radiation damage monitoring [369]. The technique has also found applications in the microelectronics industry for metal interconnect metrology [376].

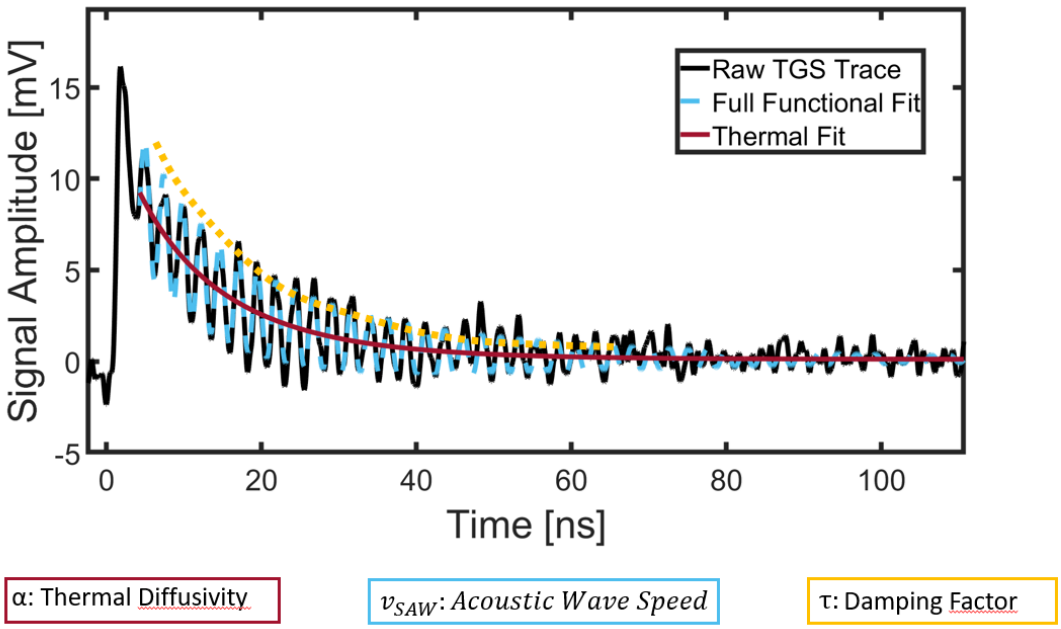

Figure 1.13: TGS calibration measurement conducted on the W reference sample. The resultant signal is visually represented as a continuous black line, while distinctive segments within the signal are color-coded to emphasize the corresponding pieces of extractable information.

The grating systems utilized in this study incorporated a specifically customized diffraction grating to optimize the first diffraction orders, generating two excitation beams. Including this diffraction grating facilitates the achievement of phase-stable optical heterodyne detection [377]. Moreover, by employing a phase mask, the grating period can be modified by alternating between various periodic patterns, thereby enhancing the adaptability of the process.

In this configuration, a 532 nm pump beam was dispersed using a grating, and the first order diffracted beams were made to intersect at the prepared sample surface. This interference, which occurred in an open-air setting, resulted in periodic thermal expansion, a critical mechanism in transient grating spectroscopy. The relaxation of this induced fluctuation in both the temperature field and the surface contour was observed to rely solely on the grating wavevector and thermal diffusivity [378]. The pulse energies were intentionally selected to minimize surface heating below 5 K, ensuring negligible variation in TGS readings, as substantiated by recent extended-duration TGS trials [379].

A 785 nm quasi-continuous wave laser was modulated at 1 kHz using a chopper wheel and divided for subsequent data acquisition. The probes that traversed the same grating split into two probe beams and two reference beams. These beams converged simultaneously with the pump during the diffraction of the transient grating. The first-order responses of the two probe beams were mixed (heterodyned) with the zeroth order components of the reference beams and captured by Silicon avalanche photodiodes with a frequency range of 50 kHz to 1 GHz. The timescale for

the TGS signal development, approximately 1-10 ns, was comfortably accommodated by these detectors, thus preventing bandwidth-related distortions.

The thermoelasticity equation and the heat equation, when applied in the grating direction to this pumped surface impulse [378], demonstrate that the surface displacement behavior, $u_z(x,t)$, adheres to the complementary error function:

$$\frac{\delta u_z(x,t)}{\delta x} \propto erfc(q\sqrt{\alpha t}) \tag{1.9}$$

while the surface thermal field $T(x,t)$, decays exponentially:

$$T(x,t) \propto \frac{1}{\sqrt{t}} e^{-q^2 \alpha t} \tag{1.10}$$

In this context, q is $2\pi/\Lambda$, where Λ is the grating wavelength and excitation wavevector and α is the thermal diffusivity.

Figure 1.13 illustrates how the displacement and thermal influences on probe intensity can be modeled based on Equations 1.9 and 1.10. Hofmann and his colleagues [380] have introduced a supplementary damped sinusoidal term to account for the decreasing SAW oscillations shown by the orange dotted line in Figure 1.13. This added term has demonstrated a decrease in the sensitivity of thermal diffusivity outcomes to the starting point of the fit. To extrapolate the thermal diffusivity α, the frequency of the induced SAW f and the observed decay τ of the SAW the measured signal is fitted using an iterative parameter estimation integrated into a nonlinear least squares calculation. This calculation was used to determine the anticipated intensity of the acoustic temporal response, represented as I_P, and its parameters [369]:

$$I_P = A\left[erfc(q\sqrt{\alpha t}) - \frac{\beta}{\sqrt{t}} e^{-q^2 \alpha t}\right] + Bsin(2\pi f t + \theta) e^{-\frac{t}{\tau}} + C \tag{1.11}$$

A, B, and C are constants used in fitting, β symbolizes the ratio of signal contributions from both displacement and thermally modulated reflectivity, and θ stands for the acoustic phase. The phase difference denoted as ϕ, between the two probe beams is usually necessary to measure in transient grating analysis. Yet, as demonstrated by Dennet and Short [381], this measurement process is simplified when employing a dual-heterodyne setup.

The thermal diffusion length L_{th}, represents the extent inside the bulk material where a noticeable decrease in the thermal field can be observed in relation to the surface. It is the distinctive depth during TGS investigations [376, 382]. In this particular instance, a general Gaussian thermal profile is considered. This depth represents the range over which the heat diffuses when the SAW dwindles to 1/e of its initial height. Even though there might be some seepage into the bulk, its impact is minimal due to its tiny magnitude.

$$L_{th} \approx \frac{\Lambda}{\pi} \tag{1.12}$$

Similarly, the Rayleigh grating induced wave showcases a displacement field that diminishes exponentially with depth (L_{disp}). The scale and the elastodynamic equations uniquely define the decay length of this wave [382].

$$L_{disp} \approx \frac{\Lambda}{2} \tag{1.13}$$

Consequently, modifying the grating wavelength makes it feasible to utilize the Rayleigh wave and the thermally induced field as a probe, allowing for determining the medium's properties up to that particular depth. The primary constraint on investigating increasingly superficial surface segments, for SAW speed determination, is intrinsically linked to the bandwidth of the oscilloscope utilized in the acquisition process. Indeed, to ascertain the speed, it is requisite to measure the frequency of the oscillation induced at the surface. In this specific work, the maximum frequency limit attributable to the electronic chain was quantified at 1 GHz. Given the acoustic wave velocity (v), previously measured in [166] to be approximately 4300 m/s, and the established relation correlating wavelength (λ) and frequency (ν), where $\lambda \cdot \nu = v$, the smallest exploitable grating wavelength (Λ) was determined to be 4.3 μm. This corresponded to a shallower analysis depth of 2.2 μm. Given that the decay of thermal diffusivity is independent of the SAW frequency propagation as stated in Equation 1.11, no restrictions were imposed on the grating wavelength in the case of thermal diffusivity measurements.

The comprehensive ellipsometry examinations, delineated in the earlier section, have provided the indispensable foundation for the initial blueprint of TGS measurements. This blueprint is built upon a profound understanding of the light transmission coefficient as it passes through the alumina. It is crucial to acknowledge that alumina consistently exhibits transparency in the visible frequency spectrum when fabricated through the PLD a-Al_2O_3. This feature, although significant, presents an inconsistent correlation with the operational requirements of TGS measurements: pump laser's absorption and probe's reflection.

To address this technical difficulty, a thin, sputtered coating of gold was deposited on the surface of the alumina to function as an effective transducer. The thickness of this gold layer was expertly fine-tuned to maintain a delicate balance: thin enough to minimally interfere with the outcomes yet sturdy enough to ensure the efficient absorption and reflection of the lasers. This led to a gold layer with a thickness of 100 nanometers, thereby successfully navigating the inherent intricacies and facilitating the way for precise TGS measurements. Without a shadow of a doubt, the presence of the gold layer impacts the ultimate response observed in TGS measurements. However, empirical validation has demonstrated that any gold layer thickness below the designated threshold fails to produce a reflection of the requisite magnitude for obtaining a suitable dataset. Nevertheless, given TGS's inherent ability to manipulate wavelength and,

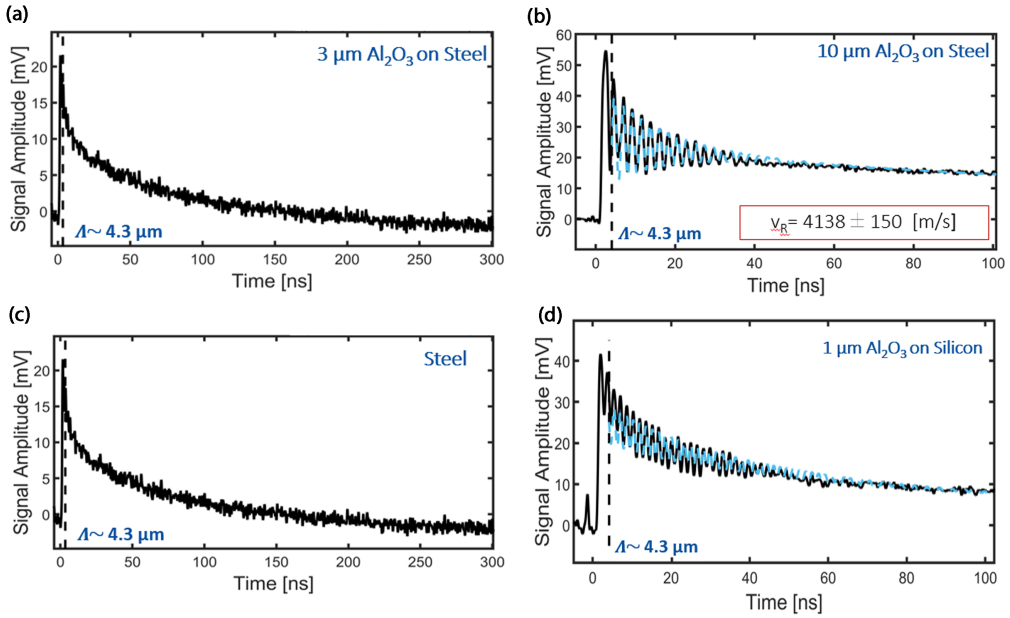

Figure 1.14: This figure illustrates the substantial influence of substrate and coating thickness on the acoustic response of the TGS measurements: (a) decay in thermal diffusion with absent SAW oscillations in thinner samples; (b) acoustic response influence by substrate-thickness in thicker samples; (c) steel substrate response; (d) SAW Oscillation resurgence in alumina samples on monocrystalline silicon

thereby, the depth of analysis, diligent efforts have consistently been made to operate at depths of analysis that facilitate the infinitesimal gold layer's affect the measurements the least.

For this set of investigations, alumina coatings were fabricated onto steel substrates using a frequency of 50 Hz. The fabrication process yielded coating thicknesses that varied between 1 and 10 micrometers.

The decision to utilize steel as the substrate was made considering the experimental matrix that integrated heavy ion irradiation and thermal annealing processes. Empirical evidence has revealed that alumina exhibits superior adherence properties on steel substrates, reinforcing this decision.

The initial findings are delineated in Figure 1.14. Specifically, Figure 1.14 (a) shows the representative behavior of measurements conducted across the range of samples with lesser thicknesses. This figure reveals a result that deviates from prior observations. There is clear evidence of decay attributed to thermal diffusion, yet the oscillations associated with the SAW propagation are conspicuously absent. To investigate this discrepancy, additional measurements were executed on samples of greater thickness (Figure 1.14 (b)) and on an uncoated substrate (Figure 1.14 (c)). The reappearance of oscillations in the 10 micrometer sample, coupled with the consistent absence of oscillations in the substrate, suggest that the substrate-thickness combination affects the acoustic response of the system.

As previously discussed in the previous section, it is recognized that when the the depth over which the amplitude of the surface wave (L_{disp} in Equation 1.13) equals or exceeds the coating's thickness, the travelling elastic wave can be influenced by the substrate's presence. In this instance, it appears the substrate has a damping factor (τ in Equation 1.11) of the SAW wave that is so substantial it likely leads to the immediate disappearance of the oscillation. This is a fascinating phenomenon related to the steel substrate, yet it remains largely unexamined. Further investigation was not pursued as it would not yield additional quantitative information on the alumina coatings. To lend credibility to the hypothesis, alumina samples were also produced on monocrystalline silicon, and as demonstrated in Figure 1.14 (d), the resurgence of oscillations aligns with the aforementioned observations.

In this work phase, an introductory comparative analysis was executed between the results garnered from Brillouin spectroscopy and those procured via TGS. The data extracted from TGS measurements illustrated an impressive alignment with the findings extracted from Brillouin spectroscopy. The TGS results denoted a value of 4138±150 m/s, whereas the Brillouin measurements showed a resultant value of 4328±42 m/s.

The congruity observed in the results underscores the feasibility of TGS as a potent instrument for evaluating layered structures, dismissing the limitation related to Brillouin spectroscopy. Additionally, the concordance between the two data sets enhances the reliability and credibility of the previously recorded outcomes employing Brillouin spectroscopy. Therefore, applying TGS broadens the range of methodologies available for such investigations and corroborates and fortifies the conclusions drawn from Brillouin spectroscopy.

It is essential to acknowledge a slight discrepancy observed in the numerical outcomes yielded by the two methodological approaches. This divergence inspires the formulation of different theoretical explanations. The primary hypothesis attributes the aforementioned discrepancy to the influence of a thin gold layer on the alumina surface used for the TGS measurements. Prior investigations have confirmed that gold demonstrates a lower SAW speed [383]. Consequently, this distinct property of gold could produce a minor reduction in the final mean value of the SAW speed. An alternative hypothesis, which should not be outrightly discounted, suggests that the marginally lower values documented by the TGS methodology might be attributed to the inherent characteristics of the material. As highlighted earlier, the samples scrutinized during this part of the research were fabricated utilizing a laser frequency of 50 Hz, a departure from the 20 Hz frequency used to create the samples whose results were published in [166]. As of this writing, to the best of the author knowledge, there is a lack of literature exploring the potential impact of laser pulse frequency on the ultimate elastic behavior exhibited by amorphous coatings. Additional analysis could also be directed toward evaluating the governing Equation 1.6 of the Rayleigh wave propagation within the system.The solutions of Equation 1.6 provide the wave velocities, whose dependence on the elastic constants and on mass density turns out to be of the type:

$$v_{SAW} \propto \sqrt{\frac{C_{ijkl}}{\rho}} \tag{1.14}$$

The inverse relationship with the square root of the density implies that this parameter could also influence the final velocity. The section on ellipsometry measurements suggests that a film deposited at a 50 Hz frequency might exhibit higher density, potentially leading to a reduced wave speed if the elastic stiffness matrix remains constant. To authenticate any of these hypotheses, it is crucial to establish the resolution of the wave's secular equation. This procedure would require the implementation of several simplifying assumptions to enable the derivation of an analytical solution. However, a detailed calculation of velocities in a multi-layered structure would likely be necessary to ultimately distinguish between the effects of different layers and their properties. This can be achieved numerically without resorting to simplifying assumptions. Currently, adopting such a methodology remains beyond this research. Interpreting the gathered data, an initial conclusion could infer no substantial differentiation in the elastic properties of materials manufactured at laser frequencies of 20 Hz and 50 Hz. This supposition, proposed with prudent scepticism, considers the slight deviation observed in this study compared to previous research. Nonetheless, it is important to consider that such a tentative conclusion may instigate further inquiries in subsequent investigations.

1.4.3. Evaluation of Thermal Diffusivity in Alumina Coatings

As previously elucidated, the strength of TGS lies in its ability to concurrently and without correlation, measure the wave propagation frequency and hence, the SAW speed, along with the thermal diffusivity of the outermost layers of a material. These collective attributes render TGS exceptionally suited to the revelation of coating properties.

Thermal diffusivity assumes significant relevance when evaluating the characteristics of alumina coatings, particularly considering their intended applications. Indeed, this parameter, which quantifies the heat transfer rate, emerges as a pivotal parameter in contexts such as anticorrosion coatings applied to nuclear fuel cladding, or as an anti-radiation damage coating in space applications. These are environments where the material may be subjected to rapid thermal fluctuations and high temperatures and consequently an efficient heat transfer is necessary.

Given the foregoing, thermal diffusivity was evaluated at the opposite ends of the thickness range, thereby revealing no discernible dependence of thermal diffusivity on thickness. The thermal diffusivities ar room temperature for 1 μm and 10 μm were respectively 13.6 $\pm$ 3.5 mm^2/s and 14.5 $\pm$ 1 mm^2/s, and are graphically represented in the Figure 1.15. Here, the data are presented in the form of a box plot to encapsulate, concisely and visually, the sensitivity statistical analysis employed to derive these results.

The value obtained from the measurements exceeds those reported in several scholarly references for bulk alumina [384] in alumina coatings [385]]. This suggests that Pulsed Laser Deposition

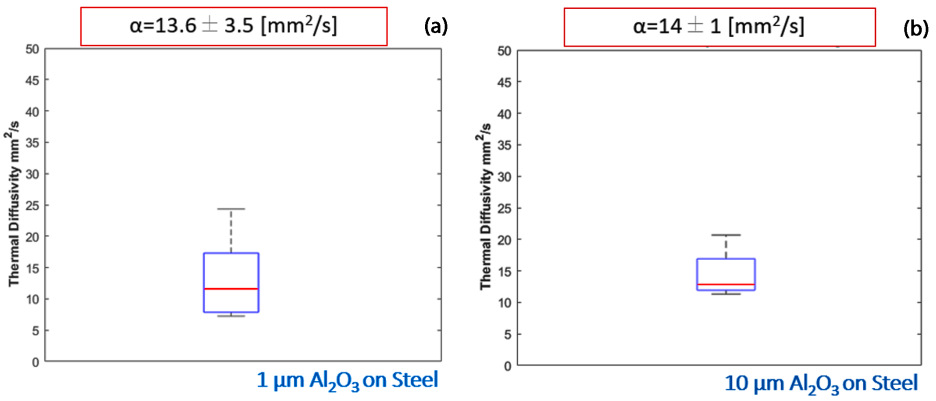

Figure 1.15: Box plot representing the thermal diffusivities of alumina coatings with thicknesses of 1 μm and 10 μm,

PLD Al_2O_3 exhibits enhanced performance, attributable to its distinct structural formation. Interestingly, the derived values are not significantly distant from those conventionally observed for steels [384], which typically gravitate around 30 mm^2/s.

1.4.4. Exploring Surface Acoustic Wave Speed and Thermal Diffusivity in Shallow Coating Layers

Leveraging the advantage of modulating the characteristic investigatory depth, an exhaustive analysis was conducted on the 10 μm coatings. The paramount objective of this analysis was to delve into the modifications in both SAW speed and thermal diffusivity when increasingly superficial segments of the coatings were taken into consideration. The investigation embraced depths ranging from the least analyzable depth, approximately 2.5μm, extending up to about 5μm.

Regarding the SAW speed, the notable observation from this study was an enhancement of the SAW speed by an estimated 5%, when the analysis depth increased.

Given that the SAW speed is directly proportional to the square root of the ratio between Young's modulus and mass density, several hypotheses may be proposed to elucidate the observed trend, as previously indicated. One conjecture could be the existence of a less rigid material, as suggested by a diminished Young's modulus, in the more superficial regions of the coating. Another supposition could be the presence of denser material in these same superficial areas. Yet another hypothesis might be a heightened contribution of the thin gold layer towards reducing the average SAW speed when the volume under analysis is minimized. It becomes crucial to validate any of these theories through the execution of additional meticulous and thorough investigations. It can be observed that the observed reduction in the SAW speed can be delineated by a power law of the form $ax^b + c$, exhibiting a fitting quality R-square value of 0.99. The parameters assume the values a= -906, b=-2.066, and c=4155.

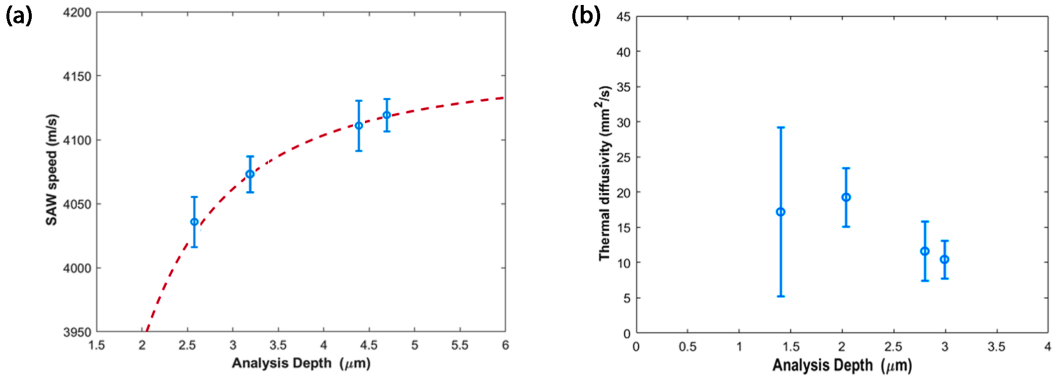

Figure 1.16: The plot (a) illustrates changes in Surface Acoustic Wave (SAW) speed and the associated fitting curve denoted by a dotted line. Thermal diffusivity against the depth of coating, is represented in the part (b).

The experimental data acquired are represented in the Figure 1.16 (a), wherein the fitting curve is also depicted (red dotted line). It is important to mention that the fitting and, consequently the equation and its parameters do not inherently convey any physical meaning, but rather epitomize the empirical evolution of the observed system.

Conversely, when considering the thermal diffusivity in relation to thickness, no discernible trend could be identified. This is due to increased margin of error tied to this specific parameter. Consequently, the inconsistencies in the thermal diffusivity data do not provide a decisive point of reference within the current context. Similar to the previous case, these results are also illustrated in Figure 1.16 (b).

1.4.5. Crystallization Effect on Acoustic Wave Speed and Thermal Diffusivity in Alumina coatings

The research objective at this juncture was to carry out an examination of the property evolution in amorphous alumina as it undergoes microstructural alterations. It is noted in the introductory discussion, that the remarkable properties of the PLD Al_2O_3 coatings only manifest when the material remains in its amorphous state. However, scrutinizing any potential effects is deemed pivotal in situations where crystallization cannot be entirely prevented.

This interest was fueled by the knowledge that the onset of alumina crystallization commences at temperatures exceeding 600 °C. This threshold coincidentally aligns with the target operating temperature for LFR. Furthermore, the potential impact of radiation-induced crystallization warrants consideration, given that the projected applications will invariably involve exposure to radiation. As a result, crystallization merits further study, especially to accumulate additional data when required.

In order to conduct an exhaustive exploration of the phenomena transpiring both before and after the crystallization, four unique thermal annealings were executed in vacuum. The selected

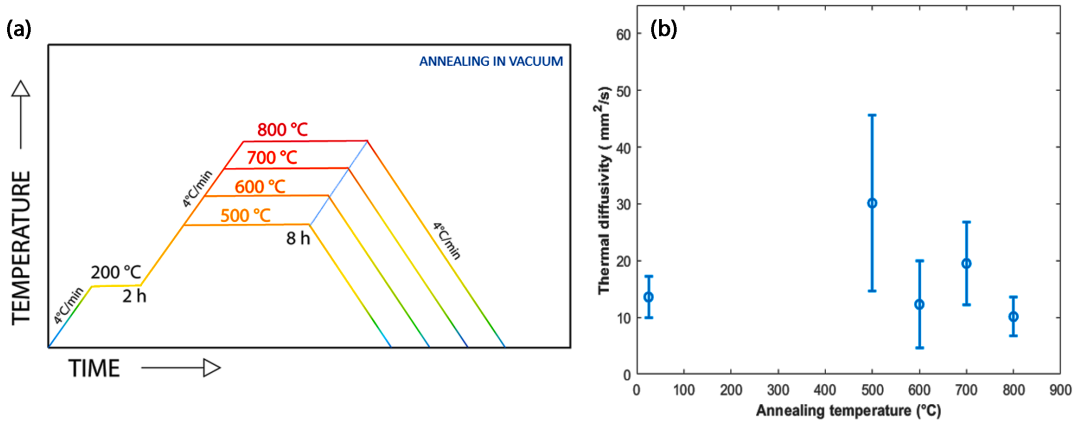

Figure 1.17: (a) Graphical representation summarizing the annealing cycle performed on amorphous alumina at four selected temperatures - 500, 600, 700, and 800 °C. (b) Thermal diffusivity results after thermal annealing

temperatures for this procedure were 500, 600, 700, and 800 °C, with an 8-hour annealing duration and a heating/cooling rate maintained at 4°C per minute. This annealing cycle for all the temperatures mentioned is summarized in Figure 1.17 (a). Then thermal diffusivity and SAW speed were measured exploiting TGS.

Observations indicated that thermal diffusivity did not present any clear trend of evolution. This can be ascribed to the considerable intrinsic error linked to its measurement, which complicates the extraction of insightful data (Figure 1.17 (b)).

In stark contrast to the ambiguous trends seen in thermal diffusivity, the SAW response to the crystallization process yielded significantly more decisive results. A notable observation was an increase in the stiffness of alumina as a direct consequence of the crystallization process.

The speed of the SAW maintained a state of equilibrium until the annealing temperature was elevated to 600°C. Subsequently, a gradual increase was observed up to the 700°C mark before this trend was reversed upon analyzing samples tested at 800°C. The evolution is graphically illustrated in the corresponding Figure 1.18 (b), with the light blue dotted line serving purely as a visual aid.

The recorded increase in the SAW speed has to be attributed to the sequential crystallization process influencing alumina's structural characteristics. Conversely, the observed decline in SAW speed may be associated with the initial coating cracking and delamination stages due to the densification process in alumina during crystallization. This hypothesis was confirmed by Scanning Electron Microscopy (SEM) images collected after each annealing, which provide visual corroboration of these events.

The comprehensive depiction of these findings, including the SEM images and the SAW speed variations with annealing temperature, is provided in the following Figure 1.18. This visual

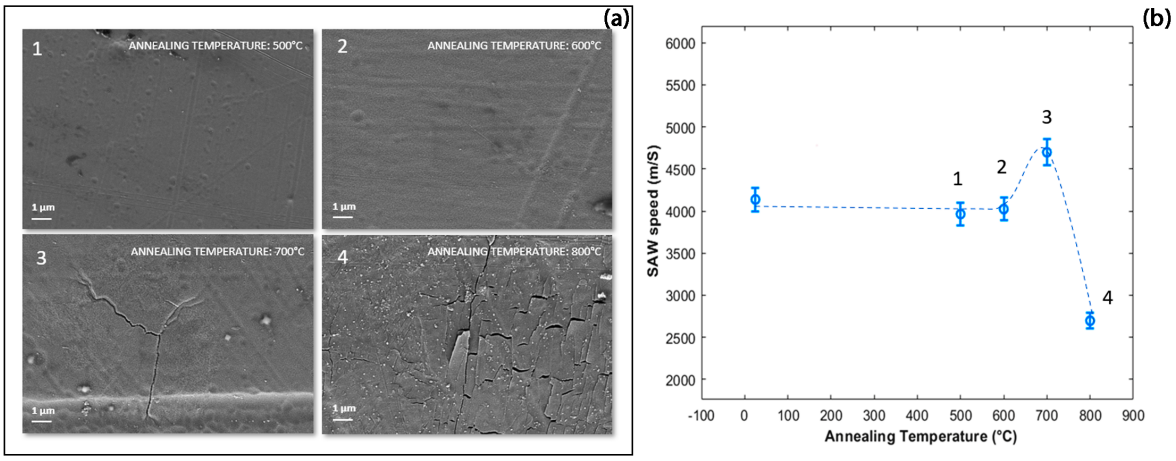

Figure 1.18: SEM images of the alumina coating surface after each annealing. (b) A comprehensive depiction of the Surface Acoustic Wave (SAW) speed evolution as a function of annealing temperature, ranging from 600°C to 800°C. The light blue dotted line serves as a visual guide.

representation succinctly encapsulates the intricate interplay between thermal annealing, crystallization, and the consequential properties alterations in alumina.

This discovery substantiates the critical necessity of averting crystallization in the material to maintain its structural resilience and functional properties. It highlights the urgent call for the formulation of comprehensive strategies that can effectively control the crystallization process induced by both thermal changes and radiation exposure. Such strategic developments could bolster the performance of the material, enhancing its resilience and adaptability even in the face of more demanding and challenging conditions. Moreover, the implementation of these control strategies would not only help sustain the preferred state of the material but also extend its operational life and efficacy, thereby enhancing the overall efficiency in its intended applications. This, in turn, could lead to significant improvements in the robustness and reliability of the systems where this material is utilized.

1.4.6. Interplay Between Coating Thickness and the Measurement of Thermal Diffusivity

As previously outlined, SAW displacement and stress fields experience an exponential decay with depth, characterized by a penetration depth proportional to the acoustic wavelength [386]. Consequently, SAWs with a wavelength substantially smaller than the coating's thickness remain unaffected by the substrate. Similarly, when a coating is much thinner than the wavelength, it influences only in a marginal way the wave velocity, which remains close to the substrate velocity. However, when the thickness aligns closely with the wavelength, the finite thickness of the coating begins to affect the wave velocity. This scenario leads to a wavelength-dependent SAW, typically visualized in a dispersion curve where the SAW phase velocity is mapped as a function of the wave's wavelength or frequency. Correspondingly, the thermal diffusion depth can be

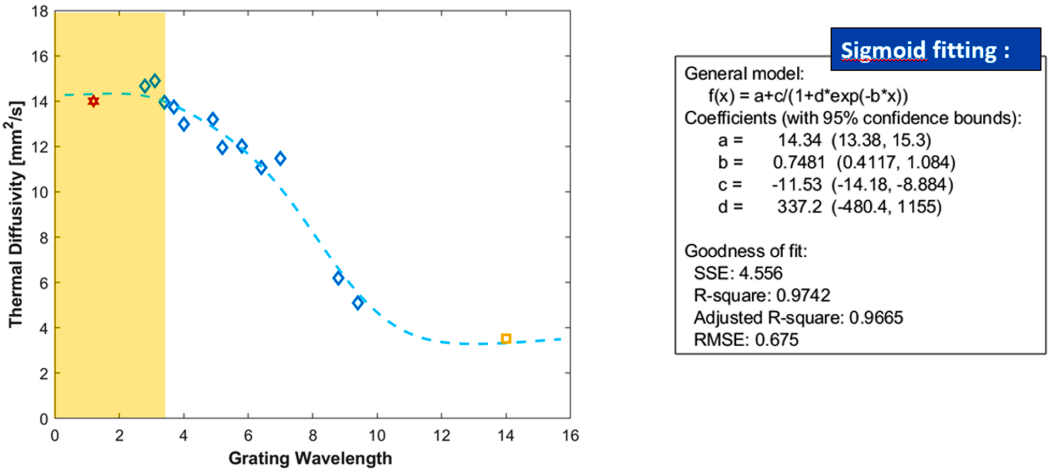

Figure 1.19: Effective thermal diffusivity dispersion curve for 1 μm alumina coating, showing the monotonic decrease of effective diffusivity with increasing diffusion depth. The dotted line represents the best-fitting sigmoid curve obtained from Matlab analysis, indicating the transition from pure alumina (red star) to steel (yellow square) values as the analysis depth increases. On the left the fitting parameters and goodness of fit values are reported. The optimal grating wavelength range containing only coating-specific information is highlighted in yellow.

perceived as the depth to which the surface temperature field responds to the structure's thermal characteristics. When the thermal diffusion depth is close to or exceeds the coating thickness for a specified film thickness, the substrate's thermal properties will predominantly determine the thermal decay process and the inverse holds. By manipulating different grating spacings, one can probe the depth-dependent thermal attributes of the multilayer. For intermediate thermal diffusion depths, where the thermal diffusion depth is approximately equal to the coating thickness, the concept of effective thermal diffusivity has been suggested [386]. This effective thermal diffusivity represents the average value between the thermal diffusivities of the coating and substrate materials, and it allows for the fitting of the thermal decay in the multilayered structure using a complementary function to derive the effective diffusivity.

Experimental measurements were performed for 1 μm alumina coatings to evaluate the effect of the substrate influence on the final outcomes. While as mentioned, thin coatings demonstrated no SAW oscillation, the results for thermal diffusivity were intriguing. Hence, by defining the effective thermal diffusivity as the average diffusivity value incorporating the substrate and the coating's contributions and modifying the grating wavelength and the analysis depth accordingly, the relative contributions of the two components were ascertained. This procedure facilitated the construction of a thermal diffusivity dispersion curve, as illustrated in Figure 1.19.

In the scenario of minimal diffusion depth, the effective diffusivity is congruent with the coating diffusivity, as anticipated. With increasing diffusion depth, the effective diffusivity exhibits a monotonic decrease, converging to the thermal diffusivity of the substrate layer. The effective

thermal diffusivity equaled the pure alumina value when the analysis depth was less than the nominal coating thickness. Still, it gradually reduced, following a sigmoid trend, up to the steel value when deeper regions were analyzed. A best-fitting procedure in Matlab determined the parameters describing the sigmoid curve, represented by the figure's dotted line in the Figure 1.19. On the left the fitting parameters and goodness of fit values are reported.

This study section was pivotal in establishing the measurement conditions for subsequent irradiation experiments. For reasons that will be discussed later, a 1 μm coating had to be employed during the irradiation experiments. The observed sigmoid progression facilitated determining the grating wavelength range that could be used during TGS measurements to extract solely the coating-related information. This useful grating range is highlighted in yellow in the Figure 1.19.

1.5. Investigating the Mechanical Properties and Plastic Deformation Behavior of Amorphous Alumina Coatings

Thus far, investigations about the mechanical properties of alumina coatings produced via PLD have predominantly focused on the material's behavior in an elastic regime. Indeed the already presented part of the work has granted valuable comprehension into the prospective development of the material's reaction to minor deformations, which are restricted to a scant strain percentage. However, the necessity to understand the material's response to plastic deformation cannot be ignored, especially considering the potential applications within the intricate sphere of the nuclear industry. Indeed, of particular interest for PLD Al_2O_3 possible applications, are the fuel pins within LFR. The fuel cladding endures incessant deformation throughout the operational lifespan of the reactor [387]. Reproducing these exact real-life conditions during short-term mechanical testing poses a considerable challenge due to the complex evolution of the variables involved.

The integrity of coatings on a stressed or strained substrate has always been the epicenter of scholarly attention [388, 389, 390, 391]. Indeed, one of the critical prerequisites for a functional coating is its soundness, implying the continuous preservation of a stable structure that maintain its features. In this context, the ideal coating remains free from cracks and delamination. This research endeavours, motivated by this prerequisite, is pivoting towards the analysis of fracture mechanisms of thin brittle ceramic films deposited on less brittle strained substrates. The primary objective is to derive an analytical model,which can help to extrapolate further useful information.

Prior research, as outlined in the introduction [175], has explored the behavior of alumina coatings under plastic conditions by reconstructing the material's stress-strain curve. Nevertheless, this study confronts certain limitations when juxtaposed with real-world scenarios. Information gleaned from tensile tests of free-standing, nanometrically thin lamellae in an SEM apparatus may not fully represent the behavior of material possessing a *bulk thickness* on the order of micrometers.

As a solution, a simplified experiment has been designed to probe the plastic properties of alumina coatings. A more straightforward 'dog bone' tensile test has been adopted to circumvent all the experimental complexities mentioned. The ultimate goal of these studies is to scrutinize and predict the circumstances that might lead to the failure of the external protective film. This part of the work will be a significant milestone toward enhancing the understanding of alumina coating failure and further developing preventative measures. This approach harbors the aspiration to expand these experimental findings to more intricate geometries as soon as dependable and controllable tests can be conducted. Moreover, this investigation will detail other technological issues, explicitly addressing the mechanical behavior of the coating/substrate tandem system upon straining. These short-term tensile tests will probe the mechanical performance of alumina films and the film's response will be engineered by adjusting the internal stresses

within the coating. A profound understanding of these phenomena is fundamental to effectively engineering the coating. The experiments have been supplemented by studies involving FEM designed to support the experimental results. This tandem approach promises a more comprehensive exploration of the topic.

1.5.1. Mechanical Behaviour and Failure Modes of Amorphous Alumina Thin Films under Tensile Stress

In the present investigation, a fragmentation test was executed. This test aims at evaluating the adhesion and durability of a coating system by simulating the impact of an external load experienced by the coating. The test entailed the application of a coating onto a substrate; in this case, PLD produced amorphous Al_2O_3 thin films with varied thicknesses. The fabrication of test samples and the full characterization transpired at the IIT-CNST@PoliMi facility in Milan, while the mechanical characterization via tensile tests was supervised by the J-Tech@PoliTo laboratories in Turin.

A cold-finished AISI 316 stainless steel sheet, acknowledged for its exceptional ductility, served as the substrate. This material was leveraged to manufacture several tensile specimens in a dogbone shape, as depicted in Figure 1.20 (b). The specimens bear dimensions of 74 mm × 15 mm × 4 mm. The region of interest for further characterization is the middle section, which holds a rectangular cross-section of about 6×4 mm^2. The deposition protocol implemented the steps detailed in the preceding sections, selecting a deposition frequency rate of 50 Hz within an axially symmetric deposition configuration as presented in [392]. Using 50 Hz was indispensable due to the extensive area deposition demanded in this scenario, necessitating an accelerated deposition procedure. Upon undergoing tensile tests, the amorphous Al_2O_3/AISI316 specimens were analyzed to comprehend the behavior of alumina coatings within the planar geometry. Fragmentation tests were also conducted at varying temperatures. A spectrum of sample thicknesses was chosen, ranging from 250 nm to 3 μm, to thoroughly investigate the impact of thickness (and consequently the impact of the previously assessed residual stresses) on the final response, and the test temperatures spanned from room temperature to 600 °C. The upper limit of 600 °C was chosen to mirror the crystallization conditions of Al_2O_3 closely; this temperature also exemplifies the first target operational temperature for LFR reactors.

The apparatus for this experimental campaign was the ZwickRoell Z050™ testing machine, renowned for its extensive array of features, notably the capacity to perform tests at both rooms and raised temperatures. In instances requiring high-temperature testing, a durable, integrated 3-zone furnace was activated within the testing device, with the possibility to achieve a maximum temperature of 1250°C. It is crucial to emphasize that tensile tests are generally carried out by applying a static load or sustaining a constant strain rate. Considering the considerable effect that varying strain rates may exert on the tensile characteristics of specific materials, this study prioritized using fragmentation tests under the control of a consistent strain rate. For this purpose, the ZwickRoell device was programmed to reach a predetermined final load at a steady

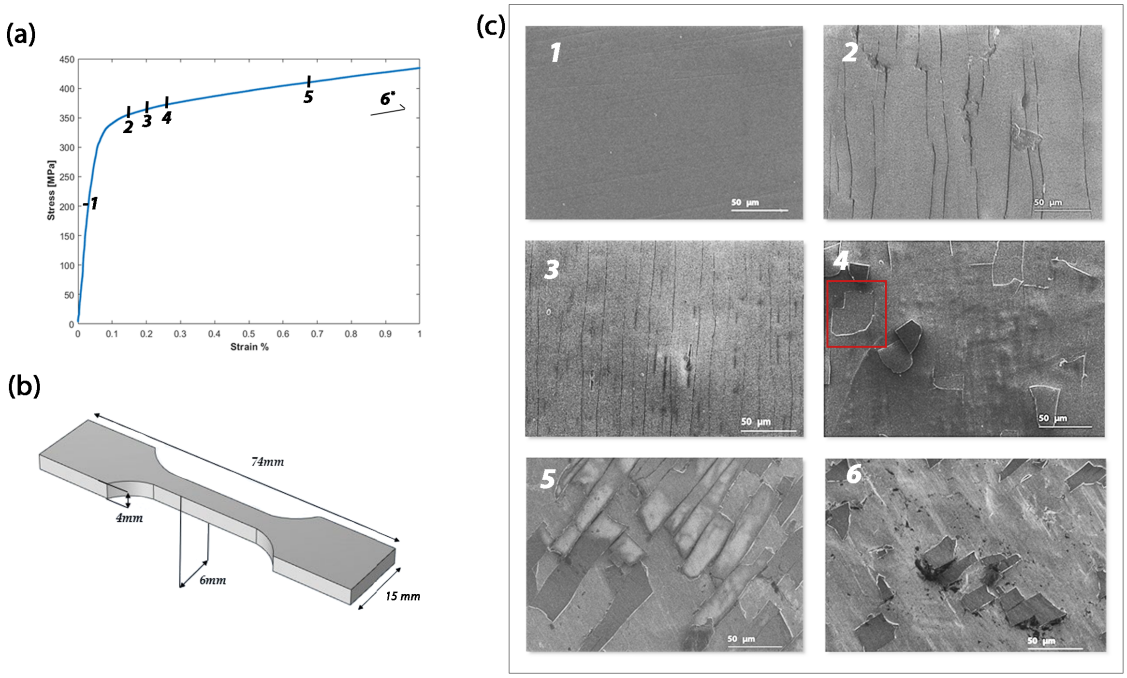

Figure 1.20: (a) Partial stress-strain curve from a tensile test, showing key references (numerals) for coating's top-view SEM micrographs reported in (c) representing each sample after the corresponding strain values. (b) CAD representation of the sample geometry. The red box in the section (c) highlights the presence of induced buckling.

speed. Throughout the process, the integrity of the coating was continuously scrutinized by a laser extensometer enabling in-situ video contactless measurements. Capturing 5 images per second, the video extensometer detected the emergence of cracks by identifying changes in the sample surface's reflectance. The unstressed specimens were assigned an initial or gauge length equal to the length of the central portion of each dog-bone sample (15mm). Consequently, the induced strain in each sample could be directly ascertained from the measurement of the stage displacement. To secure the sample within the die and ensure precise alignment, an initial composite pre-stress of about 15 MPa was administered. Subsequently, a mechanical stage, attached to one of the grips, was moved at a consistent speed of 2 mm/min until the predetermined final load was achieved. Data collection was a continuous process, recording the necessary information to produce the resulting $\sigma(\epsilon)$ curve.

After applying several external loads, the extent of the induced deformation was analyzed to scrutinize the coating's response preceding and after the strain-initiated cracking process. Figure 1.20 (a) presents the initial part of the stress-strain curve derived from the tensile test. Various numerals on the curve are references for the top-view SEM micrographs (reported in Figure 1.20 (c)) conducted on the ex-situ sample after reaching the respective strain value. It is noteworthy that, due to the relative insignificance of the thicknesses of the different coatings compared to the dimensions of the dogbone, the stress-strain curve primarily exemplifies the dogbone's behavior.

Under a specific load, the material may encounter elastic deformation, plastic deformation, or a combination of both. Upon unloading, a material subjected to elastic deformation will revert to its original state, whereas a material exposed to plastic deformation will endure a permanent change. As the substrate is loaded and varying mechanical responses occur, shear forces are transferred across the interface from the strained substrate to the film, instigating and perpetuating the film's cracking [389, 390, 391]. The cracking method is significantly influenced by the magnitude of the effective modulus, (E_{eff}), also called perceived stiffness , that the thin film experiences during its cracking phase. Mathematically, E_{eff} can be calculated as the first derivative to the strain of the stress-strain relationship [391]:

$$E_{eff} = \frac{\delta}{\delta\epsilon}\sigma(\epsilon) \tag{1.15}$$

This quantity represents the substrate modulus "felt" by the coating upon cracking and its definition holds, irrespective of the method used to calculate stresses and strains (engineering or true). However, from now on, σ and ϵ will henceforth be referred to as engineering stress and strain. It is worth noting that E_{eff} can vary significantly with strain over the range of strain at which film fracture occurs; it is a strain-dependent property. Thus, the assumption made by several investigators of a constant substrate modulus for analysis involving low-elongation thin films on high-elongation substrates must be evaluated with caution for each specific case.

Several factors contribute to how a coating fails when it cannot endure the imposed strain state. These include the properties of the coating, interface, and substrate, in addition to the distribution of stresses. As Hutchinson [390] indicates, three potential failure mechanisms may arise if the coating is under tensile stress, irrespective of whether this stress results from external or internal forces: a brittle coating may crack through the film thickness, tougher coatings may fail by delamination along the interface edges, or a crack may propagate within the substrate. For the specific case of this study, it is determined that through-the-thickness, multiple cracking is the principal active failure mode when tensile tests are conducted.

The material remained intact (Figure 1.20 (c.1)) up to the point where the linear relationship between stress and strain held true (elastic region). Under varying imposed strain conditions, the subsequent cracking process is depicted in the Figure 1.20 (c) for the 3 μm Al_2O_3 case and aligns with numerous literary papers [393, 394, 395].

The cracking process can be classified into three distinctive stages:

- Crack Initiation (Stage I): Multiple vertical cracks occur in a direction normal to the loading, instigating sporadically throughout the film (Figure 1.20 (c.2)), and start at the critical strain, termed as Crack Initiation Strain (CIS) or first failure strain (ϵ_{ff}). A decreasing ϵ_{ff} is observed with an increase in film thickness, reinforcing the assumption that thinner films exhibit higher ductility [393, 394]. The initial onset of cracking leads to the stress formerly supported by the coating being transferred to the substrate. Despite

causing greater, nonuniform strains in the substrate, these strains are not substantial enough to induce failure [395].

- Crack Propagation (Stage II): Vertical cracks continue to develop upward and downward upon increasing the strain, remaining perpendicular to the tensile direction (Figure 1.20 (c.3)). The number of cracks within the sample length grows swiftly increasing the tensile stress.
- Crack Saturation and Delamination (Stage III): The generation of vertical cracks subsides, and transverse cracks, i.e., cracks in the direction of the tensile load, become discernible across fragments due to the effects of Poisson's ratio and/or stress relaxation in the tensile direction (Figure 1.20 (c.4)). This comprehensive failure process is referred to as transverse buckling. The appearance of buckling is represented in Figure 1.20 (c.4) by the red box. The phenomenon can be described considering the lateral shrinkage of the film layer, which concurrently induces the formation of transverse cracks, as consequence of Poisson's ratio effects. With additional strain, the amplified transverse compressive stress instigates an increase in transverse cracks, leading to buckling, fracture, and subsequent delamination [393]. After the first induced buckling occurred, delamination takes place, becoming the predominant failure mechanism.

Figure 1.20 (c.5) and Figure 1.20 (c.6) illustrate the resultant complete delamination of the coating, revealing patches of coating islands enveloped by the bare substrate.

In summarizing the cracking phenomena, the literature proposes a parameter known as crack density (CD) [μm^{-1}], which denotes the quantity of vertical cracks per unit length in the tensile direction. An alternative approach is to calculate the average distance between two closest cracks and subsequently determine its inverse. This latter methodology is employed in the analyses herein. It is of noteworthy significance to mention that as strain increases, the emergence of vertical cracks diminishes, culminating in crack saturation. This occurrence is contingent upon the inherent characteristics of the material system and the thickness of the film deposited, as corroborated by the works of Wojciechowski [391] , Zhou [393], and Yanakana [394].

Various empirical models have been formulated to elucidate the relationship between crack spacing and substrate strain. The initial model, put forth by Grosskreutz and McNeil [396], postulates that when film cracking occurs at a macroscopic strain, a consequential relaxation in the stresses at the coating/substrate interface occurs. Uniform cracks with equal spacing arise for each strain and a linear correlation can be observed between the reciprocal of the spacing, which constitutes the crack density and the strain. However, one of the principal limitations of this model is the absence of the coating thickness parameter, which plays an instrumental role in the commencement of cracking as it will be shown later.

To introduce a relationship that considers the impact of thickness on the onset strain, an empirical relation proposed in the literature [391] may be utilized. The following Equation 1.16 portrays the crack density CD as a function of the applied strain ϵ, film thickness t_f, and two

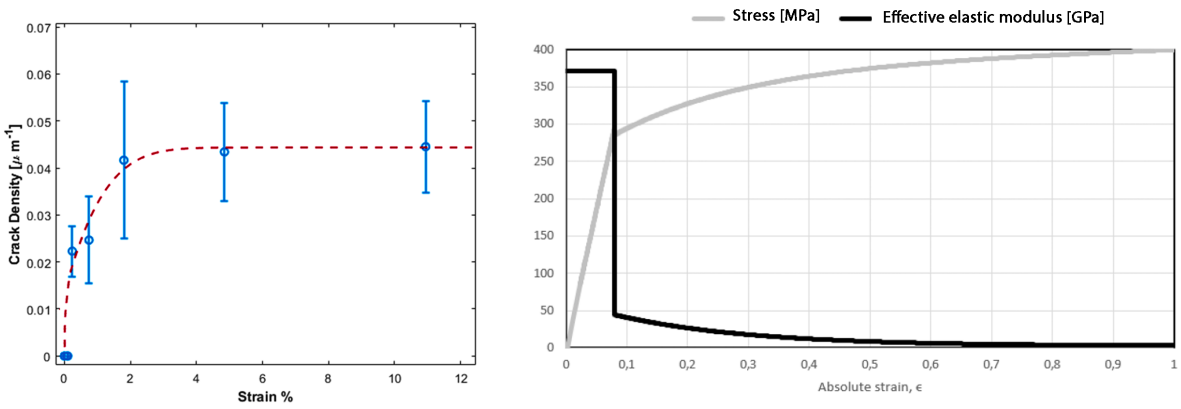

Figure 1.21: On the left , the evolution of crack density for a specific film thickness of 3 μm. The dotted line represents the fitting outcome procured utilizing Equation 1.16. On the right, the stress versus strain curve depicted by the solid grey line, which is derived from an analytical function based on experimentally acquired data from the tensile test. In contrast, the solid black curve denotes the first derivative of the stress-strain curve, commonly referred to as the effective modulus or apparent stiffness (Equation 1.15). The effective modulus of the substrate embodies the modulus experienced by the film.

empirical system constants A and B:

$$CD = \frac{A}{t_f^{2/3}} + \frac{B}{t_f \cdot \epsilon} \tag{1.16}$$

The evolution of crack density for the specific instance of a 3 μm thickness is demonstrated in Figure 1.21, where the dotted line represents the fitting result obtained via Equation 1.16. For the system of interest in this study, the following values were derived: A=0.092783 $\mu m^{-1/3}$ and B=1.6001×10^{-2}. It is imperative to highlight that neither A nor B signifies any physical quantity. They have been included in the discussion merely for completeness.

1.5.2. Crack Formation and Evolution in Film/Substrate Composites: A Focus on Shear-Lag Models

While the underlying physics and models explaining these processes are exceptionally intriguing, the comprehensive delineation of every aspect is not feasible. Hence, this discussion narrows down to encapsulating key points and highlighting vital parameters that can be inferred from the following reported models.

The issue of crack failure in bulk materials was first systematically approached by Griffith, who postulated an energy-based theory suggesting that fractures transpire if potential energy persistently reduces from an intact to a fractured state [397]. Griffith surmised that the surge in surface energy from a new crack is counterbalanced by the release of the elastic strain energy

harbored within the material [397]. However, this theoretical framework does not entirely correspond to film/substrate composites. Wojciechowski and Mendolia further examined the intricate issue of crack failure in their investigation of a Permalloy-Kapton composite system [391]. They proposed that stress relaxation mechanisms are triggered when the film-substrate system is subjected to a load exceeding its elastic limit, reducing the film's strain energy upon cracking. To explain this phenomenon, they identified multiple mechanisms, such as plastic deformation and substrate and film flow, tensile fracture of the film, compressive buckling, and adhesive failure at the interface. They discovered that the effective elastic modulus, E_{eff}, decreases monotonically and can drastically vary with strain over the strain range in which film fracture happens, influencing the system's ultimate response.

In the case of alumina coating deposited onto steel, the stress-strain curve was experimentally extrapolated and then represented using an analytical function defined on two intervals; one for the linear part and the other for the plastic region (Figure 1.21 (right)). The effective elastic modulus was evaluated and illustrated in Figure 1.21 (right) exploiting Equation 1.15. Comprehending the failure of thin brittle films adhered onto high elongation substrates necessitates the understanding that a significant amount of energy release and stress relaxation mechanisms are related to the substrate and its non-conservative behavior. Consequently, the strains experienced by the coating are transferred exclusively through the substrate, which undergoes direct mechanical extension. A more profound comprehension of the cracking process necessitates focusing on the shear-lag model depicted on the Figure 1.22 on the right [391, 398]. This model hinges on the premise that when the substrate is strained, the adhering film segments fracture due to tensile stress accumulation transferred by the substrate across the film's thickness until saturation.

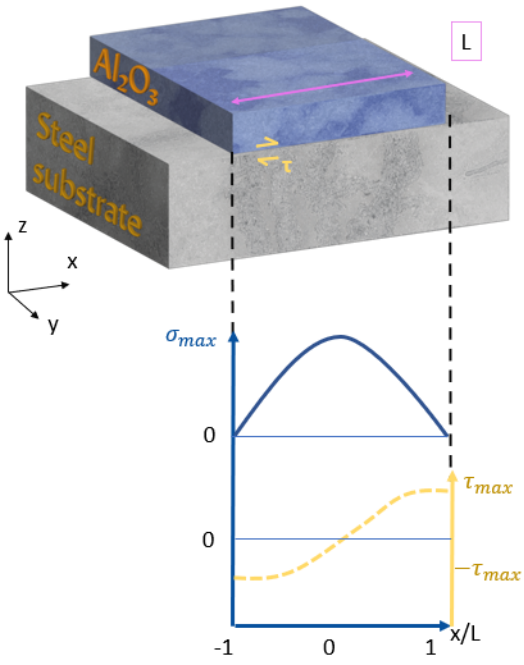

Figure 1.22: Shear lag model representation for a film segment after cracking. The normal (tensile) stress (σ) distribution for thin-film segment and the interfacial shear stress distribution (τ) are depicted.

After the initial crack formation due to surpassing the maximum stress limit, the film's end segments, free from direct tension, are subjected to interfacial shear stress. The evolution of the shear-lag model orbits around determining the interfacial shear stress (τ) between the fractured film element and the substrate. The maximum shear stress emerges at the fractured ends and quickly decays towards the segment's center. Then cracking occurs when the film normal stress

exceeds a critical threshold, potentially instigated by internal or external factors. This load can be directly evaluated starting from the shear stress distribution and it is subsequently absorbed by the high elongation substrate. Increasing the strain, new stress distributions arise and further cracking until equilibrium, or saturation, is reached. Each crack formation reduces the maximum induced stress, as seen from the concept of the effective modulus described earlier.

The shear-lag model was first deployed by Cox to dissect the mechanics of fiber-matrix composites, particularly the strength and stiffness of fibrous materials [398]. This method was subsequently expanded and utilized to analyze cross laminates by Aveston, Kelly, Garrett, and Bailey [399, 400, 401]. Multiple approaches exist, all rooted in the fundamental shear-lag concept [388, 391, 393, 394, 402, 403]; but, although various formulations of interfacial shear stress exist in the literature, the central concept remains uniform. Many authors have suggested different functions to describe τ behavior, from exponential [391, 394] to sinusoidal functions [388, 404]. Several enhancements encompass the use of Weibull statistics for coating strength distribution [393, 405] or the consideration of residual stresses induced by the deposition process [394]. While as stated before, thorough review of all models is beyond this discussion's scope, emphasis is given to the model proposed by Wojciechowski and Mendolia [391], which is considered the most comprehensive.

The impact of residual stress and the distinct model proposed by Agrawal and Raj [388] are also explored in the following.

The model proposed by Wojciechowski et al. [391] originates from the fundamental notion that failure can be described by the equation $\sigma_s = E_s \cdot \epsilon_{ff}$, where σ_s represents the stress in the substrate approaching a critical stress value. When the coating reaches its critical failure stress, ϵ_{ff}, a crack is formed and the stress is released in the substrate. It can be expressed as a function of the relative displacement between the substrate and the film, which depends on the mechanics of shear transfer across the interface. By imposing an equilibrium condition following the occurrence of cracking and differentiating the value of this released stress concerning the direction of straining, a second-order, non-linear, homogeneous differential equation for the released stress can be determined. Additionally, applying a force balance to the unit element makes it possible to derive the values of the maximum shear stress (τ_{max}) and the maximum stress in the coating segment (σ_{max}) and also an evaluation of the mean crack spacing L.

$$\tau_{max} = \left[\left(\frac{E_s t_f + E_f t_s}{t_f + t_s}\right)\epsilon\right]\left(1 + \frac{t_f}{t_s}\right)\frac{[(E_f t_c / E_c t_f)/1 + (E_f t_c / E_c t_f)]^{1/2}}{[2 + (1 + \nu_s)]^{1/2}} \tag{1.17}$$

$$\sigma_{max} = \frac{E_f}{E_s}\left[\left(\frac{E_s t_f + E_f t_s}{t_f + t_s}\right)\epsilon\right]\left[1 - exp\left(-\left(\frac{E_s}{2(1+\nu_S)}\frac{E_s t_f + E_f t_c}{E_s E_f t_c t_f^2}\right)^{1/2}\right)\frac{L}{2}\right] \tag{1.18}$$

$$L = -\left(\frac{E_s}{2(1+\nu_S)}\frac{E_s t_f + E_f t_c}{E_s E_f t_c t_f^2}\right) ln\left[1 - \frac{\epsilon_{ff}}{\epsilon}\right] \tag{1.19}$$

A comprehensive derivation of the equations can be found in [391]. In the presented equations, the subscripts f and s correspond to the quantities associated with the film and substrate, respectively. The symbol t denotes the thickness, E represents the Young's modulus, and ν signifies the Poisson's ratio, as previously mentioned. Specifically, ϵ_{ff} is the critical strain value at which the film experiences cracking, while ϵ generally denotes strain. In the case in which also the residual stresses have to be taken into account the formulation can be further modified [394]:

$$\sigma_{max} = \frac{t_f}{t_s}\left[\left(\frac{E_s t_f + E_f t_s}{t_f + t_s}\right)\epsilon\frac{E_s E_f t_s \epsilon''}{E_f T_s + E_s t_f}\right]\frac{\left(1 - exp(-L/2\lambda)\right)^2}{1 + exp(-L/\lambda)} \tag{1.20}$$

where $\lambda = -\left(\frac{E_s}{2(1+\nu_S)}\frac{E_s t_f + E_f t_c}{E_s E_f t_c t_f^2}\right)^{1/2}$ and the parameter ϵ'' encapsulates all the relevant information concerning the strain experienced by the coating resulting from the presence of residual stress. The detailed formulation of this parameter can be found in [394]. Specifically λ is equivalently designated as the 'shear transfer length'. This term characterizes the specific span along which the stress intensities depreciate from their peak value, to zero, transpiring through the thickness of the coating. This concept is of substantive relevance in the fields of structural design and analysis, given its considerable impact on structural behavior.

To complete the picture, the outcomes of the model developed in [388] are provided below. The model, employing a sinusoidal trend for stress formulation, enables the derivation of a simplified expression for the maximum induced value in the system based on the experimental measurement of the average crack spacing at a specific strain level (L). Moreover, the model facilitates the assessment of the ultimate shear strength (τ_{uss}) and can be modified to consider the influence of residual stresses ($\sigma_{residual}$), if necessary.

$$\tau_{uss} = \frac{\pi t_f}{1.5L}(E_f \cdot \epsilon_{ff}) \tag{1.21}$$

$$\tau_{uss} = \frac{\pi t_f}{1.5L}(E_f \cdot \epsilon_{ff} + \sigma_{residual}) \tag{1.22}$$

Furthermore, it is significant to highlight a series of papers delineating a connection between adhesive characteristics and the shear lag model. Mittal and his team [406] elucidated a qualitative relationship between adhesive properties and phenomena related to the formation of cracks. They emphasized the observation that the presence of consistently spaced, parallel cracks is

indicative of optimal adhesion. Despite these empirical results, their investigation fell short of an analytical structure linking the distance between cracks to quantifiable information about the adhesive and cohesive characteristics of the composite system. To bridge this research gap, multiple studies [407, 408, 409, 410] set forth an effort to provide a comparatively unequivocal and meticulous treatment of adhesion in brittle films. According to their theoretical studies, a thin film exhibiting low elongation can fail due to cohesive cracking or adhesive failure. The corresponding analytical model used fracture mechanics and Griffith's energy criterion to establish a relationship. In an equilibrium or quasi-steady state, this relationship connects the adhesion of the low-elongation layer to the substrate to the critical tensile force required to instigate adhesive failure.

Griffith's derivation articulates that the composite system's internal energy consists of two components [397]: the elastic strain energy and the energy associated with crack propagation. The latter represents the energy involved in forming new material surface areas due to cracking. The criterion for crack propagation posits that the modification in strain energy is equivalent to the upsurge in surface energy consequential to the expansion of the crack. This suggests that the surface energy of the newly fractured region originates from the release of elastic strain energy during the crack's progression. In alignment with this concept under the thin-film approximation ($t_f << t_s$), an analytical formulation to assess the adhesion energy (γ) [N/m], which is also the negative of the energy release rate (ERR), can be found [407, 408, 409, 410]:

$$\gamma = -ERR = E_C \frac{t_s + t_f}{2} \left(\frac{F_{ff}}{E_s t_f} \right) \delta (1-\delta)^2 \left[1 + \frac{\delta}{4D} \right] \tag{1.23}$$

where

- $E_C = \frac{E_S t_f / 1-\nu_s + E_f t_s / 1-\nu_f}{t_s + t_f}$
- F_{ff} is the first failure load, defined as the critical stretching force (per unit width) at which adhesion failure commences
- $\delta = E_f t_s / 1 - \nu_f (t_f + t_s)$
- D is the non-dimensional flexural rigidity of the two-layer composite, and can be evaluated by: $D = [(E_s/1-\nu_s)t_f^3 + (E_f/1-\nu_f)bt_s^3 + 3\delta(1-\delta)E_C(t_s+t_f)^3]/12(t_s+t_f)^3 E_c$

Equation 1.23 establishes a functional correlation between the force at film fracture and the film thickness, contingent on the system moduli and a given adhesion value. Experimental validation of this relationship was achieved via tensile tests on samples of varying thicknesses. However, the model is predicated on a few debatable assumptions, including an undifferentiated consideration of strains in the coating and substrate. The model assumes that the displacement of the film and substrate at the interface must be identical, which holds only before film fracture. Post-initial crack, the film becomes discontinuous, leading to potentially significant changes in the modulus and flexural rigidity of the composite.

An alternative methodology, reported in [405], consistently begins with the shear lag model as a basis to define the energy release rate. This approach leverages the Dundurus parameters' definition (D_1,D_2), further employing the non-dimensional crack opening displacement function (g). However, the detailed definition of the Dundurus parameter[411] and the opening displacement function [403] are left to the existing literature to prevent overcomplicating the discussion.

In this context, the energy release rate assumes a final formulation as follows:

$$ERR = \frac{\pi t_f}{2E_f}\left(\frac{E_f \epsilon}{1-\nu_f} + \sigma_{residual}\right)^2 \cdot g[D_1, D_2] \tag{1.24}$$

This method also elucidates that when the energy release rate ERR, as presented in Equation 1.24, hits the critical threshold necessary for the films to fracture, it implies the onset of the crack. Then this could be directly associated with the film's tensile, or mode I, fracture toughness, symbolized as K_{IC} (Pa $m^{0.5}$),

$$ERR_{crit} = \frac{K_{IC}^2}{E_f} \tag{1.25}$$

In the foregoing discourse, an attempt was made to present the theoretical underpinnings of the aforementioned equations succinctly. These equations served as crucial instruments to ascertain the parameters needed to construct a practical comparative analysis to gain comprehensive insights into the performance and characteristics of these alumina coatings. By examining them in light of various thicknesses and temperature conditions, the study aimed at drawing meaningful conclusions about these variables' influence on the coatings' properties. These findings are reported below.

1.5.3. Applications of Shear-Lag Models to Tensile Testing of Amorphous Alumina Coatings

The phenomenological behavior detailed in the previous section has been determined to exhibit a remarkable uniformity across all the thicknesses sets investigated, independent of the individual conditions assessed. The primary results derived from this research are summarized in the subsequent sections.

When subjected to tensile testing, the 3 μm-thick amorphous -Al_2O_3 coatings analysis suggests the multi-stage failure process described above, beginning with no observable cracking at low substrate strains (around 0.1%). In this domain, the film exhibits primarily elastic properties. Cohesive failure is seen to commence when the strain reaches a threshold value of approximately 0.239%, indicating the start of the coating's cracking.

The cracks that form, called primary cracks, emerge randomly, probably originating from film's morphological inhomogeneities—likely droplets resulting from the PLD deposition process.

These cracks, vertical to the tensile direction and regularly spaced, are sharp and approximately parallel. A complete crack morphology is observed at higher tensile strains (around 1.8%), where the substrate has wholly entered the plastic regime. Secondary cracks, characterized by their wiggly and uneven nature, eventually develop and are nearly normal to the primary ones. This arises due to the Poisson effect— a mismatch of the Poisson's ratio between the film and substrate, perpendicular to the tensile axis. Consequently, an adhesive failure mechanism involving some film buckling comes into effect. Following the initiation of film cracking, the density of the cracks increases rapidly as more plastic strain is applied to the metal substrate until reaching saturation.

The shear-lag model by Wojciechowski and Mendolia [391] provided a relation for the maximum interfacial shear stress, i.e., the maximum shear stress transferred at the coating/substrate interface. Due to the absence of an oriented crystalline structure or a mesostructure, the mechanical isotropy of the coating was assessed within the framework of an isotropic model. Furthermore, perfect adhesion between the film and substrate was assumed.

The numerical results obtained are summarized in Table 1.6 for the most important different strain values: failure buckling onset and crack saturation. It's worth remarking the coating failure started at a strain ≈0.239%, and after the commencement of coating failure occurred at a strain ≈0.25%. At the end the crack saturation occurred far beyond coating failure (strain ≈4.847%).

In the detailed equation's application, the parameters represented as t_s and t_f, symbolizing the thicknesses of the film and substrate respectively, are set to values of 3 μm and 4 mm. The Poisson ratio is for the film and substrate, precisely 0.29 and 0.30, and the film elastic modulus E_f = 195 [MPa]. The coating's parameter where extrapolated from [166].

Parameters		**Conditions**	
		At Failure ($\epsilon \approx 0.26\%$)	At Saturation ($\epsilon \approx 4.8\%$)
τ_{max} [MPa]	Maximum interfacial shear stress	18.04	68.07
σ_{max} [MPa]	Maximum normal stress	132.06	260.18
$L[\mu m]$	Crack segment length (theoretical)	86.59	22.1875

Table 1.6: Parameters calculated according to the shear-lag model proposed by Wojciechowski and Mendolia [391] evaluated for the 3 μm alumina coating

Immediately after its failure, the alumina film fractures in segments whose width, resulting from SEM analysis, is 44.8±10.8 μm, corresponding to a crack density of 0.0223±0.01 μm^{-1} . The shear-lag model theoretically predicts the crack spacing is L =86.8 μm, corresponding to a crack density of % ≈0.012μm^{-1}. Much satisfactory agreement is found at saturation, where the average crack spacing experimentally observed is 23.03±5.5 μm, corresponding to a crack density

of 0.0434±0.011 μm^{-1}. The theoretically predicted average crack spacing is, in this case, L =22.19 μm, corresponding to a crack density of 0.0450 μm^{-1}. Hence, the model seems to be much more consistent when saturation in the density of cracks is attained. Nevertheless, this model does not consider the considerable influence of residual stresses from the PLD process. The modification to the shear-lag model by Yanaka et al. [394] does provide a more comprehensive understanding of the system. Since no residual stress measurements on the coatings of this thickness was carried out during this work, which stopped at 2 um, the evaluation of the parameters considering the residual stress started from the work by Vanazzi [165], where the measures residual stress is assumed to be nearly equal to -300 MPa for a 3 μm-thick alumina film.

Parameters		**Conditions**	
		At Failure ($\epsilon \approx 0.26\%$)	At Saturation ($\epsilon \approx 4.8\%$)
τ_{max} [MPa]	Maximum interfacial shear stress	0.33	0.55
σ_{max} [MPa]	Maximum normal stress	6.03	5.51
$L[\mu m]$	Crack segment length (theoretical)	61.2310	15.6890

Table 1.7: Parameters calculated according to the shear-lag model proposed by by Yanaka et al. [394] evaluated for the 3 μm alumina coating

Naturally, the physical quantities characterizing the composite system, i.e., the effective modulus, remained unchanged independently from the model chosen. In the Yanaka model .[394] the main Equation 1.18 incorporates an additional exponential term for analyzing interfacial shear stress maximums considering residual stresses. This particular term introduces modifications to the second-order partial differential equation describing the stress evolution in the system. It is worth stressing the most important feature of the Yanaka model, which, differently from the previous case, accounts for the decline in σ_{max} increasing strain, explaining the consequent crack density saturation. This can be elucidated by the overlap of shear stresses at the fractured segment ends, resulting in partial cancellation of them. This process diminishes the magnitude of the σ_{max}, ultimately leading to crack density saturation.

As predicted by this modified shear-lag model post-initial crack formation, the average crack spacing is L =61.23 μm, resulting in a crack density of ≈0.02 μm^{-1}. SEM empirical observations report a figure of 44.8408±10.8024 μm, equating to a crack density of 0.0223±0.0054 μm^{-1}. An agreeable correlation is also identified between analytical and experimental values at the saturation point, where the theoretical average crack spacing is L= 15.7 μm, leading to a crack density of 0.06 μm^{-1}. The experimentally observed spacing is 23.03±5.5467 μm, correlating to a crack density of 0.04±0.01 μm^{-1}.

While the variety of models persistently yields diverse values for the evaluated quantities, the

different shear-lag models uphold their validity as an attempt to describe the evolution in the stress. The solidity of the shear-lag theory is rooted in its theoretical foundation, with its efficacy in addressing the issue at a qualitative level being incontrovertibly proven. Nonetheless, the current landscape is marred by the absence of a universal analytical model, one that is capable of quantitatively elucidating the fracture behavior of low elongation films on high elongation substrates for any condition. This absence represents an opportunity for further exploration, offering a challenge for the scientific community to address.

The adhesive characteristics of the interface between 3 μm-thick amorphous alumina films deposited on AISI316 stainless steel substrates have been meticulously investigated following the approach described above. These properties have been qualitatively assessed through the series of fragmentation tests.

The adhesion energy measured at the film/substrate interface equates to 4.20 N/m (or J/m^2). This value, in modulus, corresponds to the steady-state energy release rate ERR, as defined previously. Consequently, the stress intensity factor K_{IC} of the crack can be definitively estimated, yielding a final result of $\approx$ 0.9169 MPa m $^{0.5}$.

Despite the shortage of direct papers to enable a comparative study of the values for this type of coating; the gathered data harmonize with the trends outlined in existing scholarly works concerning their order of magnitude. This congruence provides an encouraging sign that, even in the void of direct comparisons, the comprehension of this subject coincides with the broader academic discourse, paving the way for continued inquiry and deepened understanding.

1.5.4. Impact of Thickness Variation on the Failure Response of Alumina Coatings

Various thicknesses were experimented upon, specifically 250 nm, 500 nm, 2 μm, and 3 μm . As previously mentioned, the behavior of the different coatings demonstrated a similar pattern to what had been observed for the 3 μm thick alumina coating. Additionally, the stress-strain curves exhibit a close alignment, implying that approximating an "infinitely thick" substrate can be deemed acceptable. To put it concisely, the deposition of a substantially thinner film, which is at least three orders of magnitude smaller than the substrate, does not notably influence the mechanical behavior of the composite. The predominant factor determining the composite's mechanical behavior stems from the substrate's properties. Garnering a comprehensive dataset, the crack density was reconstructed, albeit solely for the 3 μm case (Figure 1.21). Indeed, to enrich the breadth and depth of the investigation, a more diverse assortment of samples was introduced, thereby encapsulating an expanded spectrum of thicknesses, but reducing the number of samples for each of them. Even though a complete sigmoidal curve cannot be reconstructed for the other thicknesses, specific observations concerning crack density about possible thickness effects can be made and are detailed below. The thicker layers exhibit a lower crack density at high strains than their thinner counterparts. This can be intuitively rationalized from an energy

viewpoint: creating cracks in thicker films generates a larger surface area, distributing a given force over a larger region and decreasing stress. Consequently, thicker layers are expected to sustain less stress per unit area and crack less under a given composite strain, implying an inverse correlation between crack density and film thickness. This conclusion aligns with numerous reports in the existing literature [391, 393, 412] and is consistent with the empirical Equation 1.16 that describes the evolution of crack density as a function of the coating's thickness.

Conversely, when analyzing low-strain data, it is evident that thicker layers crack under lower substrate strain values than thinner layers. This can be attributed to compressive residual stresses that increase in magnitude with decreasing film thickness. Therefore, a higher tensile stress is required to counteract the more considerable residual compressive stress in a thinner film, leading to a higher strain value. The described pattern applies to the composite system studied in this work, as shown in Figure 1.23, where the initial failure strain, or crack initiation strain (CIS), decreases as the film thickness increases, giving credence to the theory that thinner films exhibit superior ductility. The failure onset strain for the thinnest (250 nm) is nearly seven times that of the thickest (3 μm). However, potential errors in determining the crack initiation strain should not be overlooked, and experimental results must be interpreted cautiously.

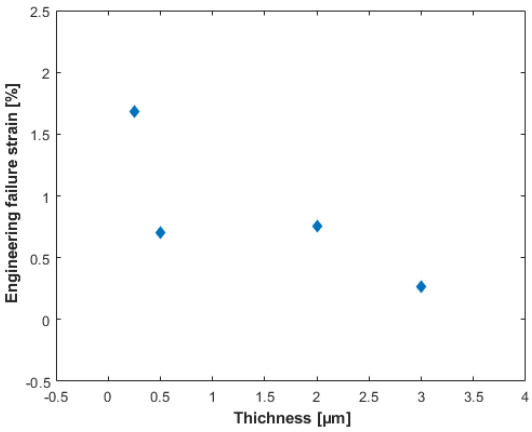

Figure 1.23: First failure strain ϵ_{ff} of alumina coatings of various thicknesses deposited onto AISI316 stainless steel substrates and tensile tested at room temperature.

In order to enable reliable quantitative comparisons of interfacial parameters across varying film thicknesses, identical conditions, especially concerning imposed tensile strain, must be maintained. Since some parameters rely heavily on the cracked film segment length, identical crack spacing must be employed to assess the effects of thickness on coating response. Regrettably, these conditions are unfeasible due to the difficulties in precisely controlling the experimental conditions during tensile testing. Therefore, the only parameter evaluated here is the maximum interfacial shear stress at coating failure, according to the Wojciechowski model Wojciechowski and Mendolia [391], independent of factors other than the geometric and physical parameters characterizing the composite system. This stress approximates 18 MPa and 16 MPa for coating thicknesses of 250 nm and 500 nm, respectively, and increases to approximately 37.5 MPa for 2 μm-thick alumina films. The maximum value of nearly 68 MPa is reached for a film thickness of 3 μm. However, given the difficulties above, the data set was obtained under slightly different conditions, and the maximum interfacial shear stresses were calculated at different imposed strain values.

Nonetheless, the most interesting result is the preliminary qualitative trend found, indicating the trend in the first failure strain ϵ_{ff} of alumina coatings of various thicknesses. As previously stated, these numerical results must be carefully interpreted, but it is noteworthy that a similar thickness dependency has been reported in the literature [394].

The adhesive energy and energy release rate for various film thicknesses were calculated and the results are presented in Table 1.8.

Parameters		**Thickness**			
		3 μm	2 μm	0.5μm	0.25 μm
F_{max} [kN/μm]	First failure load	8	7.9	8.99	9.99
γ [N/m]	Adhesive energy	4.20	66.67	13.69	37.25
K_{IC} [MPa m$^{0.5}$]	Stress intensity factor	0.92	3.65	1.65	2.73

Table 1.8: Adhesive parameters computed for alumina films of various thicknesses.

The stress intensity factor and the energy release rate increased as film thickness decreased. For instance, 250 nm-thick alumina films exhibit a stress intensity factor of 2.73 MPa m$^{0.5}$, three times the value measured for their 3 μm-thick counterparts. Data for a film thickness of 2 μm are anomalously inconsistent and thus deemed unreliable. Consequently further testing on this thickness is required to verify the preliminary observations. In essence, this study elucidated the superior performance of thinner coatings. Exhibiting both lower crack density and enhanced ductility, these thinner films prove resilient and capable of bearing strain more effectively. The uncovered advantages spotlight the potential of thinner coatings, sparking intriguing avenues for future research and innovation in the alumina coating industrial application.

The existing body of literature underscores the significant implications of residual stresses on mitigating mechanical failure. One compelling study [317], evaluates the bending strength of ceramic films concerning their residual stress. It was discovered that amplifying the compressive stress had the favorable outcome of augmenting the deformability of TiN coatings. This led to a twofold increase in the critical deflection before the advent of cracking in tri-point bending tests. Moreover, this research further illustrated an enhancement in the adherence of the coatings, attributable to the rise in the critical load - interpreted as the load at which cracks initiate. Parallel findings were illuminated in [413], demonstrating an escalation in the first critical loads, achieved by adeptly calibrating the relative thicknesses of the multi-layered Ti-TiN system. Another study by Lin et al. [414] reported on CVD-grown amorphous alumina, highlighting that the critical load witnessed a staggering rise of nearly 300% upon fine-tuning the compressive residual stress.

In summary, the results posit a promising proposition: the potential for engineering ceramic coatings systems through the deliberate instigation of a suitable stress state, thereby serving to amplify their in-operation performances.

1.5.5. Impact of Temperature on the Failure Response of Alumina Coatings

To broaden the scope of accessible information, this part of the study evaluated the impact of temperature on the stability and structural integrity of coatings through in temperature tensile tests performed at 400°C, 500°C, and 600°C. Two key findings were drawn by observing the overall mechanical response: Firstly, AISI 316 exhibited unstable characteristics at elevated temperatures, as reflected in the continuous fluctuation within the stress-strain curve shown in Figure 1.24 (a), which complicated the data interpretation process. Additional information extrapolation is made even more complex because the Al_2O_3 crystallization process occurs at 600°C.

The results demonstrated a modest decrease in the steel yield stress as temperature increased, starting from approximately 350 MPa at room temperature and tapering down to around 200 MPa at 600°C. As suggested in [415], this indicates temperature-dependent dislocation motion tied to the substrate's plastic deformation. However, the yield strain values remained relatively stable, with minor changes compared to room temperature readings.

Due to several challenges, the extraction of information from these tests was limited. The first cracks began appearing in the 3 μm test at a strain that inconsistently changed with temperature. This discrepancy is credited to the observed thermal instability and measurement errors, necessitating further investigation (Figure 1.24 (b)). Furthermore, the behavior of 2 μm-thick amorphous aluminum oxide coatings was studied under the same temperatures (400°C, 500°C, and 600°C) at a constant strain rate of 2 mm/min. The initial failure stress of the 2 μm-thick Al_2O_3 coatings appeared to decrease more consistently with temperature (Figure 1.24 (b)). However, this aspect has to be further investigated due to limited experimental data and a scarcity of literature on the subject. To the best of the author's understanding, there appears to be a singular study that has undertaken similar temperature variant testing, underscoring the novelty and importance of our present investigation [416]. Due to the limited sample size, the experiment did not yield exhaustive data, limiting the crack density comprehension. It was, however, noted that the distance between cracks reduced as the temperature increased, resulting in a threefold increase in crack density at 600°C compared to room temperature or 400°C in the saturation region of the crack density.

More research is needed to reliably determine temperature's effects on crack morphology evolution within the coating. Present findings suggest a consistent crack pattern from room temperature to higher levels but fail to conclude the physical mechanisms controlling crack formation and distribution definitively.

Additionally, using analytical models for in-temperature tests is constrained and calls for innovation to account for temperature-dependent physical parameters, such as the elastic modulus. One possibility involves modifying the equation with temperature as a variable. An alternative method could introduce a new parameter in the previously presented equations to account for the temperature-induced elastic modulus reduction.

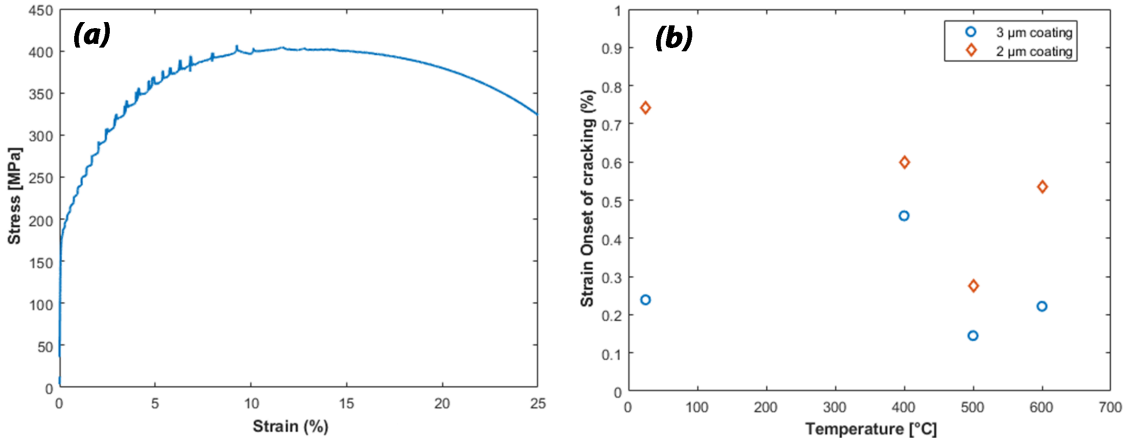

Figure 1.24: (a) Stress strain curve of the AISI316 at 600°C, showing the temperature induced instability in its mechanical response. (b) Strain Cracking Onset for different thicknesses alumina coatings tensile tested at various temperatures

To recap, the research so far closely examined the complex and unique behavior of thin Al_2O_3 films under various temperature conditions. Although this investigation has led to several observations, it is crucial to recognize the limitations of the current research. Constraints such as data insufficiency and experimental limitations add complexity to the complete understanding of the subject. These hurdles should not be perceived as impediments but illuminate areas ripe for further research and discovery. The complexity of the field underlines the need for more extensive and rigorous research. The study of Al_2O_3 films under various thermal conditions remains a promising field with the potential for novel discoveries.

1.5.6. Comprehensive Investigation of Alumina Coating under tension through Finite Element Modeling

In light of the extensive discourse that precedes, employing tensile specimens of films on compliant substrates is a widely recognized technique for elucidating interfacial properties. This methodology juxtaposes the experimentally observed delamination buckling with a mathematical construct, wherein the interface properties function as key parameters. Presently, the methods discussed predominantly adhere to two-dimensional models for explicating the cracking process, often overlooking the significant contribution of the delamination buckling process. Such models fall short of adequately encapsulating the intricate states of stress and deformation that emerge from the uniaxial tension test.

Consequently, a paradigm shift towards three-dimensional models has been initiated, leveraging a multi-scale approach for improved representation. Finite Element Modeling has been identified as a beneficial tool to foster enhanced extraction of knowledge. The application of this modeling tool has been made feasible through the utilization of COMSOL Multiphysics®, a commercially available simulation software recognized for its efficacy in setting up finite element studies, espe-

cially about thermal transport issues. While alternative software programs are often employed to resolve mechanically based problems owing to their superior convergence and optimization capabilities, COMSOL was the chosen platform in this instance, owing to its accessibility within the Politecnico di Milano software suite. Additional factors influencing this choice include its user-friendly interface and the ability to couple diverse problem sets.

Additionally, this selection was influenced by a comprehensive review of existing literature. To the best of the author's knowledge, there has been limited research in this field. This scarcity is probably due to the complexity and convergence difficulties associated with the multiscale nature of the problem, as well as the highly nonlinear equation describing the issue of coating delamination. The work of Toth et al. [417] presents one of the few explorations of a comparable problem regarding coating delamination on compliant substrates, using the capabilities of COMSOL for the evaluation.

The proposed strategy of 3D modeling is posited as a marked enhancement over existing 2D models and shear-lag theory. It does so by accounting for many experimentally observed effects, thus facilitating a more precise dissection of the stress, strain, and deformation states. This approach employs a multi-stage model to illuminate some of the effects on 3 μm-thick alumina coatings when tensile tested at ambient temperature. This includes crucial considerations such as the appropriate load transfer between the film and substrate preceding the film's cracking and the shear-stress-induced local out-of-plane deformation of the film.

The initiation of this investigation employs an initial macro model to determine the cracking stress of the film, defined as the stress condition corresponding to the global strain level where cracking is observed in experiments. This pivotal macro model is essential for setting the boundary conditions for subsequent models. Shell elements represent the coating in the model, a method echoing the earlier Section 1.2.2 that analyzed thermal transport in the curvature setup, based on the same motivation.

Establishing the film's cracking stress and examining the area of uniform stress in the external coating layer requires the definition of several steps within COMSOL® to conclude the stationary study accurately. While an in-depth explanation of the physics central to each step and its execution in the software extends beyond this work's scope, the procedure's critical elements are detailed here, leaving comprehensive descriptions of different modules and software components to the relevant program manuals [336].

The substrate component, known for its dog-bone geometry, is constructed using INVENTOR® CAD software before being imported into COMSOL®. Following the project's initial declaration to extrapolate before cracking behavior, the substrate is presumed linearly elastic and perfectly isotropic, working far from the plastic region. Under these assumptions, the mechanical properties needed for the substrate's study, included the elastic modulus, Poisson ratio, and density. The values used in this study are as follows: E_s=187 GPa, ν_s=0.29, and ρ_s=7850 Kg/m^3. In this context, COMSOL® enables the upload of the complete stress-strain curve of the material,

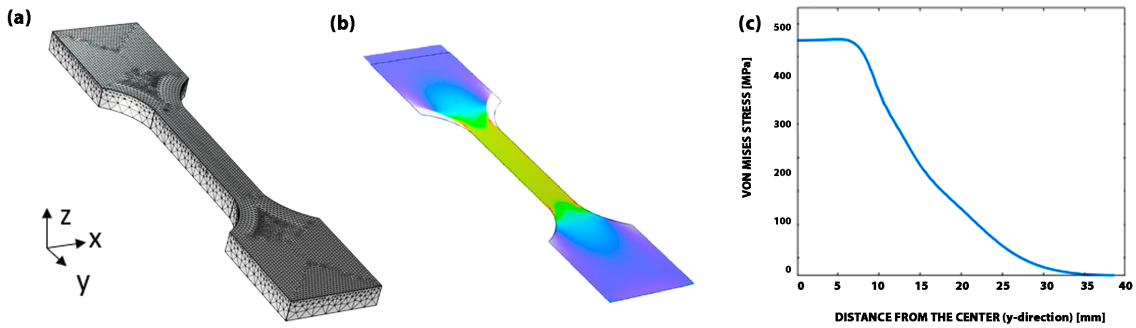

Figure 1.25: (a) CAD dogbone representation with the implemented mesh used in the FEM analysis. (b) and (c): Visual representation of the stress state induced in the coating at an initial strain level of 0.239%. Figure (b) illustrates the high stress value in the central green area, which gradually diminishes with increasing distance from the sample center, this stress evolution is numerical represented in the plot in (c). In the figures (c) and (d) the reference system is the same.

which allowed the software to calculate the corresponding elastic modulus. At the same time, the Poisson ratio and the density have been selected as an average value obtained by the different classes of AISI steel in the COMSOL library. Conversely, the elastic physical properties of the amorphous alumina coating, associated with the outer shell element, have been extrapolated from literature [166]: E_f=195 GPa, ν_f=0.29, and ρ_f=3450 Kg/m^3.

Following the geometry creation and the physics assignment to the model, the next crucial step was constructing the mesh. The mesh of the model geometry greatly influences how the model is resolved; hence it was created automatically through a physics-controlled sequence to take advantage of COMSOL's internal optimization tools. Particular attention was given to meshing the coating shell elements using a multi-dimensional mesh of tetrahedral geometries with user-defined sizes. Considering the study's focus on the outer layer's behavior within the elastic regime, it was considered logical to use a gradient mesh, the size of which refines as it approaches the shell element. The CAD geometry representation and the mesh obtained are illustrated in Figure 1.25 (a).

Alongside the shell interface implementation, the solid-thin structure connection multiphysics node sets up a suitable interface between the modeled film/substrate domains. The connection type is arranged as shared boundaries, enabling the shell element to be modeled on a boundary—the upper face of the 3D solid substrate. The loading edge, rigidly fixed, is translated in the y-direction, replicating the global straining of the test specimen. The displacement-controlled analysis starts from a stress-free, undeformed state, disregarding potential residual stresses from the deposition process.

Then the stress state generated in the coating was evaluated, specifically at the initial stage of strain where cracking is experimentally observable ($\epsilon \approx 0.239\%$). This result assumes that the

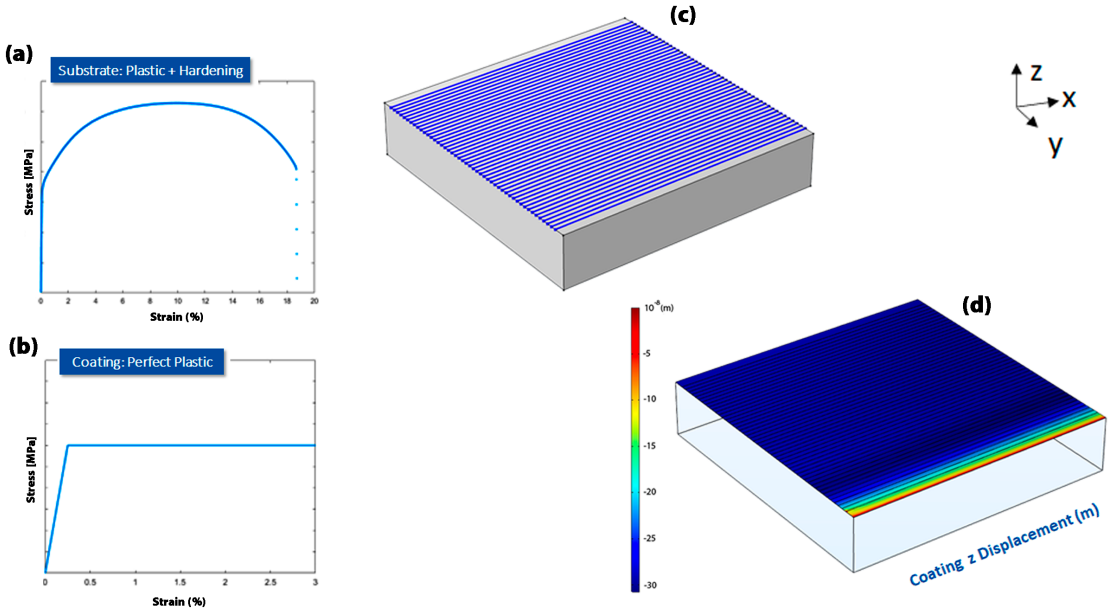

Figure 1.26: Graphical depictions of stress-strain relationships for the models developed for the substrate(a) and the coating (b). (c) Illustration of the model employed to assess the influence of the cracked film under tensile strain (truss elements are distinguished in blue). (d) Display of coating displacement along the vertical z-direction, indicating no particular effects triggered by the presence of the modeled cracked film.

substrate and film materials remain in the elastic regime. These findings are detailed in Figure 1.25 (b) and Figure 1.25 (c). In particular, Figure (b) provides a visual representation of the induced stress, where the central green area illustrates a high stress value that gradually reduces with increasing distance from the sample center, as demonstrated in Figure 1.25 (c).

The validity of these findings must be viewed with an understanding that the assumption of elasticity for the coating may be significantly different from the reality, especially when considering we are near the point of induced cracking. Figure 1.25 (c) reveals that the tensile stress induced in the outer shell element is just under half a GPa, a value that aligns closely with the calculated value of 478 MPa.

It is imperative to note that the primary goal of this preliminary study was not to ascertain numerical results. Instead, it aimed at determining the uniform distribution of film stress across the central region of the dog-bone sample. This information was vital for guiding the implementation of the experimental protocol. It helped to focus the SEM observations within the section of the component experiencing uniform stress for the determining the crack densities discussed above.

Then since the film exhibits a loss of stiffness in a specific direction when it undergoes transverse cracking relative to the global straining direction. A second macro model is established by employing the approach detailed in [417]. In this model, truss elements are used to simulate the

film strips, separated by these cracks, and are aligned with the y-direction shell node lines in a model containing a condensed section of the dogbone system. Truss elements are fundamentally one-dimensional and characterized by their two-node structure. They are solely designed to handle axial tension and compression, eliminating shear forces or bending moments. Each node in these elements has two degrees of freedom in a two-dimensional space (or three in a 3D model), thus capturing the movement of the structure. The elements are assumed to deform only along the length of the element, indicating that all loads are applied exclusively at the nodes and align with the axis of the truss elements [336]. Consequently, these truss elements can accurately represent the sections of the film affected by the cracks, thereby determining areas where shear forces cannot be transferred between two film strips due to the cracked region. Shared nodes on the shell reference surface are utilized by both truss and shell elements. To accurately represent the composite's bending stiffness, shell elements are offset by $t_f/2$ as suggested in [336] where t_f is the coating thickness equal to 3 μm. Symmetry boundary conditions are applied to the edges to prevent the emergence of any dimensionally induced phenomena, while the remaining assumptions remain consistent with those used in the previous model.

In contrast to the first macromodel, this second model requires considering the plasticity in both the film and the substrate. The uniaxial stress-strain curve for the substrate is obtained from experimental results. The film's material behaviour is assumed to be linearly elastic and ideally plastic, with a yield stress slightly higher than the cracking stress identified earlier. The stress-strain curves for both materials are depicted in Figure 1.26 (a,b). An imposed strain of $\epsilon \approx 0{,}75\%$ is applied, equivalent to the initial strain at which the 3 μm alumina coating displayed the first signs of buckling formation experimentally.

Figure 1.26 (d) summarizes the results of this model, showcasing the z-displacements and illustrating that the center of the specimen predominantly remains flat throughout the simulation process. As an initial hypothesis, the induced deformation appears incapable of producing buckling since the z-displacement results do not highlight any variations in the cracked regions.The line at the edge, where the displacement is zero, represents a boundary where the boundary conditions dictate null displacements. The observations made in these findings align closely with a similar behavior delineated in [417]. This congruity between this study and the referenced work suggests the reliability of the observed phenomena.

The evidence gathered shows that the characteristics of buckling, and the subsequent processes observed, are not solely triggered by crack formation. Hence, to gain insights about buckling or delamination in the computational model, the introduction of a minor imperfection is required. This proposition is supported by the findings in [417], where it is shown that the concentration of shear stresses near introduced imperfections prompts buckling, leading to the localization of debonding failure at these sites. In light of these findings, a 3D continuum model was employed for a portion of the film strip adhered to a part of the underlying substrate. This model's scale is judiciously set to be expansive enough to encapsulate local phenomena while remaining compact enough for feasible parameter studies. The model considers two types of potential

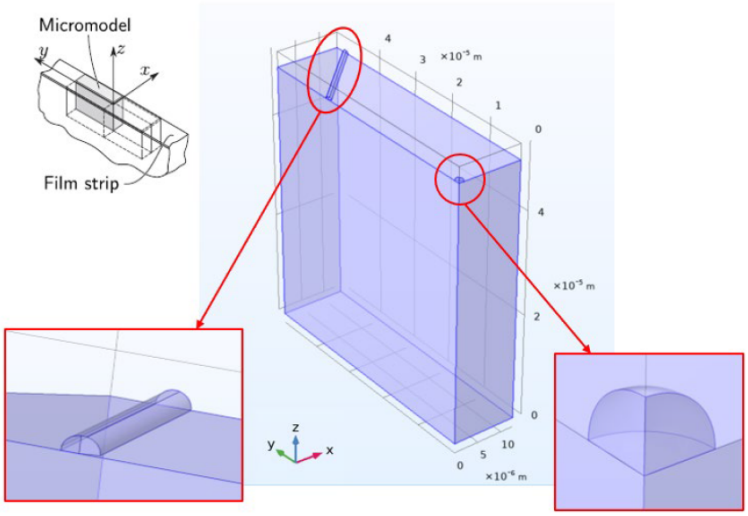

Figure 1.27: Visualization of geometric model including two imperfections: a polishing line and a droplet.

imperfections resulting from the finishing, polishing procedure, and the pulsed laser deposition process, all integrated into a complete assembly to ensure geometric continuity. The model's visual representation can be found in Figure 1.27.

Drawing from the outcomes of the previous model in the coating's behavior, rotations are minimal and thus not factored into computing local displacement boundary conditions. Continuity is maintained by ensuring equal film and substrate displacements in the y-direction. The micromodel also allows for disregarding global shear deformations due to their minimal impact aas verified by the previous model. Verification of this assumption is provided by examining the reaction forces generated. The substrate and film are connected via cohesive zone elements that maintain zero thickness in their undeformed state, based on the concept proposed by Tvergaard and Hutchinson [418]. The decohesion functionality proves useful for simulating delamination between layers or describing crack growth in a continuous material. It is worth noting that for the latter, the crack path must be predetermined before initiating the analysis. A cohesive zone model (CZM) formulation hinges on a material model where certain conditions apply. In this instance, a multilinear separation decohesion model was utilized. In finite element modeling, selecting an appropriate decohesion model is crucial to accurately represent the material behavior under different load conditions. Specifically, the multilinear decohesion model is highly applicable because it offers a versatile way to simulate complex failure processes. It provides a robust framework to interpret the relationship between the traction-separation behavior of the material interfaces, with each phase of the model representing different stages of the decohesion process - from elastic deformation and damage initiation to final rupture. This approach is particularly effective in the simulation of composite materials and interfaces, where failure is often a result of complex load interactions [419, 420, 421]. A more detailed description of the different model

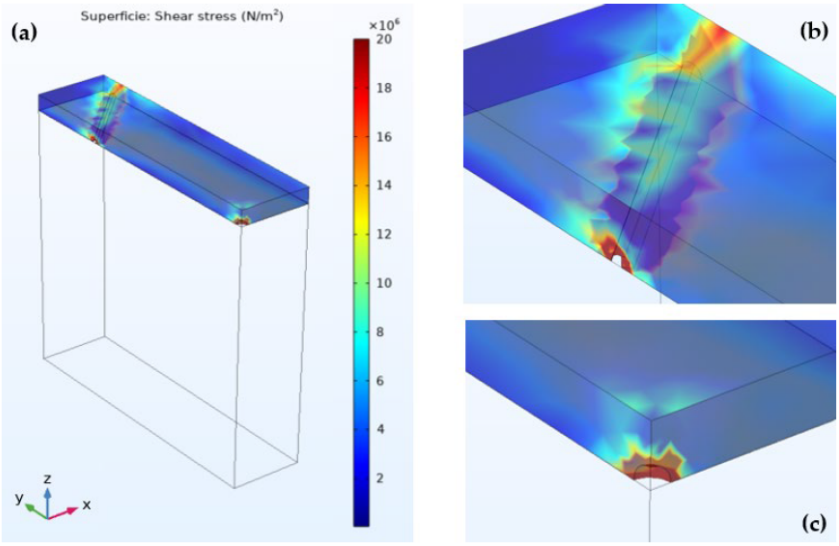

Figure 1.28: (a) Shear stress commencing on the 3 μm-thick outer block, simulating an infinitesimal portion of the amorphous alumina coating. Notice the intensification of stresses in correspondence of the geometrical imperfections simulating (b) a polishing line defect; (c) a droplet resulting from the deposition process.

approaches used in COMSOL are reported in [327].

The multilinear decohesion law can be determined using five distinct parameters: maximum tensile strength, maximum shear strength, tensile and shear energy release rate, and a shape factor, a function of in-plane and out-of-plane separations. As these parameters are unknown for this case, the most effective approach involved setting a parameter sweep. The basic premise was to replicate the displacement at which buckling was experimentally observed, allowing for determining the parameter combination and their values, which best can reproduce the experimentally observed behavior. However, despite the robustness of the parametric sweep, full convergence was unattainable due to the highly non-linear nature of the problem when the decohesion zone element analysis was incorporated. Although no explicit outcomes could be measured from this segment of the modeling study, It provides a strong foundation for future research, shedding light on both explored and uncharted pathways. The study remains a starting point for further investigation and was reported to promote innovative methodological advancements. While the model failed to determine the delamination behavior of the coating due to the described issues, it remains relevant, enabling us to understand the coating behavior, particularly near the imposed defects. The shear stress intensification, which theoretically could lead to cracking and subsequent film delamination, occurs precisely near the defects. It confirms the empirical observation that achieving the lowest possible surface roughness via polishing is crucial for well-adhered coatings. Therefore, efforts to improve the polishing or deposition processe to prevent external inclusions deposition, are crucial for enhancing the mechanical behavior of the coating.

Transitioning from the detailed exploration of material behavior under mechanical stress, including the processes of crack formation and delamination, it is essential to expand this inquiry to understand how this material react when subjected to irradiation. This interaction between material and radiation can result in changes to its physical and mechanical properties, influencing their performance and durability under operational conditions, as discussed in the introduction. The forthcoming chapter pivots from the initial focus on mechanical factors to a comprehensive investigation of material response under irradiation conditions. This crucial shift allows for a broader understanding of material behavior, introducing the new variables and effects that radiation exposure brings to the table. The upcoming exploration encapsulates the analysis of radiation-induced defects and their accumulation and their impact on the microstructure. This comprehensive approach permits a complete understanding of the material's performance under irradiation environments. As it will be shown, this following section contributes significantly to expanding the knowledge needed for material selection and design for its specific applications.

2 | An In-depth Examination: Unraveling the Response of Amorphous Alumina to Heavy Ion Irradiation

The systematic evaluation of pioneering alumina's potential as a radiation-resistant material is paramount to fostering its applicability in the related domains, necessitating an in-depth exploration of its irradiation response.

In the light of evolving nuclear power generation systems, neutron irradiation experiments are often hailed as the ideal choice. However, these procedures come with their own sets of challenges such as hefty financial implications, machine-time limitations, extensive duration of experiments, handling of activated samples, and the requirement of thorough post-experiment analyses. Amidst these obstacles, heavy ions have successfully showcased their potential in emulating radiation-induced effects on metallic and ceramic substances [263, 422, 423]. However, an elaborative discussion on the variances between neutron and heavy ion irradiation, along with the impact of different irradiation parameters on the final material responses, can be found in the closing part of the introduction (Section 0.5).

Wishing to provide a succinct summary, the behavior of amorphous Al_2O_3 films deposited by PLD on steel has been studied under irradiation by 12 MeV Au^{5+} and 18 MeV W^{8+} at 600 °C, up to 150 dpa [178], and under Ni [179] and Au [424] irradiation at room temperature, with ex-situ post-irradiation analyses. The general picture which emerges from these studies is a temperature dependent response to irradiation, with no major modification occurring at room temperature, whilst, at 600 °C, a general trend towards the formation of nanocrystals. In particular, in all the studied conditions, nanocrystals with mean size growing with dpa in a sub-linear way have been observed. Some effect of the ion used has been observed as a second order effect on the growth kinetics [179]. The occurrence of radiation induced crystallization (RIC) is particularly noteworthy because most structural materials subjected to irradiation typically experience radiation-induced amorphization. However, in certain cases like the amorphous PLD alumina, a dynamic equilibrium can be achieved between ordering and disordering processes, leading to the material's crystallization [425, 426]. If the driving force for crystallization exceeds the defect creation rates, the irradiated material undergoes RIC. Numerous models have

been proposed to illuminate these phenomena. The detailed discussion on the potential physical explanations for this behavior, particularly in relation to irradiation-induced crystallization in amorphous materials, is available in Section 0.5.1.

Sections 0.2.6 and 0.5.1 provide a critical review of prior findings on the irradiation of PLD-grown alumina, where the radiation-induced crystallization process was identified as the main outcome of these studies. Starting from the initial amorphous material, a continuous grain growth coupled with the emergence of various crystalline phases was documented [168, 427].

This research extends these studies by conducting further analyses and irradiation experiments to enhance our understanding of the effects on the irradiated material. The study aims at filling the knowledge voids by implementing ion irradiations with various characterization techniques. By doing so, it strives to offer an enriched, comprehensive perspective that would fuel future research and application developments in this domain.

2.1. Exploring the Evolution of PLD Alumina's Microstructural, Thermo-Mechanical, and Optical Properties under Irradiation

As part of the GEMMA project, a research visit was conducted to the Ruder Boskovic Institute (RBI) in Zagreb, Croatia. The institute is home to the Dual-beam Ion Irradiation Facility for Fusion Materials (DiFU), which facilitates irradiating nuclear material samples with one or two ion beams. This is made possible by using two accelerators housed at the RBI: the HV 6 MV Tandem VDG and the HV 1 MV Tandetron.

The primary objective of the research visit was to complete a significant irradiation experiment designed to provide further insights into the impact of radiation on the crystallization process. The focus of this experiment was a unique sample: a steel plate with dimensions 5 x 10 x 2 mm^3, coated with 1 μm of PLD Al_2O_3. A corresponding sample was simultaneously placed and shielded from the irradiation to facilitate the distinction between thermal and irradiation plus thermal effects.

The irradiation of the PLD Al_2O_3-coated steel samples was carried out at the DiFU facility at the RBI using 12 MeV Au ions to a level of 10 dpa. These specific ions and irradiation parameters were chosen to replicate conditions reported in previous studies [178, 428]. Throughout the irradiation process, the samples' steel substrate temperature was kept steady at 600°C, which is the thermal onset crystallization temperature of PLD Al_2O_3. Two sets of horizontal and vertical slits continuously tracked the ion flux, which defined the 10x5 mm^2 irradiation area on the sample. The beam spots for both ion beams were defocused to align closely with the dimensions of the irradiation area. During irradiation, high-frequency ion beam scanning was also employed, specifically at 6.6 kHz horizontally and 444 Hz vertically.

The potential consequences of utilizing a raster beam instead of a defocused one are explored in

Section 0.5.4. Prior findings suggest that pulsing or raster scanning should be conducted at a sufficiently high frequency to prevent in-cascade annealing during the beam's off period within a volume element. This rationale guided the decision to apply an increased range of scanning frequencies. The Table 2.1 summarizes the main irradiation parameters.

Spot size	Average current	Dose rate	Irradiation time	Au fluence
0.5 cm^2	46.2 nA	1.15 x 10^{-4} dpa/s	23 (h)	9.57 x10^{15} ions/cm^2

Table 2.1: Irradiation parameters for the Al_2O_3 irradiations

The samples within the DiFU are heated by an Ohmic heater equipped with molybdenum heat shields and fused quartz to monitor the ion beam scanning area. A K-type shielded thermocouple managed the heater's temperature control, and the sample temperature was supervised by two additional thermocouples located at the edges of the sample. Given the critical nature of dose measurement in ion irradiation, precision in this regard was ensured by using a pair of slits and a large Faraday cup.

Post-irradiation, the samples were analyzed using various characterization techniques. These included FIB/TEM, carried out by PhD Andrea Fazi at the Microstructure Physics section of the Chalmers University of Technology Department of Physics. Nanoindentation and ellipsometry measurements were also carried out.

Figure 2.1 offers a compelling visualization of the primary findings obtained from the TEM analysis. During thermal annealing, sustaining a temperature of 600 °C on the sample's surface required the temperature of the steel substrate to be elevated beyond the set level. This subsequently induced crystallization at the coating and steel substrate interface. The observable preferential columnar orientation in Figure 2.1 (a) further supports this hypothesis. A comparison of samples that underwent merely thermal treatment with those exposed to both thermal treatment and irradiation demonstrates contrasting behaviors. The thermally annealed sample, maintained at a temperature of 600 °C, retained an amorphous state in its upper coating layer. The Selected Area Electron Diffraction (SAED) pattern shown in Figure 2.1 (a 1.2) and (a 2.2) further validates this expected outcome. Specifically, the analysis of the area marked by the red circle in Figure 2.1 (a 1.1) confirmed the amorphous nature of this segment.

On the other hand, the irradiated sample showcased a state of complete crystallization, marked by a homogeneous dispersion of crystalline domains devoid of any evident preferential orientation. The SAED images in the Figure 2.1 (b 1.2) and (b 2.2) corroborate the presence of the crystallized material in this case.

Interestingly, the irradiated sample transformed an amorphous to a homogenous crystalline state. This highlighted the impact of irradiation in inducing the coating's crystallization and its enhancement effect during the process, a finding that echoes the conclusions of previous

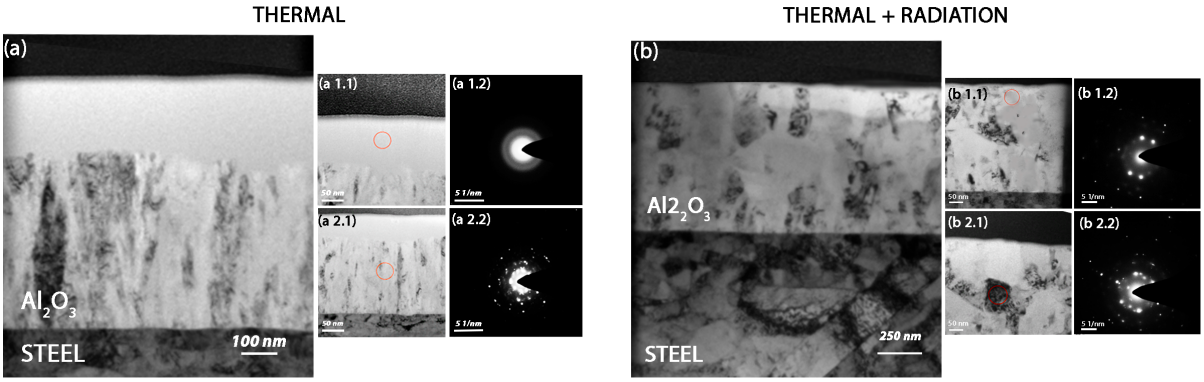

Figure 2.1: Transmission Electron Microscopy (TEM) Analysis: The figure compares the microstructural changes between thermally annealed (a) and irradiated(b) samples at 600°C. The thermally annealed sample shows partial crystallization with an observable preferential columnar orientation. This is also confirmed by the selected area electron (SAED) diffraction images for the different regions in (a 1.2) and (a 2.2). Conversely, the irradiated sample showcases complete crystallization with a homogenous dispersion of crystalline domains. Also in this case the SAED images (b 2.1) and (b 2.2) give confirmations to the observed microstructures.

research.

In exploring the transformation of a material's structure, a sequence of nanoindentation were been performed, allowing for the monitoring of changes in its mechanical characteristics. These tests were conducted under normal environmental conditions using a Berkovich-shaped diamond indenter. A set of ten forces, ranging from 0.5 mN to 5 mN, was utilized to form indents. The Oliver and Pharr model [429] serves as a computational foundation for extracting nano-hardness (H) and reduced Young's modulus (E*) from unloading data. The collated results, including average values and standard deviations, are documented in Table 2.2.

Non Irradiated		**Irradiated**	
H [GPa]	**E*[GPa]**	**H [GPa]**	**E*[GPa]**
14.6 ± 2.5	273.8 ± 21.9	21.5 ± 1.75	340.9 ± 37

Table 2.2: Summary of the results of the nanoindentation tests (hardness and reduced Young modulus) for the thermally annealed and the irradiated sample.

As reported in Figure 2.2, an enhancement in hardness and Young's modulus is observable in unirradiated and irradiated samples compared to the as-deposited material's properties. This behavior can be linked to the induced crystallization process and explained through the inverse Hall-Petch model. The Inverse Hall-Petch Law is an empirical concept in nanomaterials, denoting a decrease in mechanical hardness or strength as the grain size diminishes to nanometer scales. This theory initially appears counter-intuitive, considering it contradicts the standard

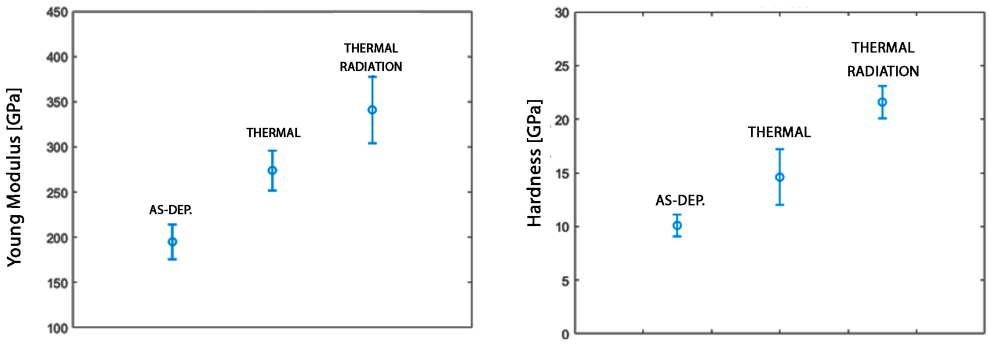

Figure 2.2: Comparing hardness and reduced Young's modulus in unirradiated (@600°C), irradiated (@600°C), and as-deposited material samples

Hall-Petch relationship that emphasizes increased hardness and strength with reduced grain size in polycrystalline materials. At extremely small grain sizes, typically below 10-15 nanometers, the inverse Hall-Petch effect is postulated to arise due to increased grain boundaries grain volume ratio. This shift encourages alternative deformation mechanisms, such as grain boundary sliding or diffusion, which dominate over dislocation slip. Moreover, the increased surface-to-volume ratio can potentially induce a higher concentration of defects, thereby fostering these alternate deformation mechanisms [430, 431, 432]. Existing literature data on alumina coatings and thin films are compared to the findings from these experiments. Notably, Ferré et al. [178, 428] documented a sub-linear increase in Young's Modulus under irradiation, achieving similar levels to those observed in this study only after extensive nucleation of the specific α-phase of Al_2O_3.

The hardness of amorphous Al_2O_3 is found to be between 6 and 13 GPa [173, 433], with crystalline alumina showing increased hardness values, ranging from 12 to 26 GPa [434, 435]. Specific transition phases such as γ-Al_2O_3 or θ-Al_2O_3 are identified within the 12 – 21 GPa range [436], while for α-Al_2O_3, the recorded value is about 21 – 26 GPa [437, 438]. In conclusion, a handful of authors have reported the extraordinary mechanical properties of meta-stable alumina, presenting hardness levels up to 26 GPa [437, 438]. Ion-irradiated coatings in this study demonstrate higher hardness and, thanks to the Hall-Petch mechanisms' role it is even possible to think to control the PLD alumina's mechanical properties.

Proceeding with the protocol established in Section 1.3, where ellipsometry measurements were employed to gather information on the refractive index and absorption coefficient, enabling the computation of the material's density, further ellipsometry analyses were executed on the samples involved in this study. The outcomes are represented in Figure 2.3.

Unlike the thermally annealed sample, which displayed negligible alterations from the as-deposited case, a noteworthy increase was documented in the irradiated material's refractive index and absorption coefficient. This change can be unequivocally traced back to the substantial crys-

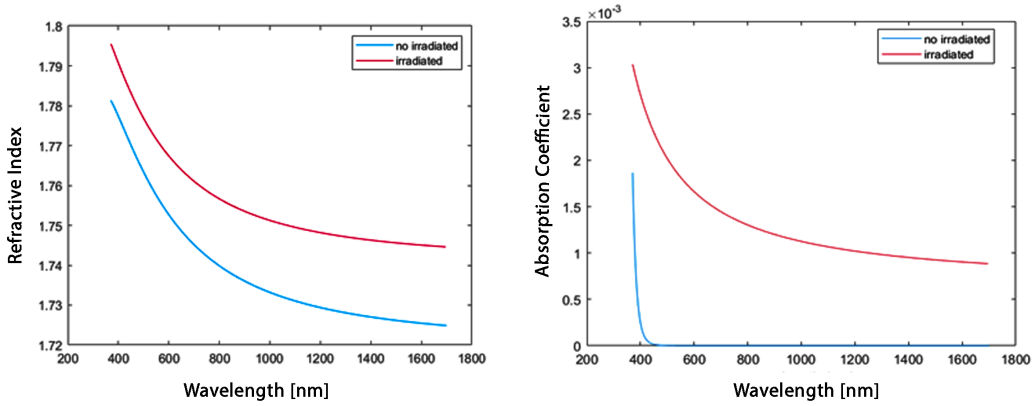

Figure 2.3: Depiction of the evolution of refractive index (presented on the left) and absorption coefficient (displayed on the right) spectra in both thermally treated and irradiated conditions. The results for the as-dep materials were reported in Figure 1.10.

tallization provoked by the combined action of radiation and thermal exposure. The resulting value closely mirrors that of crystallized α-alumina or corundum, identified by a refractive index of 1.76 at 1000 nm [439].

Observing the increased refractive index of the material and in light of the Lorentz-Lorenz Equation 1.5, the conclusion can be drawn that alumina exhibits a higher density after RIC. This indicates that the material is subject to decreased volume during crystallization. This fact becomes particularly pertinent when addressing the potential for radiation-induced void swelling within the material – a condition potentially exacerbated by volume contraction due to the RIC. PLD alumina void swelling is reported in the literature [168, 179]. Specifically, Ferré et al. found voids solely in conjunction with α-Al_2O_3 crystals. Indeed, the creation of vacancy clusters is a specific radiation-induced event observed in crystalline bulk alumina, with multiple researchers reporting void swelling phenomena in α-Al_2O_3 bulks [85, 264]. This finding holds significant implications, as the development of voids within the material can threaten its functionality as a protective coating. Thus, it is suggested that improving the material's stability under irradiation is a critical step if it is to be successfully utilized as a protective coating for nuclear materials.

2.1.1. Thermal diffusivity evolution in irradiated amorphous alumina

As previously discussed, thermal diffusivity is critical, particularly in nuclear fuel cladding applications where effective thermal exchange is crucial. To further understand this, the Massachusetts Institute of Technology hosted a supplementary ex-situ irradiation experiment at the CLASS General Ionex 1.7 MV tandem ion accelerator. The intent was to irradiate the samples and subsequently employ Transient Grating Spectroscopy (TGS) to trace the evolution of properties at room temperature and 600°C. Gold ions were employed to simulate the conditions replicating neutrons with an energy of 12 MeV. This selection was driven by the aim at aligning as closely as possible with previous studies. This specific energy implants ions at a depth of

1.2 μm, necessitating the use of the 1 μm coating to circumvent any effect of the implanted ions. Regrettably, this condition hindered the evaluation of wave speed evolution via TGS, as substantial damping in wave propagation rendered wave speed detection in the thinner samples unattainable, as discussed in Section 1.4.2. Nevertheless, the earlier study, referred to in Section 1.4.6, proved beneficial. It enabled the determination of the TGS wavelength range in which the thermal diffusivity measurement remained unaltered by substrate influence.

The irradiation was configured to yield a Gaussian damage profile on the sample surface.2.4 (a). This method allowed us to generate a damage gradient ranging from 0 dpa to 10 dpa in a single irradiation session. The parameters set for irradiation included an ion current of 1.23 x 10^{11} ion/s and an ion flux of 6.26E x 10^{11} ion/cm^2 s. The irradiation covered a circular area on the surface, measuring approximately 0.2 cm^2 in diameter, which was substantially larger than the laser beams' spots used in TGS. This difference in size, facilitated the use of TGS as a small probe to observe the property evolution as the damage dose increased in the material. Furthermore, SEM was employed to analyze the surface morphology in regions subjected to varying radiation doses.

The plots denoted by Figure 2.4 (b) and Figure 2.4 (c) effectively illustrate the progression of thermal diffusivity throughout the radiation profile, spanning a range of approximately 2.5 mm from the center. This investigation is conducted under two distinct temperature conditions: ambient temperature and a high temperature of 600°C. In an attempt to enhance clarity and visual simplicity, error values are omitted from the graphics. However, it is worth noting that each plotted point signifies the mean value derived from fifteen separate measurements. Furthermore, the corresponding standard deviation value falls within an 8-15% range of the final data point depicted in the visual representation.

The thermal behavior exhibited under room temperature conditions is particularly intriguing. From the boundaries of the radiation profile ($\pm$ 2.8 mm), which symbolize the section where no damage has occurred, the thermal diffusivity closely approximates a value of 11.2 $\pm$ 1.6. This figure aligns with the previously documented range of 13.6 $\pm$ 3.5 as referenced in Section 1.4.3. As we progress further into the zone characterized by the onset of damage, a notable decline in thermal diffusivity is observed. This diminishing pattern of thermal diffusivity as radiation damage escalates is a well-documented phenomenon in scientific literature [369, 440, 441]. Thermal transport within materials can be perceived as a composite of two distinct components: electronic and phononic. Radiation exposure induces the development of defects which can ultimately contribute to the reduction of both components. Higher defect density disrupts the motion of electrons and phonons throughout the medium, resulting in less efficient heat transfer [369, 442]. However, an unanticipated pattern emerges in the sample exposed to room temperature radiation. As we navigate towards the center of the radiation profile, where the dpa and associated damage level rise, an increase in thermal diffusivity values is observed. This pattern echoes a certain symmetry, climaxing at a thermal diffusivity value of 16.7 $\pm$ 2.4, in direct correlation with the maximum radiation level of 10 dpa. Figure 2.4 (b) displays these

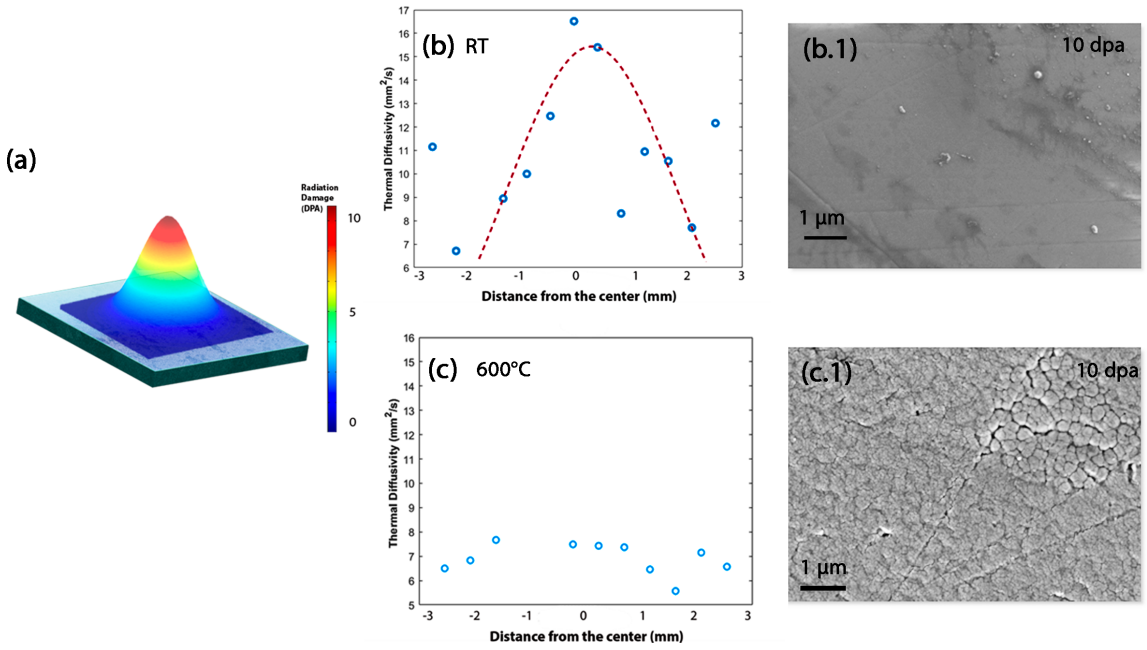

Figure 2.4: (a) Gaussian damage profile on the sample surface. Evolution of thermal diffusivity following irradiation at room temperature(b) and 600°C (c). Figures (b.1) and (c.1) represents top view SEM of the alumina coatings at the maximal level of radiation reached (10 dpa).

results, with an added red dotted line serving as a guideline to visualize the trajectory that forms as a result of the thermal diffusivity augmenting alongside increasing dpa values.

Within the context of published literature, enhancement in thermal diffusivity is frequently justified by an increase in the crystalline fraction present within the system [443]. This notion aligns with the theoretical proposition that an extensive crystalline network can augment long-range phonon and electronic transport, thereby bolstering the overall efficacy of thermal transportation [442]. Nevertheless, the findings presented in the referenced article [443] do not coincide entirely with the observations made regarding pulsed laser deposition (PLD) alumina. Specifically, the PLD alumina seems to resist crystallization at room temperature, even when subjected to an exposure of 25 dpa [180]. Hence, one would reasonably conjecture that the material at 10 dpa remains entirely amorphous. This assumption is further corroborated by the SEM analysis carried out around the 10 dpa region, depicted in Figure 2.4 (b.1). The film morphology displayed i bears a striking resemblance to the structures previously recorded for amorphous materials. However, the spatial variation in dpa is so restricted that XRD measurements alone cannot conclusively confirm this hypothesis. As a result, future analyses must be orchestrated to substantiate these assumptions. An alternate proposition suggests that irradiation could induce short-range structural ordering through successive thermal spikes, without leading to full-blown crystallization. While this theory also remains to be definitively verified, it also does present its own unique set of challenges to overcome.

Turning the attention to the material irradiated at a temperature of 600°C, a decrease in ther-

mal diffusivity relative to the standard value is observed throughout the entire profile. This phenomenon can be explained by intense crystallization, evident in Figure 2.4 (c.1), which initiates the formation of cracks within the film, subsequently generating a myriad of new interfaces within the material. The consequential increase in interface thermal resistance hampers heat transport efficiency within the material [444].

Summarizing, the study unveils a compelling correlation between irradiation damage and thermal diffusivity in the context of nuclear fuel cladding materials. Atypical patterns in thermal diffusivity under room temperature irradiation hint at potential structural changes necessitating further scrutiny. Conversely, the study observes a decrease in thermal diffusivity in materials irradiated at 600°C, a likely consequence of pronounced crystallization and interface creation.

It is paramount to underscore that the observed phenomenon is a secondary consequence of crystallization. Precisely, the crystallization process induces a diminution in volume, leading to the formation of cracks, which serve as formidable impediments to thermal conduction.

These findings underline the necessity for ongoing research to unravel the effects of irradiation on thermal properties, with the potential to inform the development of advanced nuclear materials. Pursuing this line of inquiry, an in situ irradiation study for the comprehensive analysis of RIC kinetics has been conducted and is presented in the ensuing discussion.

2.2. Evaluating Radiation-Induced Crystallization: Exploration via In Situ Transmission Electron Microscopy

Radiation-induced crystallization (RIC) has been shown to increase the material's hardness and stiffness, in contrast to its unaltered state. Interestingly, despite the structural modifications, the irradiated films retain some resilience. Other post-ion irradiation nano-indentation and nano-scratch tests revealed also a residual level of plasticity within the system [427, 428] . Although these studies have clarified the overall trends, a complete kinetic understanding of RIC in amorphous Al_2O_3 films has been elusive.

This Part of the work aimed at bridging this knowledge gap through ion beam irradiations with in-situ TEM observation. This method led to an extensive understanding of the combined effects of ion irradiation and temperature on the structural evolution of amorphous alumina. This level of detail cannot be attained through conventional post-irradiation examination.

Understanding thermodynamically metastable materials' high-temperature and neutron irradiation behavior is critical, yet remains a complex field. This knowledge gap is particularly vital in deploying barrier technology. This part of the work represents a pioneering step toward addressing this gap. It does so through the in-situ, dynamic monitoring of RIC processes in amorphous Al_2O_3 thin films. RIC was investigated across a wide temperature range (400 - 800 °C), at the Argonne National Laboratory's Intermediate Voltage Electron Microscope (IVEM)-Tandem Facility, thanks to different international grants won in the framework of the NSUF (Nuclear Science User Facilities) founded by the American Department of Energy. The findings, that will be shown latter, provide critical insight into the grain growth's dependence on ion dose and temperature. A kinetic approach helped extract the process activation energies and key parameters.

Films with nominal thicknesses of 100 nm were grown on monocrystalline substrates obtained by cleaving a NaCl crystal. After deposition, each sample was put in warm distilled water, where the salt dissolved and the oxide film floated on the water's surface. TEM grids were used to pick up the films, to be ready for analysis in the TEM. Additional information about this floating technique is included in [176]. Films with thickness og 50 nm were also been produce to analyze the final effect of the thickness on the RIC.

The thickness of 100 nm was selected as a reference, to steer clear of the spatial resolution degradation in TEM resulting from an augmented number of inelastically scattered electrons due to the increased thickness, as well as to prevent any surface effects that may be induced by lower thicknesses. Samples tested at temperatures below 600 °C were laid on PELCO ® 2000 mesh Cu grids from Ted Pella, Inc. To perform the irradiation tests at temperatures above 600 °C, ceramic Si_3N_4 membranes and Molybdenum grids (PELCO ® from Ted Pella, Inc.) are used to pick and support the floating films.

2.2.1. Irradiation Experiment Details

The in situ irradiation experiments were carried out in the IVEM facility. It includes an intermediate voltage transmission electron microscope and an ion implanter. The combination of these instruments offers a unique capability for a wide range of in situ experiments involving ion irradiation or ion implantation with simultaneous transmission electron microscopy. More information about the IVEM facility is covered in [445].

The PLD deposited alumina films were subjected to thermal heating until stabilization thermal equilibrium at different temperatures (400, 500, 600, 700, 800 °C), then irradiated with A 700 keV Kr^{2+} ion flux of 6.25 10^{11} ions/cm^{2}s. Fluences required for reaching 1 dpa were 8.5 10^{14} ions/cm^2. For each experiment, the ion flux was measured to an accuracy of ±10% by an annular Faraday cup located within the microscope at 4 cm from the sample [445].

The above choices were based on simulations performed by the SRIM code [446]. The main outcomes, such as implantation profile, ENSP ratio and damage events, are summarized in different plots in Figure 2.5. The discrepancies between the damage production in the SRIM two modes of calculation (Full Cascade and Quick Damage) are reported in Fig. 2.5 (c). In this case the Quick Damage mode was employed for the dpa calculation. A more detailed discussion of their use for the dpa calculation is reported in the Irradiation section.

In the present work, the values exploited for displacements threshold energies for Al_2O_3 are the ones given by default by SRIM: 25 eV for Al and 28 eV for O. It is worth remembering that these values are averages of direction dependent values [447].

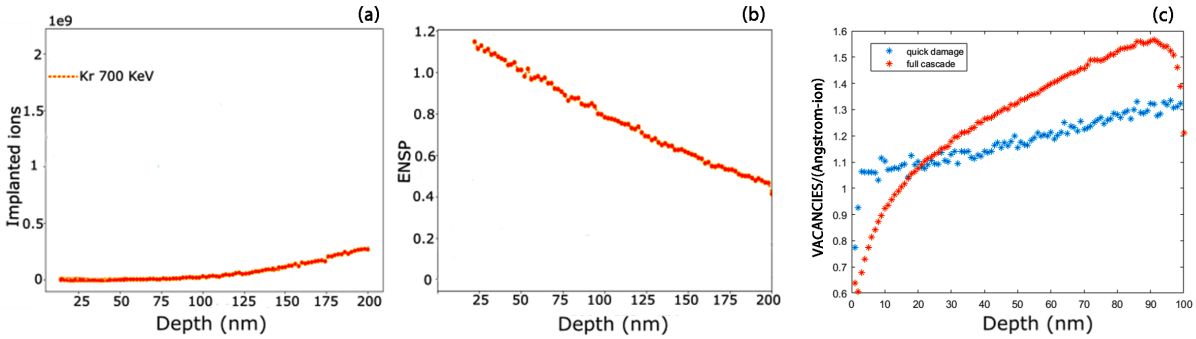

Figure 2.5: SRIM simulation outputs:(a) implantation depth and (b) electronic to nuclear stopping power (ENSP) ratio. Notably, the picture on the left reveals a complete absence of ions implantations since the 700 KeV Kr implantation peak is beyond 100 nm.(c) Depth profile of the total number of vacancies produced under irradiation of alumina by 700 keV Kr ions at the as calculated using two alternative damage simulation methods of the SRIM software.

Direct observation of the films under irradiation revealed the ion irradiation-induced particle nucleation and then their growth, as it can be observed in Fig. 2.6. Crystallite growth occurred for all irradiation temperatures examined, even below 600 °C, which is the boundary temperature below which thermally induced crystallization does not occur in PLD Al_2O_3, as reported in [178],

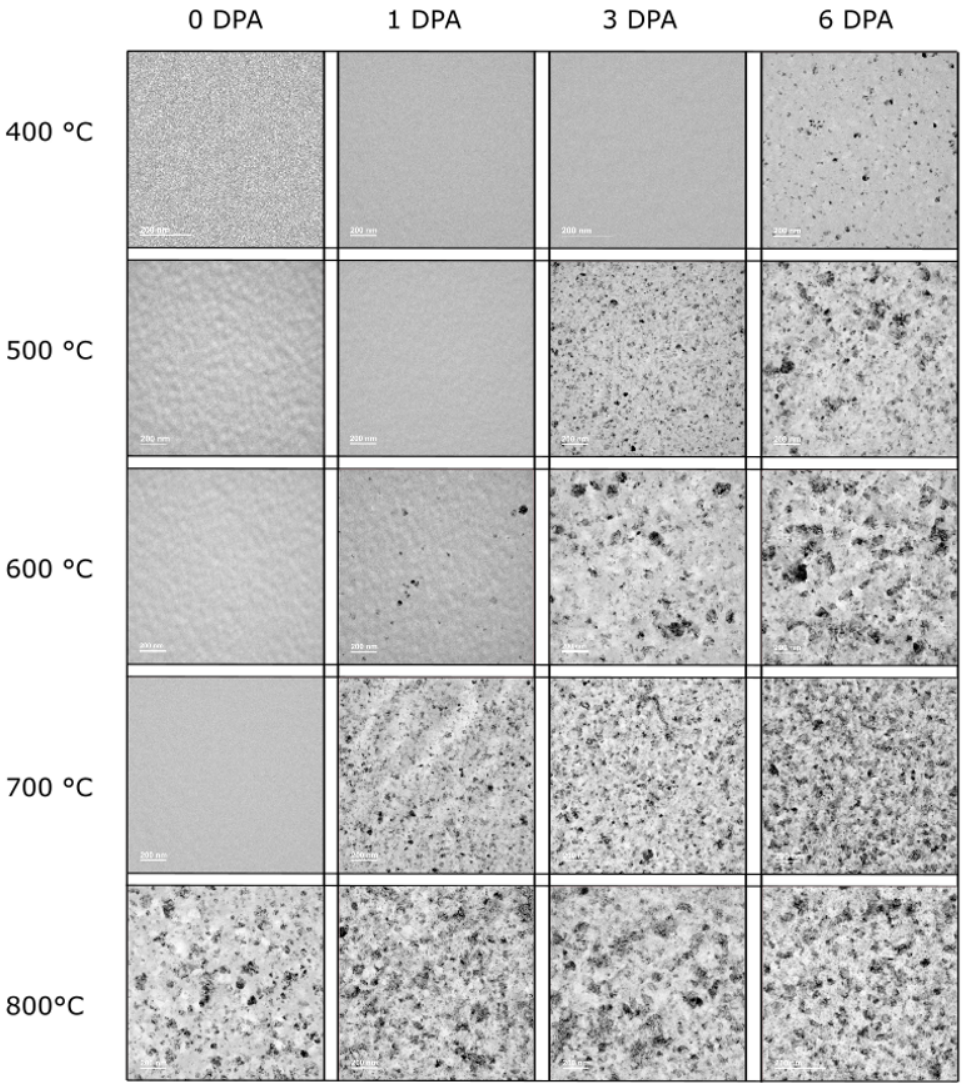

Figure 2.6: Bright field images of the radiation induced crystallization in Al_2O_3 film at different temperatures.

where no discernible crystallization or grain growth are found during annealing for 90 minutes at 600°C. The evolution of the microstructure was followed by sequentially taking bright-field images (BF), dark field images (DF) and diffraction patterns (SAED) of the films while they were being irradiated.

2.2.2. Irradiation-Induced Nucleation and Phase Evolution: An Analytical Study of Crystallite Growth Kinetics Using Selected Area Electron Diffraction and Dark Field Imaging

During the various in-situ irradiation experiments SAED patterns were recoded to precisely identify the onset of crystallization (Fig. 2.7). In each pattern, rings dimensions were measured, determining the crystalline phases present in the system by a direct comparison between the

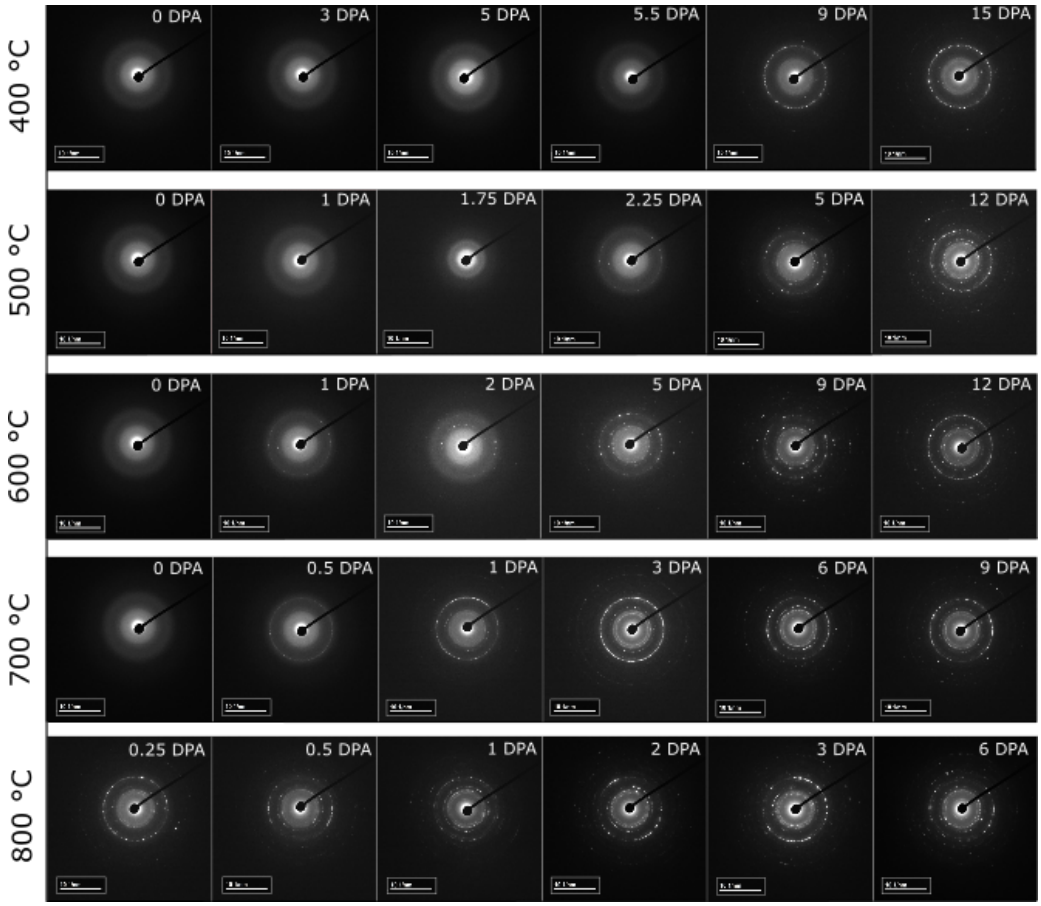

Figure 2.7: Radiation-induced crystallization diffraction pattern evolution in Al_2O_3 films at different temperatures.

interplanar distances (d-spacings) obtained and the databases present in literature [448, 449].

The phase recognition was not straightforward because each pattern consists of an overlapping signal from grains of different phases. Indeed, alumina has an abundant number of metastable transition phases that appear before the only stable α-phase as discussed in [450], and at least for the thermally induced crystallization, the phase transformations are strongly related to the deposition method and temperature [451]. Furthermore, the different crystalline planes often present d-spacings very close to each other, making a unique attribution to one of the possible crystalline structures sometimes impossible. Apart from the principal γ-Al_2O_3 directions, which produce in any experiment the brightest reflections, several other contributions (Table 2.3) have been detected : according to database, θ-Al_2O_3 or δ-Al_2O_3 meta-stable phases [448, 449].

To have a more precise representation of the evolution, SAEDs were also analyzed by a rotational average procedure, using the DiffTools script in DigitalMicrograph™ [452]: the two-dimensional SAED patterns are rotationally averaged about a chosen center, obtaining a one dimensional intensity profile, in reciprocal space, as shown in Fig. 2.8. The peaks corresponding to the different phases are thus better identified; these one dimensional profiles will be called SAED

Order of appearance	d-spacing	phases attributed	Temperature of appearance
1	1.438 ± 0.0053	γ [440]	400, 500, 600, 700, 800
2	2.034 ± 0.0028	γ [400]	400, 500, 600, 700, 800
3	2.884 ± 0.001	δ / θ [401]	500, 600, 700, 800
4	2.46 ± 0.0024	θ [111] /δ [312]	500, 600, 700, 800

Table 2.3: Phase appearance evolution at different temperatures.

diffraction patterns. Furthermore, the Fig. 2.8 is a valuable tool for visually demonstrating the impact of temperature on the nucleation of particles and the resulting phase transformations in the material induced by ion irradiation. Notably, the identification and classification of these distinct phases are detailed in the Table 2.3.

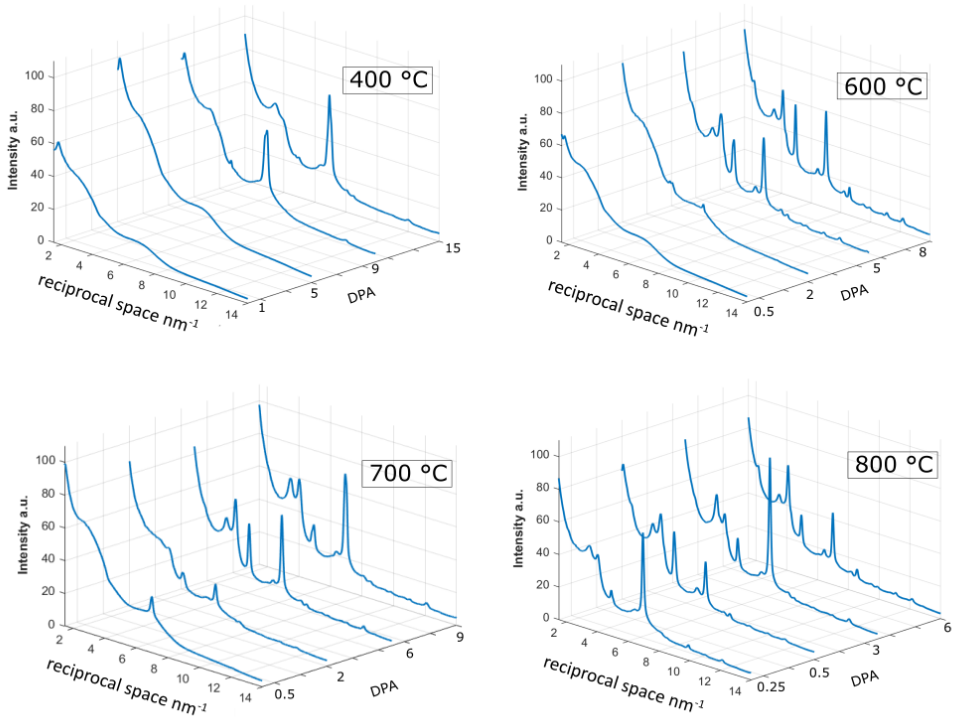

Figure 2.8: *Diffraction patterns* in reciprocal space, obtained from an intensity profile extraction from SAEDs. The appearance of different peaks highlights the phase evolution at different temperatures.

Another important feature always present in each analyzed SAED, is connected to the central bright halo, visible in Fig. 2.7. This contribution comes from the crystal lattice incoherence, highlighting that a complete crystallization did not occur in the system [453], also at high levels of dpa. When the intensity profile is extracted, the halo is converted into a small hump grafted between 5 and 8 nm^{-1}. When the crystallization starts, the first reflection produces a peak growing from this hump, and with the crystallization progress, the hump progressively diminishes. Moreover, as the crystallization continues, the intensity of the γ-[400] peak, is

gradually reduced, indicating that other phases (δ/θ) are growing in the system. Regarding the phase recognition beyond the primary reflections, reported in Table 2.3, several small other peaks are present, showing the complex structure present in the system Fig. 2.8. Considering the 600 °C case, the crystallization started with the γ polymorph nucleation, showing a high-intensity reflection linked to the γ [400] plane. Increasing the dose to the system, other peaks appear. Different behaviors can be noticed at different temperatures. At 500 °C (and 700 °C), the phase evolution is essentially the same as the one described for 600 °C, being only slightly retarded (or accelerated) due to the lower (or higher) temperature. At 400 °C, instead, only the first two reflections reported in Table 2.3 were present also at the highest dpa level reached (15 dpa), and if compared with other cases, the crystallization starting dose was highly shifted. Indeed, in this case, a value of 5.5 dpa was needed for the RIC onset.

The evolution was further dissimilar at 800 °C, since the lowest dose analyzed (0.25 dpa). Moreover, a very complex pattern of reflections was present. At 0.25 dpa (Figure 2.8), the diffraction intensity profile resembles the reflections that appeared at lower temperatures only at much higher values of dpa. The above considerations allow to perform a first distinction among three crystallization regimes: a high temperature one, which includes the 800 °C range, an intermediate temperature one, evident in the behaviors at 500, 600 and 700 °C, and a lower temperature one, visible at 400 °C.

As reported above, alumina has several phases with d-spacings very close to each other, hence a unique attribution to different phases is difficult. This problem was overcome thanks to the availability of an extensive set of XRD diffractograms, obtained in a previous study which investigated the thermal crystallization of alumina samples deposited by PLD. Exploiting Bragg's law in the form:

$$Q[nm^{-1}] = \frac{4\pi}{\lambda} \sin\left(\frac{2\theta}{2}\right) \tag{2.1}$$

where Q is the wavevector in the reciprocal space, λ is the working wavelength of the diffractometer and 2θ is the diffraction angle. Each XRD diffractogram was converted into the form of a one dimensional intensity profile in reciprocal space, i.e. the same form of the SAED patterns. After the conversion, being both the diffractograms (SAED and XRD) in the same form, a direct comparison can be done, as shown in Fig. 2.9. A perfect overlap is found between the peaks in the RIC and in the thermally induced one, allowing to achieve a more reliable identification of phases in the irradiated samples, confirming the results reported above.

The whole procedure described and summarized in Fig. 2.9, shows that the phase evolution of the radiation induced crystallization retraces exactly the same phase evolution induced by thermal crystallization. As discussed in [454] the PLD Al_2O_3 has the γ phase as the first appearing phase during the thermally induced crystallization, then passing through the δ/θ phases and reaching the only stable phase when temperature exceeds 1100 °C. The comparison between

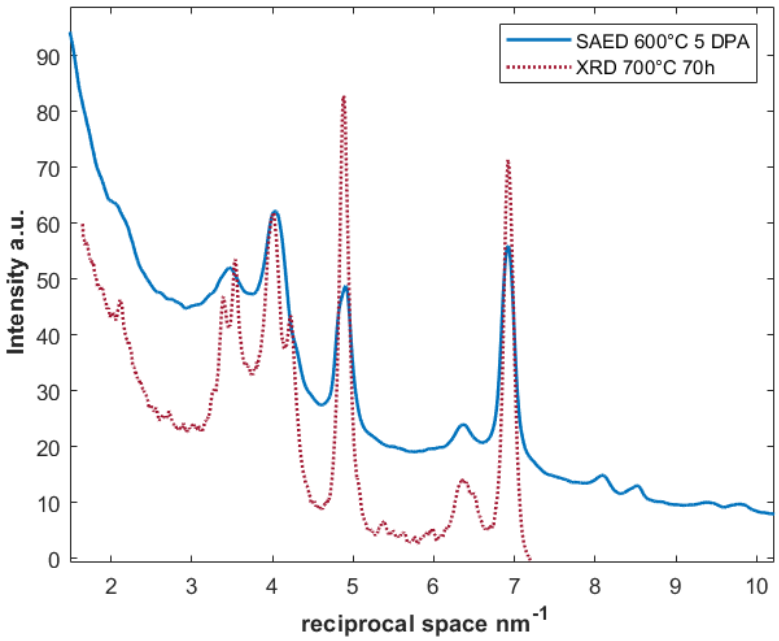

Figure 2.9: *SAED diffraction patterns* in reciprocal space, [600°C 5 dpa] and XRD pattern annealed sample [70h 700 °C] in reciprocal space compared.

Figure 2.9 and the evolution of thermal crystallization [454] confirms that irradiation has an accelerating effect in the crystallization process. Indeed the features observable for the case of thermal annealing at 700 °C for 70 h are the same that in the case of RIC are observable at 600°C after a radiation dose of 5 dpa. The similarity between the phase evolution of radiation-induced crystallization and thermally-induced crystallization at higher temperatures implies that thermal spikes, including both ballistic and electronic effects, may be more significant factors than displacement or atomic mobility in causing local temperature increases. This finding could have important implications for understanding the mechanisms behind crystallization and could potentially lead to new methods for controlling the crystalline structure of materials. Further research is needed to elucidate the role of thermal spikes in radiation-induced crystallization fully and to explore their potential applications in science for these amorphous materials.

Particle Growth kinetic

The average crystallite size evolution was studied, measuring it from DF (Fig.2.10) at the different fluences for the first appearing reflection in SAED . This is related to the [440] plane of the γ polymorph.

For each micrograph, from 15 to 130 particles were analyzed, and the area of each particle was measured through the open-source program ImageJ [455]. The variability in the number of particles analyzed depends on two factors: in low dose micrographs, few particles were present, while at high dpa values, due to the overlapping of different particles, only the discernible,

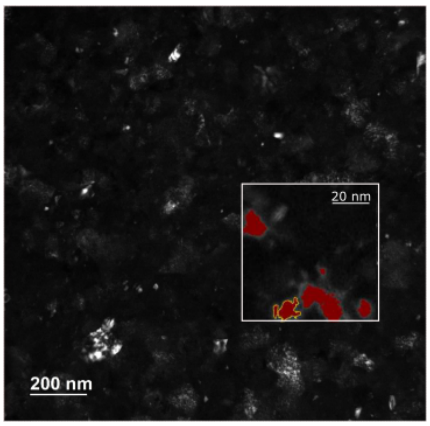

Figure 2.10: *Dark field picture* with a magnification of a specific region of the image where the crystallite selection process is highlighted

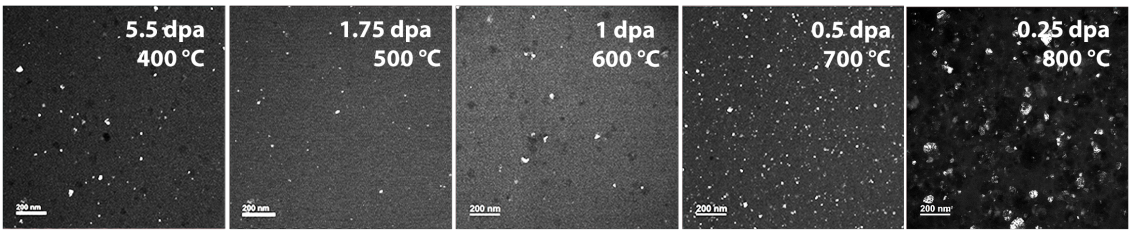

Figure 2.11: The DF images show the temperature's impact on nucleation. The number of particle nucleated increases when temperature is higher than crystallization temperature.

not-overlapped, single particles were analyzed.

The figure 2.11 summarizes the DF images, highlighting the initial dose at which radiation-induced nucleation occurred for each temperature analyzed. It is important to note the effect of temperature on the number and size of particles nucleated. At temperatures below the crystallization temperature of alumina (i.e., 600°C), a consistent and nearly uniform number of particles (typically ranging between 15-30 particles) is observed. Conversely, at higher temperatures, more particles are detected, even at the lowest dpa value analyzed. Remarkably, in the latter case, the number of recognizable particles consistently exceeded 100, and the size of particles at 800°C was observed to be even bigger than other temperatures.

Describing the effect of particle density with increasing doses is more complex. While at temperatures lower than the crystallization temperature, the nucleation of particles increases with the dose, as evident from Figure 2.11 for the specific case of 600°C. However, at 700°C and 800°C temperatures, it is difficult to determine whether the initially nucleated particles are growing solely or if there is concurrent nucleation occurs. This is due to the uniform crystallized region and the fact that images at progressively higher doses analyze different regions of the material and are, therefore, uncorrelated.

The average crystallite size was then plotted versus ion dose for the different irradiation temperatures (Figure 2.12). As discussed above, to compare the crystallite growth kinetics between different materials, the dpa is the most helpful parameter. Hence, although the data are plotted as a function of both dpa and fluence, the fitting procedure, discussed later, is done with dpa values.

It is worth underlining that each point is plotted with its corresponding Standard Error of the Mean (SEoM) as error bar. The SEoM is the standard deviation σ divided by the number of elements of the statistical population. It represents the precision of the value of the mean, rather than the dispersion of particle sizes. Indeed, as it can be easily understood, the standard deviation of the crystallite dimension grows as the dose increases, also because, at a high dose level, new crystallites nucleate while the older ones continue to grow.

The crystallization kinetic models for different classes of materials have been discussed in detail [456, 457, 458, 459]. In one of the first proposed models, Burke and Tumbull [457] deduced a parabolic relationship for the thermally induced grain growth kinetics:

$$D_g^2 - D_0^2 = kt \tag{2.2}$$

Where D_0 isd the initial grain size, k is the proportionality constant that depends on absolute temperature and activation energy, t is holding time at a steady temperature T. For the proportionality constant k of a temperature dependence of the Arrhenius type is proposed:

$$k = k_0 e^{-\frac{E_a}{RT}} \tag{2.3}$$

where E_a is the activation energy for grain growth, k_0 is the total pre-exponential constant and R is the gas constant. The relation of Equation 2.2 turns out to accurately describe the experimentally observed behaviors only in limited sets of cases. Mechanisms can be active, which slow down the kinetics of grain growth. In order to represent these cases, a generalization of Equation 2.2 has been proposed [460].

$$D_g^n - D_0^n = kt \tag{2.4}$$

where the exponent 2 is substituted by other values. Values of n between 2 and 5 have been reported for various metallic systems [461, 462, 463]. Grain growth kinetics have been extensively measured also in ceramics, and the data reveal a similar range of grain growth exponents [464, 465, 466, 467]. Most of the investigators tried to explain the exponents in terms of the parabolic grain-growth kinetics (n = 2) and of phenomena that can explain the deviation from this value. In the literature [457, 468], different n dependences from external stress, recrystallization path and grain shapes have been reported. In [469] the possible relationships between n and the

crystallization temperature and materials purity have been investigated, without finding general trends. It is worth mentioning that in Equations 2.3 and 2.4 both n and Ea are considered constant during the transformation process [470]. When the Grain growth process occurs under irradiation, a modified version of Equation 2.4 can be derived accordantly [471]. Grain size increases with the ion fluence (ϕ) (when the ion flux is constant, $\Phi = \phi$t) according to an analogous power law relation

$$D_g^n - D_0^n = k_{irr}\Phi = k_{irr}\phi t \tag{2.5}$$

where n and t have the same meaning of Equation 2.4, and k_{irr} is the kinetic constant for the irradiation induced process, which depends on the materials properties and the irradiation conditions. The equation (2.5) can be further modified in order to express the evolution as a function of the dpa value:

$$D_g^n - D_0^n = K \cdot dpa \tag{2.6}$$

For the k_{irr} and K kinetic constants, the same Arrhenius form of Equation(2.3) is assumed. Kaoumi et al. [472] could analytically extrapolate the Equation (2.5) with an exponent equal to 3 using the concepts of radiation-enhanced diffusion, rate theory, and the thermal spike hypothesis. Kaoumi et al. [472] developed this grain growth model under ion irradiation based on the impact of thermal spikes induced by irradiation on the grain boundaries. In these conditions, grain growth occurs thanks to the enhanced radiation diffusion and the local driving force of the grain boundary curvature. The same model can also explain the grain growth in the so-called thermally assisted regime. Furthermore, by analyzing the self-diffusion constant under atomic displacement environments, a different paper [473] elucidates how the growth of grains accelerates as a result of the combined impacts of temperature and radiation.

Before proceeding with the further presentation of the result, it is essential to address a specific point. This study focuses on the nucleation and subsequent growth of crystallite particles. So far, a general equation for irradiation induced particle growth in an amorphous material, does not exist. The equations 2.5 and 2.6 presented above were derived based on crystalline materials and considering the diffusion rate of atoms and defects that lead to their interactions with the existing grain boundaries. Therefore these equations cannot be considered valid to describe the growth of crystallite particles nucleated in an amorphous material.

Considering the fact that in a crystalline material, the grain growth is well described by a sublinear correlation with the fluence and, hence of dpa; and given the clear evidence of an incubation dose prior particle nucleation (at temperatures lower than the crystallization temperature), a semi-empirical model is formulated to characterize the crystallite growth:

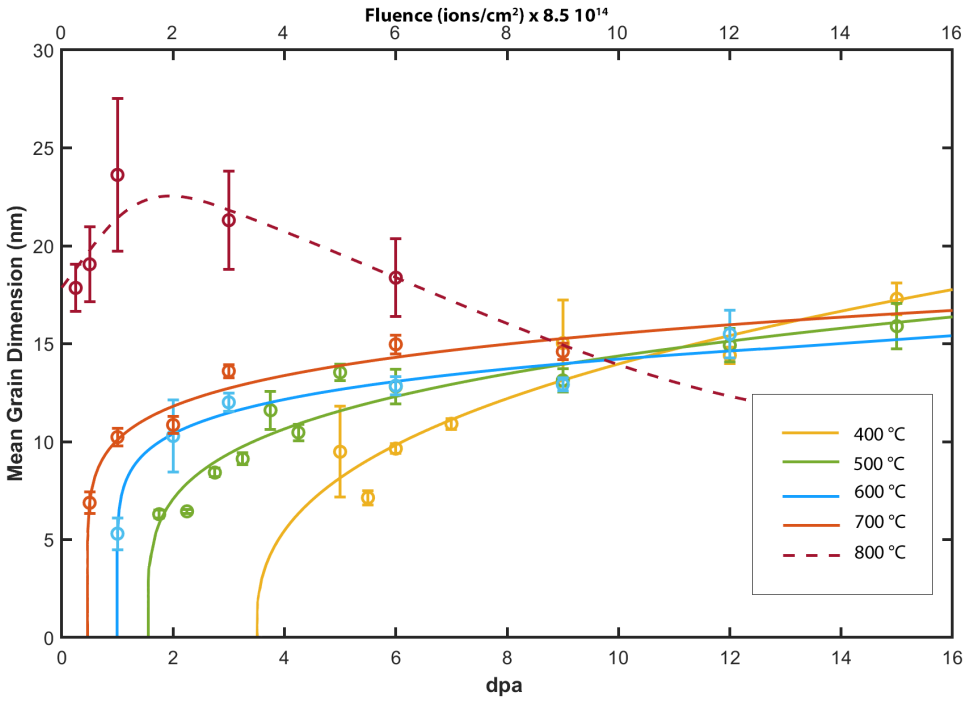

Figure 2.12: Mean crystallite dimension evolution for each temperature. The model fitted using equation 2.7 is here represented by the solid lines. The 800°C case can not be represented by the model discussed (dotted line). The data relates the 700 keV Kr^{2+} ions in the 100 nm Al_2O_3 film.

$$D_g^n = k_a \cdot (dpa - dpa_0) \tag{2.7}$$

Regarding the previous Equation 2.6, in this case, the initial grain dimension D_0 has been assigned a value of zero since the material is initially amorphous and lacks crystals. K_a denotes the updated kinetic constant for the amorphous material, and the same Arrhenius form of Equation(2.3) is assumed. While dpa_0 is the incubation dose required before the onset of radiation-induced crystallization.

In Figure (2.12), the average nucleated particle sizes are plotted vs. the dpa values, for each irradiation temperature. A fitting procedure, performed by a Matlab script, allows to determine k_a, n and dpa_0. The parameter dpa_0 has been established as a fitting parameter since the dpa values at which the first picture of the crystallized material was captured represents a progressed stage, and may not necessarily correspond to the dpa_0 value at which nucleation begins. Then by the Arrhenius equation (Equation 2.3) the activation energies and the k_0 prefactors are obtained.

A clear dependence of the phases transformation on temperature is present, and several considerations can be made by direct observation. First, the temperature strongly determines the

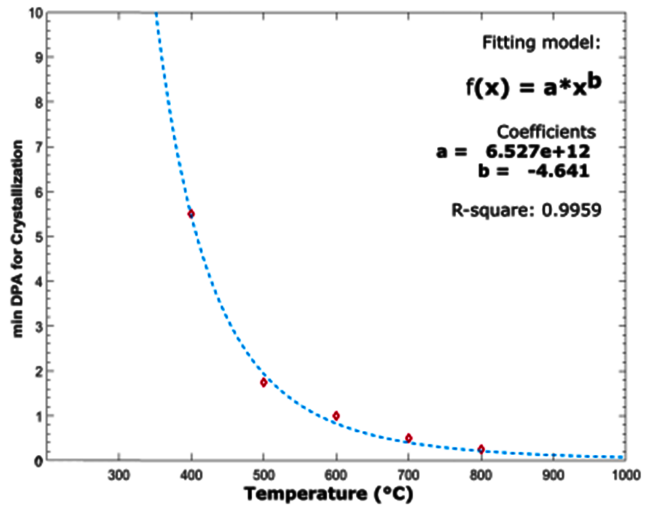

Figure 2.13: Dose at which RIC is experimentally observed, for various temperatures. The trend is well described by a power law [R-square = 0.99]

dose level at which RIC begin. For example, while at 400 °C the first hint of crystallization is visible at about 5.5 dpa, at 600 °C a similar hint is visible at 1 dpa, and, at 800 °C, at 0.25 dpa a substantial crystallization is already present.

The relation between the dpa for the onset crystallization and temperature is shown in Fig. 2.13 The relationship between these two parameters is well described by a power law with a negative exponent larger than 4. Due to this exponent, the extrapolation of this trend towards lower temperatures would suggest that at room temperature a practically infinite dose is required to induce crystallization. This is consistent with the recent observation of no crystallization hints even at 25 dpa at room temperature [180], and supports the indication of amorphous Alumina should be 'radiation tolerant coating'.

The other parameters (n and dpa_0) of the crystallite growth semi-empirical model in Equation 2.7, obtained by fitting the experimental data, are presented in the Table 2.4 and further discussed later.

As mentioned previously, the ion induced particle growth kinetics was obtained from the analysis of the DF images at different fluences. A systematic analysis, in terms of the average crystallite size evolution, is presented here for the reflection due to the [440] plane of the γ polymorph. The experimental data and the curves obtained, at each temperature, by a best fit procedure for the behavior of Equation 2.7 are reported in Figure 2.12. The distinction, already emerging in the discussion of the SAED results, between the behaviors at higher (800 °C), lower (400 °C) and intermediate temperatures is confirmed.

A specific consideration has to be done for the 800 °C case in which a decreasing trend in the mean particle dimension appears at 1 dpa after a steep initial growth. Indeed, while all the

Temperature (°C)	n	dpa_0
400	3.7	3.9
500	4.9	1.63
600	6.2	0.98
700	6.8	0.45

Table 2.4: Crystallite growth model parameters extracted from the fitting of the experimental points.

other curves represent the best fit of Equation 2.7, the behavior at 800 °C cannot be described by the particle growth kinetic of Equation 2.7, and is therefore plotted as a dotted line in Figure 2.12. A physical explanation of the observed decreasing trend can be proposed remembering that the data of Fig. 2.12 come from the reflection due to the [440] plane of the γ polymorph. While this is the only, or at least the dominant, one at lower and intermediate temperatures, at 800 °C it is probably the first one to nucleate and grow, but other phases also nucleate, and eventually grow also consuming the γ crystallites. Considering now only the temperatures for which the growth kinetic model is valid, it can be noticed how, at least for low dose levels, there is a satisfactory correspondence with experimental points, confirming the validity of the chosen model. At higher dpa levels, the lines begin to tangle one with the other, even though all the curves converge towards an approximate value of 15-20 nm. The kinetic growth law, previously reported, can describe the growth of a single phase in the absence of other competing phases. This could explain why each fitting curve is well shaped describing the experimental points in the first part of the RIC at low radiation levels. While they lose the describing capability at higher levels of dose.

Wishing to proceed the dicussion, although a general model to describe the temperature dependence of n does not exist, as discussed previously, a linear dependence of these two quantities as shown in Fig. (2.14). It should be noted that the parameter n describes the particle growth speed, hence a strong temperature dependence was expected. Indeed, considering the typical relationships describing crystallization, a clear inverse dependence between temperature and crystallization time exists [474].

Furthermore, the kinetic constant K has a clear Arrhenius-type dependence on temperature (Figure 2.15). This allowed the calculation of the activation energy for the crystallization process. The γ [440] reflection's activation energy obtained is E_a = 147.2 kJ/mol (1.5 eV/particle). Interestingly, the value obtained is close to the values reported in the literature for crystallization activation energies in other glassy ceramic materials [475, 476, 477]. The values represent the activation energies for elementary steps in the phase evolution mechanism of the system. In literature, this energy is usually called apparent activation energy because it is the value that can be found experimentally but that does not represent the real difference between the initial and final state [478, 479]. A more rigorous approach should be used if the Gibbs free energies should be found. This approach is inapplicable in this case, because thermodynamic parameters

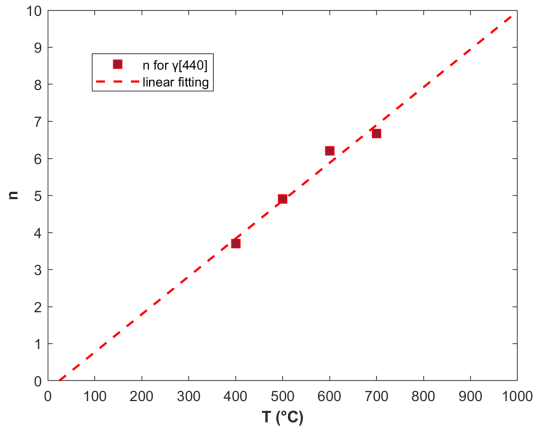

Figure 2.14: Linear fitting for n

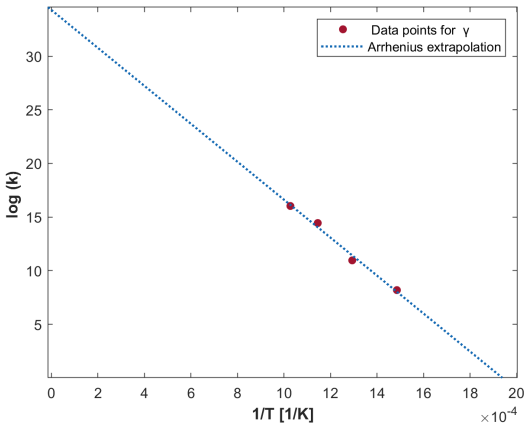

Figure 2.15: Arrhenius plots for the reflection analyzed.

such as the formation enthalpy of each step in the process [480] are unknown.

2.2.3. Particle Distribution

Despite a lack of physical basis, a log-normal function has widely been used to describe experimentally-observed size distributions in many studies [481] [482] [483] [484] [485]; although, the general applicability of this distribution to crystallite growth is not universally accepted, as pointed out by Atkinson [486]. However, also in this study the log-normal distribution is adopted, due to its similarity to the measured distributions of particle, particularly when the number of particles is high.

The evolutions of particle distribution for different doses at 700°C is reported in Fig. 2.16

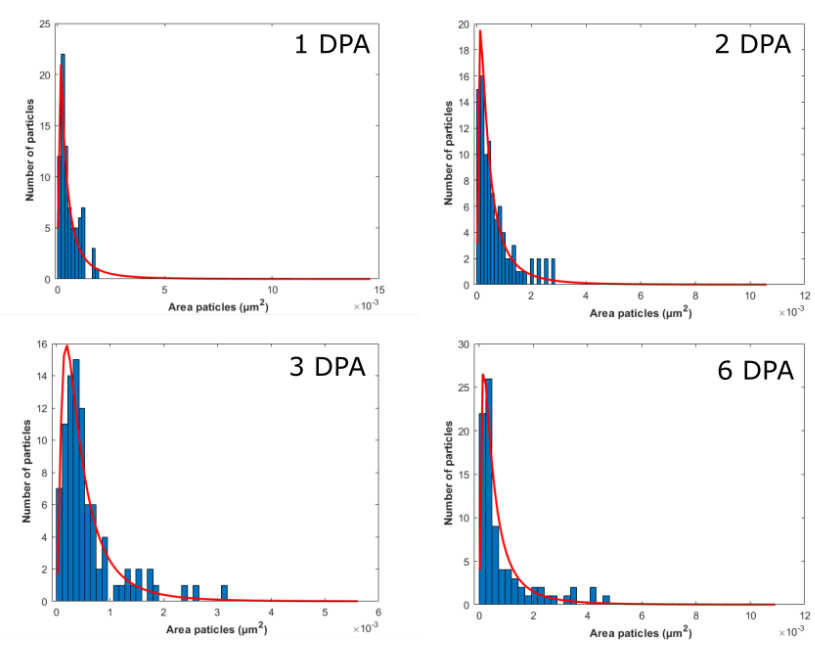

Figure 2.16: Histograms evolution of particle distribution for the 700 °C case. All different radiation dose can be represented by a lognormal distribution. highlighted by the red line.

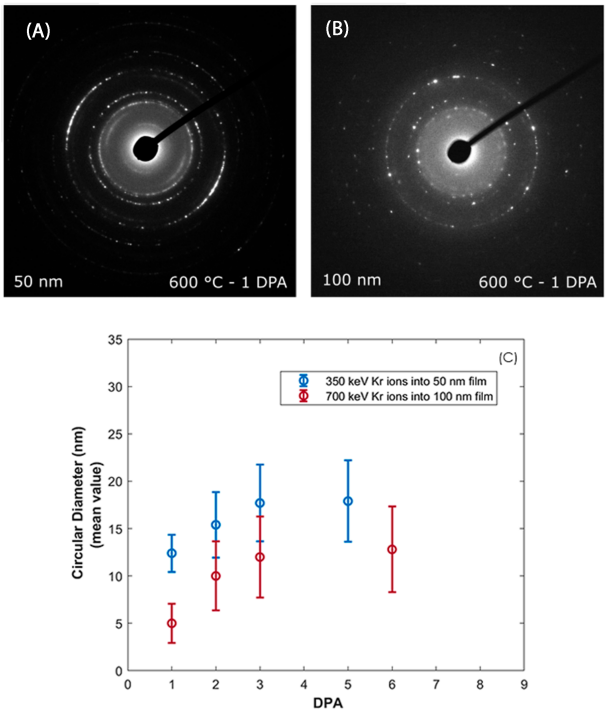

Figure 2.17: SAED patterns for films with 50 nm thickness (A) and 100 nm (B). crystallite growth evolution for the two different thicknesses (C).

2.2.4. Film Thickness and Ion Energy Effects on Crystallite Kinetic.

As previously discussed, a thickness of 100 nm was employed as the benchmark for these investigations. However, a series of additional experiments were designed to investigate the influence of thickness on the RIC by testing a 50 nm film at 600 °C. As per the results from the SRIM simulations, ENSP ratio was slightly lower for the 350 KeV Kr case than for the 700 keV Kr ion case. Instead, no difference on the resultant defects production when an energy of 350 keV was selected for the Kr ions was observed. Notably, the 350 kEV energy prevented ion implantation in the 50 nm coating.

The identical signals detected in the diffraction patterns and the same phases recorded in the Table 2.3 confirm the formation of γ-Al_2O_3 as the initial nucleation phase. This result aligns with the expectations, given both experiments were designed with the same dpa level and almost the same ENSP ratio. A few other important considerations can be made starting from the diffraction patterns in Figure 2.17 , where the film thickness's effect is shown. Figure 2.17 (A) is related to the 50 nm thin film, while Figure 2.17 (B) is of the 100 nm one. In Figure 2.17(B), the crystallite size is larger than in Figure 2.17 (A), as the rings are made up of discrete spots. Indeed, a finer crystallite size usually produces a more continuous ring pattern, while larger crystallite size gives a more speckled pattern, as discussed in [487]. It is possible to conclude that the crystallite growth process is probably more affected by surfaces in the 50 nm thick films than in the 100 nm one, producing arcs in SAED instead of rings made of discrete spots. A similar fragmentation is also reported in [453], where the incompleteness of the diffraction rings was correlated to the growing crystals' anisotropy due to the surface effect. A second important feature is connected to the central halo. This contribution comes from the crystal lattice incoherence, highlighting that a complete crystallization did not occur in the system [453]. Both these features, ring pattern and halo, were present in all measures in which crystallization had occurred, also at the highest levels of dose reached for each value of temperature, meaning that a complete ordering process had not occurred in the system in any case. Although the high associated error of each individual point, combined with a low statistical data strength, makes it difficult to draw any definitive conclusions about the effect of ion energy on the final crystallites' kinetic, the Figure 2.17 (C) suggests that the mean crystallite size for 700 keV Kr may be smaller than that for 350 keV Kr. To speculate on the factors that could produce this effect, the role of the ENSP ratio may be considered.

As mentioned in the introduction, Thomè et al., [263, 268, 269] reported how an ENSP ratio higher than one could lower defects balance. Assuming that this hypothesis also applies to PLD amorphous alumina, it is reasonable to suggest that because for the 700 keV Kr case where the electronic energy loss are more significant than the nuclear energy losses, this could result in a final defects healing effect. This could explain the smaller crystallite size. It should be stressed again that the results obtained can not confirm this hypothesis. Unfortunately, there has been a lack of research conducted on amorphous alumina to assess the effects mentioned above. Therefore, this observation should be considered a preliminary phenomenon to be further

investigated.

2.2.5. Bright Field Images analysis: Amorphous Fraction Evolution

Since the outstanding properties of PLD alumina can be related to its peculiar amorphous/nanocrystalline microstructure, understanding how the amorphous fraction (AF) in the system evolves through the RIC is fundamental. For this reason, a procedure has been developed in order to obtain qualitative trends in AF at different temperatures. BF images were used to achieve this goal.

In BF images the amorphous region turns out to be brighter. Therefore, an average value of brightness is evaluated for the AF, then the appreciably darker parts are attributed to the crystalline component area fraction, and the AF is calculated from each image. It should be pointed out that some criticalities are present in this procedure. In order to reduce them, for each value of dose, BF images are taken from three different angles in random areas. However, the outcome should be considered only a first order analysis.

Indeed in BF, the crystalline part far from the Bragg condition has a low diffraction contrast, and it would have similar brightness as the amorphous part. Moreover, as the dose increases and the amorphous fraction decreases, it becomes more challenging to determine the standard brightness for the amorphous part, and errors can occur in opposite directions. Either the brightest crystallite could be counted as amorphous, or the lower brightness amorphous parts counted as bright crystallite. For this reason, for each dose three BF images are taken from different orientations, and the results are averaged. Upon comparing the results obtained from various tilt measurements, it was observed that the standard deviation between the acquired values was approximately 10%. However, it is noteworthy that the observed standard deviation does not necessarily represent all the possible sources of measurement error. Whilst this procedure is to be perfected in order to be considered fully quantitative, yet it gives a coherent trend of the evolution of the amorphous fraction with dpa and temperature.

Another uncertainty comes from the fact that the nucleated particles are smaller than the film thickness, and the measured value of the crystalline transverse area fraction, from particle projection in BFs is larger than the actual volume fraction. For this reason, the particles projected area, measured in BFs, should have been converted in particle volume before making any evaluation of AF. Several statistical and experimental procedures to perform this conversion have been discussed [488] [489]. However, due to the difficulties in their implementation and to the uncertainties which unavoidably affect the results, they have not been adopted because they could not introduce essential improvements. In the light of the limitations highlighted above, the presented values of the fraction should be considered as affected by a limited accuracy. However, since they are all obtained by the same procedure, their differences, and therefore the resulting trends, should be more reliable than the absolute values. As a matter of fact, these fractions turn out to show meaningful trends.

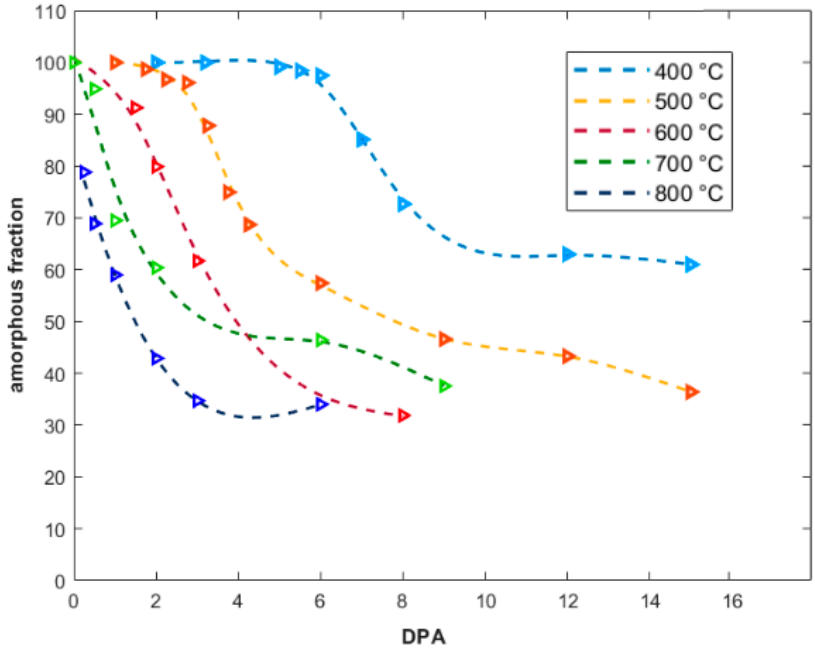

Figure 2.18: The amorphous fractions at different temperatures. The dashed lines, obtained by smoothing spline fitting are just a guide to the eye.

The amorphous fraction evolutions at different temperatures are reported in Fig. 2.18. The trends suggest the existence of an incubation dose, which decreases at increasing temperatures. Moreover, at higher temperature crystallization occurs at lower doses and causes a more pronounced decrease of the amorphous fraction. Nevertheless, it seems that a residual amorphous fraction is always present even at the highest doses and temperatures. However, the latter result shall be considered affected by a more severe uncertainty since, the identification of the amorphous fraction becomes increasingly difficult the lower it is. It is anyhow consistent with the observation of the central halo in the SAED images.

2.2.6. Physical mechanisms of irradiation induced nucleation and particle growth

At this point, the mechanisms governing crystallite nucleation and subsequent particle growth observed can be speculated.

As briefly discussed in the introduction, the phase change phenomenon induced by electron or ion irradiation between amorphous and crystalline states has long been a complex, puzzling problem [271]. One of the most straightforward models used to explain the observed nucleation process in an amorphous system is the “thermal spike” model [271]. According to this model, a highly localized energy deposition region, the thermal spike, is created when an ion passes through the amorphous material. In this region, structural changes, chemical reactions, and the formation of nanoscale features could occur [271]. Recent molecular dynamics simulations

suggest that thermal spikes could effectively be explained starting from the collision cascades produced by the ion passage. First, during each ion passage, many target's atoms are dislodged from their lattice sites. Then, the subsequent thermal spike phase comes, in which the cascade region attains thermal equilibrium with its surrounding [272]. Moreover, the deposited energy to the electrons by slowing down the incident ions, as part of an inelastic collision, could be essential in the thermal spike creation. Indeed, the released energy diffuses within the electron subsystem by electron-electron interactions before being transferred and finally localized in the lattice system via the electron-phonon coupling [273]. This second energy transfer mode could become even more important for the irradiation process analyzed in this study, because the ENSP ratio is close to 1.0 over the film thickness (Fig. 2.5) for the case of 700 keV Kr ions.

The energy deposited could ultimately lead to atomic motion and the creation of cylindrical damage along the ion path [271]. Moreover, during the thermal spike, the atoms inside the displacement cascade may reach a partially melted state (cascade melting)[272]. The combined electronic and ballistic thermal spikes associated with each ion trajectory are often used to describe and model the observed ion irradiation grain growth in ceramic policrystalline oxides [273] and carbides and may even be used for describing the nanocrystals nucleation in amorphous materials.

Koroni et al explained the radiation induced nucleation in amorphous material through a theoretical investigation in their paper [271]. They described the irradiation induced nucleation as a process of disordered state progressing from ordered configurations toward crystalline states by irradiation-assisted atomic rearrangement. The underlying assumption is that atomic ordering may occur as the free energy reduction of the irradiated amorphous region declines. Whether the ordered atomic configurations evolve into crystal nuclei depends on whether the crystal nuclei are more stable than the disordered situation.

Therefore, creating the thermal spike region can account for the induced nucleation observed in the alumina thin film. After the nucleation of particles occurs, the growth of the crystallites can benefit from the radiation-enhanced diffusivity. Moreover, the differences in the exponents n found and reported in Table 2.4 of the Equation (2.7), compared to those found in the literature, may be attributed to the different initial matrices (polycrystalline or amorphous).

It is also worth stressing that the similarities in the phase evolution of radiation induced crystallization and thermally induced crystallization at high temperatures (Figure 2.9) may further confirm the validity of this thermal spike model.

The findings of this study are particularly intriguing with regards to the activation energy, as the conversion of 147.2 kJ/mol to 1.5 eV/particle are similar to the reported values for point defect migration energies in Al_2O_3 for both the Al-vacancy (1.8-2.1 eV/particle) and O-vacancy (1.8-2 eV/particle) [490]. This suggests a potential correlation between point defect migration and the growth of crystallite particles.

Considering that the amorphous alumina coatings initiate the crystallization process at 600°C,

and subsequently achieve complete crystallization at higher temperatures as delineated above, a zero-order approximation permits the assumption that the melting temperature of alumina coatings produced via Pulsed Laser Deposition may be equivalent to the melting temperature of conventional alumina ($T_m \approx 2000°C$ [491]). Moreover, taking into account the discussion in Kaoumi [472] regarding crystalline material, it can be inferred that the particle growth process occurs in a thermally-assisted regime (irradiation temperature above 0.15-020 T_m) where grain growth is enhanced with increasing temperature. This is precisely what was observed in this study.

All the evidence indicates that the observed processes occur in a regime where radiation can induce initial nucleation, followed by a combination of radiation-enhanced diffusion and temperature-assisted processes that facilitate further particle growth. These combined effects result in crystallization at a temperature lower than typically observed ($T < 600°C$).

2.2.7. Exploring the Potential of Alumina Coatings: Strategies for Enhancing Radiation Resistance

Radiation-resistant materials, capable of maintaining their inherent properties under high-energy radiation, are integral to various applications, from nuclear reactors to satellite casting and solar cells. The resistance these materials exhibit to radiation is predominantly a factor of their lattice structure, defect loss, magnetic conductivity, temperature, and displacement damage dose. The importance of radiation-resistant materials is well recognized and discussed in this work, specifically in developing resilient coatings for use under the strenuous LFR conditions.

Several strategies have been employed to improve the radiation resistance of materials, including selecting or modifying materials based on their inherent resistance, utilizing composite materials, and designing microstructures for optimal resistance [492, 493, 494]. Moreover, surfaces, grain boundaries, and interphase boundaries are recognized as sinks for radiation-induced point defects and traps for implanted species [248, 492]. In the case of PLD alumina, it is unfeasible to increase the density of grain boundaries due to its amorphous structure. However, strategies to maintain the amorphous nature of a material, particularly alumina, under radiation are not well-understood in literature.

PLD Alumina has displayed compelling properties as a radiation-resistant material, demonstrating exceptional incubation doses before any radiation effects appear - a characteristic that further increases as temperatures decrease. However, the key challenge lies in adapting these properties to the demanding environments of LFRs.

Despite the inherent complexity of its structural evolution, bulk alumina continues to captivate significant technological interest. This is largely due to its abundant potential, which has been the focus of various studies. Numerous research endeavors have been centered on stabilizing the amorphous matrix of alumina or certain metastable phases, such as γ-Al_2O_3. Conversely, other studies have aimed at expediting the crystallization process [495, 496, 497, 498, 499].

Given that the thermal spike model has demonstrated its proficiency in representing the RIC in PLD Al_2O_3, it's becoming abundantly clear that RIC is indeed a thermally activated effect. Consequently, it's feasible to draw analogies from the mechanisms witnessed in alumina, stabilized against phase transition under elevated temperatures. Such insights potentially offer avenues to enhance mastery over the RIC process.

Many elements have been evaluated for their potential to stabilize alumina. Several papers studied how using compounds such as alkaline and alkaline earth metals, lightweight metalloids, and heavy transition metals can induce distortion in the oxide lattice, postponing the transition from an amorphous to a crystalline structure or the evolution among different crystalline phases [497, 498, 499]. Specifically, for the PLD Al_2O_3 case, the doping effect of Y_2O_3, as substantiated in [454], has been found to shift the crystallization onset temperature by approximately 150 °C. The underlying assumptions behind this effect suggest that Yttria doping could either instigate a process of disorder within the alumina structure or stabilize the first appearing phase that nucleates (γ-Al_2O_3).

Given the compelling evidence reported, a comprehensive study utilizing at the IVEM facility was instigated. The study's objective was to pinpoint parameters (such as the Yttria doping) that could be adjusted to ensure the amorphous microstructure of a material is preserved for as long as feasible when subjected to high temperatures and radiation fields. Coatings were produced utilizing the aforementioned floating technique, with attention directed towards individual parameters pertinent to the study. The fabricated coatings exhibited a thickness of 100 nm, and the irradiation parameters were consistently maintained, adhering to the parameters reported earlier (700 keV Kr ions). These steadfast protocols ensure a reliable basis for comparison and evaluation, further enhancing the credibility of the ensuing results. As an initial analytical step, SAED patterns were collected and converted into diffraction patterns in reciprocal space through the rotational average procedure. This procedure offered a primary instrument for the assessment of diverse effects.

Three essential parameters were chosen for this study: Pulsed laser frequency, plasma plume shadow removal, and Yttria doping effect.

Pulsed Laser Frequency Effect on Radiation Induced Crystallization

The first parameter investigated was the pulsed laser frequency used during deposition. As detailed in Section 1.3, it has been demonstrated that frequency can influence the refractive index and, consequently, the density of the final coating. There is a paucity of literature examining how the density of amorphous material can affect its radiation response, making it an intriguing parameter for investigation. Additionally, given that utilizing a frequency of 50 Hz expedites the deposition process, it is emerging as the favored method for coating larger surfaces. This underlines the importance of investigating the effects of this parameter.

The findings from this preliminary investigation, as depicted in Figure 2.19, reveal that the

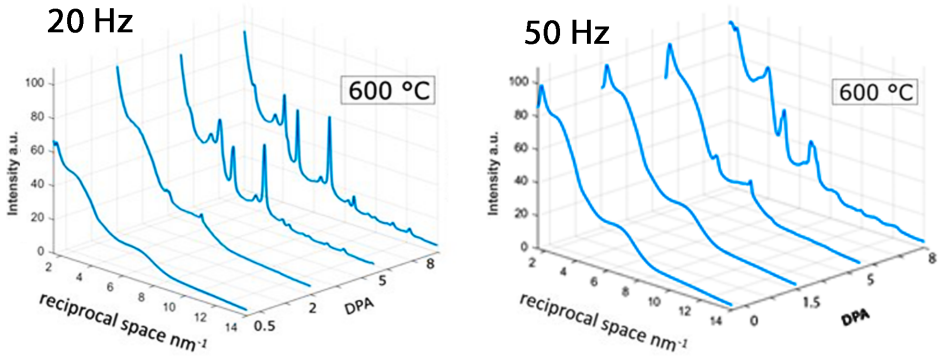

Figure 2.19: Comparison of diffraction patterns in reciprocal space for alumina coatings produced under different pulsed laser frequencies. The material created with a higher laser frequency (50Hz) showcases superior radiation resistance, evidenced by diffraction pattern peaks with lower intensity and less pronounced, indicative of a less well-formed crystalline structure.

material produced with a higher laser frequency (50Hz) exhibits superior radiation resistance compared to other conditions. This is evident upon examining the diffraction patterns at 5 dpa and 8 dpa. The 50 Hz pattern displays lower intensity and less pronounced peaks, suggesting a less well-formed crystalline structure than the other case.

Although the varying final density of the materials is noteworthy, discerning whether the material harbors short-order differences due to deposition process variations is challenging. Therefore, despite the intriguing nature of these findings, providing a tangible physical explanation for this behavior remains a complex task at this stage of the work, since no consistent modification are found also in the SRIM irradiation simulations obtained for the two different densities.

Plasma Plume Shadow Removal Effect on Radiation Induced Crystallization

Pulsed Laser Deposition presents many advantages, but the films it produces often suffer from subpar surface morphology, a consequence of laser droplets, particulates, and various inconsistencies. Efforts to counter these surface imperfections or diminish particulate counts have led to an examination of several adaptations of traditional PLD [346, 500]. These droplets, result from hydrodynamic instabilities at the target surface, target superheating, and the ejection of liquid phase driven by vapor and plasma pressure. These droplets migrate within the ablation plume and end up deposited on the substrate surface, obstructing the ideal growth of the coating.

Various methods to confront these challenges encompass the adjustment of the laser wavelength fluence , target damage , and deposition angle. Implementations of 'laser-induced plume heating', 'off-axis laser deposition' , 'synchronous velocity filter', and 'shadow mask' have been explored [500, 501, 502, 503, 504, 505, 506, 507, 508, 509] .

The shadowing mask method's central principle involves strategically placing a mask between the PLD target and the substrate holder. This arrangement is designed to filter the dispersion

of the ablation plume. In this method, as the ablation plume expands, the mask acts as a barrier that intercepts the peripheral components of the plume, which typically carry less energy. This filtering process refines the ablation plume, allowing only the most energetic parts and potentially in a complete plasma state to interact with the substrates. As a result, the shadowing method improves the overall quality of the coating morphology [500, 508, 509].

This part of the research falls on employing the shadow mask method, first proposed by Kinoshita et al. It was successfully applied by Kinoshita et al. on $YBa_2Cu_3O_3$ (YBCO) thin films, resulting in nearly droplet-free surfaces. The method's effectiveness is further confirmed by reports of droplet-free $SrTiO_3$ films [500, 508, 509].

In this instance as well, the concept of evaluating this deposition method under RIC is intrinsically tied to the evolving trend of the mask usage becoming a standard in deposition methodologies. This shift is due to the significant enhancements the mask brings to the process, demonstrating its growing importance and relevance in the field. Moreover, in recent scholarly developments [392], Boris Paladino leveraged this method in his doctoral research to enhance the surface quality of alumina films produced by PLD, addressing the enduring challenge of surface droplets. Paladino proposed that these droplets transition from a liquid phase to a final amorphous state during deposition, implying the potential for a more structured micro-architecture in the resultant droplet material. This hypothesis provides an explanatory framework for the distinct RIC observed between materials generated with and without the mask, as depicted in Figure 2.20.

Notably, the material deposited with the mask exhibits enhanced radiation resistance. This material shows no signs of crystallization, even at the highest examined damage level of 15 dpa at the temperature of 400°C. This observation deviates from prior studies where materials exhibited crystallization at similar doses. The increased radiation resistance is further substantiated by the less pronounced diffraction pattern at 600°C when the material deposited with the mask is compared to its counterpart without the mask.

It is postulated here that droplets could serve as opportune crystallization centers due to their potentially more structurally ordered configuration relative to their surrounding material. Under high temperature or radiation conditions, these droplets might crystallize ahead of other constituents, potentially acting as nuclei for heterogeneous nucleation and thereby accelerating the system's crystallization process. This proposition offers an outlook on crystallization dynamics, inspiring further research and discourse.

Given the novelty of this research, the absence of supporting literature for the hypotheses set forth presents a challenge for their verification. However, the potential ramifications of this study are substantial, shedding new light on techniques to improve the surface quality and radiation resistance of PLD films. Further investigation is necessary to consolidate and broaden our understanding of these preliminary findings. As a pioneering endeavor, this research sets the groundwork for future studies, demonstrating the potential to effectively control surface

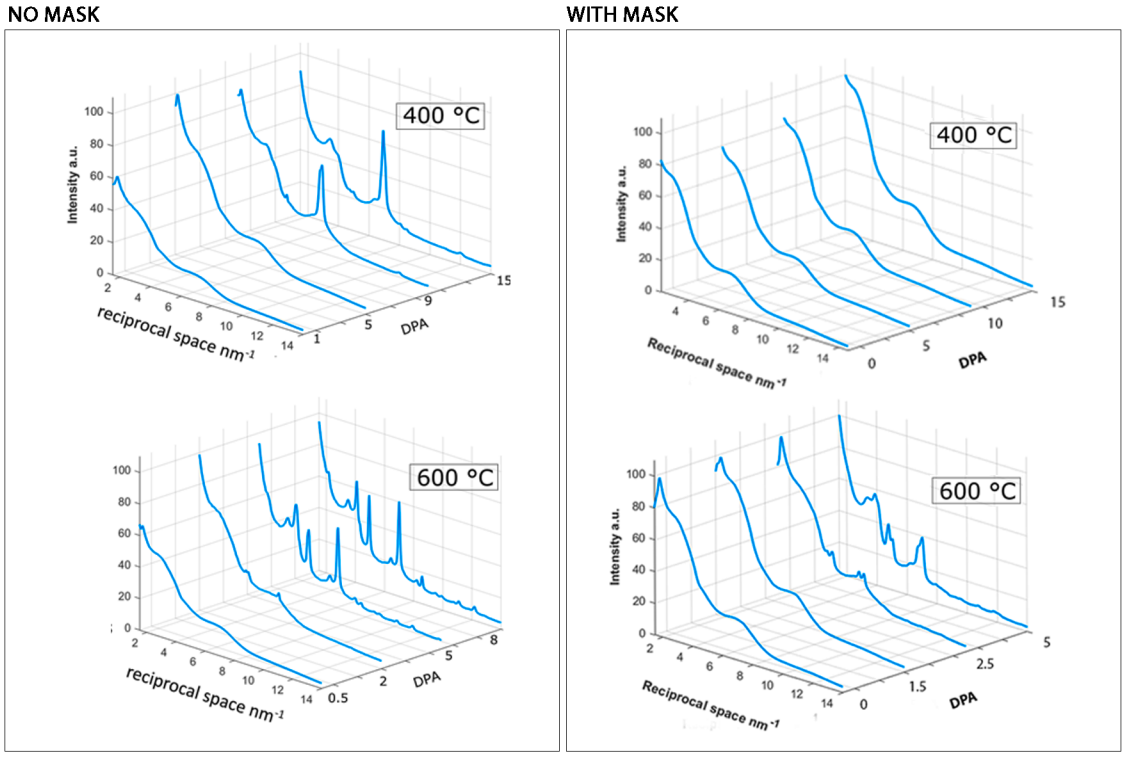

Figure 2.20: Comparative analysis of radiation-induced crystallization in alumina films produced via Pulsed Laser Deposition, with and without the utilization of the mask shadowing method at 400°C and 600°C.

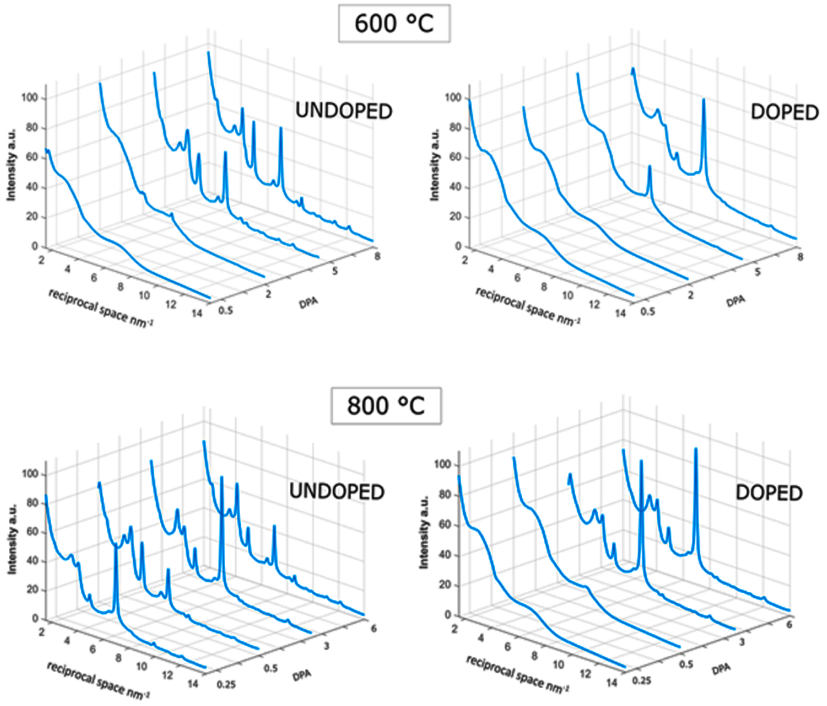

Figure 2.21: Comparative analysis of radiation-induced crystallization in alumina and doped alumina films produced via Pulsed Laser Deposition at 600°C and 800°C.

morphology in PLD, with possible wide-reaching effects on various technological applications.

Investigating the Impact of Yttria Doping on Radiation-Induced Crystallization in Alumina

Incorporating insights from Vanazzi's research [454], it has been demonstrated that Yttria (Y_2O_3) may exhibit a slowing effect on the crystallization of alumina. As a result, the study of RIC in yttria-doped alumina was extended, adopting the same doping level as specified by Vanazzi [454]. Coatings of 100 nm thickness, comprising 3% yttria-doped alumina, were fabricated for a deeper analysis of these multifaceted phenomena.

Since the only known study examining the effects of irradiation on doped Al_2O_3 is by Yu et al. [510], who found a general reduction in the crystallization rate for iron-doped samples in their comparison of pure alumina under Ar irradiation, a new campain at IVEM was settled to study in situ the RIC. In order to establish the initial parameters for an in-depth kinetic study, three separate temperatures ranging from 600 to 800 degrees Celsius were meticulously examined. This investigative approach is a natural progression from the foundational studies previously undertaken, adhering to the methodologies delineated earlier. The rationale behind selecting this specific temperature range was to provide an enriched understanding of the underlying kinetics, thereby building a robust framework for further scientific exploration. Applying the same method of diffraction pattern extrapolation as previously discussed, the influence of doping

on the radiation resistance of the material was clarified. As illustrated in the Figure 2.21, it became apparent that the doped material tends to crystallize at higher damage levels.

In light of the initial findings, coupled with the time constraints at the IVEM facilities, a strategic decision was made to prioritize the examination of the doping effect on RIC control, thus deferring a potential kinetic study on the other two effects. The exceptional ability of Yttria doping to inhibit crystallization in alumina, especially at temperatures exceeding the typical onset crystallization temperature of alumina (600°C), underscores the value of investigating the consequences of doping. Despite the emphasis placed on this particular facet of the study, other areas of the research also provided promising results. This suggests a landscape rich in potential strategies for effective process control, ripe for exploration and subsequent discovery in future studies.

The conclusions from the current study are presented in a cohesive summary. The initial observation suggested a slower radiation-induced crystallization in doped materials. This was ascertained by examining the kinetics of the process, depicted in Figure 2.22, and calculated by assessing the grain size via dark field images. This deceleration implies that greater radiation damage doses are needed to stimulate crystallization.

Furthermore, upon analysis, it was observed that the mean grain size within the yttria-doped alumina was consistently smaller compared to that in pure alumina at similar dpa levels. This observation is depicted in Figure 2.22, which shows particle growth measurements for each dpa analyzed, along with the fitted equations for each condition, effectively comparing the doped and undoped cases for each temperature studied. The crystallization rate at all the temperatures studied in doped materials can be properly represented by the previously discussed Equation 2.7. Of notable importance is the inhibitory effect of yttria on the nucleated particle growth process, specifically at temperatures of 800°C. Prior to the inclusion of yttria, the process was not adequately described by Equation 2.7. However, with yttria, the process now falls within the descriptive capabilities of the equation, suggesting the significant role of yttria in influencing the crystallization process. Moreover, the phenomenon of smaller grain size production due to the presence of yttria during RIC is of great significance, as it enhances the material's resistance to radiation. This is attributed to the increased grain boundary density, widely recognized as a main factor for material radiation resistance due to its function as a sink for radiation-induced defects. In the end it also is important to emphasize that, despite the delay, the sequence of phase appearances remained equal in both doped and undoped instances.

The impact of yttria doping on the delay of crystallization is further highlighted in Figure 2.23 (a), demonstrating that higher radiation doses are required to initiate crystallization across all investigated temperatures. This observation shows an increased trend in the power law curve describing the minimum dpa for crystallization vs. temperature in the doped case. The Arrhenius plots in Figure 2.23 (b), obtained from extrapolating the K value at varying temperatures, revealed another layer of yttria doping's influence on the activation energy of radiation-induced crystallization. The resultant activation energy, calculated following this method, was 81 kJ/mol,

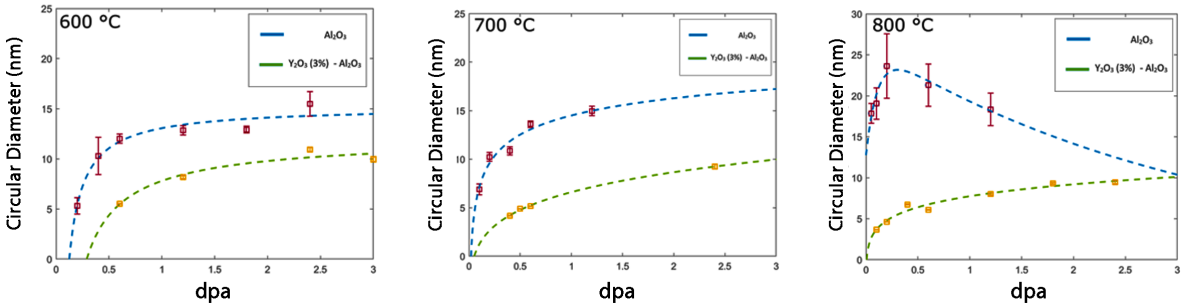

Figure 2.22: Graphic representation of the kinetics of radiation-induced crystallization in both yttria-doped and undoped alumina materials at different temperatures.

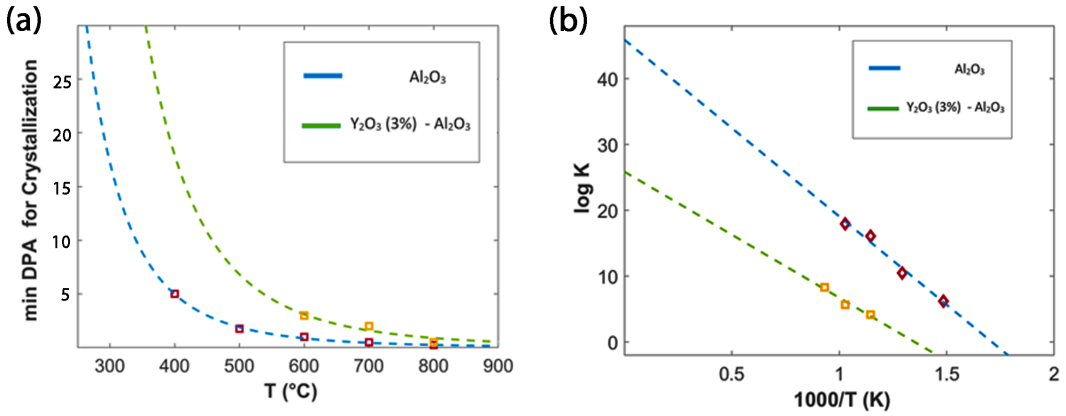

Figure 2.23: Influence of yttria doping on radiation-induced crystallization. (a) A power law curve demonstrating the increased minimum dpa required for crystallization initiation at varying temperatures with yttria doping. (b) Arrhenius plots showcasing the change in activation energy for crystallization due to yttria doping

lower than the 147.2 kJ/mol noted in the undoped case. This observation suggests that yttria may not significantly contribute to the thermodynamic stabilization of the transformation. However, it may affect the system's kinetics, possibly by limiting the diffusion capacity of the species and, consequently, the reorganization process leading to crystallization.

Hence , the introduction of 3% wt. as a dopant, yttria significantly impacted the crystallization process by slowing down the nucleation initiation and decelerating the kinetics of grain growth. However, the dopant concentration examined did not prevent crystallization at higher radiation doses.

In conclusion, the role of dopants in controlling material crystallization has been substantiated through in situ ion irradiation tests. Particularly, the stabilizing effects of Y_2O_3-doped Al_2O_3 showed promising evidence in terms of crystallization dose, grain growth, and radiation tolerance. As such, the doping technique appears to be a potential avenue for designing radiation-tolerant coatings and improving the unique properties of PLD-grown ceramic films.

3 | Summary and Future Developments

he research undertaken in this doctoral dissertation advances the understanding of amorphous ceramic coatings generated through Pulsed Laser Deposition (PLD). This explorative research pushes boundaries and illuminates new paths for sophisticated applications, specifically nuclear technology and space exploration. Our findings underscore these coatings' critical role in formulating materials that can withstand the punishing effects of ionizing radiation. The study's emphasis on nuclear technology is on Lead-cooled Fast Reactors, the revolutionary Generation-IV nuclear systems. They present us with a remarkable blend of promising safety characteristics and enhanced efficiency, thus marking notable progress in this field. This work methodically examines the application of corrosion-resistant bulk alloys, surface-alloying treatments, and coatings in nuclear environments, endeavoring to bridge the knowledge gap in materials suitable for high-temperature, corrosive, and radiation-intense environments typical of LFRs. The research uses Al_2O_3 PLD coatings to amplify existing materials' radiation tolerance and mechanical stability.

About space exploration, the research unfolds an innovative methodology to amplify the effectiveness of solar cells. The novel approach tackles issues associated with traditional solar cell stacks by embedding a protective layer directly onto the solar cell, which functions as a radiation shield while preserving optical transparency. This ingenious initiative falls under the broader umbrella of the SpaceSolarShield project, promising to revolutionize the solar cell manufacturing industry by significantly improving performance efficiency, power density, and production control. The research carried out meticulous characterizations and experiments to materialize these ambitious concepts, aiming at emulating real operational conditions. These investigations probed into the distinct attributes of the materials and their behavior under varying conditions, such as irradiation exposure, mechanical stress, and temperature fluctuations. The studies enriched the understanding of alumina coatings' mechanical performance and properties.

This work extensively analyzed alumina thin films using diverse techniques. These included residual stress measurements and coefficient of thermal expansion on alumina films of various thicknesses. Ultrasonic techniques were employed to extrapolate the thermo-mechanical properties; then it was also investigated the evolution of the refracting index by ellipsometry. SRIM simulations were comprehensively utilized to examine the radiation effect on the material. Multiple fracture phenomena in thin films have been extensively studied, providing insights into crack density saturation, stress distribution, and the interfacial behavior of the

coating/substrate system. Analytical models, finite element simulations, and experimental investigations have contributed to understanding these phenomena. However, further research is needed to address certain limitations and fully capture the complexities involved. By advancing our knowledge in this area, it is possible to develop damage-tolerant amorphous oxide coatings that enhance the mechanical resistance and reliability of nuclear applications, particularly fuel claddings, and support the advancement of GEN-IV fast fission reactor technologies.

A significant achievement of this research is an exhaustive, in-situ study of the interplay between radiation dose and temperature on the crystallization kinetics of amorphous Al_2O_3 deposited by pulsed laser deposition. A wealth of data was collected across a broad temperature range (400 – 800 °C), creating a new semi-empirical model. This model, built upon previous research on already crystallized materials, accounted for an incubation dose for radiation-induced crystallization at temperatures below the crystallization point of Al_2O_3. Various strategies have been explored to improve the radiation resistance of materials. The study investigated pulsed laser frequency, plasma plume shadow removal, and yttria doping effect. The results showed that a higher pulsed laser frequency (50Hz) during deposition led to superior radiation resistance in the alumina coating. The plasma plume shadow removal method, achieved using a shadow mask, improved the coating's surface morphology and radiation resistance. Yttria doping of alumina was found to slow down radiation-induced crystallization and inhibit grain growth, enhancing the material's radiation tolerance. The findings of this study contribute to the understanding of radiation-resistant materials and their behavior under radiation. The insights from investigating these parameters pave the way for developing improved coatings and effectively controlling surface morphology in pulsed laser deposition. The study suggests that yttria doping has potential applications in designing radiation-tolerant coatings and enhancing the properties of ceramic films produced through pulsed laser deposition.

This dissertation propels beyond the conventional boundaries of coating performance and operational range, offering creative solutions and strategies. The extensive research conducted considerably fuels both nuclear and space application research. The insights gathered have the potential to apply to a broader spectrum of systems. These findings provide a robust framework for understanding the intricate processes involved in the structural evolution of amorphous films under ion irradiation, which will be instrumental in guiding material growth and evolution. The impact of these developments, facilitated through nanotechnology, will be monumental. They promise to enhance the safety and efficiency of nuclear reactors and revolutionize space travel by protecting against harmful radiation. However, the incredible power of radiation-resistant coatings necessitates careful regulation and responsible application. As we progress, it is vital to remember that while these coatings are a beacon of scientific achievement, they also underscore a commitment to a safer, more sustainable future.

In summary, this endeavor represents a crucial step forward in successfully utilizing PLD-grown ceramic coatings for future systems. However, as has been made evident, this path is complex, replete with a need for persistent experimentation, ongoing learning, and constant validation.

There is tremendous potential in PLD-grown doped alumina, and the exploration of its usage will continue. Our preliminary findings have shown its improved performance, especially under irradiation. While promising, these findings must be supplemented by comprehensive characterization and rigorous testing to ensure the doped alumina films are a superior replacement for conventional oxide materials. In the wider picture, this work has gathered significant data concerning these ceramic coatings' behavior and potential application. While basic requirements have been met, we underscore the necessity of continued research and development efforts before reaching the final full working phase.

Bibliography

[1] Leszek A. Dobrzański. "Significance of Materials Science for the Future Development of Societies". In: *Journal of Materials Processing Technology.* Achievements in Mechanical & Materials Engineering 175.1 (June 2006), pp. 133–148. ISSN: 0924-0136. DOI: 10.1016/j.jmatprotec.2005.04.003.

[2] Koichi Yagi and Kohmei Halada. "Materials Development for a Sustainable Society". In: *Materials & Design* 22.2 (Apr. 2001), pp. 143–146. ISSN: 0261-3069. DOI: 10.1016/S0261-3069(00)00056-X.

[3] Meagan S. Mauter et al. "The Role of Nanotechnology in Tackling Global Water Challenges". In: *Nature Sustainability* 1.4 (Apr. 2018), pp. 166–175. ISSN: 2398-9629. DOI: 10.1038/s41893-018-0046-8.

[4] Lauran Oers. "Environmental Impact of Products (EIPRO) Analysis of the Life Cycle Environmental Impacts Related to the Final Consumption of the EU-25". In: *Main report : IPTS/ESTO project* (Jan. 2006).

[5] Nancy M. P. Bocken et al. "Product Design and Business Model Strategies for a Circular Economy". In: *Journal of Industrial and Production Engineering* 33.5 (July 3, 2016), pp. 308–320. ISSN: 2168-1015. DOI: 10.1080/21681015.2016.1172124.

[6] *G20 Report: Towards a More Resource-Efficient and Circular Economy - The Role of the G20 | Knowledge for Policy.* URL: https://knowledge4policy.ec.europa.eu/publication/g20-report-towards-more-resource-efficient-circular-economy-role-g20_en.

[7] Sabbie A. Miller, Arpad Horvath, and Paulo J. M. Monteiro. "Readily Implementable Techniques Can Cut Annual CO2 Emissions from the Production of Concrete by over 20%". In: *Environmental Research Letters* 11.7 (July 2016), p. 074029. ISSN: 1748-9326. DOI: 10.1088/1748-9326/11/7/074029.

[8] Sam Zhang, ed. *Thin Films and Coatings: Toughening and Toughness Characterization.* Boca Raton: CRC Press, July 28, 2015. DOI: 10.1201/b18729.

[9] Shiza Malik, Khalid Muhammad, and Yasir Waheed. "Nanotechnology: A Revolution in Modern Industry". In: *Molecules* (Jan. 2023). DOI: 10.3390/molecules28020661.

[10] Lucy Sharp. "Materials Technology: Innovations and Progress". In: *Impact* 2020.2 (Apr. 2020), pp. 52–53. DOI: 10.21820/23987073.2020.2.52.

[11] *Global warming of 1.5 C. An IPCC Special Report on the impacts of global warming of 1.5 C above pre-industrial levels and related global greenhouse gas emission pathways, in the*

context of strengthening the global response to the threat of climate change, sustainable development, and efforts to eradicate poverty. IPCC, 2018.

[12] *Net Zero by 2050 – Analysis.* IEA. 2022.

[13] *Nuclear Explained – Nuclear Energy for Net Zero.* Dec. 13, 2022. URL: https://www.iaea.org/podcasts/nuclear-explained-nuclear-energy-for-net-zero.

[14] Iea. *Renewables 2020 – analysis.* URL: https://www.iea.org/reports/renewables-2020?mode=overview.

[15] Giorgio Locatelli, Chris Bingham, and Mauro Mancini. "Small Modular Reactors: A Comprehensive Overview of Their Economics and Strategic Aspects". In: *Progress in Nuclear Energy* 73 (2014), pp. 75–85. ISSN: 0149-1970. DOI: 10.1016/j.pnucene.2014.01.010.

[16] *Generation IV International forum Anual Report.* 2021. URL: https://www.gen-4.org/gif/jcms/c_203335/gif-2021-ar.

[17] *Nuclear Power Reactors in the World.* Reference Data Series 2. Vienna: INTERNATIONAL ATOMIC ENERGY AGENCY, 2021. ISBN: 978-92-0-124421-5. URL: https://www.iaea.org/publications/14989/nuclear-power-reactors-in-the-world.

[18] N. Colonna. "Generation IV Nuclear Energy Systems and the Need of Accurate Nuclear Data". In: *Journal of Physics: Conference Series* 168.1 (May 2009), p. 012024. ISSN: 1742-6596. DOI: 10.1088/1742-6596/168/1/012024.

[19] World Nuclear Association. *Radioactive Waste Management.* 2020. URL: https://www.world-nuclear.org/information-library/nuclear-fuel-cycle/nuclear-wastes/radioactive-waste-management.aspx.

[20] United Nations Office for Disarmament Affairs. *Treaty on the Non-Proliferation of Nuclear Weapons (NPT).* https://www.un.org/disarmament/wmd/nuclear/npt/. Accessed: May 12, 2023. n.d.

[21] Sophie Grape et al. "New Perspectives on Nuclear Power—Generation IV Nuclear Energy Systems to Strengthen Nuclear Non-Proliferation and Support Nuclear Disarmament". In: *Energy Policy* 73 (Oct. 1, 2014), pp. 815–819. ISSN: 0301-4215. DOI: 10.1016/j.enpol.2014.06.026.

[22] Lucas W. Davis. "Prospects for Nuclear Power". In: *Journal of Economic Perspectives* 26.1 (Feb. 2012), pp. 49–66. ISSN: 0895-3309. DOI: 10.1257/jep.26.1.49.

[23] International Atomic Energy Agency (IAEA). *Public Acceptance of Nuclear Energy.* https://www.iaea.org/sites/default/files/publications/magazines/bulletin/bull19-6/19604794857.pdf. Accessed: May 12, 2023. 2019.

[24] A. Alemberti et al. "The European Lead Fast Reactor Strategy and the Roadmap for the Demonstrator ALFRED". In: IAEA, 2013, p. v.

[25] Alessandro Alemberti. "Advanced Lead Fast Reactor European Demonstrator–ALFRED PROJECT". In: *GEN-IV International Forum-Webinar.* Vol. 26. 2018, pp. 2018–11.

[26] Alessandro Alemberti. "ELFR: The European Lead Fast Reactor. Design, Safety Approach and Safety Characteristics". In: (2012).

[27] Abderrahim. "Multi-purpose hYbrid Research Reactor for High-tech Applications a multipurpose fast spectrum research reactor". In: *International Journal of Energy Research* 36.15 (2012), pp. 1331–1337.

[28] Didier De Bruyn et al. "Main achievements of the FP7-LEADER collaborative project of the European Commission regarding the design of a Lead-cooled Fast Reactor". In: *Korean Nuclear Society* 4 (2013), p. 281.

[29] Lorenzo Malerba et al. "Towards a single European strategic research and innovation agenda on materials for all reactor generations through dedicated projects". In: *EPJ N-Nuclear Sciences & Technologies* 8 (2022), p. 36.

[30] URL: https://www.innumat.eu/.

[31] M Frogheri, A Alemberti, and L Mansani. "The lead fast reactor: demonstrator (ALFRED) and ELFR design". In: *Fast reactors and related fuel cycles: safe technologies and sustainable scenarios (FR13)* 1 (2015).

[32] 2023. URL: https://www.newcleo.com/.

[33] Viacheslav Pershukov, Vladimir Artisyuk, and Andrey Kashirsky. "Paving the way to green status for nuclear power". In: *Sustainability* 14.15 (2022), p. 9339.

[34] Alessandro Alemberti et al. "Overview of lead-cooled fast reactor activities". In: *Progress in Nuclear Energy* 77 (2014), pp. 300–307.

[35] Yican Wu et al. "Development strategy and conceptual design of China lead-based research reactor". In: *Annals of Nuclear Energy* 87 (2016), pp. 511–516.

[36] Long Gu and Xingkang Su. "Latest research progress for LBE coolant reactor of China initiative accelerator driven system project". In: *Frontiers in Energy* (2021), pp. 1–22.

[37] Craig F Smith et al. "SSTAR: The US lead-cooled fast reactor (LFR)". In: *Journal of Nuclear Materials* 376.3 (2008), pp. 255–259.

[38] Jun Liao et al. "Development of phenomena identification and ranking table for Westinghouse lead fast reactor's safety". In: *Progress in Nuclear Energy* 131 (2021), p. 103577.

[39] Mariano Tarantino et al. "Overview on lead-cooled fast reactor design and related technologies development in ENEA". In: *Energies* 14.16 (2021), p. 5157.

[40] 2023. URL: https://www.newcleo.com/what-we-do/.

[41] 2022. URL: https://www.report.rosatom.ru/655.html.

[42] Paolo Ferroni. "Westinghouse Lead Fast Reactor Design and Safety". In: (2021).

[43] Igor Pioro. *Handbook of Generation IV Nuclear Reactors: A Guidebook*. Woodhead Publishing, 2022.

[44] T. R. Allen and D. C. Crawford. "Lead-Cooled Fast Reactor Systems and the Fuels and Materials Challenges". In: *Science and Technology of Nuclear Installations* 2007 (2007), pp. 1–11. ISSN: 1687-6075, 1687-6083. DOI: 10.1155/2007/97486.

[45] Xing Gong et al. "Environmental degradation of structural materials in liquid lead- and lead-bismuth eutectic-cooled reactors". In: *Progress in Materials Science* 126 (2022), p. 100920. ISSN: 0079-6425. DOI: https://doi.org/10.1016/j.pmatsci.2022.100920.

[46] Oy Erweko Painotuote. "Steel structures for nuclear facilities". In: *IAEA* (2013).

[47] Steven J Zinkle and Jeremy T Busby. "Structural materials for fission & fusion energy". In: *Materials today* 12.11 (2009), pp. 12–19.

[48] P Yvon and F Carré. "Structural materials challenges for advanced reactor systems". In: *Journal of nuclear materials* 385.2 (2009), pp. 217–222.

[49] KL Murty and I Charit. "Structural materials for Gen-IV nuclear reactors: Challenges and opportunities". In: *Journal of Nuclear Materials* 383.1-2 (2008), pp. 189–195.

[50] Jinsuo Zhang. "A review of steel corrosion by liquid lead and lead–bismuth". In: *Corrosion Science* 51.6 (2009), pp. 1207–1227.

[51] J Zhang, P Hosemann, and S Maloy. "Models of liquid metal corrosion". In: *Journal of Nuclear Materials* 404.1 (2010), pp. 82–96.

[52] IV Gorynin et al. "Structural materials for atomic reactors with liquid metal heat-transfer agents in the form of lead or lead—Bismuth alloy". In: *Metal Science and Heat Treatment* 41.9 (1999), pp. 384–388.

[53] Concetta Fazio et al. *Handbook on lead-bismuth eutectic alloy and lead properties, materials compatibility, thermal-hydraulics and technologies-2015 edition*. Tech. rep. Organisation for Economic Co-Operation and Development, 2015.

[54] Carl Wagner. "Theoretical Analysis of the Diffusion Processes Determining the Oxidation Rate of Alloys". In: *Journal of The Electrochemical Society* 99.10 (1952), p. 369. DOI: 10.1149/1.2779605.

[55] Seung Gi Lee et al. "High-temperature corrosion behaviors of structural materials for lead-alloy-cooled fast reactor application". In: *Applied Sciences* 11.5 (2021), p. 2349.

[56] Yuji Kurata and Shigeru Saito. "Temperature dependence of corrosion of ferritic/martensitic and austenitic steels in liquid lead-bismuth eutectic". In: *Materials transactions* 50.10 (2009), pp. 2410–2417.

[57] C Fazio et al. "Compatibility tests on steels in molten lead and lead–bismuth". In: *Journal of nuclear materials* 296.1-3 (2001), pp. 243–248.

[58] G Benamati et al. "Temperature effect on the corrosion mechanism of austenitic and martensitic steels in lead–bismuth". In: *Journal of nuclear materials* 301.1 (2002), pp. 23–27.

[59] L Soler et al. "Corrosion of stainless steels in lead–bismuth eutectic up to 600° C". In: *Journal of Nuclear Materials* 335.2 (2004), pp. 174–179.

[60] Tomohiro Furukawa et al. "Corrosion behavior of FBR candidate materials in stagnant Pb-Bi at elevated temperature". In: *Journal of Nuclear Science and Technology* 41.3 (2004), pp. 265–270.

[61] FJ Martın et al. "Oxide layer stability in lead–bismuth at high temperature". In: *Journal of nuclear materials* 335.2 (2004), pp. 194–198.

[62] L. Martinelli et al. "High Temperature Oxidation of Fe–9Cr–1Mo Steel in Stagnant Liquid Lead–Bismuth at Several Temperatures and for Different Lead Contents in the Liquid Alloy". In: *Journal of Nuclear Materials* 376.3 (June 2008), pp. 282–288. ISSN: 00223115. DOI: 10.1016/j.jnucmat.2008.02.006.

[63] D. Gorse. “EFFECT OF LBE AND LEAD ON MECHANICAL PROPERTIES OF STRUCTURAL MATERIALS”. In: 2007.

[64] MG Nicholas and CF Old. “Liquid metal embrittlement”. In: *Journal of Materials Science* 14 (1979), pp. 1–18.

[65] EE Glickman. “Mechanism of liquid metal embrittlement by simple experiments: from atomistics to life-time”. In: *NATO ASI SERIES E APPLIED SCIENCES* 367 (2000), pp. 383–402.

[66] Naoyuki Tsutsui and Hirokazu Koizumi. “Intergranular transgranular fracture in the liquid metal embrittlement of polycrystalline zinc”. In: *Procedia Structural Integrity* 13 (2018), pp. 849–854.

[67] D Gorse et al. “Influence of liquid lead and lead–bismuth eutectic on tensile, fatigue and creep properties of ferritic/martensitic and austenitic steels for transmutation systems”. In: *Journal of nuclear materials* 415.3 (2011), pp. 284–292.

[68] Mariya Yurechko et al. “Creep of 316L austenitic steel at 450–550° C in static lead-bismuth eutectic covered by argon-hydrogen gas”. In: *Journal of Nuclear Materials* 558 (2022), p. 153344.

[69] Jean-Bernard Vogt et al. “Understanding the liquid metal assisted damage sources in the T91 martensitic steel for safer use of ADS”. In: *Engineering Failure Analysis* 14.6 (2007), pp. 1185–1193.

[70] Noelia Fuentes Solis et al. “Effect of liquid metal environment on nucleation of fatigue cracks in an austenitic stainless steel”. In: *Science Talks* 6 (2023), p. 100204.

[71] GR Odette, MJ Alinger, and BD Wirth. “Recent developments in irradiation-resistant steels”. In: *Annu. Rev. Mater. Res.* 38 (2008), pp. 471–503.

[72] A Kumar and Brian Leonard Eyre. “Grain boundary segregation and intergranular fracture in molybdenum”. In: *Proceedings of the Royal Society of London. A. Mathematical and Physical Sciences* 370.1743 (1980), pp. 431–458.

[73] RG Song et al. “Grain boundary segregation and hydrogen-induced fracture in 7050 aluminium alloy”. In: *Acta materialia* 44.8 (1996), pp. 3241–3248.

[74] RA Mulford et al. “Temper embrittlement of Ni-Cr steels by phosphorus”. In: *Metallurgical Transactions A* 7 (1976), pp. 1183–1195.

[75] DR Harries. “Neutron irradiation-induced embrittlement in type 316 and other austenitic steels and alloys”. In: *Journal of Nuclear Materials* 82.1 (1979), pp. 2–21.

[76] HK Birnbaum. “Hydrogen related fracture of metals”. In: *Atomistics of fracture* (1983), pp. 733–769.

[77] Subra Suresh. *Fatigue of materials*. Cambridge university press, 1998.

[78] John Price Hirth, Jens Lothe, and T Mura. “Theory of dislocations”. In: *Journal of Applied Mechanics* 50.2 (1983), p. 476.

[79] FRN Nabarro. “Steady-state diffusional creep”. In: *Philosophical Magazine* 16.140 (1967), pp. 231–237.

[80] Terence G Langdon. “Grain boundary sliding as a deformation mechanism during creep”. In: *Philosophical Magazine* 22.178 (1970), pp. 689–700.

[81] Christopher Matthews et al. “Fuel-cladding chemical interaction in U-Pu-Zr metallic fuels: a critical review”. In: *Nuclear Technology* 198.3 (2017), pp. 231–259.

[82] CR de F Azevedo. “Selection of fuel cladding material for nuclear fission reactors”. In: *Engineering Failure Analysis* 18.8 (2011), pp. 1943–1962.

[83] Piyush Sabharwall, Shannon M Bragg-Sitton, and Carl Stoots. “Challenges in the development of high temperature reactors”. In: *Energy conversion and management* 74 (2013), pp. 574–581.

[84] William J O’Donnell, Amy B Hull, and Shah Malik. “Structural integrity code and regulatory issues in the design of high temperature reactors”. In: *High Temperature Reactor Technology*. Vol. 48548. 2008, pp. 15–24.

[85] S. J. Zinkle and G. S. Was. “Materials Challenges in Nuclear Energy”. In: *Acta Materialia*. The Diamond Jubilee Issue 61.3 (Feb. 1, 2013), pp. 735–758. ISSN: 1359-6454. DOI: 10.1016/j.actamat.2012.11.004.

[86] Chenyang Lu et al. “Enhanced void swelling in NiCoFeCrPd high-entropy alloy by indentation-induced dislocations”. In: *Materials Research Letters* 6.10 (2018), pp. 584–591.

[87] Michael Wurmshuber et al. “Helium-induced swelling and mechanical property degradation in ultrafine-grained W and W-Cu nanocomposites for fusion applications”. In: *Scripta Materialia* 213 (2022), p. 114641.

[88] Vladimir Krsjak et al. “On the helium bubble swelling in nano-oxide dispersion-strengthened steels”. In: *Journal of Materials Science & Technology* 105 (2022), pp. 172–181.

[89] TR Allen et al. “Swelling and radiation-induced segregation in austentic alloys”. In: *Journal of nuclear materials* 342.1-3 (2005), pp. 90–100.

[90] SA Fabritsiev et al. “Neutron spectrum and transmutation effects on the radiation damage of copper alloys”. In: *Fusion engineering and design* 36.4 (1997), pp. 505–513.

[91] TA Taiwo and RN Hill. *Summary of Generation-IV transmutation impacts*. Tech. rep. Argonne National Lab.(ANL), Argonne, IL (United States), 2005.

[92] JR Matthews and MW Finnis. “Irradiation creep models—an overview”. In: *Journal of Nuclear Materials* 159 (1988), pp. 257–285.

[93] V Fidleris. “The irradiation creep and growth phenomena”. In: *Journal of Nuclear Materials* 159 (1988), pp. 22–42.

[94] Johsei Nagakawa. “Calculation of radiation-induced creep and stress relaxation”. In: *Journal of nuclear materials* 225 (1995), pp. 1–7.

[95] W Primak. “Radiation-Induced Stress Relaxation in Quartz and Vitreous Silica”. In: *Journal of Applied Physics* 35.4 (1964), pp. 1342–1347.

[96] B Fayolle, L Audouin, and J Verdu. “Radiation induced embrittlement of PTFE”. In: *Polymer* 44.9 (2003), pp. 2773–2780.

[97] Yu A Nikolaev, AV Nikolaeva, and Ya I Shtrombakh. "Radiation embrittlement of low-alloy steels". In: *International journal of pressure vessels and piping* 79.8-10 (2002), pp. 619–636.

[98] EA Kuleshova et al. "Mechanisms of radiation embrittlement of VVER-1000 RPV steel at irradiation temperatures of (50–400)° C". In: *Journal of Nuclear Materials* 490 (2017), pp. 247–259.

[99] F Frisius and M Naraghi. "Measurement of radiation-induced embrittlement on steel samples by neutron small angle scattering". In: *Atomkernenergie;(Germany, Federal Republic of)* 29.2 (1977).

[100] J Kameda and X Mao. "Small-punch and TEM-disc testing techniques and their application to characterization of radiation damage". In: *Journal of Materials science* 27 (1992), pp. 983–989.

[101] RA Wullaert, DR Ireland, and AS Tetelman. "Radiation effects on the metallurgical fracture parameters and fracture toughness of pressure vessel steels". In: *Irradiation Effects on Structural Alloys for Nuclear Reactor Applications* (1970).

[102] Huilong Yang. "Anisotropic effects of radiation-induced hardening in nuclear structural materials: A review". In: *Journal of Nuclear Materials* (2022), p. 153571.

[103] Alfred K Seeger. *On the theory of radiation damage and radiation hardening*. Tech. rep. Max-Planck-Inst. fur Metallforschung, Stuttgart; Technischen Hochschule ..., 1959.

[104] Gary S. WAS. *Fundamentals of Radiation Materials Science*. 2018.

[105] Allen T. *Structural Materials for Generation IV Nuclear Reactors*. 2016.

[106] A. Iwase and S. Ishino. "Comparison between Radiation Effects in Some Fcc and Bcc Metals Irradiated with Energetic Heavy Ions – a Review". In: *Journal of Nuclear Materials* 276.1 (2000), pp. 178–185. ISSN: 0022-3115. DOI: 10.1016/S0022-3115(99)00177-4.

[107] A Ward and S Fisher. "A comparison of heavy ion-irradiated ferritic and austenitic steels in the early stages of damage". In: *Effects of Radiation on Materials: 15th International Symposium*. ASTM International, 2009, pp. 1167–1167–13.

[108] E Stergar et al. "Influence of LBE long term exposure and simultaneous fast neutron irradiation on the mechanical properties of T91 and 316L". In: *Journal of Nuclear Materials* 473 (2016), pp. 28–34.

[109] J. Van den Bosch et al. "Liquid Metal Embrittlement Susceptibility of Ferritic–Martensitic Steel in Liquid Lead Alloys". In: *Journal of Nuclear Materials* 376.3 (2008), pp. 322–329. ISSN: 0022-3115. DOI: 10.1016/j.jnucmat.2008.02.008.

[110] Y. Dai et al. "Assessment of the Lifetime of the Beam Window of MEGAPIE Target Liquid Metal Container". In: *Journal of Nuclear Materials* 356.1 (2006), pp. 308–320. ISSN: 0022-3115. DOI: 10.1016/j.jnucmat.2006.05.036.

[111] M. Brumovsky. "Irradiation Hardening and Materials Embrittlement in Light Water Reactor (LWR) Environments". In: *Understanding and Mitigating Ageing in Nuclear Power Plants*. Elsevier, 2010, pp. 357–373. ISBN: 978-1-84569-511-8. DOI: 10.1533/9781845699956.2.357. (Visited on 05/16/2023).

[112] URL: https://www.totalmateria.com/page.aspx?ID=CheckArticle&site=kts&NM=249.

[113] S Ukai et al. "Oxide dispersion-strengthened/ferrite-martensite steels as core materials for Generation IV nuclear reactors". In: *Structural Materials for Generation IV Nuclear Reactors*. Elsevier, 2017, pp. 357–414.

[114] Chenyang Lu et al. "Enhanced radiation-tolerant oxide dispersion strengthened steel and its microstructure evolution under helium-implantation and heavy-ion irradiation". In: *Scientific reports* 7.1 (2017), p. 40343.

[115] Haijian Xu et al. "Microstructure refinement and strengthening mechanisms of a 9Cr oxide dispersion strengthened steel by zirconium addition". In: *Nuclear Engineering and Technology* 49.1 (2017), pp. 178–188.

[116] Sebastien Dryepondt et al. "Development of low-Cr ODS FeCrAl alloys for accident-tolerant fuel cladding". In: *Journal of Nuclear Materials* 501 (2018), pp. 59–71.

[117] Stanislava Fintová et al. "Development of advanced Fe–Al–O ODS alloy microstructure and properties due to heat treatment". In: *Journal of Materials Research* 35.20 (2020), pp. 2789–2797.

[118] Bo Cheng, Young-Jin Kim, and Peter Chou. "Improving accident tolerance of nuclear fuel with coated Mo-alloy cladding". In: *Nuclear Engineering and Technology* 48.1 (2016), pp. 16–25.

[119] Zunqi Xiao et al. "Corrosion behavior of refractory metals in liquid lead at 1000 C for 1000 h". In: *Nuclear Engineering and Technology* 54.6 (2022), pp. 1954–1961.

[120] EN Hoffman et al. "MAX phase carbides and nitrides: Properties for future nuclear power plant in-core applications and neutron transmutation analysis". In: *Nuclear Engineering and Design* 244 (2012), pp. 17–24.

[121] Michel W Barsoum. "The MN+ 1AXN phases: A new class of solids: Thermodynamically stable nanolaminates". In: *Progress in solid state chemistry* 28.1-4 (2000), pp. 201–281.

[122] Michel W Barsoum. *MAX phases: properties of machinable ternary carbides and nitrides*. John Wiley & Sons, 2013.

[123] Michel W Barsoum and Miladin Radovic. "Elastic and mechanical properties of the MAX phases". In: *Annual review of materials research* 41 (2011), pp. 195–227.

[124] Matteo Griseri et al. "Ta-based 413 and 211 MAX phase solid solutions with Hf and Nb". In: *Journal of the European Ceramic Society* 40.5 (2020), pp. 1829–1838.

[125] Thomas Lapauw et al. "(Nb x, Zr1–x) 4AlC3 MAX Phase Solid Solutions: Processing, Mechanical Properties, and Density Functional Theory Calculations". In: *Inorganic Chemistry* 55.11 (2016), pp. 5445–5452.

[126] Bensu Tunca et al. "Synthesis of MAX phases in the Zr-Ti-Al-C system". In: *Inorganic Chemistry* 56.6 (2017), pp. 3489–3498.

[127] Bensu Tunca et al. "Synthesis and characterization of double solid solution (Zr, Ti) 2 (Al, Sn) C MAX phase ceramics". In: *Inorganic Chemistry* 58.10 (2019), pp. 6669–6683.

[128] M Utili et al. “Ti3SiC2 as a candidate material for lead cooled fast reactor”. In: *Nuclear Engineering and design* 241.5 (2011), pp. 1295–1300.

[129] Chunfeng Hu et al. “Shell-like nanolayered Nb4AlC3 ceramic with high strength and toughness”. In: *Scripta Materialia* 64.8 (2011), pp. 765–768.

[130] Leping Cai et al. “Fabrication, mechanical properties, and tribological behaviors of Ti 2 AlC and Ti 2 AlSn 0.2 C solid solutions”. In: *Journal of Advanced Ceramics* 6 (2017), pp. 90–99.

[131] Hai-jiao Yu et al. “Processing and properties of 2D SiC/SiC composites by precursor infiltration and pyrolysis”. In: *Journal of Central South University of Technology* 16.2 (2009), pp. 190–194.

[132] Darin J Tallman et al. “Effect of neutron irradiation on defect evolution in Ti3SiC2 and Ti2AlC”. In: *Journal of Nuclear Materials* 468 (2016), pp. 194–206.

[133] Darin J Tallman et al. “Effects of neutron irradiation of Ti3SiC2 and Ti3AlC2 in the 121–1085° C temperature range”. In: *Journal of Nuclear Materials* 484 (2017), pp. 120–134.

[134] Caen Ang et al. “Anisotropic swelling and microcracking of neutron irradiated Ti3AlC2–Ti5Al2C3 materials”. In: *Scripta Materialia* 114 (2016), pp. 74–78.

[135] C Amy et al. “Pumping liquid metal at high temperatures up to 1,673 kelvin”. In: *Nature* 550.7675 (2017), pp. 199–203.

[136] Ronald G Ballinger and Jeongyoun Lim. “An overview of corrosion issues for the design and operation of high-temperature lead-and lead-bismuth-cooled reactor systems”. In: *Nuclear Technology* 147.3 (2004), pp. 418–435.

[137] CP Deck et al. “Characterization of SiC–SiC composites for accident tolerant fuel cladding”. In: *Journal of Nuclear Materials* 466 (2015), pp. 667–681.

[138] Cédric Sauder. “Ceramic matrix composites: nuclear applications”. In: *Ceramic matrix composites: materials, modeling and technology* (2014), pp. 609–646.

[139] Sarbjit Kaur, Raymond A Cutler, and Dinesh K Shetty. “Short-crack fracture toughness of silicon carbide”. In: *Journal of the American Ceramic Society* 92.1 (2009), pp. 179–185.

[140] Jiwei Cao et al. “3D printing and in situ transformation of SiCnw/SiC structures”. In: *Additive Manufacturing* 58 (2022), p. 103053.

[141] Sven-Erik Wulf, Wolfgang Krauss, and Jürgen Konys. “Comparison of coating processes in the development of aluminum-based barriers for blanket applications”. In: *Fusion Engineering and Design* 89.9-10 (2014), pp. 2368–2372.

[142] Alfons Weisenburger et al. “Corrosion, Al containing corrosion barriers and mechanical properties of steels foreseen as structural materials in liquid lead alloy cooled nuclear systems”. In: *Nuclear Engineering and Design* 241.5 (2011), pp. 1329–1334.

[143] Wolfgang Krauss, Jürgen Konys, and Sven-Erik Wulf. “Corrosion barriers processed by Al electroplating and their resistance against flowing Pb–15.7 Li”. In: *Journal of Nuclear Materials* 455.1-3 (2014), pp. 522–526.

[144] V Engelko et al. “Pulsed electron beam facility (GESA) for surface treatment of materials”. In: *Vacuum* 62.2-3 (2001), pp. 211–216.

[145] V Engelko et al. “Surface modification/alloying using intense pulsed electron beam as a tool for improving the corrosion resistance of steels exposed to heavy liquid metals”. In: *Journal of Nuclear Materials* 415.3 (2011), pp. 270–275.

[146] Yukinori Yamamoto et al. “Development of creep-resistant, alumina-forming ferrous alloys for high-temperature structural use”. In: *Pressure Technology*. Vol. 40764. American Society of Mechanical Engineers. 2018, V001T04A003.

[147] Bruce A Pint et al. “Field and laboratory evaluations of commercial and next-generation alumina-forming austenitic foil for advanced recuperators”. In: *Journal of Engineering for Gas Turbines and Power* 138.12 (2016), p. 122001.

[148] Michael P Brady et al. “The development of alumina-forming austenitic stainless steels for high-temperature structural use”. In: *Jom* 60 (2008), pp. 12–18.

[149] Annette Heinzel, Masatoshi Kondo, and Minoru Takahashi. “Corrosion of steels with surface treatment and Al-alloying by GESA exposed in lead–bismuth”. In: *Journal of Nuclear Materials* 350.3 (2006), pp. 264–270.

[150] Mattia Del Giacco, Alfons Weisenburger, and Georg Müller. “Fretting of fuel cladding materials for Pb cooled fast reactors—Approach to long term prediction using fretting maps”. In: *Nuclear Engineering and Design* 280 (2014), pp. 697–703.

[151] Y Dai et al. “FeCrAlY and TiN coatings on T91 steel after irradiation with 72 MeV protons in flowing LBE”. In: *Journal of nuclear materials* 431.1-3 (2012), pp. 66–76.

[152] R Fernandez et al. “The evolution of the primary system design of the MYRRHA facility”. In: *IAEA* (2017).

[153] Xing Gong et al. “A comparative study on liquid metal embrittlement susceptibility of three FeCrAl ferritic alloys in contact with liquid lead-bismuth eutectic at 350° C”. In: *Corrosion Science* 183 (2021), p. 109346.

[154] Anna Hojna, Fosca Di Gabriele, and Jakub Klecka. “Characteristics and liquid metal embrittlement of the steel T91 in contact with lead–bismuth eutectic”. In: *Journal of Nuclear Materials* 472 (2016), pp. 163–170.

[155] Essam Serag et al. “Challenges and coating solutions for wear and corrosion inside Lead Bismuth Eutectic: A review”. In: *Surface and Coatings Technology* 441 (2022), p. 128542.

[156] ZhiChao Lu et al. “Corrosion and irradiation behavior of Fe-based amorphous coating in lead-bismuth eutectic liquids”. In: *Science China Technological Sciences* 65.2 (2022), pp. 440–449.

[157] J-W Yeh et al. “Nanostructured high-entropy alloys with multiple principal elements: novel alloy design concepts and outcomes”. In: *Advanced engineering materials* 6.5 (2004), pp. 299–303.

[158] Hui Zhang et al. “Thermally stable laser cladded CoCrCuFeNi high-entropy alloy coating with low stacking fault energy”. In: *Journal of alloys and compounds* 600 (2014), pp. 210–214.

[159] Jian Yang et al. “A novel AlCrFeMoTi high-entropy alloy coating with a high corrosion-resistance in lead-bismuth eutectic alloy”. In: *Corrosion Science* 187 (2021), p. 109524.

[160] H Glasbrenner and F Gröschel. “Exposure of pre-stressed T91 coated with TiN, CrN and DLC to Pb–55.5 Bi”. In: *Journal of nuclear materials* 356.1-3 (2006), pp. 213–221.

[161] K Geelhood and W Luscher. “Degradation and Failure Phenomena of Accident Tolerant Fuel Concepts Chromium Coated Zirconium Alloy Cladding; PNNL-28437”. In: *Pacific Northwest National Laboratory: Richland, WA, USA* (2019).

[162] Jeremy Bischoff et al. “AREVA NP’s enhanced accident-tolerant fuel developments: Focus on Cr-coated M5 cladding”. In: *Nuclear Engineering and Technology* 50.2 (2018), pp. 223–228.

[163] URL: `https://www.iit.it/cnst-polimi`.

[164] 2022. URL: `https://x-nano.it/`.

[165] MATTEO VANAZZI. “Ceramic coated fuel claddings for lead-cooled fast reactors”. In: *Thesis Politecnico di Milano* (2015).

[166] Francisco García Ferré et al. “The mechanical properties of a nanocrystalline Al2O3/a-Al2O3 composite coating measured by nanoindentation and Brillouin spectroscopy”. In: *Acta Materialia* 61.7 (2013), pp. 2662–2670.

[167] F. García Ferré et al. “Advanced Al2O3 coatings for high temperature operation of steels in heavy liquid metals: a preliminary study”. In: *Corrosion Science* 77 (2013), pp. 375–378.

[168] FRANCISCO GARCIA FERRE. “Radiation tolerant nanoceramic coatings for lead fast reactor nuclear fuel cladding”. In: (2014).

[169] Jørgen Schou. “Physical aspects of the pulsed laser deposition technique: The stoichiometric transfer of material from target to film”. In: *Applied Surface Science* 255.10 (2009), pp. 5191–5198.

[170] Francesco Fumagalli, Javier Martıé-Rujas, and Fabio Di Fonzo. “Room temperature deposition of high figure of merit Al-doped zinc oxide by pulsed-direct current magnetron sputtering: Influence of energetic negative ion bombardment on film’s optoelectronic properties”. In: *Thin Solid Films* 569 (2014), pp. 44–51.

[171] S Wicklein et al. “Pulsed laser ablation of complex oxides: The role of congruent ablation and preferential scattering for the film stoichiometry”. In: *Applied physics letters* 101.13 (2012), p. 131601.

[172] F. Di Fonzo. “Growth Regimes in Pulsed Laser Deposition of Aluminum Oxide Films”. en. In: *Applied Physics A* 93.3 (2008), pp. 765–769.

[173] G Alcala et al. “Mechanical properties of amorphous anodic alumina and tantala films using nanoindentation”. In: *Nanotechnology* 13.4 (2002), p. 451.

[174] Sergio Davis and Gonzalo Gutiérrez. “Structural, elastic, vibrational and electronic properties of amorphous Al2O3 from ab initio calculations”. In: *Journal of Physics: Condensed Matter* 23.49 (2011), p. 495401.

[175] Erkka J Frankberg. “Plastic deformation of amorphous aluminium oxide: Flow of inorganic glass at room temperature”. In: *PhD Thesis Tampere University of Technology* (2018).

[176] Erkka J. Frankberg et al. “Highly ductile amorphous oxide at room temperature and high strain rate”. In: *Science* 366.6467 (2019), pp. 864–869.

[177] DANIELE IADICICCO. “High performance ceramic coating for DEMO Breeding Blankets”. In: *PhD Thesis Politencico di Milano* (2017).

[178] F. Garciá Ferré et al. “Radiation endurance in Al2O3 nanoceramics”. In: *Scientific Reports* 6 (2016).

[179] F. García Ferré et al. “Extreme ion irradiation of oxide nanoceramics: Influence of the irradiation spectrum”. In: *Acta Materialia* 143 (2018), pp. 156–165.

[180] A. Zaborowska et al. “Absolute radiation tolerance of amorphous alumina coatings at room temperature”. In: *Ceramics International* 47.24 (2021), pp. 34740–34750. ISSN: 0272-8842.

[181] Wendy L Freedman et al. “Final results from the Hubble Space Telescope key project to measure the Hubble constant”. In: *The Astrophysical Journal* 553.1 (2001), p. 47.

[182] William J Borucki. “Kepler: a brief discussion of the mission and exoplanet results”. In: *Proceedings of the American Philosophical Society* 161.1 (2017), pp. 38–65.

[183] Laura Pernigoni, Ugo Lafont, and Antonio Mattia Grande. “Self-Healing Materials for Space Applications: Overview of Present Development and Major Limitations”. In: *CEAS Space Journal* 13.3 (July 1, 2021), pp. 341–352. ISSN: 1868-2510. DOI: 10.1007/s12567-021-00365-5.

[184] John R. Williamson. “Advanced Materials for Space Structures”. In: *Acta Astronautica* 24 (Jan. 1991), pp. 197–202. ISSN: 00945765. DOI: 10.1016/0094-5765(91)90167-4.

[185] Todd A. Schneider et al. “Space Environment Testing of Photovoltaic Array Systems at NASA’s Marshall Space Flight Center”. In: *2015 IEEE 42nd Photovoltaic Specialist Conference (PVSC)*. June 2015, pp. 1–6. DOI: 10.1109/PVSC.2015.7355861.

[186] C. Y. Yang and K.K. de Groh. “Challenges on Materials in Space”. In: *MRS BULLETIN* 35 (Jan. 2010).

[187] Claus G. Zimmermann. “Materials Challenges in Photovoltaic Energy Generation in Space”. In: *MRS Bulletin* 35.1 (Jan. 2010), pp. 48–54. ISSN: 0883-7694, 1938-1425. DOI: 10.1557/mrs2010.616.

[188] Sharon K. R. Miller and Bruce Banks. “Degradation of Spacecraft Materials in the Space Environment”. In: *MRS Bulletin* 35.1 (Jan. 1, 2010), pp. 20–24. ISSN: 1938-1425. DOI: 10.1557/mrs2010.612.

[189] Alessandro Figini-Albisetti et al. “Effect of outgassing temperature on the performance of porous materials”. In: *Applied Surface Science* 256.17 (2010), pp. 5182–5186.

[190] Zilong Jiao et al. “Outgassing environment of spacecraft: An overview”. In: *IOP Conference Series: Materials Science and Engineering*. Vol. 611. 1. IOP Publishing. 2019, p. 012071.

[191] David Bashford. "A Review of Advanced Metallic and Ceramic Materials Suitable for High Temperature Use in Space Structures". In: *Acta Astronautica* 22 (Jan. 1, 1990), pp. 137–144. ISSN: 0094-5765. DOI: 10.1016/0094-5765(90)90015-D.

[192] Anderson Bermudez-Garcia, Philippe Voarino, and Olivier Raccurt. "Environments, Needs and Opportunities for Future Space Photovoltaic Power Generation: A Review". In: *Applied Energy* 290 (May 15, 2021), p. 116757. ISSN: 0306-2619. DOI: 10.1016/j.apenergy.2021.116757.

[193] Alan R. Chambers. "Materials in Space: An Introduction and Overview". In: *Encyclopedia of Aerospace Engineering*. John Wiley & Sons, Ltd, 2010. DOI: 10.1002/9780470686652.eae235.

[194] Pilar Espinet-Gonzalez et al. "Impact of Space Radiation Environment on Concentrator Photovoltaic Systems". In: *2017 IEEE 44th Photovoltaic Specialist Conference (PVSC)*. June 2017, pp. 512–516. DOI: 10.1109/PVSC.2017.8366020.

[195] Bruce A Banks, Kim K de Groh, and Sharon K Miller. "Low earth orbital atomic oxygen interactions with spacecraft materials". In: *MRS Online Proceedings Library (OPL)* 851 (2004), NN8–1.

[196] Thierry Woignier et al. "Aerogels materials as space debris collectors". In: *Advances in Materials Science and Engineering* 2013 (2013).

[197] Shu-hao Deng, Hao Lu, and DY Li. "Influence of UV light irradiation on the corrosion behavior of electrodeposited Ni and Cu nanocrystalline foils". In: *Scientific Reports* 10.1 (2020), pp. 1–16.

[198] RC O'Brien et al. "Safe radioisotope thermoelectric generators and heat sources for space applications". In: *Journal of Nuclear Materials* 377.3 (2008), pp. 506–521.

[199] Rosaria Verduci et al. "Solar energy in space applications: review and technology perspectives". In: *Advanced Energy Materials* 12.29 (2022), p. 2200125.

[200] Marie-Martine Bé et al. *Table of radionuclides (Vol. 8-A= 41 to 198)*. 2016.

[201] RD King-Smith et al. "A first-principle calculation of the temperature dependence of the indirect band gap of silicon". In: *Europhysics Letters* 10.6 (1989), p. 569.

[202] *SpectroLab - A boeing company*. URL: www.azurspace.com/index.php/en/.

[203] *Azur Space Solar Power*. URL: www.azurspace.com/index.php/en/.

[204] *Space Solar Cells | CESI*. URL: https://www.cesi.it/space-solar-cells/.

[205] *SolAero Technologies*. URL: https://solaerotech.com/.

[206] Juan Bisquert. *The Physics of Solar Energy Conversion*. CRC Press, 2020.

[207] Arno HM Smets et al. *Solar Energy: The physics and engineering of photovoltaic conversion, technologies and systems*. UIT Cambridge, 2015.

[208] Enrico Da Como et al. *Unconventional Thin Film Photovoltaics*. Royal Society of Chemistry, 2016.

[209] Joel E Moore. "Optical properties of Weyl semimetals". In: *National Science Review* 6.2 (2019), pp. 206–208.

[210] William Shockley and Hans J Queisser. "Detailed balance limit of efficiency of p-n junction solar cells". In: *Journal of applied physics* 32.3 (1961), pp. 510–519.

[211] Antonio Ricardo Zanatta. "The Shockley–Queisser limit and the conversion efficiency of silicon-based solar cells". In: *Results in Optics* 9 (2022), p. 100320.

[212] Luceno Sanchez and Capilla Rafael. "Materials for photovoltaics: State of art and recent developments". In: *International journal of molecular sciences* 20.4 (2019), p. 976.

[213] Steven Hegedus and Antonio Luque. *Handbook of photovoltaic science and engineering*. John Wiley & Sons, 2011.

[214] J Li et al. "A brief review of high efficiency III-V solar cells for space application". In: *Frontiers in Physics* 8 (2021), p. 631925.

[215] Simon P Philipps and Andreas W Bett. "III-V Multi-junction solar cells and concentrating photovoltaic (CPV) systems". In: *Advanced Optical Technologies* 3.5-6 (2014), pp. 469–478.

[216] MA Quintana et al. "Commonly observed degradation in field-aged photovoltaic modules". In: *Conference Record of the Twenty-Ninth IEEE Photovoltaic Specialists Conference, 2002.* IEEE. 2002, pp. 1436–1439.

[217] Yongguang Tu et al. "Perovskite solar cells for space applications: progress and challenges". In: *Advanced Materials* 33.21 (2021), p. 2006545.

[218] Shaobing Xiong et al. "Surface charge-transfer doping for highly efficient perovskite solar cells". In: *Nano Energy* 79 (2021), p. 105505.

[219] Michael Saliba et al. "Perovskite solar cells: from the atomic level to film quality and device performance". In: *Angewandte Chemie International Edition* 57.10 (2018), pp. 2554–2569.

[220] Martin Kaltenbrunner et al. "Flexible high power-per-weight perovskite solar cells with chromium oxide–metal contacts for improved stability in air". In: *Nature materials* 14.10 (2015), pp. 1032–1039.

[221] Zhaoning Song et al. "High remaining factors in the photovoltaic performance of perovskite solar cells after high-fluence electron beam irradiations". In: *The Journal of Physical Chemistry C* 124.2 (2019), pp. 1330–1336.

[222] Shuang Yang et al. "Organohalide lead perovskites: more stable than glass under gamma-ray radiation". In: *Advanced Materials* 31.4 (2019), p. 1805547.

[223] Hehe Zhang et al. "Graphene as a transparent conductive electrode in GaN-based LEDs". In: *Materials* 15.6 (2022), p. 2203.

[224] Janet L Barth. "Prevention of spacecraft anomalies—The role of Space climate and Space weather models". In: *Effects of Space Weather on Technology Infrastructure*. Springer. 2005, pp. 123–145.

[225] Vincent L Pisacane. *The space environment and its effects on space systems*. American Institute of aeronautics and Astronautics, 2008.

[226] John D Wrbanek and Susan Y Wrbanek. "Space radiation and impact on instrumentation technologies". In: *NASA* (2020).

[227] Glenn F Knoll. *Radiation detection and measurement*. John Wiley & Sons, 2010.

[228] Joseph R Tesmer and Michael Nastasi. "Handbook of modern ion beam materials analysis". In: *Materials Research Society, 9800 McKnight Rd, Suite 327, Pittsburgh, PA 15237, USA, 1995. 700* (1995).

[229] PR Sharps et al. "Proton and electron radiation data and analysis of GaInP2/GaAs/Ge solar cells". In: *Progress in Photovoltaics: Research and Applications* 10.6 (2002), pp. 383–390.

[230] J Li et al. "1 MeV electron and 10 MeV proton irradiation effects on inverted metamorphic GaInP/GaAs/InGaAs triple junction solar cell". In: *Solar energy materials and solar cells* 224 (2021), p. 111022.

[231] Gabriele Gori and Roberta Campesato. *Photovoltaic cell having a high conversion efficiency*. US Patent 9,240,514. Jan. 2016.

[232] Elena A Plis et al. "Effect of simulated GEO environment on the properties of solar panel coverglasses". In: *IEEE Transactions on Plasma Science* 49.5 (2021), pp. 1679–1685.

[233] Roman Herschitz and Alex Bogorad. "Space environmental testing of blue red reflecting coverglasses for gallium arsenide and high efficiency silicon solar cells". In: *Proceedings of 1994 IEEE 1st World Conference on Photovoltaic Energy Conversion- WCPEC (A Joint Conference of PVSC, PVSEC and PSEC)*. Vol. 2. IEEE. 1994, pp. 2189–2191.

[234] C Kitchen et al. "Solar cell coverglasses for satellites in the intermediate Earth orbit". In: *Conference Record of the Twenty Sixth IEEE Photovoltaic Specialists Conference-1997*. IEEE. 1997, pp. 1011–1014.

[235] Arifur R Khan et al. "Electrostatic discharge threshold on coverglass used to protect solar cells in the low Earth orbit". In: *IEEE Transactions on Plasma Science* 47.2 (2018), pp. 1445–1452.

[236] Daniel P Engelhart et al. "XPS investigation of the source of GPS arc contamination". In: *IEEE Transactions on Plasma Science* 47.8 (2019), pp. 3848–3851.

[237] JJ Schermer et al. "Photon confinement in high-efficiency, thin-film III–V solar cells obtained by epitaxial lift-off". In: *Thin Solid Films* 511 (2006), pp. 645–653.

[238] Chao Peng et al. "Investigation of radiation-induced degradations in four-junction solar cell by experiment and simulation". In: *Microelectronics Reliability* 108 (2020), p. 113646.

[239] Richard Stall et al. "UV degradation of space solar cell assemblies under high temperature and irradiance". In: *2018 IEEE 7th World Conference on Photovoltaic Energy Conversion (WCPEC)(A Joint Conference of 45th IEEE PVSC, 28th PVSEC & 34th EU PVSEC)*. IEEE. 2018, pp. 3339–3343.

[240] PA White and DE Jones. "Teflon bonding of silicon solar cells". In: *The Conference Record of the Twenty-Second IEEE Photovoltaic Specialists Conference-1991*. IEEE. 1991, pp. 1508–1511.

[241] H Zhao et al. "Design and implementation of an auto bonding manufacturing process for space solar cells". In: *Materials and Manufacturing Processes* 22.7-8 (2007), pp. 851–858.

[242] Joyce A Dever et al. “Contamination and space environmental effects on solar cells and thermal control surfaces”. In: *Journal of Spacecraft and Rockets* 32.5 (1995), pp. 850–855.

[243] Luigi Fazzi et al. “Monitoring of silicone adhesive in space solar cells with an embedded multi-parameter TFBG sensor in a simulated space environment”. In: *Measurement Science and Technology* 33.8 (2022), p. 085108.

[244] XY Xiong. “Influence of silk screen printing to SMT quality and game”. In: *World of Printing* 3 (2001), pp. 20–21.

[245] Ya-Yu Huang and Kan-Sen Chou. “Studies on the spin coating process of silica films”. In: *Ceramics international* 29.5 (2003), pp. 485–493.

[246] Robert A Divine and Robert Alexander Divine. *The sputnik challenge*. Oxford University Press, 1993.

[247] Louis K. Mansur. “Foreword”. In: *Comprehensive Nuclear Materials*. Ed. by Rudy J.M. Konings. Oxford: Elsevier, 2011, pp. xxiii–xxiv. ISBN: 978-0-08-056033-5. DOI: 10.1016/B978-0-08-056033-5.09014-5. URL: https://www.sciencedirect.com/science/article/pii/B9780080560335090145.

[248] Michael P. Short and Sidney Yip. “Materials Aging at the Mesoscale: Kinetics of Thermal, Stress, Radiation Activations”. In: *Current Opinion in Solid State and Materials Science* 19.4 (Aug. 2015), pp. 245–252. ISSN: 13590286. DOI: 10.1016/j.cossms.2014.12.005.

[249] SI Golubov, BN Singh, and H Trinkaus. “Defect accumulation in fcc and bcc metals and alloys under cascade damage conditions–Towards a generalisation of the production bias model”. In: *Journal of Nuclear Materials* 276.1-3 (2000), pp. 78–89.

[250] Todd R Allen. “High dose radiation effects in steels”. In: *Radiation Effects in Solids*. Springer. 2007, pp. 99–121.

[251] T Niu et al. “Recent studies on void shrinkage in metallic materials subjected to in situ heavy ion irradiations”. In: *JOM* 72 (2020), pp. 4008–4016.

[252] J Knaster, A Moeslang, and T Muroga. “Materials research for fusion”. In: *Nature Physics* 12.5 (2016), pp. 424–434.

[253] Mark T Robinson. “Basic physics of radiation damage production”. In: *Journal of nuclear materials* 216 (1994), pp. 1–28.

[254] Kai Nordlund et al. “Primary Radiation Damage in Materials. Review of Current Understanding and Proposed New Standard Displacement Damage Model to Incorporate in Cascade Defect Production Efficiency and Mixing Effects”. In: (2015).

[255] LR Greenwood. “Neutron interactions and atomic recoil spectra”. In: *Journal of nuclear materials* 216 (1994), pp. 29–44.

[256] Don M Parkin and C Alton Coulter. “Displacement cascades in polyatomic materials”. In: *Journal of Nuclear Materials* 117 (1983), pp. 340–344.

[257] T Muroga, K Kitajima, and S Ishino. “The effect of recoil energy spectrum on cascade structures and defect production efficiencies”. In: *Journal of nuclear materials* 133 (1985), pp. 378–382.

[258] Yue Fan et al. “Mechanism of void nucleation and growth in bcc Fe: atomistic simulations at experimental time scales”. In: *Physical review letters* 106.12 (2011), p. 125501.

[259] FA Garner, MB Toloczko, and BH Sencer. “Comparison of swelling and irradiation creep behavior of fcc-austenitic and bcc-ferritic/martensitic alloys at high neutron exposure”. In: *Journal of Nuclear Materials* 276.1-3 (2000), pp. 123–142.

[260] Stanislav I Golubov, AV Barashev, and Roger E Stoller. “Radiation damage theory”. In: *Comprehensive Nuclear Materials* 1 (2012), pp. 357–391.

[261] C. Abromeit. “Aspects of simulation of neutron damage by ion irradiation”. In: *Journal of Nuclear Materials* 216 (1994), pp. 78–96.

[262] Sun J. et al. “Study of the magnetic modifications of Fe3O4 ferrite thin films induced by 2.03 GeV Kr ions irradiation”. In: *Nuclear Instruments and Methods in Physics Research, Section B: Beam Interactions with Materials and Atoms* 269.9 (2011), pp. 873–875.

[263] Lionel Thomé et al. “Radiation effects in nuclear materials: Role of nuclear and electronic energy losses and their synergy”. In: *Nuclear Instruments and Methods in Physics Research Section B: Beam Interactions with Materials and Atoms* 307 (2013). The 18th International Conference on Ion Beam Modifications of Materials (IBMM2012), pp. 43–48. ISSN: 0168-583X.

[264] S.J. Zinkle. “Effect of irradiation spectrum on the microstructure of ion-irradiated Al2O3”. In: *MRS Symposium Proceedings* 373 (1994), pp. 287–292.

[265] Khalfaoui N. et al. “Damage creation threshold of Al 2O 3 under swift heavy ion irradiation”. In: *Nuclear Instruments and Methods in Physics Research, Section B: Beam Interactions with Materials and Atoms* 286 (2012), pp. 247–253.

[266] Ji Miaomiao. “Computational characterization of radiation-induced defect dynamics and material response”. PhD thesis. Massachusetts Institute of Technology. Department of Nuclear Science and Engineering, 2019.

[267] Yanwen Zhang et al. “Coupled electronic and atomic effects on defect evolution in silicon carbide under ion irradiation”. In: *Current Opinion in Solid State and Materials Science* 21.6 (2017), pp. 285–298. ISSN: 1359-0286.

[268] Lionel Thomé et al. “Combined effects of nuclear and electronic energy losses in solids irradiated with a dual-ion beam”. In: *Applied Physics Letters* 102.14 (2013), p. 141906. DOI: 10.1063/1.4801518.

[269] Lionel Thomé et al. “Behavior of nuclear materials irradiated with a dual ion beam”. In: *Nuclear Instruments and Methods in Physics Research Section B: Beam Interactions with Materials and Atoms* 326 (2014). 17th International Conference on Radiation Effects in Insulators (REI), pp. 219–222. ISSN: 0168-583X. DOI: https://doi.org/10.1016/j.nimb.2013.09.054.

[270] S.J. Zinkle. “Effect of irradiation spectrum on the microstructural evolution in ceramic insulators”. In: *Journal of Nuclear Materials* 219 (1995). Fabrication and Properties of Ceramics for Fusion Energy, pp. 113–127. ISSN: 0022-3115. DOI: https://doi.org/10.1016/0022-3115(94)00662-8.

[271] Cyrus Koroni et al. “Irradiation-Induced Amorphous-to-Crystalline Phase Transformations in Ceramic Materials”. In: *Materials* 15.17 (2022). ISSN: 1996-1944. DOI: 10.3390/ma15175924.

[272] A Meldrum et al. “A Transient Liquid-Like Phase in the Displacement Cascades of Zircon, Hafnon and Thorite”. In: *Nature* 395 (Sept. 1998), pp. 56–58. DOI: 10.1038/25698.

[273] Marcel Toulemonde, E. Paumier, and Christian Dufour. “Thermal spike model in the electronic stopping power regime”. In: *Radiation Effects and Defects in Solids* 126 (Mar. 1993), pp. 201–206. DOI: 10.1080/10420159308219709.

[274] James F. ZieglerJochen P. Biersack. *The Stopping and Range of Ions in Matter*. 1977.

[275] MP Short et al. “Modeling injected interstitial effects on void swelling in self-ion irradiation experiments”. In: *Journal of Nuclear Materials* 471 (2016), pp. 200–207.

[276] R. E. Stoller et al. “On the use of SRIM for computing radiation damage exposure”. In: *Nuclear Instruments and Methods in Physics Research, Section B: Beam Interactions with Materials and Atoms* 310 (2013), pp. 75–80.

[277] NUCLEAR ENERGY AGENCY. *Primary Radiation Damage in Materials*. Report. OECD/NEA, 2015.

[278] S. Agarwal et al. “On the use of SRIM for calculating vacancy production: Quick calculation and full-cascade options”. In: *Nuclear Instruments and Methods in Physics Research Section B: Beam Interactions with Materials and Atoms* 503 (2021), pp. 11–29. ISSN: 0168-583X.

[279] M.J. Norgett, M.T. Robinson, and I.M. Torrens. “A proposed method of calculating displacement dose rates”. In: *Nuclear Engineering and Design* 33.1 (1975), pp. 50–54. ISSN: 0029-5493. DOI: https://doi.org/10.1016/0029-5493(75)90035-7.

[280] GS Was et al. “Emulation of reactor irradiation damage using ion beams”. In: *Scripta Materialia* 88 (2014), pp. 33–36.

[281] Louis Kenneth Mansur. “Void swelling in metals and alloys under irradiation: an assessment of the theory”. In: *Nuclear Technology* 40.1 (1978), pp. 5–34.

[282] LK Mansur. “Correlation of neutron and heavy-ion damage: II. The predicted temperature shift if swelling with changes in radiation dose rate”. In: *Journal of Nuclear Materials* 78.1 (1978), pp. 156–160.

[283] GS Was et al. “Emulation of neutron irradiation effects with protons: validation of principle”. In: *Journal of nuclear materials* 300.2-3 (2002), pp. 198–216.

[284] JL Brimhall, LA Charlot, and EP Simonen. “Effect of pulsed irradiation on void swelling in nickel”. In: *Journal of Nuclear Materials* 104 (1981), pp. 1147–1150.

[285] E Getto et al. “Effect of irradiation mode on the microstructure of self-ion irradiated ferritic-martensitic alloys”. In: *Journal of Nuclear Materials* 465 (2015), pp. 116–126.

[286] A Hishinuma et al. “Effects of pulsed and/or dual ion irradiation on microstructural evolution in a Ti and Si modified austenitic alloy”. In: *Journal of Nuclear Materials* 122.1-3 (1984), pp. 260–265.

[287] EA Little and DA Stow. "Void-swelling in irons and ferritic steels: II. An experimental survey of materials irradiated in a fast reactor". In: *Journal of Nuclear Materials* 87.1 (1979), pp. 25–39.

[288] AD Braislford and R Bullough. "Void growth and its relation to intrinsic point defect properties". In: *Journal of Nuclear Materials* 69 (1978), pp. 434–450.

[289] Scott R Messenger et al. "Modeling solar cell degradation in space: A comparison of the NRL displacement damage dose and the JPL equivalent fluence approaches". In: *Progress in Photovoltaics: Research and Applications* 9.2 (2001), pp. 103–121.

[290] Tetsuo F Miyahira, Farokh Irom, and Allan H Johnston. "Measurements of radiation effects on optoelectronics conducted by the jet propulsion laboratory". In: *2006 IEEE Radiation Effects Data Workshop*. IEEE. 2006, pp. 72–76.

[291] RJ Walters et al. "Space radiation effects in InP solar cells". In: *IEEE transactions on nuclear science* 38.6 (1991), pp. 1153–1158.

[292] URL: https://www.spacesolarshield.polimi.it/.

[293] URL: https://www.fondazionecariplo.it/it/index.html.

[294] URL: https://www2.pvlighthouse.com.au/resources/courses/altermatt/The%20Solar%20Spectrum/The%20extraterrestrial%20%28AM0%29%20solar%20spectrum.aspx.

[295] Bo Meng, Tao Jing, and Wen-Zhi Xiao. "Two-dimensional Al2O3 with ultrawide bandgap and large exciton binding energy for solar-blind ultraviolet photodetectors". In: *Computational Materials Science* 200 (2021), p. 110775.

[296] Takafumi Kamimura et al. "Band alignment and electrical properties of Al2O3/β-Ga2O3 heterojunctions". In: *Applied Physics Letters* 104.19 (2014), p. 192104.

[297] WY Ching and Yong-Nian Xu. "First-Principles Calculation of Electronic, Optical, and Structural Properties of α-Al2O3". In: *Journal of the American Ceramic Society* 77.2 (1994), pp. 404–411.

[298] *Aluminum Oxide | Al2O3 Material Properties*. https://accuratus.com/alumox.html.

[299] JS Dugdale and DKC MacDonald. "The thermal expansion of solids". In: *Physical Review* 89.4 (1953), p. 832.

[300] *Properties: Alumina - Aluminium Oxide - Al2O3 - A Refractory Ceramic Oxide*. https://www.azom.com/properties.aspx?ArticleID=52.

[301] Alain Dubreuil, Martin Malenfant, and AD Pelton. "Thermodynamic stability of beta alumina". In: *Journal of The Electrochemical Society* 128.9 (1981), p. 2006.

[302] Thomas B Reed and Julius Klerer. "Free Energy of Formation of Binaray Compounds: An Atlas of Charts for High-Temperature Chemical Calculations". In: *Journal of The Electrochemical Society* 119.12 (1972), 329Ca.

[303] Emiliano Laudadio et al. "Phase properties of different HfO2 polymorphs: A DFT-based study". In: *Crystals* 12.1 (2022), p. 90.

[304] B Zhou et al. "The simulated vibrational spectra of HfO2 polymorphs". In: *Journal of Physics D: Applied Physics* 47.11 (2014), p. 115502.

[305] Ryan P Haggerty et al. “Thermal expansion of HfO2 and ZrO2”. In: *Journal of the American Ceramic Society* 97.7 (2014), pp. 2213–2222.

[306] Basil Ohnysty and FK Rose. “Thermal expansion measurements on thoria and hafnia to 4500° F”. In: *Journal of the American Ceramic Society* 47.8 (1964), pp. 398–400.

[307] Yuniarto Widjaja and Charles B Musgrave. “Atomic layer deposition of hafnium oxide: A detailed reaction mechanism from first principles”. In: *The Journal of chemical physics* 117.5 (2002), pp. 1931–1934.

[308] Qi-Ya Liu et al. “Band alignment and band gap characterization of La2O3 films on Si substrates grown by radio frequency magnetron sputtering”. In: *Chinese Physics Letters* 31.2 (2014), p. 027702.

[309] CN Chu, N Saka, and NP Suh. “The Coefficients of Thermal Expansion of La2O3, TaVO5 and Ta16W18O94 Below Room Temperature”. In: (1986).

[310] Costas M Soukoulis. *Photonic band gap materials*. Vol. 315. Springer Science & Business Media, 2012.

[311] M Dutta, JM Kalita, and G Wary. “Optical processes and apparent increase of optical band gap in Y2O3: Eu2+ nanoparticles synthesised by a gradually-heated solution combustion method”. In: *Optik* 240 (2021), p. 166946.

[312] JD Mihalov and R Stephen White. “Low-energy proton radiation belts”. In: *Journal of Geophysical Research* 71.9 (1966), pp. 2207–2216.

[313] J Mompart et al. “Calculation of range and energy loss of fast ions with Z 30 using a corrected Bethe-Bloch formula”. In: *Nuclear Instruments and Methods in Physics Research Section B: Beam Interactions with Materials and Atoms* 107.1-4 (1996), pp. 56–61.

[314] Andrew Brown and Herman Suit. “The centenary of the discovery of the Bragg peak”. In: *Radiotherapy and Oncology* 73.3 (2004), pp. 265–268.

[315] FC Marques et al. “Stress and thermomechanical properties of amorphous hydrogenated germanium thin films deposited by glow discharge”. In: *Journal of applied physics* 84.6 (1998), pp. 3118–3124.

[316] Edoardo Besozzi. “Thermomechanical characterization of fusion-relevant nanostructured coatings”. In: *PhD Thesis Politecnico di Milano* (2018).

[317] H Oettel and R Wiedemann. “Residual stresses in PVD hard coatings”. In: *Surface and coatings technology* 76 (1995), pp. 265–273.

[318] Grégory Abadias et al. “Stress in thin films and coatings: Current status, challenges, and prospects”. In: *Journal of Vacuum Science & Technology A: Vacuum, Surfaces, and Films* 36.2 (2018), p. 020801.

[319] Akhilesh Pandey et al. “Growth and evolution of residual stress of AlN films on silicon (100) wafer”. In: *Materials Science in Semiconductor Processing* 52 (2016), pp. 16–23.

[320] AM Engwall, Z Rao, and E Chason. “Origins of residual stress in thin films: Interaction between microstructure and growth kinetics”. In: *Materials & Design* 110 (2016), pp. 616–623.

[321] Alireza Moridi et al. “Residual stresses in thin film systems: Effects of lattice mismatch, thermal mismatch and interface dislocations”. In: *International Journal of Solids and Structures* 50.22-23 (2013), pp. 3562–3569.

[322] Soichan Lei, Jia-Hong Huang, and Haydn Chen. “Measurement of residual stress on TiN/Ti bilayer thin films using average X-ray strain combined with laser curvature and nanoindentation methods”. In: *Materials Chemistry and Physics* 199 (2017), pp. 185–192.

[323] R Huang et al. “Apparatus for measuring local stress of metallic films, using an array of parallel laser beams during rapid thermal processing”. In: *Measurement Science and Technology* 21.5 (2010), p. 055702.

[324] Shankar Dutta et al. “Estimation of boron diffusion induced residual stress in silicon by wafer curvature technique”. In: *Materials Letters* 164 (2016), pp. 316–319.

[325] Eric Chason. “A kinetic analysis of residual stress evolution in polycrystalline thin films”. In: *Thin Solid Films* 526 (2012), pp. 1–14.

[326] George Gerald Stoney. “The tension of metallic films deposited by electrolysis”. In: *Proceedings of the Royal Society of London. Series A, Containing Papers of a Mathematical and Physical Character* 82.553 (1909), pp. 172–175.

[327] URL: `https://www.comsol.com/`.

[328] Carlos A Felippa. “Introduction to finite element methods”. In: *University of Colorado* 885 (2004).

[329] Zhuming Bi. *Finite element analysis applications: a systematic and practical approach*. Academic Press, 2017.

[330] Frank P Incropera et al. *Fundamentals of heat and mass transfer*. Vol. 6. Wiley New York, 1996.

[331] D Demange, M Bejet, and B Dufour. “New methods for measuring the thermal emissivity of semi-transparent and opaque materials”. In: *Proceedings of the 2006 International Conference on Quantitative InfraRed Thermography*. 2006.

[332] COMSOL Multiphysics. “Comsol multiphysics reference manual”. In: *COMSOL: Grenoble, France* 1084 (2013), p. 834.

[333] COMSOL Multiphysics. “Introduction to Heat Transfer Module”. In: *User’s Guide, version* 5 (2016).

[334] Vinh Tung Le, Nam Seo Goo, and Jae Young Kim. “Experimental investigation on thermal contact resistance of alumina fibrous insulation material with Ti-6Al-4V alloy at high temperature and its effective thermal conductivity”. In: *Heat and Mass Transfer* 55 (2019), pp. 1705–1721.

[335] Seval Donertas et al. “Case Study for Thermo Mechanical Performance of an Integrated Optic Device via Equation-Based Modelling”. In: *Gazi University Journal of Science Part A: Engineering and Innovation* 8.1 (2021), pp. 135–145.

[336] AB Comsol. “Structural mechanics module user’s guide”. In: *COMSOL Multiphysics (TM) v* 5 (2012).

[337] C Cibert et al. “Properties of aluminum oxide thin films deposited by pulsed laser deposition and plasma enhanced chemical vapor deposition”. In: *Thin Solid Films* 516.6 (2008), pp. 1290–1296.

[338] Chi-Hui Chien et al. “The effects of film thickness variations on the residual stress distributions in coated Cr thin films”. In: *Strain* 53.2 (2017), e12222.

[339] Yeting Xi et al. “Film thickness effect on texture and residual stress sign transition in sputtered TiN thin films”. In: *Ceramics International* 43.15 (2017), pp. 11992–11997.

[340] CHIH Chen et al. “Residual Stress in C54 Titanium Silicide Formed in Silicon-on-Insulator”. In: *Electrochemical Society Proceedings*. Vol. 96. 3. 1996, pp. 189–195.

[341] MP Hughey, RF Cook, and J Thurn. “Stress stability and thermo-mechanical properties of reactively sputtered alumina films”. In: *Journal of materials science* 40 (2005), pp. 6345–6355.

[342] Harland Tompkins and Eugene A Irene. *Handbook of ellipsometry*. William Andrew, 2005.

[343] Hiroyuki Fujiwara. *Spectroscopic ellipsometry: principles and applications*. John Wiley & Sons, 2007.

[344] Rémi Boidin et al. “Pulsed laser deposited alumina thin films”. In: *Ceramics International* 42.1 (2016), pp. 1177–1182.

[345] Guenter Reisse et al. “Deposition of optical coatings by pulsed laser ablation”. In: *Applied surface science* 96 (1996), pp. 752–759.

[346] Douglas B Chrisey, Graham K Hubler, et al. “Pulsed laser deposition of thin films”. In: *University of Nebraska - Lincon documents* (1994).

[347] William D Callister, David G Rethwisch, et al. *Materials science and engineering: an introduction*. Vol. 7. John wiley & sons New York, 2007.

[348] Bharat Bhushan. *Introduction to tribology*. John Wiley & Sons, 2013.

[349] HN Ritland. “Relation between refractive index and density of a glass at constant temperature”. In: *Journal of the American Ceramic Society* 38.2 (1955), pp. 86–88.

[350] Rajendra K Krishnaswamy and Jay Janzen. “Exploiting refractometry to estimate the density of polyethylene: the Lorentz–Lorenz approach re-visited”. In: *Polymer testing* 24.6 (2005), pp. 762–765.

[351] Li Guan et al. “Role of pulse repetition rate in film growth of pulsed laser deposition”. In: *Nuclear Instruments and Methods in Physics Research Section B: Beam Interactions with Materials and Atoms* 266.1 (2008), pp. 57–62.

[352] K Antonova et al. “Influence of laser pulse frequency on the microstructure of aluminum nitride thin films synthesized by pulsed laser deposition”. In: *Applied Surface Science* 394 (2017), pp. 197–204.

[353] Viét Gabriel et al. “Effect of pulse laser frequency on PLD growth of LuFeO3 explained by kinetic simulations of in-situ diffracted intensities”. In: *Scientific Reports* 12.1 (2022), p. 5647.

[354] Goby A Govindassamy et al. “Effect of laser repetition rate on the growth of Sc2O3 via pulsed laser deposition”. In: *Applied Physics A* 128.7 (2022), p. 577.

[355] AG Every. "The elastic properties of solids: Static and dynamic principles". In: *Handbook of Elastic Properties of Solids, Liquids and Gases* 1 (2001), pp. 3–36.

[356] Marco G Beghi et al. "Ultrasonic and Spectroscopic Techniques for the Measurement of the Elastic Properties of Nanoscale Materials". In: *Nanomechanics-Theory and Application*. IntechOpen, 2021.

[357] Tribikram Kundu. "Mechanics of elastic waves and ultrasonic nondestructive evaluation". In: *Ultrasonic Nondestructive Evaluation: Engineering and Biological Material Characterization (CRC press, New York, 2003)* (2003), pp. 1–95.

[358] MG Beghi et al. "Combined surface Brillouin scattering and x-ray reflectivity characterization of thin metallic films". In: *Journal of applied physics* 81.2 (1997), pp. 672–678.

[359] RJ Jiménez Riobóo et al. "Elastic properties by Brillouin spectroscopy of sol–gel (Pb, Ca) TiO 3 films". In: *Journal of applied physics* 85.10 (1999), pp. 7349–7354.

[360] William Hayes, Rodney Loudon, and Joseph L Birman. "Scattering of light by crystals". In: *Physics Today* 33.4 (1980), p. 55.

[361] Giovanni Carlotti. "Elastic characterization of transparent and opaque films, multilayers and acoustic resonators by surface Brillouin scattering: a review". In: *Applied Sciences* 8.1 (2018), p. 124.

[362] Gerald W Farnell and EL Adler. "Elastic wave propagation in thin layers". In: *Physical acoustics* 9 (2012), pp. 35–127.

[363] Virginio Bortolani et al. "Theory of Brillouin scattering from surface acoustic phonons in supported films". In: *Journal of Physics C: Solid State Physics* 16.9 (1983), p. 1757.

[364] V Bortolani et al. "Strong interference effects in surface Brillouin scattering from a supported transparent film". In: *Physical Review B* 25.5 (1982), p. 3442.

[365] CF Lü, Chee Wah Lim, and WQ Chen. "Size-dependent elastic behavior of FGM ultrathin films based on generalized refined theory". In: *International Journal of Solids and Structures* 46.5 (2009), pp. 1176–1185.

[366] Alexander I Fedorchenko, An-Bang Wang, and Henry H Cheng. "Thickness dependence of nanofilm elastic modulus". In: *Applied Physics Letters* 94.15 (2009), p. 152111.

[367] Hans Joachim Eichler, Peter Günter, and Dieter W Pohl. *Laser-induced dynamic gratings*. Vol. 50. Springer, 2013.

[368] John A Rogers et al. "Optical generation and characterization of acoustic waves in thin films: Fundamentals and applications". In: *Annual Review of Materials Science* 30.1 (2000), pp. 117–157.

[369] APC Wylie et al. "Thermal diffusivity in ion-irradiated single-crystal iron, chromium, vanadium, and tungsten measured using transient grating spectroscopy". In: *Journal of Applied Physics* 132.4 (2022), p. 045102.

[370] I Malfanti et al. "Evidence of slow acoustic surface waves on a 1D phononic surface by a pulsed laser spectroscopic technique resolved in time and space". In: *Europhysics Letters* 97.4 (2012), p. 44010.

[371] Kenji Katayama et al. “Generation and detection of tunable phonon polaritons using a single transmission grating”. In: *Applied Physics Letters* 92.3 (2008), p. 031906.

[372] Jeremy A Johnson et al. “Direct measurement of room-temperature nondiffusive thermal transport over micron distances in a silicon membrane”. In: *Physical review letters* 110.2 (2013), p. 025901.

[373] Shengchang Tang, Muzhou Wang, and Bradley D Olsen. “Anomalous self-diffusion and sticky Rouse dynamics in associative protein hydrogels”. In: *Journal of the American Chemical Society* 137.11 (2015), pp. 3946–3957.

[374] N Osada et al. “Photoexcited carrier dynamics of double-layered CdS/CdSe quantum dot sensitized solar cells measured by heterodyne transient grating and transient absorption methods”. In: *Physical Chemistry Chemical Physics* 16.12 (2014), pp. 5774–5778.

[375] Darius H Torchinsky et al. “Fluctuating charge-density waves in a cuprate superconductor”. In: *Nature materials* 12.5 (2013), pp. 387–391.

[376] AA Maznev et al. “Laser-based surface acoustic wave spectrometer for industrial applications”. In: *Review of scientific instruments* 74.1 (2003), pp. 667–669.

[377] AA Maznev, KA Nelson, and JA Rogers. “Optical heterodyne detection of laser-induced gratings”. In: *Optics letters* 23.16 (1998), pp. 1319–1321.

[378] OW Käding et al. “Transient thermal gratings at surfaces for thermal characterization of bulk materials and thin films”. In: *Applied Physics A* 61 (1995), pp. 253–261.

[379] Abdallah Reza et al. “Non-contact, non-destructive mapping of thermal diffusivity and surface acoustic wave speed using transient grating spectroscopy”. In: *Review of Scientific Instruments* 91.5 (2020), p. 054902.

[380] Felix Hofmann et al. “Non-contact measurement of thermal diffusivity in ion-implanted nuclear materials”. In: *Scientific reports* 5.1 (2015), pp. 1–7.

[381] Cody A Dennett and Michael P Short. “Thermal diffusivity determination using heterodyne phase insensitive transient grating spectroscopy”. In: *Journal of Applied Physics* 123.21 (2018), p. 215109.

[382] Felix Hofmann, Michael P Short, and Cody A Dennett. “Transient grating spectroscopy: An ultrarapid, nondestructive materials evaluation technique”. In: *MRS Bulletin* 44.5 (2019), pp. 392–402.

[383] Eduardo Salas et al. “Surface acoustic wave velocity of gold films deposited on silicon substrates at different temperatures”. In: *Journal of Applied Physics* 110.2 (2011), p. 023503.

[384] Engineers Edge. *Thermal diffusivity table*. URL: `https://www.engineersedge.com/heat_transfer/thermal_diffusivity_table_13953.htm`.

[385] A Rudajevová. “Thermal diffusivity of plasma sprayed alumina coatings”. In: *Materials research bulletin* 26.12 (1991), pp. 1363–1369.

[386] Bart Verstraeten et al. “Determination of thermoelastic material properties by differential heterodyne detection of impulsive stimulated thermal scattering”. In: *Photoacoustics* 3.2 (2015), pp. 64–77.

[387] JR Matthews. "The quantitative description of deformation and stress in cylindrical fast reactor fuel pins". In: *Advances in Nuclear Science and Technology*. Elsevier, 1972, pp. 65–104.

[388] Dinesh C Agrawal and R Raj. "Measurement of the ultimate shear strength of a metal-ceramic interface". In: *Acta Metallurgica* 37.4 (1989), pp. 1265–1270.

[389] John A Nairn and Kim Sung-Ryong. "A fracture mechanics analysis of multiple cracking in coatings". In: *Engineering Fracture Mechanics* 42.1 (1992), pp. 195–208.

[390] John W Hutchinson. "Stresses and failure modes in thin films and multilayers". In: *Notes for a Dcamm Course. Technical University of Denmark, Lyngby* 1 (1996), p. 14.

[391] Paul H Wojciechowski and Michael S Mendolia. "Fracture and cracking phenomena in thin films adhering to high-elongation substrates". In: *Physics of thin films*. Vol. 16. Elsevier, 1992, pp. 271–340.

[392] BORIS PALADINO. "Amorphous alumina coatings for next generation nuclear systems". In: *PhD Thesis Politecnico di Milano* (2022).

[393] Jiali Zhou et al. "Mechanical Properties of Tensile Cracking in Indium Tin Oxide Films on Polycarbonate Substrates". In: *Coatings* 12.4 (2022), p. 538.

[394] M Yanaka et al. "Cracking phenomena of brittle films in nanostructure composites analysed by a modified shear lag model with residual strain". In: *Journal of Materials Science* 33 (1998), pp. 2111–2119.

[395] Ramesh Talreja. "Transverse cracking and stiffness reduction in composite laminates". In: *Journal of composite materials* 19.4 (1985), pp. 355–375.

[396] JC Grosskreutz and MB McNeil. "The fracture of surface coatings on a strained substrate". In: *Journal of Applied Physics* 40.1 (1969), pp. 355–359.

[397] Alan Arnold Griffith. "VI. The phenomena of rupture and flow in solids". In: *Philosophical transactions of the royal society of london. Series A, containing papers of a mathematical or physical character* 221.582-593 (1921), pp. 163–198.

[398] HL Cox. "The elasticity and strength of paper and other fibrous materials". In: *British journal of applied physics* 3.3 (1952), p. 72.

[399] J Aveston and A Kelly. "Theory of multiple fracture of fibrous composites". In: *Journal of Materials Science* 8 (1973), pp. 352–362.

[400] J Aveston and Anthony Kelly. "Tensile first cracking strain and strength of hybrid composites and laminates". In: *Philosophical Transactions of the Royal Society of London. Series A, Mathematical and Physical Sciences* 294.1411 (1980), pp. 519–534.

[401] KW Garrett and JE Bailey. "Multiple transverse fracture in 90 cross-ply laminates of a glass fibre-reinforced polyester". In: *Journal of materials science* 12 (1977), pp. 157–168.

[402] Y Liu et al. "Evaluation of the interfacial shear strength and residual stress of TiAlN coating on ZIRLO™ fuel cladding using a modified shear-lag model approach". In: *Journal of Nuclear Materials* 466 (2015), pp. 718–727.

[403] JL Beuth Jr. "Cracking of thin bonded films in residual tension". In: *International Journal of Solids and Structures* 29.13 (1992), pp. 1657–1675.

[404] Lu Gan, Jian Wang, and Robert M Pilliar. "Evaluating interface strength of calcium phosphate sol–gel-derived thin films to Ti6Al4 V substrate". In: *Biomaterials* 26.2 (2005), pp. 189–196.

[405] Mikko Ruoho et al. "Thin-film engineering of mechanical fragmentation properties of atomic-layer-deposited metal oxides". In: *Nanomaterials* 10.3 (2020), p. 558.

[406] KL Mittal. "Adhesion measurement of thin films". In: *Electrocomponent Science and technology* 3.1 (1976), pp. 21–42.

[407] TS Chow. "Theory of unsymmetric laminated plates". In: *Journal of Applied Physics* 46.1 (1975), pp. 219–221.

[408] TS Chow. "Adhesion of Brittle Films on a Polymeric Substrate". In: *Bulletin of the American Physical Society*. Vol. 20. 3. AMER INST PHYSICS CIRCULATION FULFILLMENT DIV, 500 SUNNYSIDE BLVD, WOODBURY ... 1975, pp. 481–481.

[409] TS Chow, CA Liu, and RC Penwell. "Direct determination of interfacial energy between brittle and polymeric films". In: *Journal of Polymer Science: Polymer Physics Edition* 14.7 (1976), pp. 1305–1310.

[410] RC Penwell, KS Liang, and TS Chow. "The effect of interfacial bonding on the adhesion of brittle film-polymer multilayered structures". In: *Thin Solid Films* 60.2 (1979), pp. 133–139.

[411] J Dundurs. "Discussion:"Edge-bonded dissimilar orthogonal elastic wedges under normal and shear loading"(Bogy, DB, 1968, ASME J. Appl. Mech., 35, pp. 460–466)". In: (1969).

[412] 1Y Leterrier et al. "Adhesion of silicon oxide layers on poly (ethylene terephthalate). II: Effect of coating thickness on adhesive and cohesive strengths". In: *Journal of Polymer Science Part B: Polymer Physics* 35.9 (1997), pp. 1463–1472.

[413] R Ali, M Sebastiani, and E Bemporad. "Influence of Ti–TiN multilayer PVD-coatings design on residual stresses and adhesion". In: *Materials & Design* 75 (2015), pp. 47–56.

[414] Chau Hsien Lin, Hsiao Lei Wang, and Min Hsiung Hon. "The effect of residual stress on the adhesion of PECVD-coated aluminum oxide film on glass". In: *Thin Solid Films* 283.1-2 (1996), pp. 171–174.

[415] Sergio Neves Monteiro et al. "High temperature plastic instability and dynamic strain aging in the tensile behavior of AISI 316 stainless steel". In: *Materials Research* 20 (2017), pp. 506–511.

[416] Martin Smolka et al. "Novel temperature dependent tensile test of freestanding copper thin film structures". In: *Review of scientific instruments* 83.6 (2012), p. 064702.

[417] Florian Toth et al. "Detailed modelling of delamination buckling of thin films under global tension". In: *Acta materialia* 61.7 (2013), pp. 2425–2433.

[418] Viggo Tvergaard and John W Hutchinson. "The influence of plasticity on mixed mode interface toughness". In: *Journal of the Mechanics and Physics of Solids* 41.6 (1993), pp. 1119–1135.

[419] MF Kanninen et al. “Elastic-plastic fracture mechanics for two-dimensional stable crack growth and instability problems”. In: *Elastic-Plastic Fracture, ASTM STP* 668 (1979), pp. 121–150.

[420] Donato Girolamo et al. “Cohesive laws and progressive damage analysis of composite bonded joints, a combined numerical/experimental approach”. In: *56th AIAA/ASCE/AHS/ASC Structures, Structural Dynamics, and Materials Conference*. 2015, p. 1578.

[421] N Chandra et al. “Some issues in the application of cohesive zone models for metal–ceramic interfaces”. In: *International Journal of Solids and Structures* 39.10 (2002), pp. 2827–2855.

[422] William J Weber and Yanwen Zhang. “Predicting damage production in monoatomic and multi-elemental targets using stopping and range of ions in matter code: Challenges and recommendations”. In: *Current Opinion in Solid State and Materials Science* 23.4 (2019), p. 100757.

[423] Marquis A Kirk et al. “Predicting neutron damage using TEM with in situ ion irradiation and computer modeling”. In: *Journal of Nuclear Materials* 498 (2018), pp. 199–212.

[424] A Zaborowska et al. “Absolute radiation tolerance of amorphous alumina coatings at room temperature”. In: *Ceramics International* 47.24 (2021), pp. 34740–34750.

[425] Weilin Jiang, Liang Jiao, and Haiyan Wang. “Transition from irradiation-induced amorphization to crystallization in nanocrystalline silicon carbide”. In: *Journal of the American Ceramic Society* 94.12 (2011), pp. 4127–4130.

[426] Takeshi Nagase et al. “MeV electron irradiation induced crystallization in metallic glasses: Atomic structure, crystallization mechanism and stability of an amorphous phase under the irradiation”. In: *Journal of non-crystalline solids* 358.3 (2012), pp. 502–518.

[427] Francisco Garcıéa Ferré et al. “Radiation endurance in Al2O3 nanoceramics”. In: *Scientific Reports* 6.1 (2016), p. 33478.

[428] F. G. Ferré et al. “Corrosion and radiation resistant nanoceramic coatings for lead fast reactors”. In: *Corrosion Science* 124 (2017), pp. 80–92.

[429] Warren Carl Oliver and George Mathews Pharr. “An improved technique for determining hardness and elastic modulus using load and displacement sensing indentation experiments”. In: *Journal of materials research* 7.6 (1992), pp. 1564–1583.

[430] M Dao et al. “Strength, strain-rate sensitivity and ductility of copper with nanoscale twins”. In: *Acta materialia* 54.20 (2006), pp. 5421–5432.

[431] Yinmin Wang et al. “High tensile ductility in a nanostructured metal”. In: *nature* 419.6910 (2002), pp. 912–915.

[432] Jakob Schiøtz, Francesco D Di Tolla, and Karsten W Jacobsen. “Softening of nanocrystalline metals at very small grain sizes”. In: *Nature* 391.6667 (1998), pp. 561–563.

[433] J Musil et al. “Thermal stability of alumina thin films containing γ-Al2O3 phase prepared by reactive magnetron sputtering”. In: *Applied surface science* 257.3 (2010), pp. 1058–1062.

[434] Priyanka Nayar et al. “Structural, optical and mechanical properties of amorphous and crystalline alumina thin films”. In: *Thin Solid Films* 568 (2014), pp. 19–24.

[435] Quan Li et al. “Low-temperature magnetron sputter-deposition, hardness, and electrical resistivity of amorphous and crystalline alumina thin films”. In: *Journal of Vacuum Science & Technology A: Vacuum, Surfaces, and Films* 18.5 (2000), pp. 2333–2338.

[436] M Sridharan et al. “Pulsed DC magnetron sputtered Al2O3 films and their hardness”. In: *Surface and coatings technology* 202.4-7 (2007), pp. 920–924.

[437] R Cremer et al. “Comparative characterization of alumina coatings deposited by RF, DC and pulsed reactive magnetron sputtering”. In: *Surface and coatings technology* 120 (1999), pp. 213–218.

[438] Viktoria Edlmayr et al. “Thermal stability of sputtered Al2O3 coatings”. In: *Surface and Coatings Technology* 204.9-10 (2010), pp. 1576–1581.

[439] URL: `https://www.directindustry.it/prod/union-optic-inc/product-173804-1761577.html`.

[440] Jemila Habainy et al. “Thermal diffusivity of tungsten irradiated with protons up to 5.8 dpa”. In: *Journal of Nuclear Materials* 509 (2018), pp. 152–157.

[441] Abdallah Reza et al. “Thermal diffusivity degradation and point defect density in self-ion implanted tungsten”. In: *Acta Materialia* 193 (2020), pp. 270–279.

[442] Matthew C Wingert et al. “Thermal transport in amorphous materials: a review”. In: *Semiconductor Science and Technology* 31.11 (2016), p. 113003.

[443] Chang Jun Jeon, Won Jae Yeo, and Eung Soo Kim. “Effect of crystallization on thermal conductivity of diopside”. In: *Journal of the Ceramic Society of Japan* 118.1383 (2010), pp. 1079–1082.

[444] Ce-Wen Nan, Xiao-Ping Li, and R Birringer. “Inverse problem for composites with imperfect interface: determination of interfacial thermal resistance, thermal conductivity of constituents, and microstructural parameters”. In: *Journal of the American Ceramic Society* 83.4 (2000), pp. 848–854.

[445] Meimei Li, Wei-Ying Chen, and Peter M. Baldo. “In situ transmission electron microscopy with dual ion beam irradiation and implantation”. In: *Materials Characterization* 173 (2021), p. 110905.

[446] James F. Ziegler, M.D. Ziegler, and J.P. Biersack. “SRIM – The stopping and range of ions in matter (2010)”. In: *Nuclear Instruments and Methods in Physics Research Section B: Beam Interactions with Materials and Atoms* 268.11 (2010). 19th International Conference on Ion Beam Analysis, pp. 1818–1823.

[447] Kai Nordlund et al. “Primary radiation damage: A review of current understanding and models”. In: *Journal of Nuclear Materials* 512 (2018), pp. 450–479.

[448] P. Souza Santos, H. Souza Santos, and S.P. Toledo. “Standard transition aluminas. Electron microscopy studies”. In: *Materials Research* 3 (Oct. 2000), pp. 104–114.

[449] Balaraman Sathyaseelan, Iruson Baskaran, and Kandasamy Sivakumar. "Phase Transition Behavior of Nanocrystalline Al2O3 Powders". In: *Soft Nanoscience Letters* 03 (Jan. 2013), pp. 69–74.

[450] Linus Pauling and Sterling B. Hendricks. "THE CRYSTAL STRUCTURES OF HEMATITE AND CORUNDUM". In: *Journal of the American Chemical Society* 47.3 (1925), pp. 781–790.

[451] Samir Lamouri et al. "Control of the γ-alumina to α-alumina phase transformation for an optimized alumina densification". In: *Boletín de la Sociedad Española de Cerámica y Vidrio* 56.2 (2017), pp. 47–54. ISSN: 0366-3175.

[452] David Mitchell. "DiffTools: Electron diffraction software tools for DigitalMicrograph™". In: *Microscopy research and technique* 71 (July 2008), pp. 588–93.

[453] Alwyn Eades. "Electron Crystallography: Electron Microscopy and Electron Diffraction, X. Zou, S. Hovmoeller, and P Oleynikov. Oxford University Press (IUCr Texts on Crystallography16), 2011, 335 pages. ISBN 978-0-19-958020-0(Hardcover)". In: *Microscopy and Microanalysis* 18.3 (2012), pp. 645–646.

[454] M. Vanazzi. "Development of advanced nano-ceramic coatings for future generation nuclear reactors". PhD Thesis. Politecnico di Milano, 2019.

[455] Rasband W. S. Schneider C. A. and K. W. Eliceiri. "NIH Image to ImageJ: 25 years of image analysis". In: *Nature Methods* (2012).

[456] A. A. Othman, K. Tahon, and M. Osman. "Glass transition and crystallization kinetic studies in Mg0.10As0.34Se0.56 chalcogenide glass by using non-isothermal techniques". In: *Physica B-condensed Matter* 311 (2002), pp. 356–365.

[457] D. Turnbull J.E. Burke. "Recrystallization and grain growth". In: *Progress in Metal Physics* 3 (1952), pp. 220–292. ISSN: 0502-8205.

[458] Corrado Spinella, Salvatore Lombardo, and Francesco Priolo. "Crystal grain nucleation in amorphous silicon". In: *Journal of Applied Physics* 84.10 (1998), pp. 5383–5414.

[459] R. Nuernberg and O. Montedo. "Crystallization Kinetics of β-Spodumene/Cordierite-Based Glass-Ceramics". In: *Materials Science Forum* 881 (2016), pp. 83–88.

[460] Jaromir Moravec. "Determination of the grain growth kinetics as a base parameter for numerical simulation deman". In: *MM Science Journal* (2015), pp. 649–653.

[461] Alan Giumelli. "Auskinetics and the grain size distributionetnite grain growth". Univeristy og Wollongong, 1991.

[462] Peng Cao, Li Lu, and M.O. Lai. "Grain growth and kinetics for nanocrystalline magnesium alloy produced by mechanical alloying". In: *Materials Research Bulletin* 36 (Mar. 2001).

[463] Shu Hu and Paul C. McIntyre. "Nucleation and growth kinetics during metal-induced layer exchange crystallization of Ge thin films at low temperatures". In: *Journal of Applied Physics* 111.4 (2012), p. 044908.

[464] S. K. DUTTA and R. M. SPRIGGS. "Grain Growth in Fully Dense ZnO". In: *Journal of the American Ceramic Society* 53.1 (1970), pp. 61–62.

[465] C. M. KAPADIA and M. H. LEIPOLD. "Grain Growth in Pure Dense MgO". In: *Journal of the American Ceramic Society* 57.1 (1974), pp. 41–42.

[466] V PETROVIC and M.M. Ristic. "Isochronal and isothermal grain growth during sintering of cadmium oxide". In: *Metallography* 13 (Dec. 1980), pp. 319–327.

[467] T. Y. TIEN and E. C. SUBBARAO. "Grain Growth in Ca0.16Zr0.84O1.84". In: *Journal of the American Ceramic Society* 46.10 (1963), pp. 489–492.

[468] T. Spassov and U. Koester. "Grain-growth in nanocrystalline zirconium-based alloys". In: *Journal of Materials Science* 28.10 (1993), pp. 2789–2794.

[469] G. T. Higgins. "Grain-Boundary Migration and Grain Growth". In: *Metal Science* 8.1 (1974), pp. 143–150.

[470] Jiang Shi et al. "Kinetic analysis of crystallization in Li2O-Al2O3-SiO2-B2O3-BaO glass-ceramics". In: *Journal of Non-Crystalline Solids* 491 (2018), pp. 106–113.

[471] D. Kaoumi, Arthur Thompson Motta, and R. C. Birtcher. "Grain growth in nanocrystalline metal thin films under in situ ion-beam irradiation". In: *Effects of Radiation on Materials*. ASTM Special Technical Publication. Effects of Radiation on Materials: 23rd International Symposium ; Conference date: 13-06-2006 Through 15-06-2006. ASTM International, 2008, pp. 206–218.

[472] D. Kaoumi, A. T. Motta, and R. C. Birtcher. "A thermal spike model of grain growth under irradiation". In: *Journal of Applied Physics* 104.7 (2008), p. 073525. DOI: 10.1063/1.2988142.

[473] Hanns Gietl et al. "Neutron irradiation-enhanced grain growth in tungsten and tungsten alloys". In: *Journal of Alloys and Compounds* 901 (2022), p. 163419. ISSN: 0925-8388. DOI: https://doi.org/10.1016/j.jallcom.2021.163419.

[474] Donald R. Askeland and Wendelin J. Wright. *The science and engineering of materials*. 2016.

[475] M. Ghasemzadeh et al. "Crystallization kinetics of glass-ceramics by differential thermal analysis". In: *Ceramics - Silikaty* 55 (June 2011), pp. 188–194.

[476] R. B. Nuernberg, C. A. Faller, and O. R. K. Montedo. "Crystallization kinetic and thermal and electrical properties of β-spodumeness/cordierite glass–ceramics". In: *Journal of Thermal Analysis and Calorimetry* 127.1 (2016), pp. 355–362.

[477] M.I. Abd-Elrahman et al. "The activation energies at glass transition temperatures and dynamic fragility of (Se90Te10)100-x Inx glassy alloys". In: *Thermochimica Acta* 672 (2019), pp. 86–92.

[478] Ioannis Nikolakakis and Kyriakos Kachrimanis. "Crystallization kinetics of orthorhombic paracetamol from supercooled melts studied by non-isothermal DSC". In: *Drug Development and Industrial Pharmacy* 43 (2017), pp. 257–263.

[479] Siuli Dutta et al. "Microstructural evolution, recovery and recrystallization kinetics of isothermally annealed ultra low carbon steel". In: *Materials Research Express* 7 (Jan. 2020).

[480] Zhongtian Mao and Charles T. Campbell. “Apparent Activation Energies in Complex Reaction Mechanisms: A Simple Relationship via Degrees of Rate Control”. In: *ACS Catalysis* 9.10 (2019), pp. 9465–9473.

[481] B. -. Kim, K. Hiraga, and K. Morita. “Kinetics of normal grain growth depending on the size distribution of small grains”. In: *Nippon Kinzoku Gakkaishi/Journal of the Japan Institute of Metals* 68.10 (2004), pp. 913–918.

[482] Kenji Okazaki and Hans Conrad. “Grain Size Distribution in Recrystallized Alpha-Titanium”. In: *Transactions of the Japan Institute of Metals* 13.3 (1972), pp. 198–204.

[483] “Grain growth in metals”. In: *Acta Metallurgica* 5.2 (1957), pp. 97–105. ISSN: 0001-6160.

[484] “A stochastic theory of grain growth”. In: *Acta Metallurgica* 35.7 (1987), pp. 1723–1733. ISSN: 0001-6160.

[485] C.S. Pande and E. Dantsker. “On a stochastic theory of grain growth—II”. In: *Acta Metallurgica et Materialia* 38.6 (1990), pp. 945–951. ISSN: 0956-7151.

[486] H.V. Atkinson. “THEORIES OF NORMAL GRAIN GROWTH IN PURE SINGLE PHASE SYSTEMS”. In: *Acta metall.* (1988).

[487] D.B. Williams and C.B Carter. *Transmission Election Microscope*. 2009.

[488] D Jensen. “Estimation of the size distribution of spherical, disc-like or ellipsoidal particles in thin foils”. In: *Journal of Physics D: Applied Physics* 28.3 (1995), pp. 549–558.

[489] Thomas M. Hare, John C. Russ, and Jay E. Lane. “Volume determination of TEM specimens containing particles or precipitates”. In: *Journal of Electron Microscopy Technique* 10.1 (1988), pp. 1–6.

[490] S.J. Zinkle and C. Kinoshita. “Defect production in ceramics”. In: *Journal of Nuclear Materials* 251 (1997). Proceedings of the International Workshop on Defect Production, Accumulation and Materials Performance in an Irradiation Environment, pp. 200–217. ISSN: 0022-3115. DOI: https://doi.org/10.1016/S0022-3115(97)00224-9.

[491] R. F. Geller and Paul J. Yavorsky. “Melting point of alpha-alumina”. In: *Journal of research of the National Bureau of Standards* 34 (1945), p. 395.

[492] EA Little. “Development of radiation resistant materials for advanced nuclear power plant”. In: *Materials Science and Technology* 22.5 (2006), pp. 491–518.

[493] Yuexin Su and Yuting Ye. “The Review of Types of Radiation Resistance Materials and Proposed Experiments”. In: *Journal of Physics: Conference Series*. Vol. 2386. 1. IOP Publishing. 2022, p. 012090.

[494] Mikhail Zhernenkov et al. “Design of radiation resistant metallic multilayers for advanced nuclear systems”. In: *Applied Physics Letters* 104.24 (2014).

[495] Paola Palmero and Claude Esnouf. “Phase and microstructural evolution of yttrium-doped nanocrystalline alumina: A contribution of advanced microscopy techniques”. In: *Journal of the European Ceramic Society* 31.4 (2011), pp. 507–516.

[496] Boro DJURICIC et al. “Thermal stability of transition phases in zirconia-doped alumina”. In: *Journal of materials science* 32 (1997), pp. 589–601.

[497] Jon Martin Andersson. “Controlling the formation and stability of alumina phases”. PhD thesis. Institutionen för fysik, kemi och biologi, 2005.

[498] Erik Wallin et al. “Effects of additives in α-and θ-alumina: an ab initio study”. In: *Journal of Physics: Condensed Matter* 16.49 (2004), p. 8971.

[499] Ketan Patel et al. “Structural effects of lanthanide dopants on alumina”. In: *Scientific reports* 7.1 (2017), p. 39946.

[500] Aurelian Marcu et al. “Pulsed laser deposition of YBCO thin films in a shadow mask configuration”. In: *Thin Solid Films* 360.1-2 (2000), pp. 166–172.

[501] G Koren et al. “Laser wavelength dependent properties of YBa2Cu3O7- δ thin films deposited by laser ablation”. In: *Applied Physics Letters* 55.23 (1989), pp. 2450–2452.

[502] RE Leuchtner, JS Horwitz, and DB Chrisey. “Particulate distributions in Pt films prepared by pulsed laser deposition”. In: *Journal of applied physics* 83.10 (1998), pp. 5477–5483.

[503] HL Spindler, Ronald M Gilgenbach, and JS Lash. “Effects of laser-ablation target damage on particulate production investigated by laser scattering with deposited thin film and target analysis”. In: *Applied physics letters* 68.23 (1996), pp. 3245–3247.

[504] Soon-Gul Lee et al. “Deposition angle-dependent morphology of laser deposited YBa2Cu3O7 thin films”. In: *Applied physics letters* 65.6 (1994), pp. 764–766.

[505] G Koren et al. “Particulates reduction in laser-ablated YBa2Cu3O7- δ thin films by laser-induced plume heating”. In: *Applied physics letters* 56.21 (1990), pp. 2144–2146.

[506] B Holzapfel et al. “Off-axis laser deposition of YBa2Cu3O7- δ thin films”. In: *Applied Physics Letters* 61.26 (1992), pp. 3178–3180.

[507] EV Pechen et al. “Pulsed-laser deposition of smooth high-T c superconducting films using a synchronous velocity filter”. In: *Applied physics letters* 66.17 (1995), pp. 2292–2294.

[508] Kazuya Kinoshita, Hiroshige Ishibashi Hiroshige Ishibashi, and Takeshi Kobayashi Takeshi Kobayashi. “Improved surface smoothness of YBa2Cu3Oy films and related multilayers by ArF excimer laser deposition with shadow mask “Eclipse method””. In: *Japanese journal of applied physics* 33.3B (1994), p. L417.

[509] Minoru Tachiki et al. “SrTiO 3 films epitaxially grown by eclipse pulsed laser deposition and their electrical characterization”. In: *Journal of applied physics* 83.10 (1998), pp. 5351–5357.

[510] S Yu Sokovnin et al. “Effect of iron doping on the properties of nanopowders and coatings on the basis of Al 2 O 3 produced by pulsed electron beam evaporation”. In: *Nanotechnologies in Russia* 8 (2013), pp. 466–481.

List of Figures

List of Tables

Acknowledgments

Venturing upon this research odyssey was a fulfilling yet arduous endeavor, compounded by the formidable obstacles posed by COVID-19. However, I persevered, ultimately attaining my goals. This remarkable achievement would not have been possible without exceptional individuals and organizations' unwavering support and invaluable contributions. To all those who lent a helping hand along this intricate path, I am forever grateful for their assistance, which has left an indelible mark on my journey.

I have immense appreciation for the Space Solar Shield Cariplo project, as its funding has enabled the realization of my doctoral research. The objective of advancing the development of space solar cells with high efficiency and radiation resistance is of utmost importance for upcoming space missions. However, it also serves as a testament to the unwavering commitment to innovation and pursuit of excellence of the Cariplo Foundation.

I am also thankful for the GEMMA European project, whose dynamic and visionary research approach broadened my horizons and equipped me with invaluable experience in proposing innovative materials for the next generation of nuclear power plants.

My journey would not have been complete without the Progetto Rocca Foundation. Through their boundless generosity, I was bestowed with the extraordinary opportunity to immerse myself in the MIT realm of brilliance alongside the esteemed Prof. Michael Short and his awe-inspiring Mesoscale Nuclear Material group at MIT. This life-altering expedition has unleashed a metamorphosis within me, kindling a relentless passion that will forever burn bright. I shall forever hold in my heart an indelible debt of gratitude for prof Short and his group support and unparalleled mentorship.

I express my deepest gratitude to my supervisor, Marco Beghi, and to Fabio Di Fonzo, whose unwavering guidance and mentorship were paramount to the triumph of this project. Their profound wisdom and unparalleled expertise shaped the course of my academic voyage. I am profoundly indebted to them for their unwavering support and profound influence, for they have been the cornerstone of my growth and development.

I owe a great debt of gratitude to my family, whose constant love, support, and encouragement have been my pillar of strength and motivation. I am also grateful to my friends, whose unwavering support and positivity have been the driving force behind my success.

In conclusion, I am deeply grateful to all the collaborators, organizations, and individuals who

contributed to this work. Their support and contributions were instrumental in the success of this project, and I am honored to have had the opportunity to work with such remarkable people.

Hey gang, guess what? I'm not going to mention names. Why, you ask? Because every single one of you pitched in and helped make this a home run. Now, if I start saying names and my memory decides to play tricks, well, I'd unintentionally leave someone out. That'd be a bummer, wouldn't it? So here's to everyone! Every one of you is the secret ingredient in my recipe of success. Now, how about a conga line of celebration?